ECCI ANALYSIS OF SLIP ACCOMMODATIONS IN POLYCRYSTAL ALPHA TITANIUM DURING HETEROGENEOUS PLASTIC DEFORMATION

By

Songyang Han

A DISSERTATION

Submitted to
Michigan State University
in partial fulfillment of the requirements
for the degree of

Materials Science and Engineering – Doctor of Philosophy

2020

ABSTRACT

ECCI ANALYSIS OF SLIP ACCOMMODATIONS IN POLYCRYSTAL ALPHA TITANIUM DURING HETEROGENEOUS PLASTIC DEFORMATION

By

Songyang Han

Heterogeneous deformation is particularly important in polycrystalline α-titanium, because the hexagonal crystal structure makes it more prone to polycrystalline compatibility issues. At the dislocation scale, this compatibility involves the process of how dislocations being initiated, propagating through grains, and the ability of grain boundaries accommodating dislocation shear in one grain with shear in its neighboring grain. To characterize the development of plasticity in a polycrystalline array due to dislocation nucleation, and slip across grains and grain boundaries, electron channeling contrast imaging (ECCI) based analysis is used, since this special scanning electron microscopy (SEM) technique possesses variety observation scopes, providing a linkage between the macro- and the micro- world.

The first study presented a robust comparison between several techniques for the very first time: the digital image correlation (DIC), atomic force microscope (AFM), ECCI, and EBSD (cross-correlation). In this study, a Ti7Al alloy was deformed to 3% plastic tensile strain. The plasticity evolution of the sample was assessed through BESD-slip trace analysis, digital image correlation, and ECCI contrast analysis. The comparison between different methods revealed ECCI as a powerful technique in slip system identifications.

The second project was more focused on the interactions between slip systems around the grain boundary area. The geometry of slip planes and grain boundaries was assessed as a function of depth, allowing the analysis of slip transfer parameters, including the geometric

compatibility factor m’, the global Schmid factor of active slip systems, and the angles between slip planes. Locally accommodation behavior at the grain boundaries were revealed by ECCI.

The third project was the identification of the propagation direction of a slip system across a polycrystalline grain patch by ECCI. Analysis indicated that slip bands would likely to become broader as they propagated further into the grain from the nucleation points, possibly due to cross-slipping. Together with the trace analysis, a better understanding of the development of plasticity within polycrystals during heterogeneous deformation was achieved.

The highlight of this work not only focusing on the infinitesimal change in the local lattice structure in terms of dislocation nucleation and propagation in a grain, but also involves the plasticity development of deformation in a macroscopic view, such as the mechanism of dislocation across grain boundaries, and the estimation of overall deformation behavior within a region of grains. More importantly, together with other powerful characterization methods, ECCI in this study shows a strong potential that successfully links the macroscopic deformation with dislocation movement during the deformation.

To my wife Dongqing Tao and daughter Freya Han. Thank you for your love and supports.

ACKNOWLEDGEMENTS

First and foremost, I would like to gratefully acknowledge my advisor, Dr. Martin Crimp. Over the numerous conversations of research ideas, paper discussions, and even non-academic topics, I continuously sharpen my writing skills, being more diligent as a researcher, and becoming more confident and expressive as an overall person. These improvements are mostly relied on his wisdom, patience, and the confidence in me. It will be an honorable memory as a graduate student of his.

I also give my thanks to the committee members, Professor Philip Eisenlohr, Professor Carl Boehlert, and Professor Thomas Pence, for their enlightening discussions.

To past and current of members of the “Metal Group”, Yang Su, Bret Dunlap, Quan Zhou (Jason), Harsha Phukan, Mingming Wang for helping me in the research. I also want to thank Dr. Per Askeland on training the scanning electron microscope and teaching me the maintenance of microscope.

Many thanks go to Dr. Christopher Cowen, formerly at National Energy Technology Laboratory, Albany OR, for supplying the titanium studied in this work. Acknowledgements also go to Professor Samantha Daly, and Dr. Zhe Chen, at University of California Santa Barbara, for the DIC support, and Professor David Fullwood, at Brigham Young University, for the CC-EBSD support.

Finally, the research is supported by the United States Department of Energy, Office of Basic Energy Science Division, through grant number DE-SC0001525 and DE-FG02-09ER46637.

TABLE OF CONTENTS

LIST OF TABLES

LIST OF FIGURES

KEY TO ABBREVIATIONS AND SYMBOLS

AFM	Atomic Force Microscopy
Au	Gold
AuNP	Gold Nanoparticles
BSE	Backscattered Electron
CC-EBSD	Cross-Correlation Electron Backscattered Diffraction
CRSS	Critical Resolved Shear Stress
CSL	Coincident Site Lattice
DIC	Digital Image Correlation
EBSD	Electron Backscattered Diffraction
EBSPs	Electron Backscattering Patterns
ECCI	Electron Channeling Contrast Imaging
ECPs	Electron Channeling Patterns
EDM	Electronic Discharge Machining
FEG-SEM	Field Emission Gun Scanning Electron Microscope
FIB	Focused Ion Beam
FSE	Forward-Scatter Electron
GNDs	Geometrically Necessary Dislocations
hcp	hexagonal close-packed crystal structure
HR-EBSD	High Resolution Electron Backscattered Diffraction
LRB	Lee–Robertson–Birnbaum

MATLAB	Matrix Laboratory
Ni	Nickel
OIM	Orientation Imaging Microscopy
OPS	Colloidal Silica Suspension
SACPs	Selected Area Channeling Patterns
SE	Secondary Electron
SiC	Silicon Carbide
TBAF	Tetra-n-Butylammonium Fluoride
TEM	Transmission Electron Microscopy
Ti	Titanium
Ti-7-Al	Titanium Aluminum Alloy
b	Burgers vector
g	vector that describes the electron imaging/channeling condition
κ	angle between Burgers vectors
l	rotation axis between intersecting lattices
M	Schmid factor
m'	predictive parameter of slip transfer using κ and Ψ
n	slip plane normal
S	stress
Ψ	angle between slip plane normals
s	deviation factor from the exact Bragg’s angle
t	intersection line of a slip system on the grain boundary plane

τ	resolve shear stress
τ_c	critical resolved shear stress
u	dislocation line direction
Σ	the reciprocal of total atoms at Coincident Site Lattice to the total atoms
ω	rotation angle between two intersecting lattices
ε	strain
P	stress on the slip system
Θ	angle between intersection lines of slip systems at a grain boundary plane
Å	Angstrom, 10^{-10} meters

1. Introduction

1.1 Heterogeneous deformation of commercially pure titanium

With the increasing demand for α-titanium and titanium alloys across a wide range of industries, due to their good corrosion resistance, high strength to density ratio, and biomedical compatibilities [1-5], the desire to manipulate and precisely predict the performance of such hexagonal materials during service also grows stronger. However, wide replacement of cubic materials (i. e. steel) with such promising metals is still impossible, because the detailed deformation evolution mechanisms of hexagonal titanium are not yet well understood. Cubic materials usually show “stable” orientation changes in a certain deformation mode, which makes it easier to precisely model the deformation textures [6-8]. On the contrary, such “common” expectations do not always exist in commercially pure α-titanium (and other hcp metals) [9-12] since the orientation change and slip-twin distribution are not consistent to give predictable textures under the same deformation mode [13, 14]. Nevertheless, such inconsistency challenges the establishment of a reliable model, and the key to elucidate this unpredictable deformation behavior is the full understanding of the mechanisms of heterogeneous deformation of hcp titanium.

1.1.1 Plastic heterogeneity of commercially pure titanium

Heterogeneous deformation is common in all polycrystalline metals. Plastic heterogeneity happens due to strain variations from grain to grain since all the grains experience different deformation processes due to varying crystal orientations. In plastic deformation models, Talyor and Houttee [15, 16] suggested that strains could be equally distributed among all the grains under a macroscopically uniform deformation. This worked well for materials with cubic symmetry because each grain is able to activate multiple slip systems with comparable critical resolved shear stress (CRSS, τ_c) to accommodate the partitioned strain. Thus, heterogeneous deformation is not a serious problem for cubic materials. However, this assumption failed on materials with lower symmetry, such as hcp titanium. As shown in **Figure 1**, there are several deformation slip systems in commercially pure titanium, including $\{10\bar{1}0\}$ <$1\bar{2}10$ > prismatic <a> slip, $\{0001\}$ <$1\bar{2}10$ > basal <a> slip,

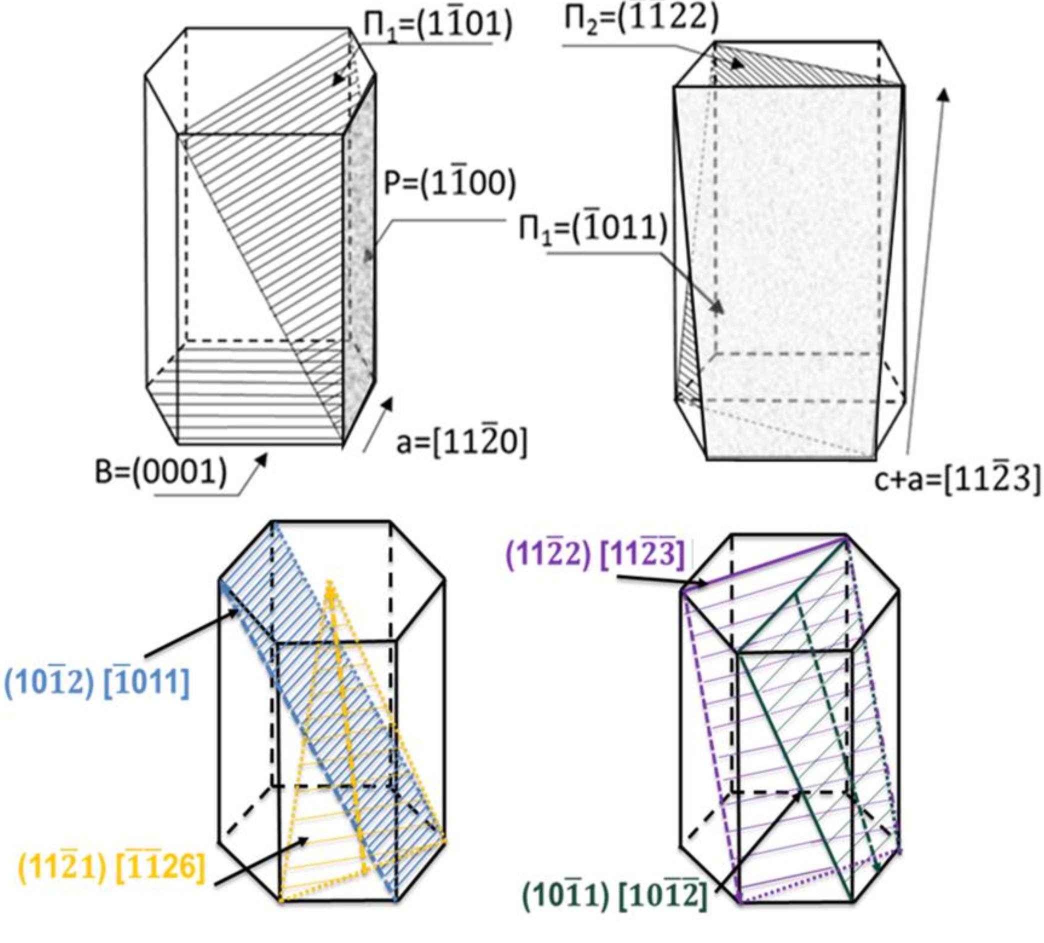

Figure 1 Top two crystals present the major slip systems activated during deformation, namely: (Top left) prism <a> slip system on $\{1\bar{1}00\}$ prismatic plane, basal <a> slip system on {0001} basal plane, and pyramidal <a> slip system on $\{1\bar{1}01\}$ pyramidal plane with <11$\bar{2}$0> Burgers vector; (Top right) type I <c + a> slip system on $\{\bar{1}011\}$ pyramidal plane, and type II <c + a> on $\{\bar{1}\bar{1}22\}$ pyramidal plane. Bottom two crystals show the geometry of two tensile twinning (labeled in blue and yellow) and two compression twinning (labeled in purple and dark green), which is not readily observed in room temperature deformation and not the interest of this study.

$\{10\bar{1}1\}$ $<1\bar{2}10>$ pyramidal <a> slip, and $\{10\bar{1}1\}$ $<\bar{1}\bar{1}23>$ pyramidal <c + a> slip ($\{\bar{1}\bar{1}22\}$ pyramidal <c + a> is rare). Tensile and compressive twinning does exist as additional deformation systems, but twinning activation is dependent on elemental composition [17] and thus not easily predictable. Due to the anisotropic nature of the low symmetry of hexagonal crystal lattice, the activities of these deformation systems are dramatically different, with the prismatic <a> slip systems being the most observed among all deformation systems [18-25]. Such different activation of deformation systems is due to a large deviation in the CRSS value among these deformation systems [26]. Although CRSS values are sensitive to elemental compositions [27-30] and dependent on testing methods [31-38], the CRSS of the prismatic slip system is more likely found to be the lowest at room temperature in commercially pure titanium[1]. The CRSS value of the basal slip system is the second lowest, around 1.2 ~ 2.6 times larger than the prism <a> slip [28, 36, 37]. Pyramidal deformation systems, including pyramidal <a> and pyramidal <c + a> slip systems, usually have CRSS values around 1.3 ~ 8 times larger than the prism <a> slip system [25-28, 34-37]. As a result, it is much harder for other slip systems, especially pyramidal slip systems, to be activated. As indicated by Von Mises [39], an individual grain needs at least five independent slip systems to accommodate change shape. Thus, every titanium crystal needs to activate multiple different slip system types to maintain polycrystalline integrity. In reality, this constraint is hard to achieve since slip activities in titanium is not uniformly distributed due to the variability of CRSS of the different slip system types. Thus, plasticity models of titanium often fail since heterogeneity is not able to be

---

[1] Basal may become lower than prism slip system at levitated temperature and in some alloys [38], that is why CRSS value is material dependent.

correctly modelled to reflect the real-life deformation.

In addition to the CRSS issue, due to the low symmetry of titanium, the deformation of a single crystal through one type of slip system at a certain orientation usually means the activation of the other slip system is not favorable. For example, if $[11\bar{2}0]$ is favorably activated with a high Schmid factor, then $[1\bar{2}10]$ and $[2\bar{1}\bar{1}0]$ slip are typically not equally activated at the same time since their Schmid factors are usually low. Thus, the deformation of a crystal has to follow a certain direction, with other slip activation somewhat suppressed. However, in polycrystal deformation, it is not quite possible to relief all the strain by the activation of the primary slip system, and the suppression of other slip systems cause incomplete strain relaxation, thus cause strain accumulation within the grain. In a polycrystal, some grains are "soft" because it is easy to activate some slip systems with low CRSS values based on their lattice orientations. However, other grains may appear "hard" because their crystal orientations only allow high-CRSS-value deformation systems [40-42]. Based on the uneven distribution of plastic strain among the grains and the incomplete strain relaxation due to lack of slip activation, strains that are not fully relaxed may accumulate at the grain boundaries.

1.1.2 Accommodation at grain boundaries

Micro-cracks will form at the grain boundaries if they fail to sufficiently accommodate the strain localization on both sides [43-46]. At the grain-scale level, in order to maintain grain boundary integrity, the resulting strain must be released by either transferring across the grain boundary into the neighboring grain, or sometimes reflecting back to the original grain. At the nanoscale or atomic level, dislocations that are carrying the strain get restrained at a grain boundary, because the extensive atomic disordered grain boundary interface disrupts the propagation of dislocations within a confined plane. The continuous piling-up of dislocations around the grain boundary can be sources for the dislocation activations in either grains [47-48], and cause strain hardening of the grain boundary if the strain is not completely carried away [49]. Finally, incomplete accommodation of the boundary strain at the "blocked" tip of dislocation slip encourages the further disruption of the grain boundary atomic configuration, creating more defects and voids at the interface between the joining grains, and eventually create micro-cracks on the grain boundary. This is believed as the precursor of material failure [45, 50, 51]. In the heterogeneous deformation of titanium, the capability of a grain boundary to accommodate the strain is difficult. As discussed previously, individual grains with varying crystal orientations deform differently, so the grain boundaries have to deal with different amounts of strain from different directions at the same time. As a result, it is critical to understand the nature of grain boundaries and how grain boundaries accommodate the heterogeneous strain from the grains.

1.1.3 The geometry of grain boundary and its effect on dislocations

It is important to understand how a grain boundary reacts to dislocation shear based on its geometric characters. Compared with the unique atomic arrangement within a lattice, a grain boundary is a disordered interface between the joining crystals. Such disordered structural defects are usually high energy sites and can be dislocation sinks and sources [52-55] based on how the lattice is misorientated at the grain boundary.

By and large, there are several different ways to describe the crystallography of a grain boundary, namely: tilt/twist boundary, symmetric/asymmetric boundary, and the **Σ** boundary. Tilt and twist boundaries are formed when two adjoining crystal lattices share a same rotation axis **l**, as illustrated by **Figure 2 a&b**. For a pure tilt boundary, the rotation axis **l** lies in the boundary plane. On the contrary, the axis **l** lies perpendicular to boundary plane in a pure twist boundary [56]. This approach defines the configuration of a grain boundary by five-degrees of freedom, including the grain boundary normal **n**, two crystallographic orientations of the neighboring crystals $\mathbf{n_1}$ and $\mathbf{n_2}$, the rotation axes **l**, and the rotation angles $\boldsymbol{\omega}$ (the total misorientation can be broken down into a combination of $\boldsymbol{\omega}_{\textbf{tilt}}$ and $\boldsymbol{\omega}_{\textbf{twist}}$ about the respective

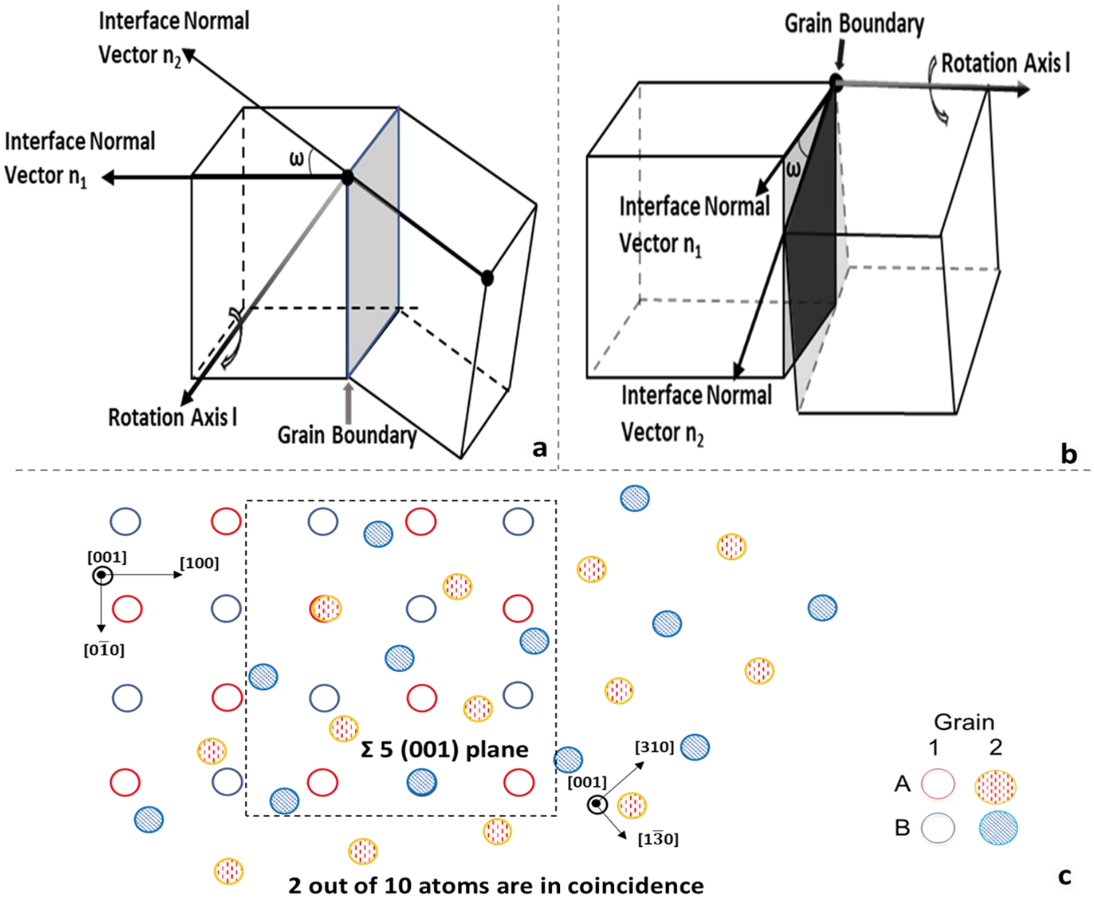

Figure 2a) Sketch of a pure tilt boundary, indicating two crystals are rotated by angle $\boldsymbol{\omega}_{\textbf{tilt}}$ about a rotation axis lying on the grain boundary plane. b) A pure twist boundary is formed, which looks like a single crystal is twisted into half along a rotation axis lying perpendicular to the grain boundary with misorientation angle $\boldsymbol{\omega}_{\textbf{twist}}$. c) Sketch of **Σ 5** boundary, formed by a 36.9° rotation between two same lattices about a common [001] axis. In this picture, the atom A and B in grain 1 are represented by circles with no fill, while the same atom in grain 2 are pattern filled circles, and the grain boundary lattice area is limited by the dotted square. After carefully counting, it can be found that every 2 out of 10 atoms are sharing the same lattice position. It is noticeable that **Σ** value may different about different rotation axis. (Amended from [57, 65])

rotation axes **l**)[57]. In this approach, the geometry of a grain boundary cannot be simply defined by a fixed rotation and twist angle, since different rotation and twist combinations can achieve the same misorientation structure of the boundary lattice. Specifically, to further describe a pure tilt/twist boundary, the concept of symmetric and asymmetric boundary is then applied based on the relationship of the tilt axis direction to the grain boundary plane. For example, the symmetric boundary is defined when the grain boundary plane is mirrored about the shared axis direction. By specifying the family of the rotation axis and the information discussed above (i. e. {210}<001> symmetric tilt boundary, with misorientation angle 53.1°), a more precise definition of the grain boundary is thus presented to outline the grain boundary atomic structure [58-64] for molecular dynamic modeling. Another common approach that describes the geometric configuration of the grain boundary is the **Σ** boundary, usually used together with the coincident site lattice (CSL) model [65]. The grain boundary is simply viewed as a region of interpenetrating lattice points between the neighboring misorientated grains. There will be some lattice points in that region where the atoms from the adjacent grains overlap. Those points are called coincident site lattice points. The **Σ** value is the value of the total number of atoms over the number of atoms that are in coincident sites. An example of **Σ** 5 boundary is presented in **Figure 2c,** since 2 out of 10 atoms on the grain boundary plane are in coincident sites. This boundary is formed by a 36.9° rotation between two perfect cubic lattices about a common [001] axis. This pure geometric model categorizes some specific grain boundaries out of the common boundaries and provides another way to quantify the misorientation. Grain boundaries with low **Σ** values (more atoms share the coincident sites) suggest there are little mismatch and little lattice disorder between the adjacent grains.

Further studies have found that low **Σ** boundaries usually show unique behaviors than non-**Σ** ones during deformation. For instance, some low **Σ** boundaries are found to prevent creep formation in a Ni alloy [66], while coherent twin **Σ**3 boundaries are particularly good for inhabiting cracks [67], etc. Nonetheless, the energy barrier of the grain boundary for dislocation transmission and nucleation is also found to be related to the **Σ** value. As indicated by Sangid et al [62], the energy barrier for dislocation transmission and nucleation at a **Σ**3 boundary was particularly high, suggesting this boundary was an effective block to dislocations. In that study, kinetic factors including the geometry of the loading orientations of the bicrystals, and the Schmid factors, were also found to have strong impacts on the dislocation/grain boundary interactions. It should be realized that the grain boundary models discussed above are mainly developed from cubic or other higher symmetry systems [52-69], until recently, K. Glowinski et al [70] applied this concept to hexagonal systems. In the study, they categorized the grain boundary geometry with rotation axes/planes and Σ boundaries, and specified the similarity and difference with the cubic systems in the atomic configuration. That study helped establish a system to correctly represent the grain boundary configuration for the hcp system.

All in all, these lattice models indeed provide clues on plasticity transfer across grain boundaries in plasticity modeling, and specifically, reveal how dislocations dissociate and cross-slip at/within special grain boundary interfaces [58, 62, 68, 69]. However, for the convenience of modeling-based studies and to reduce complexities, there are some assumptions or simplifications in these models. Such compromises make the modeling less effective at representing real-life heterogeneous deformation of polycrystals, with the reasons listed as follows:

- Although there have been a considerable amount of studies of special grain boundaries (i. e. Σ 3, 5, 11, etc.) that show consistent behaviors of the dislocations, the behaviors of dislocations at non-Σ boundaries with uncategorized disordered lattice configurations cannot be easily predicted. The understanding of grain boundary accommodations with dislocation shear in heterogeneous deformation should also include general boundaries, and these special models do not work well.
- In the models, the dislocation shear is usually started from an intentionally induced defect within a grain and then propagated to the grain boundary. For convenience, the dislocation type was also given, and the shear was considered to be homogeneous among the same type slip bands within the grain. However, the direction of real-life deformation shear as well as the activation of dislocations are not always predetermined since the heterogeneous deformation is not limited to only one grain, but also its surrounding grains. The amount of shear carried by each slip band was also not equal during the deformation.
- Modeling studies until recent usually limit the interactions between one incoming dislocation with one grain boundary, including new dislocation initiations or the absorption/reflection of the incoming dislocation. However, except in special cases, there will typically be activation of multiple slip systems, which make the grain boundary accommodation events more complicated than the models.

Collectively, a more reliable approach is thus needed to study the accommodation behavior by efficiently revealing the dislocation/grain boundary interactions in hexagonal titanium. The active slip systems should be correctly identified, the direction of shear transfer should be grasped, and the models should be also applied on common grain boundaries. As is discovered by Sangid et al [62], the Schmid factors, the orientation of crystals, and the geometry of grain boundary interfaces are all important elements affecting the interaction between dislocations and boundaries. Moreover, since dislocations are found to dissociate into dislocation partials or cross-slip during propagation within grain boundary lattices, these studies also suggest that residual dislocations left in the grain boundary will be an important factor in the dislocation/grain boundary interaction studies.

1.1.4 Interactions between dislocations at general grain boundaries

Different from studies that focused on the effect of grain boundary atomic configurations on the dislocations, numerous studies have successfully illustrated the interactions between dislocation slip and unspecified grain boundaries. Bayerschen et al. and other researcher [71-75] have summarized several possible accommodating mechanisms when an incoming dislocation meets a grain boundary. These mechanisms are illustrated in **Figure 3**, namely: a) The direct slip transfer of an incoming dislocation into the neighboring grain without leaving any residual dislocations in the grain boundary. b) The direct transfer of an incoming dislocation across the grain boundary by initiating a different type of outgoing dislocation in the joining grain and thus leaving residual dislocations in the grain boundary. c) The full absorption of an incoming dislocation into the grain boundary. This process creates grain boundary dislocations that can be moved elsewhere under applied stress. d) An indirect slip transfer process, including the absorption of an incoming dislocation, and the re-emission of an outgoing dislocation at the boundary. Since the incoming and outgoing dislocations are not

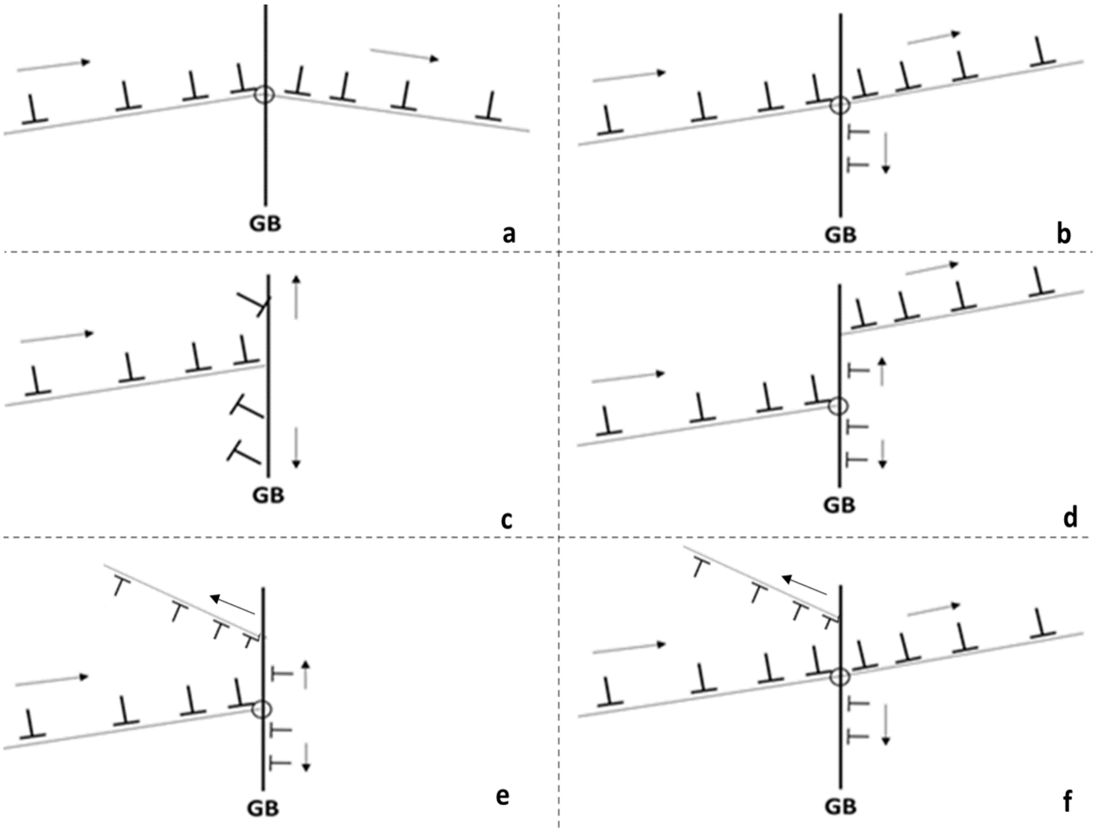

Figure 3a) Direct transfer of dislocation across grain boundary. b) Direct slip transfer with residual dislocations at the grain boundary. c) Absorption of dislocation slip and dissipated along grain boundary. d) indirect slip transfer by absorption and re-emission, leaving grain boundary dislocations. e) Absorption and reflection of dislocations slip with residual grain boundary dislocations. f) Complicated mechanism, involving both slip transfer and reflection with the formation of grain boundary dislocations.

directly connected, this process usually involves the participation of grain boundary dislocations. e) The absorption of an incoming dislocation and initiation of outgoing dislocations back to the same grain. f) The direct slip transfer of dislocation, creating new dislocations both in the adjacent grain and back into the original grain.

Situations e) and f) are not as common as the other accommodating models. Li et al [76] found that it was more energetically favorable for a dislocation to cross a grain boundary than being reflected back. It should be noted that, although not common, such mechanisms have been both observed by the in-situ transmission electron microscopy (TEM) studies [35, 77, 78] and included in the plastic modeling [76, 79]. The mechanism f) emphasizes the conditions for multiple activation of dislocation slip at a grain boundary during accommodation events, which is important in the heterogeneous deformation.

Livingston and Chalmers [80] were among the first of several researchers studying the activation of multiple slip systems in plastic deformation. In their studies, they induced a deformation shear that was carried to the grain boundary through a known slip system by one deforming crystal ("parent" grain A, shown in **Figure 4**) and studied how the shear was accommodated by the neighboring crystal ("receiving" grain B). A series of bi-crystal systems with different orientation combinations were tested. The strain components (ε_{zz}, ε_{xx}, and ε_{xz} shown in **Figure 4**) created by the "incoming" slip system need to be fully balanced by the activation of "outgoing" slip system(s) at the grain boundary to maintain macroscopic compatibility of the bi-crystal system. This theory was referred as tangential continuity, and it

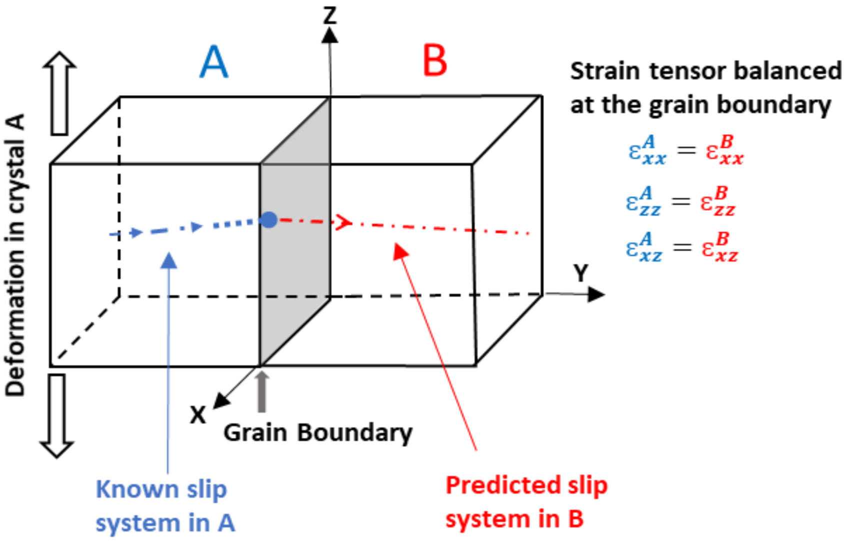

Figure 4 As crystal A with known lattice orientation is continuously deformed, a known type dislocation slip (blue) is piling up at the grain boundary, where dislocation slip (red) will be activated in crystal B due to stress build-up as it deformed with crystal A. During the slip transfer, tangential continuity constrain is required that requires the strain component induced by dislocations in crystal A be fully balanced in crystal B to maintain grain boundary integrity. (Amended from [80])

required a total of four degrees of freedom within the two adjoining grains during the accommodation events. This included the situations of one incoming slip system in the parent grain A being accommodated by three outgoing slip systems in the receiving grain B, two slip systems (including the incoming one that was already known) in A being accommodated by two slip systems in B, and three by one, respectively. This concept considered the potential for self-accommodation, where the strain accommodation was not limited to the neighboring grain, but also the grain where the strain was originated. Nonetheless, with the combination of the pile-up stress and the geometric tangential continuity, Livingston and Chalmers outlined a criterion that was used to predict the activation of the "outgoing" slip system in the "receiving" grain across the boundary based on the "incoming" slip system in the "parent" grain:

$$P_i = P\, N_{1i} = P\, [(\mathbf{n}_1 \cdot \mathbf{n}_i)\, (\mathbf{b}_1 \cdot \mathbf{b}_i) + (\mathbf{n}_1 \cdot \mathbf{b}_i)\, (\mathbf{n}_i \cdot \mathbf{b}_1)] \quad \text{...} \ 1$$

where P was the stress of the slip system, $\mathbf{n}_1$ & $\mathbf{b}_1$ was the slip plane normal and Burgers vector in the "parent" grain, and $\mathbf{n}_i$ & $\mathbf{b}_i$ was the corresponding parameters for any active slip system in the "receiving" grain.

This criterion is useful for predicting the primary (and sometimes secondary) slip systems in the "receiving" grain, but most of the time, not useful for identifying slip systems in the "parent" grain. The authors also mentioned that this criterion is not useful for the prediction of minor slip systems, due to more complicated mechanisms at the boundary. By removing the stress component that needed to be calculated/measured from case to case, this criterion was later simplified to a pure geometric constraint. This criterion is now well known as the N factor, and is widely applied in many later studies as a slip transfer criterion [81-87]:

$$N_{in\text{-}out} = (\mathbf{n}_{in} \cdot \mathbf{n}_{out})\, (\mathbf{b}_{in} \cdot \mathbf{b}_{out}) + (\mathbf{n}_{in} \cdot \mathbf{b}_{out})\, (\mathbf{n}_{out} \cdot \mathbf{b}_{in}) \quad \text{....................................} \ 2$$

Influenced by Livingston and Chalmers [80] and their collaborators [88], sequential slip transfer criteria have been developed in order to predict the slip systems activated as a result of shear accommodation at grain boundaries, with the geometry of slip systems and grain boundary illustrated by **Figure 5**. Among these criteria, the M[2] factor was established by Shen et al. [81], evaluating slip transfer events from a different perspective than the N factor:

$$M = (\mathbf{t}_{in} \cdot \mathbf{t}_{out})\,(\mathbf{b}_{in} \cdot \mathbf{b}_{out}) = \cos \Theta \cos \kappa \quad \ldots\ldots \quad 3$$

This criterion considered the angle Θ between the intersection of the line directions (**t**) of slip planes at the grain boundary plane, and the angle κ between the Burgers vectors (**b**) of the slip systems on both sides of the grain boundary. At the same time, Lee et al. [83-86] laid

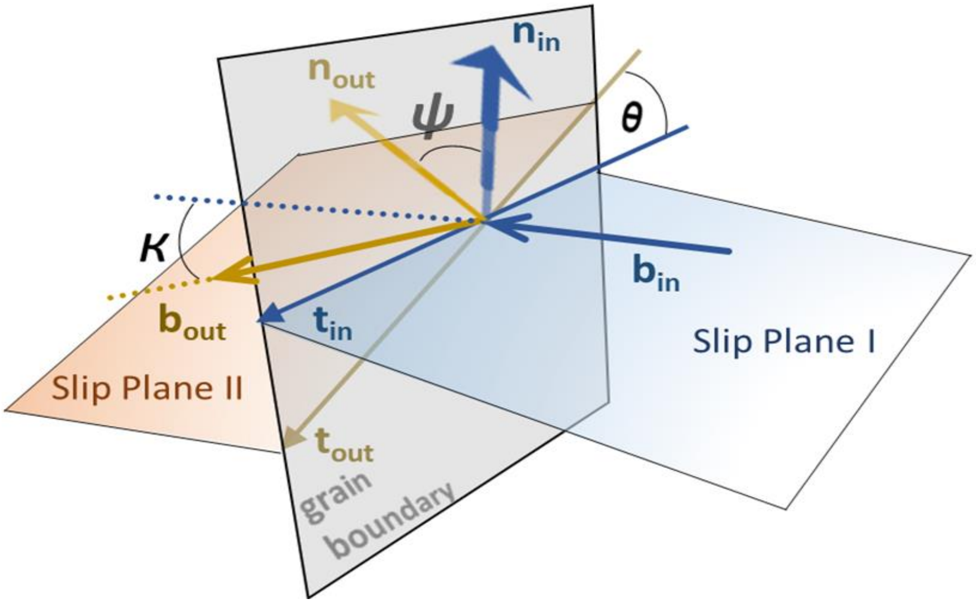

Figure 5 A sketch of the geometry of slip planes intersecting at a grain boundary plane. **b**, **t**, **n**, are the Burgers vector, the intersection line direction of the slip plane in the grain boundary plane, and the slip plane normal that are used in the various slip transmission criterion [80, 81, 95]. Slip plane I (blue) is usually considered from the “incoming” slip system in the “parent” grain, and slip plane II (brown) is the “outgoing” slip system in the “receiving” grain.

---

[2] M is usually a symbol of the Schmid factor (SF) in many research. To avoid the misuse of M, this factor is usually used as the LRB factor after Lee et al.

out criteria based on the M factor. It agreed that slip transmissions can happen when M was maximized, but two additional stress components should also be included: First, the resolved shear stress for the "outgoing" slip system should be maximized. Second, the magnitude of residual Burgers vector left in the grain boundary should be minimized. This combination criteria, known as the LRB criteria, provided significant insights regarding the importance of residual Burgers vector in slip transmissions as well as its influence on grain boundary deformation [89-94].

Another more convenient criterion was outlined by Luster and Morris [95], referred as the geometric compatibility factor:

$$m' = (\mathbf{n}_{in} \cdot \mathbf{n}_{out})\,(\mathbf{b}_{in} \cdot \mathbf{b}_{out}) = \cos\psi \cos\kappa \quad \ldots\ldots\ldots\ldots\ldots\ldots \quad 4$$

where ψ is the angle between the slip plane normals and κ is the angle between Burgers vectors. This simplified version of the N factor has been extensively used [96-100] since the angle ψ between plane normals is easily acquired from electron backscatter diffraction (EBSD), whereas the measurement of angle Θ requires grain boundary orientation assessment, which is not available only through surface analysis.

Meanwhile, a λ function was created by Werner and Prantl [101], dealing with slip transfer between different phases:

$$\lambda = \cos\left(\frac{90^{o}\psi}{\psi_c}\right) \cos\left(\frac{90^{o}\kappa}{\kappa_c}\right) \quad \ldots\ldots\ldots\ldots\ldots\ldots \quad 5$$

Slip transmission was expected only when the angle ψ and κ were both restricted within a limited value ($\psi_c = 15^{o}$ and $\kappa_c = 45^{o}$). The application of this λ function is not as wide as the m' since it was mainly for intra-phase slip transmissions.

For the most part, the application of different criteria has fulfilled different requirements in the study of slip transmissions [74, 75, 102], and in particular, combined criteria that coupled some of the geometric parameters with accumulated shear stress γ [74] or the Schmid factor M [103] have made more statistically reliable predictions of slip activity. However, one may realize that despite the factor PN_{1i} outlined by Livingston and Chalmers et al. [80, 88] that have indicated the need for multiple activations of slip systems during slip accommodation, as well as Shen et al. [81] that have discussed the observation of slip multiplicity within the vicinity of grain boundaries, many follow-up criteria have become more and more simplified, assuming:

- ➢ The "incoming" slip system is usually believed to be accommodated by only one deformation system during one slip transfer activity, although comparisons of parameters between different slip systems are quite common.
- ➢ Similar to the limitation of many modeling studies, the direction of deformation shear is monodirectional, always between a "parent" and a "receiving" grain. Many studies have focused on the cases where a known incoming slip piled-up at a grain boundary activated an "outgoing" dislocation slip that carried the shear away.

Undoubtedly, the simplified criteria are extremely useful, especially when the target of interest is limited to bicrystals. However, this is far from accurate in the study of heterogeneous deformation of polycrystals. For the first assumption, based on both the Livingston and Chalmers' tangential continuity theory [80] and the Von Mises's theory (five independent slip system to maintain integrity) [39], it is necessary to have more than one accommodating slip system to be activated to fully accommodate the strain at the grain boundary[3]. Accommodation by multiple slip systems was recently reported by Su et al. [104]. One primary “incoming” slip system from a “parent” grain was sometimes found to be accommodated by two major “outgoing” slip systems at the grain boundary. The activation of double accommodation was a complicated competition between many factors including the local/global stress state, the strain associated with the “incoming” slip system, and the residual Burgers vectors. Despite this research, until now, how other deformation systems affect slip transmission is still not clear. For the second assumption, it only worked perfectly in the bi-crystal system in an ideal condition but not precise in the heterogeneous deformation, where shear transfer is not necessarily limited to one given direction. As reviewed by Bayerschen et al. [71] and other researchers across different time spans [80, 81, 88, 105], “reflection” of “incoming” dislocations into a “parent” grains can happen even when the strain is primarily carried away by the activation of an “outgoing” slip system in the “receiving” grain. Moreover, in real-life deformation, the grain that is considered as a “receiving” grain also deforms independently due to the applied stress, and the deformation shear in the “receiving” grain also needs to be transferred out at the grain boundary. Thus, it is not reasonable to say the deformation shear from grain to grain is in one direction, since the role of “parent” and “receiving” can be switched accordingly. Nevertheless, these ideal models neglect the situation that dislocations can be nucleated at the grain boundary and carry the accumulated shear out of the grain boundary by propagating into both grains. This is also an important mechanism to

---

[3] Although grain boundary dislocations can also carry away accumulated strain at the boundary, the migration of grain boundary dislocations may cause severe grain boundary movement or cracking.

protect the integrity of the grain boundary, since the grain boundary can be a source for dislocation activation. So far, whether slip transfer criteria can be effectively applied in this situation is still unanswered.

Thus, in order to further the understanding of heterogeneous deformation of commercially pure titanium, it is necessary to figure out if the classic slip transfer criteria or relative plastic models (m', etc.) are sensitive to the direction of shear transfer (dislocation initiation at a grain boundary and propagation into the adjoining grains). Additionally, it may also be necessary to identify the direction of strain transfer within patches of grains. If possible, it is insightful to identify which grain is actively deforming with respect to the applied stress and which is deforming passively to accommodate the deformation of its neighbor. By extension, if one is able to locate the grain boundaries where the flow of strain is concentrated and is not able to be well accommodated, such grain boundaries may be vulnerable to damage nucleation during the deformation.

1.2 Introduction of experimental techniques

There are generally several analytical methods used to identify the deformation slip systems, the nature of the dislocations (in terms of Burgers vectors, slip directions and slip planes), and the relative strain distributions across the deformed material. Rather than simply laying out numerical expressions that are boring and non-intuitive, the following sections provide a brief introduction and a comparison of different analytical methods that are used for dislocation-level characterization. The purpose of this section is to elucidate the advantage of using electron channeling contrast imaging (ECCI) in this study, since it is capable of both grasping the macroscopic deformation of the material and providing microscopic detailed information including the nature and relative distribution of the dislocations. When carefully planned, ECCI is able to avoid the biasing of the free surface and provide information on how deformation shear is accommodated within and between grains associated with other techniques.

1.2.1 Electron backscatter diffraction (EBSD)

EBSD is used to acquire the crystal orientation distributions and the changes in orientation during the loading process, both of which are important information in the study of heterogeneous deformation. The overall set-up for the EBSD technique is shown in **Figure 6a**. The crystal orientation of a grain is achieved based on the electron backscattering patterns (EBSP), which appears as a map of intersecting pairs of parallel Kikuchi-lines on a phosphor screen (**Figure 6b**) [106, 107]. In order to maximize the backscattered signal collected by the detector, a high surface normal tilt angle of 70^o is generally used. As the incident beam electrons inelastically scattering in all directions within a crystal, some electrons hit the crystal lattice planes at the Braggs' angle[4] and will be elastically scattered and form reinforced beams of electrons exiting the sample surface. As the inelastically scattered electrons vary in directions, all Bragg diffracted electrons scattering at a lattice plane at the same Bragg's angle form a surface of a cone, referred as the Kossel cone. Since the scattering events occur in a very small volume and therefore can be considered to occur at single planes, a lattice plane thus will be represented as a pair of Kossel cones, which manifest as two parallel Kikuchi lines

---

[4] $n\lambda = 2\,d_{hkl} \sin \Theta_B$, where n is a positive integer, λ is the wavelength of the electron beam, d_{hkl} is the distance of the Miller indexed (h k l) lattice plane, and Θ_B is the Bragg's angle that elastically scattered electrons can form constructive signals. Based on different lattice structure, some combination of h, k, l will result in constructive reflections, enhancing the signal, while in other cases results in destructive/forbidden reflections and thus give weak signal.

when the two cones are projected onto the detector screen. With Bragg diffraction occurring from all structure factor allowed planes, cone pairs will develop from all allowed set of planes, and diffraction patterns are formed as intersections of numerous Kikuchi bands (**Figure 6b**).

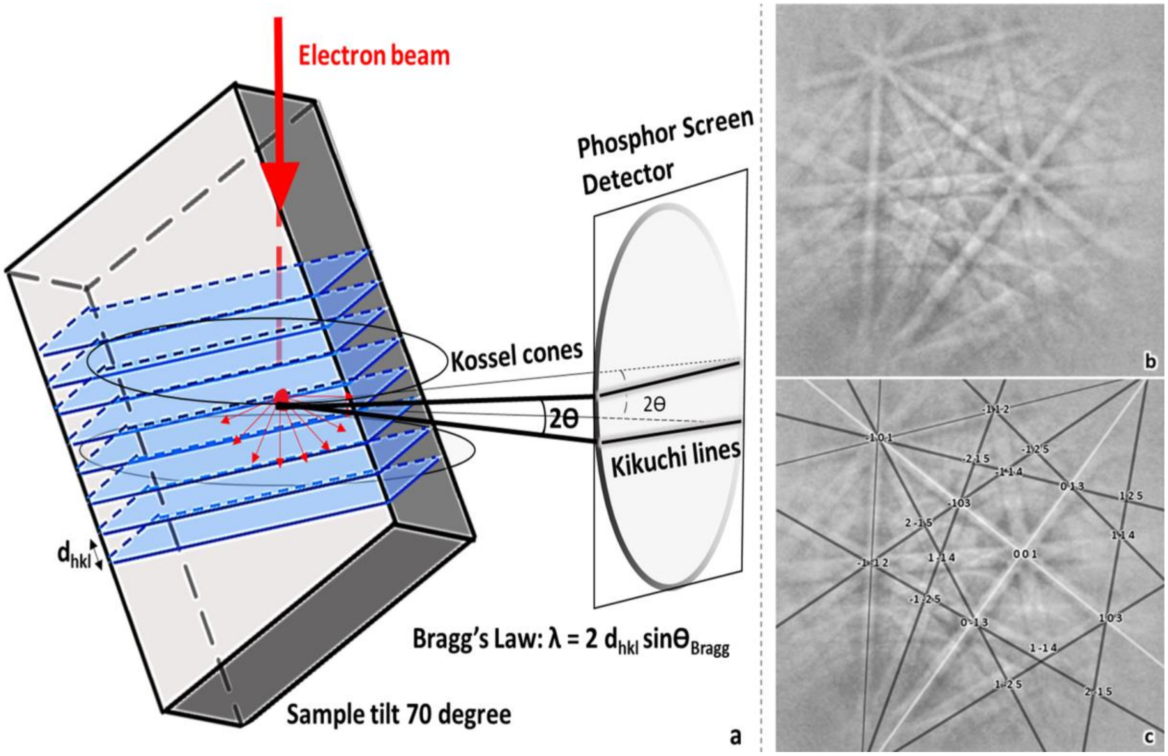

Figure 6a) The simplified mechanism of the formation of electron backscatter patterns (EBSPs). Each pair of Kikuchi lines represents the lattice planes within the crystal at Bragg's angle with the incident beam. b) A Kikuchi map is formed by collecting all the backscatter signals coming out of different planes on the phosphor screen. c) With each zone axis identified and labeled, one is able to know the crystal orientation of the scanned grain. This is extremely useful in the predication of slip systems during plastic deformation. (Amended from [107])

Based on this mechanism diffraction patterns provide angular information of the crystal. For a known material, the identification of Kikuchi bands (**Figure 6c**) through the Hough transform [108] will reveal its crystal orientation. After the application of EBSP in the 1970s [106], continuous development of automatic patterning and phase identification methods [107-110] have made the EBSD a widely used scanning electron microscopy technique for near surface characterization. EBSD is able to provide accurate information on crystalline orientation distributions, grain-scale misorientations, size and phase variations, and elastic strain distribution across a bulk sample.

A well-prepared sample is generally needed, since the highly topographical surface will leave residual deformation at the surface that leads to local strains and blurs the Kikuchi lines for a precise orientation detection [111]. It should also be realized that the inelastic electron interaction volume is strongly influenced by the sample tilt. This means, at a high tilt of 70° for EBSD, the spatial resolution along the tilt axis is usually better than perpendicular to this axis. In a large area EBSD scans, both the top and bottom part of a sample will be out of focus if the center is in well focus. Nevertheless, modern high-speed EBSD provides spatial resolution from 30 to 100 nanometers [107, 108, 111] with good angular resolutions between 0.5^o and 2.0^o, and orientation precision of 0.5^o [107, 112]. Several factors simultaneously affect the performance of the EBSD. The atomic number of material, the geometry of mounting, the probe current, the accelerating voltage, and clarity of the pattern can strongly affect the spatial resolution; while the scanning speed and the calibration of the pattern center will both affect the angular resolution [113-117].

With the development of the high-resolution EBSD technique (HR-EBSD) [118-123], the angular precision has increased to 0.01^o. This technique can resolve as low as 10^{-4} elastic strain across a deformed area by comparing the relative distortion of the pattern collected from an area to the reference pattern from a presumably strain-free area. However, this technique still needs refinement to improve the resolution and the speed for data treatment [122].

1.2.2 Transmission electron microscopy (TEM)

To understand how a crystal is deformed and to evaluate slip transfer, a method is usually needed to identify the deformation slip (and twinning) within and between polycrystal patches. As is mentioned in section 1.1.4, transmission electron microscopy (TEM) has been widely used for the characterization of slip activity. This technique uses high voltage electrons (generally 100 ~ 400 keV) that can penetrate through the sample. The sample is oriented so that the electrons that are at certain Bragg's angles with respect to the lattice planes, creating diffraction patterns and Kikuchi bands that represent the lattice parameters on the back focal plane below the sample. Thus, the lattice distortion around the defects will be resolved due to contrast variations from the defect-free background. Based on this contrast mechanism, dislocations can be visualized, with their Burgers vectors identified through the **g** · **b** = 0 and **g**

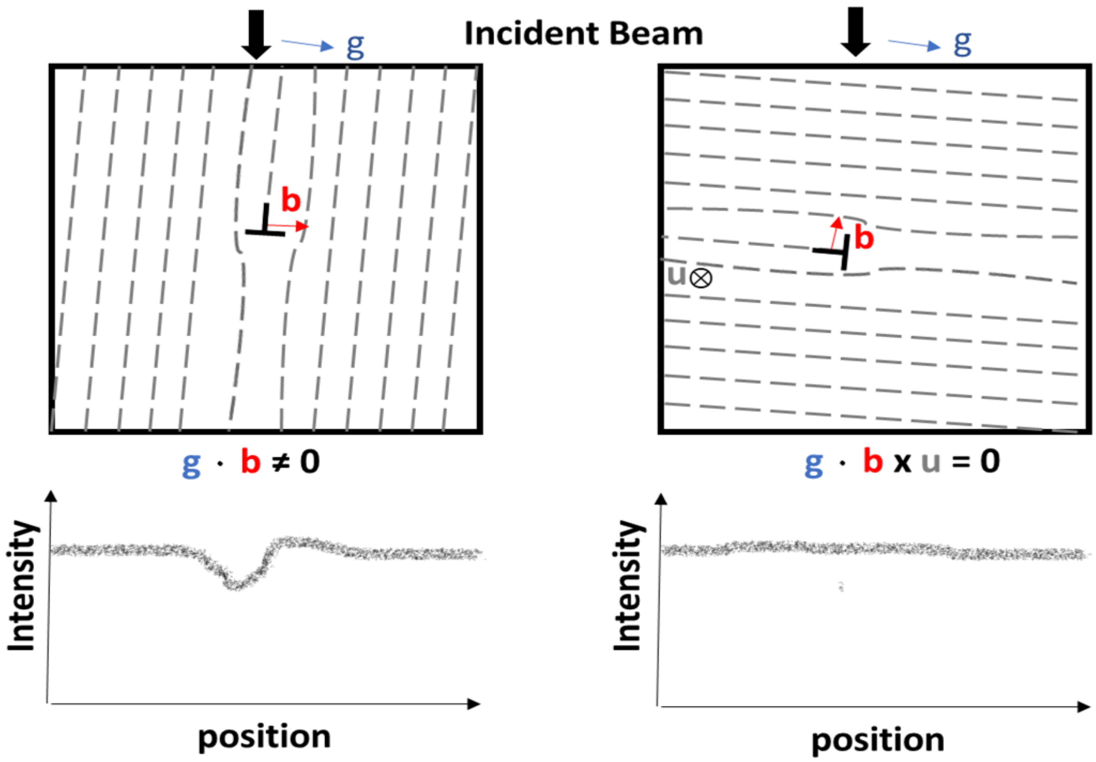

Figure 7 Sketched mechanism of **g** · **b** = 0 and **g** · **b** x **u** = 0 invisibility criteria in the determination of dislocation Burgers vector. The dislocations will go completely out of contrast or show low contrast when the dislocation plane lies parallel to the channeling direction, because the it is where almost all electrons diffracting between planes in the same way, leaving no intensity differences between distorted region and perfect lattice. On the contrary, larger value of **g** · **b** suggests more intensity variation around the distorted region, revealing dislocations in better contrast. (Amended from [124])

· **b** x **u** = 0 invisibility criteria as shown in **Figure 7** (where **g** is the channeling/diffraction vector, **b** is the Burgers vector, and **u** is the line direction) [124-126]. The dislocation line directions, the dislocation types (edge or screw), and the slip planes can also be identified by tilt-and-rotate operations. In addition to the contrast analysis for defect imaging, with continuous advancement of electron sources and the special resolution, latest TEM allows the study of grain boundary configuration and the distortions of atomic arrangement due to dislocation inductions within the vicinity of the boundaries at approximately atomic level [127-129]. Despite the high resolution and the capability of doing in-situ slip transfer experiments, TEM also suffers a series of limitations [130-134], one of which is the requirement of thin foils. Thin foil sample preparation can be difficult and time consuming, but may also result in artifacts during improper preparation. Another limitation of TEM is the observation volume, making it difficult to collect appropriate levels of information for statistical analysis.

1.2.3 Electron channeling contrast imaging (ECCI)

With the advancement of scanning electron microscope, other surface characterization techniques [135-138] have been introduced, such as the electron channeling contrast imaging (ECCI) [137-141]. Among those techniques, ECCI is particularly strong at the identifications of near surface dislocation Burgers vectors and line directions [142-145], and thus serves as competitive approach to the TEM. This technique can resolve dislocation image peak widths as small as 15 nm (comparable to bright field TEM) and is able to capture the dislocations distributed within 100 nm of the surface. ECCI is a non-destructive technique and a similar contrast analysis as TEM, but ECCI is collecting signals from backscattered electrons rather than the electrons penetrating a TEM thin foil.

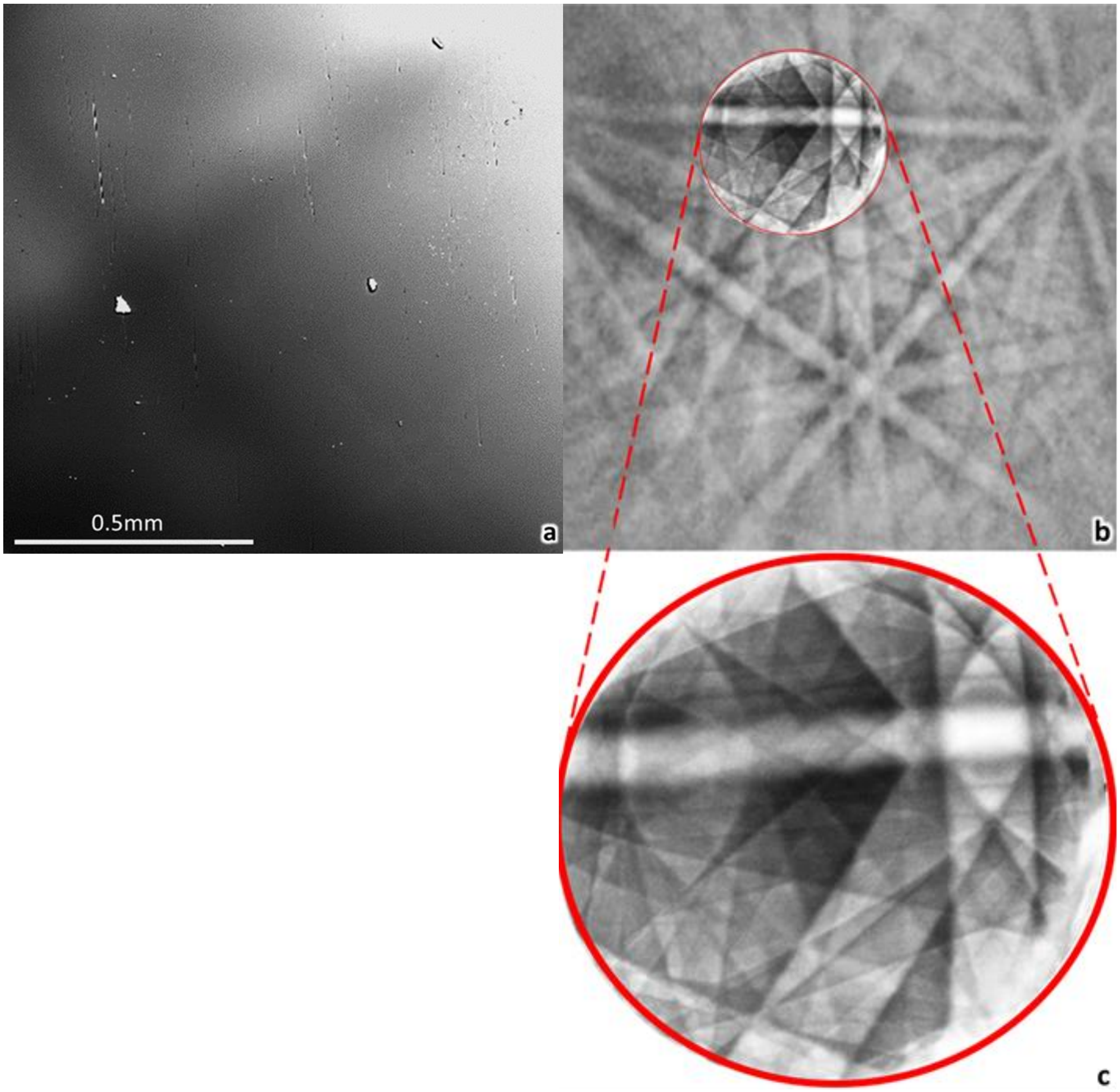

Figure 8a) An example of ECPs collected from a p-type boron doped synthetic diamond single crystal with close to [110] crystal orientation in low mag BSE mode (~ 20x). The band in the upper left corner with bright and dark contrast is one of the Kikuchi band formed during incident beam sweeping the sample. It disappeared in larger mag. The bright “droplets” are particles attached on the surface. b) An example of EBSPs collected among one of the grains from a commercially pure titanium sample in this research (sample 2). The image was taken at a working distance of 24 mm, a 30 kV accelerating voltage and a 184 µA probe current, with sample tilted at 70^{o}. The edges of Kikuchi bands are significantly sharper than that of ECPs. c) An example of SACPs collected from the same target with b) using the same voltage and current, but the working distance is around 9mm within 10^{o} tilt. SACPs provide much accurate information where the closest zone axis the crystal is orientated. With more sharp edges on the channeling bands and higher special resolution, SACPs fits ECCI analysis more than the other two options.

Equivalent to using the “two-beam” conditions in TEM diffraction contrast analysis,ECCI requires the sample to be oriented to specific channeling conditions in order to maximize contrast and facilitate defect analysis. The orientations with respect to the incoming electron beam can be established using crystallographic orientation information from either low-mag electron channeling patterns (ECPs) or higher magnification selected area channeling patterns (SACPs), with example patterns shown in **Figure 8** [146]. EBSD can also be used to facilitate ECCI by inferring the necessary tilts and rotations to achieve proper two-beam channeling conditions[111, 142]. ECPs (**Figure 8a**) are typically formed at low magnification in a single crystal or a grain with a large size. Such patterns were often used when the ECCI technique was first established. The mechanism for the ECPs formation is sketched in **Figure 9** [146]. While the electron beam will strike the sample parallel to the optic axis in the center of a scan, as the

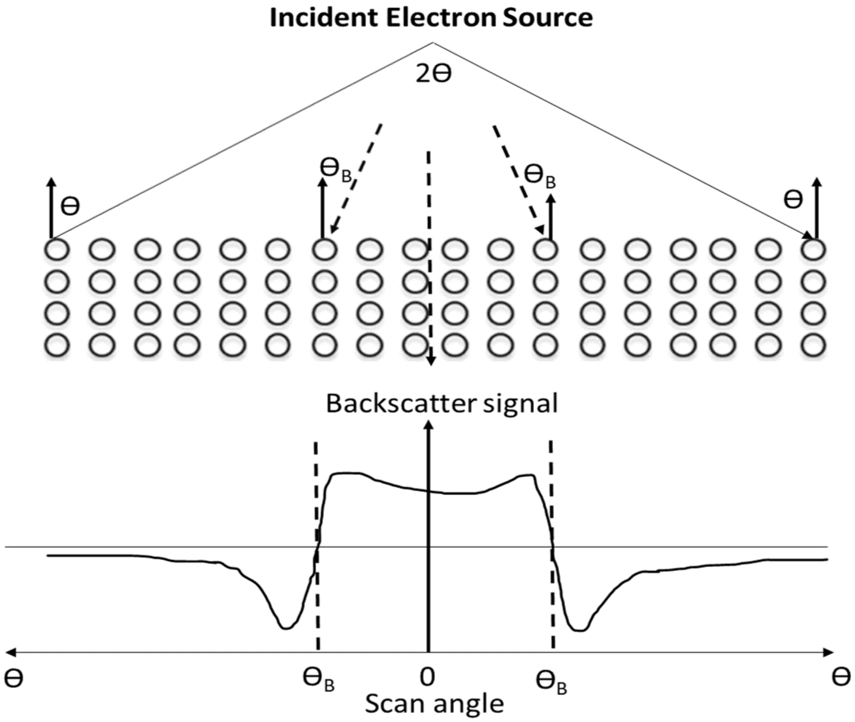

Figure 9 Schematic mechanism on the formation of ECPs (Amended from [146]), with the incident beam sweeping angle large enough, intensity of BSE signal changes significantly around the Bragg’s angle, creating the diffraction contrast at the surface.

beam is scanning across a sample, the electron beam trajectory will vary. At low magnifications this variation in trajectory angle will be maximized. As these trajectories vary, the electron beam strikes the lattice planes at different angles, and the Bragg diffraction (channeling) behavior changes. Subsequently, the backscattered electron yield varies as the beam is moving, forming a pattern of lines, known as an electron channeling pattern, indicative of the crystallography and orientation of the large single crystal. For example, the “bright” region in **Figure 8a** indicates that the lattice is oriented within Bragg’s angle to the incident beam, and thus a strong BSE signal is achieved. The edge of the band indicates the lattice planes are exactly at Bragg’s angle with the incident electrons. On the contrary, the “dark” area suggests the lattice planes are orientated away from the Bragg’s angle, thus a low backscattered signal is detected at the screen. Comparing the qualities of the patterns in **Figure 8a-c**, it appears that the ECPs are blurry and show worse contrast, which is not good for a precise establishment of channeling condition [147] . In theory, ECPs can only provide crystal orientations up to 1^o, thus are not very suitable for accurate dislocation related studies since it is hard to precisely tilt the sample to an exact channeling condition. Additionally, ECPs are limited to large-grain samples or single crystals, which are not readily applicable for heterogeneous deformation studies due to the need for large numbers of grains.

The EBSPs technique (**Figure 8b**), with a precision accuracy around $0.5\text{\textasciitilde}2.0^o$, has replaced ECPs in most applications for the determination of crystal orientation. By calculating the rotation and tilt angles needed to reach the edge of a specific channeling band, it is possible to establish channeling condition for ECCI analysis based on the EBSP-determined crystal orientation [149]. However, this approach is not intuitive, and the precise establishment of a channeling condition is challenged by the uncertainty induced during the stage movement from a high-tilt EBSD orientation to a low-tilt ECCI condition[5]. This makes the fine adjustment of the deviation angle from Bragg's condition to further adjust the channeling contrast almost impossible, since this fine adjustment typically needs angular accuracy within 0.1°, which is beyond the capability of EBSD. Although this problem can be partially resolved by doing ECCI using a forward-scatter electron (FSE) detector with a similar high-tilt setup [149, 150], this technique also suffers issues similar to EBSD, with image/diffraction contrast shadowed by the severe topography and variation of focus across the tilted area [140]. High tilt ECCI also suffers from image foreshortening.

The SACPs (**Figure 8c**), acquired by electron beam rocking about a point close to the surface rather than sweeping across the sample, overcome the limitations of ECPs and are thus able to be used on small grains (20μm). The advantages of SACPs are: 1. the SACPs technique have a smaller angular range with a better spatial resolution. 2. The SACPs have angular accuracy with respect to the beam trajectory within 0.1°, which allows the precise establishment of the channeling condition **g** and the deviation parameter **s** for the enhancement of dislocation contrast. With a precise calibration of the beam shift on a crossbeam field emission gun (FEG) SEM equipped with a Gemini column, a high-resolution SACP can be established with a spatial resolution of 500 nm, allowing the capability to perform a quantitative ECCI analysis [147, 148].

As sketched in **Figure 10a-c**, the crystal lattice "channels" switch on and off as the beam

---

[5] The pattern center of EBSP is a chronic problem in HR-EBSD that still needs improvement since many factors such as accelerating voltage, working distance, etc. can affect the position of the center. Without knowing the exact pattern center, rotation & tilt angles calculated based on EBSD is unreliable.

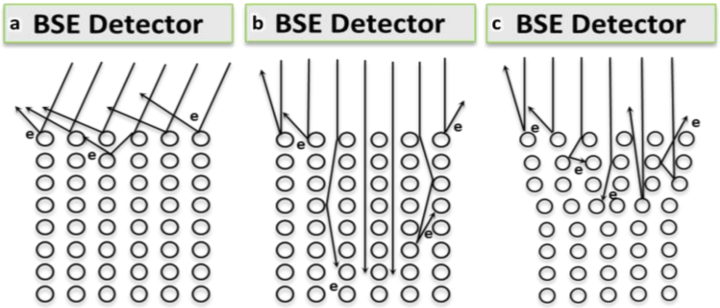

A closed channel with high backscatter electron emission η

An opened channel with low backscatter electron emission η

Lattice distortion closes the presumably opened channel

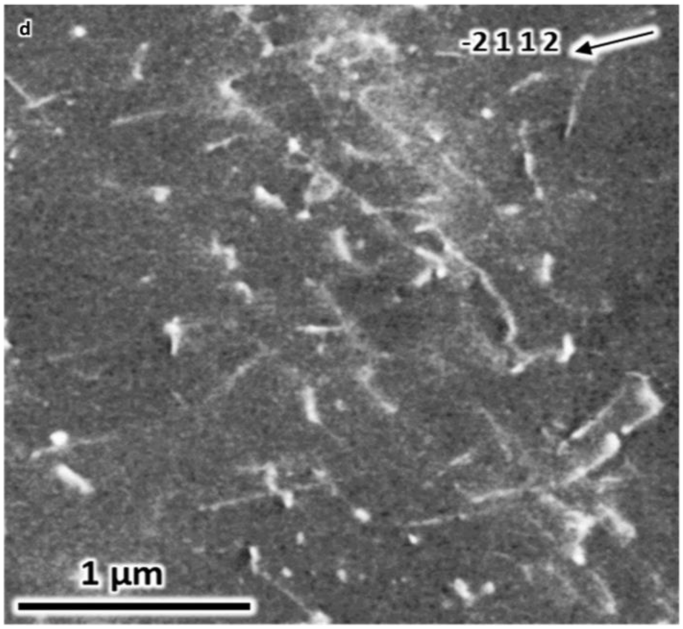

Figure 10a-c) Mechanism of the formation of SACPs. As beam trajectory changes or beam rocking around a certain point, the lattice channel become open and close with respect to the directions of the incoming electrons, providing different yield of backscatter electron η. The signal profile is collected and create a SCAPs on the detector. For a channeling condition that allows the most electrons channeling into the perfect crystal and leave an overall dark background, lattice distortion around a dislocation will make more backscatter electrons collected by the BSE detector. Dislocations will be resolved. d) An example of dislocations (bright) from the dark background.

trajectory changes when rocking around the focused point. The diffraction pattern around this point is thus created since the BSE yield changes with the rocking angle. Once a certain SACP is achieved, it is possible to set up a channeling condition based on the lattice orientation of the crystal. Any near-surface stacking fault and line defects can thus be resolved since the lattice distortion changes the diffraction interaction of electrons in defect-free lattice, providing a different BSE contrast. A typical example is shown in **Figure 10d**, where, at a specific channeling condition, the perfect crystal lattice allows most of the electrons to channel into the material, resulting in an overall dark background. Because the near-surface dislocations distort the perfect lattice, the scattering behavior between the incident electrons and the distorted lattice is different than that in the perfect crystal. With more backscatter electrons collected by the BSE detector around the dislocations, dislocations appear as brighter dots or lines depending on their orientation with respect to the surface. The mechanism responsible for the bright-dark dislocations contrast is shown in **Figure 11** [141, 152, 153]. **Figure 11** (left) shows the optic axis (red "+" in **Figure 11** left) is exactly at one of the channeling bands on a perfect lattice, with the deviation parameter **s** = 0. Due to the lattice distortion from the dislocation, the channeling planes are deviated from the exact Bragg condition, resulting in a different backscatter signal yield from the background yield level (**Figure 11** right).

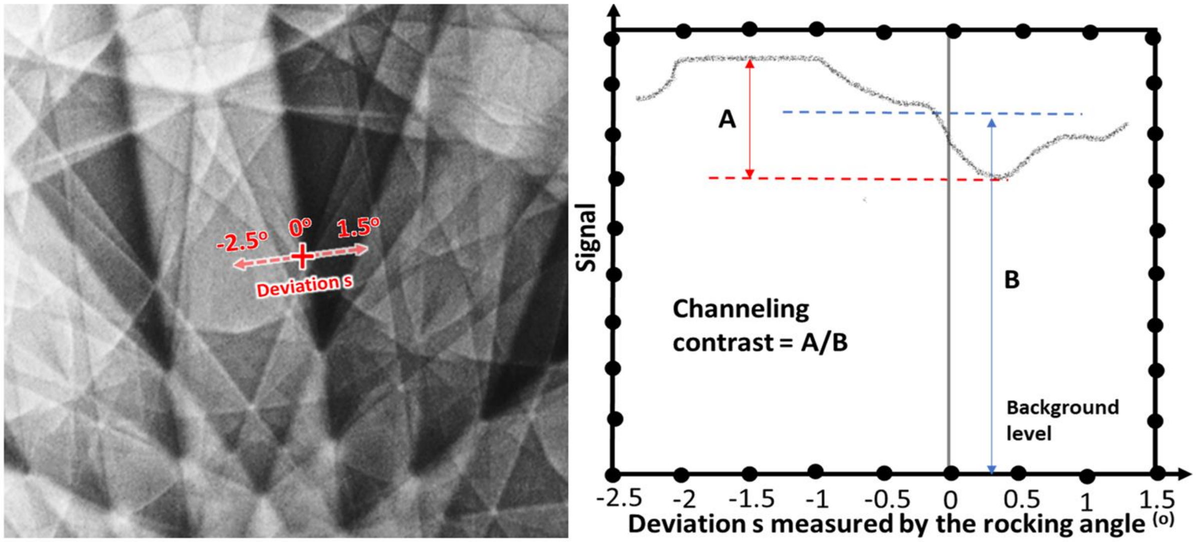

Figure 11 An example of the change of channeling contrast with respect to the deviation parameter **s**, which s = 0 indicates the optical axis is exactly at the edge of the channeling band. With optical axis move into or away from s = 0, signal intensity will change dramatically. As the lattice is no longer aligned symmetrically towards the incident beam due to dislocation distortion, contrast will occur with bright/dark contrast around a dislocation compared to the overall grey background. (Amended from [152])

Once a specific channeling conditions with a proper channeling contrast have been established, dislocation identification can be achieved through ECCI **g** · **b** = 0 and **g** · **b** x **u** = 0 contrast analysis [140, 150, 154]. It should be noted that since there is always elastic relaxation of dislocation core at the free surface, there are situations that dislocations do not fully disappear after adjusting the deviation parameter **s**, and residual "traces" can still be seen at the surface. One should also realize that because the working distance is around 10 mm for ECCI analysis at 30 kV, the tilt angle for a larger samples is often limited to about 20^{o} , which can limit the ability to carry out contrast analysis[6]. Thus, it is not always possible to obtain all the channeling conditions necessary to achieve **g** · **b** = 0 and **g** · **b** x **u** = 0, nor is it always possible to identify line directions by traveling between major zone axes following a channeling band (i. e. the sample need to tilt 35.16^{o} to travel from [110] to [111] zone axis, procedures can be found in **Appendix V**). However, it is easier to identify the inclination direction of dislocation as well as its slip plane in ECCI, since there is only one free surface for the scanned sample.

1.2.4 Other surface plastic evolution analysis techniques

A number of other techniques that are capable of providing information on the evolution of heterogeneous deformation has been developed, such as the digital image correlation (DIC) and the atomic force microscopy (AFM). DIC was first experimentally applied by Sutton et al. [155] to the full-field (2-d) measurement of the displacements during mechanical testing. With continuous improvements in computing technique and imaging qualities [156-158], this technique is now capable of resolving 1 nm horizontal displacement at the surface. The mechanism is schematically described in **Figure 12a**. In this method, the area

---

[6] the mounting stage may collide with the detector, and the dramatic drop of BSE yield at higher tilt angles depending on the material

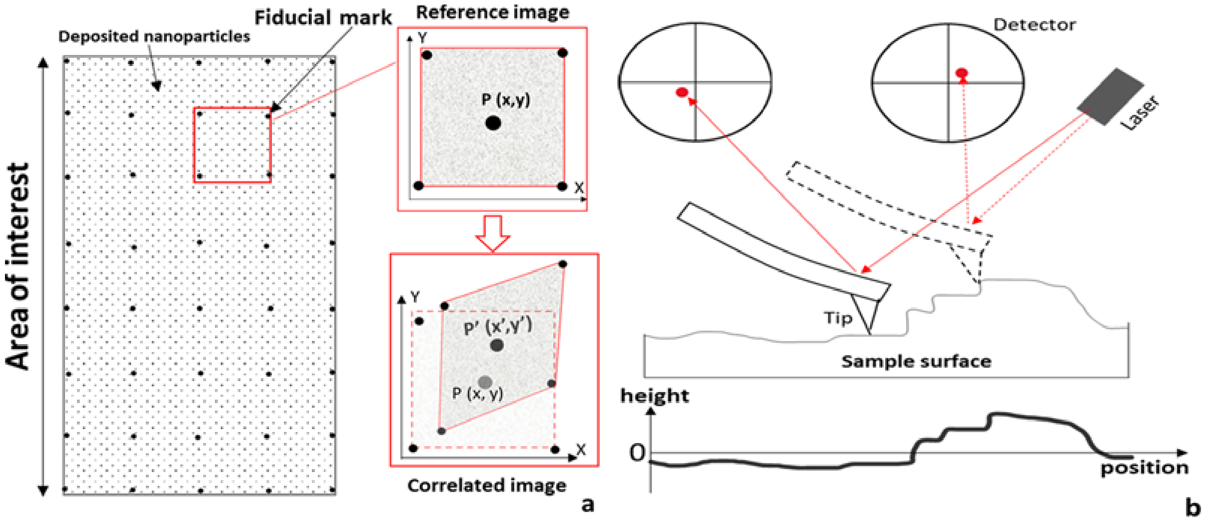

Figure 12a) Overall mechanism of DIC. The surface is coated with evenly deposition of nanoparticles, with fiducial marks. The reference image is the upper right square area labeled with four fiducial marks, with a reference point P (x,y). During deformation, arbitrary shape change and rotation of this area is reflected by the displacement of the fiducial marks and P' (x', y'). b) A Sketch of mechanism of AFM. As the probe is deviating from its original position due to surface topography, the absolute height difference (Z) is recognized by the laser reflection on the position sensitive detector and recorded upon each position (X) from the starting point. After scanning the whole area line by line, a 3-D topographic map can be created by correlating height profile (Z) with the plane profile (X,Y).

of interest is covered by nanoparticles and labeled by several fiducial marks. Following deformation, a strain map can be created since the displacement evolution history between nanoparticles within the area by correlating sequential images captured during deformation with the initial reference image [159-163]. AFM, with a vertical precision of 0.1 Å [164, 165], is able to provide a relative strain map based on the height difference across the probed area [44]. The simplified mechanism of AFM is shown in **Figure 12b**. While the probe scanned across the surface, height difference across the area will oscillate the cantilever, resulting in a deviation in laser reflection from the tip onto a photodiode. The height variation (Z) at different coordinate points (X, Y) on the surface, is then used to construct a topography map. Both techniques have their own advantages and limitations. For instance, DIC is good for measuring the in-plane displacements, but cannot observe dislocation scale movements, while

AFM offers high accuracy for tracing out-of-plane displacement, but suffers from slow probing speed and artifacts [166-168]). Thus, they usually complement with SEM-EBSD [162, 163, 44] based crystallographic information or other techniques that can compensate for the limitations in the study of polycrystal deformation. With the incorporation of different surface analytical techniques, one is able to perform the slip trace analysis that identifies the slip/twin systems that may be activated during the deformation [24, 164, 169, 170] based on the morphologies of the slip traces developed during the deformation.

1.2.5 Problems of the classic trace analysis

There have been a number of recent studies that have taken the advantages of surface analytical techniques (i.e. slip trace analysis [24]) for statistical analysis of dislocation activity since the identifications of slip systems can be much easier to achieve with computer assistance. The mechanism of slip trace analysis is shown in **Figure 13**. With the Euler angle detected by the EBSD, the crystal orientation can be visualized, the intersection line of a slip

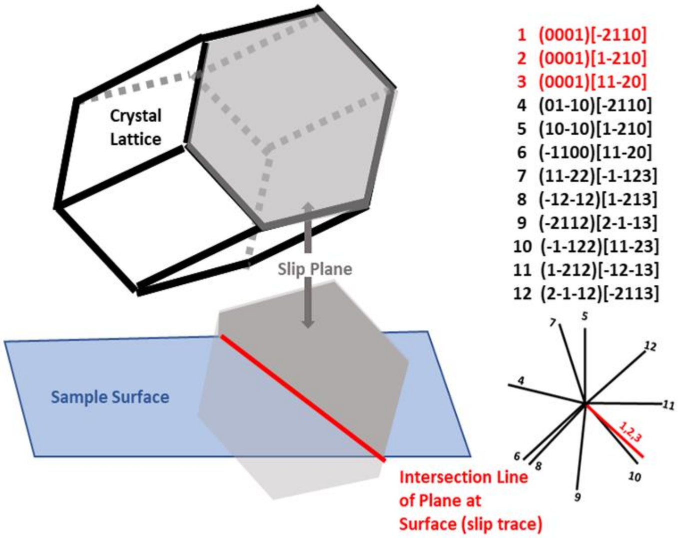

Figure 13 The overall mechanism of the slip trace analysis. The hexagonal cell presents the crystal orientation, and the red line is the intersection line between the slip plane (grey) and the sample surface (blue). With the profile of each trace (1~12) at the surface, possible slip system can be identified.

plane with the sample surface can thus be drawn, which is referred as the slip trace. With the profile of all slip traces, it can be used to identify the active slip system by comparing the observed trace to the calculated ones. Current EBSD based slip trace analysis still have some problems. For example, it cannot identify the slip system on basal plane since they show the same trace at the surface. Moreover, it cannot precisely differentiate slip systems that show similar slip traces (5 vs 9, 6 vs 12 in **Figure 13**). Additionally, this method only works on the grains that exhibit straight slip traces since the identification of slip system is solely based on the observation. Thus, this method is currently blind to cross-slip identification (and wavy traces, which will be discussed in this study). This limitation is seldom discussed because researchers will always select another grain that have easier identified slip systems, or choose the slip system with the highest Schmid factor among possible alternatives. Although the slip trace analysis is more precise in the identification of slip systems with similar slip traces with the help of AFM [168], and DIC [162, 163], current method is still not perfect, especially for wavy traces. Thus, to study the strain accommodation simply relying on the slip trace analysis is dangerous, since different slip interactions may indicate different strain accommodation mechanisms during the deformation.

1.2.6 Free surfacing biasing and limitation of surface-based analysis

Despite the limitation of the current slip trace analysis, the free surface may also bias the slip activation and slip transfer events on the surface. For example, current surface-based analysis, such as AFM and DIC, is not sensitive to the slip systems that do not contribute to the topography change at the observed surface. This means there may be some dislocations that are not correctly identified by the slip trace analysis. This may be a severe issue near the grain boundary, because dislocations from other slip systems may actually play more important role in the slip transfer, but are not detected by the slip trace analysis [171]. This ignorance will lead to improper/incomplete understanding of strain accommodation during the heterogeneous plastic deformation.

One other limitation to the surface-based analysis (AFM, DIC, EBSD) in the study of slip accommodation at grain boundary is illustrate in Figure 5. It appears that two slip systems interact differently at the grain boundary at the sample surface (meet at the same point on the grain boundary or not). No matter which type of interaction, evaluation of slip transfer events is solely based on surface observations. Because it is hard to reveal the geometry of the slip system and the grain boundary [172-174] from surface observation7, the geometrically compatibility criteria, m', is abusively used in recent studies and ignore the role of the grain boundary plane orientations [75, 97, 98]. Additionally, due to not knowing the local accommodation mechanisms at the grain boundary plane (especially in the area between the divergent slip planes below the surface), it is risky to directly use the slip transfer criteria in the real-life deformation.

1.2.7 The advantage of ECCI over other techniques

To solve the problems in current surface-based analysis, ECCI is thus needed. One major advantage of ECCI over other surficial techniques (DIC, AFM) is the capability to identify slip planes, slip directions, and the Burgers vectors, which is critical in the plasticity study [143, 144]. Additionally, with controlled electropolishing technique, ECCI is able to reveal the "3-D"

---

[7] Unless using destructive FIB milling on the grain boundary area [172-174]. However, FIB milling may lose information on slip interactions at the milled area.

geometry of a grain boundary plane and the slip planes by the correlation of images taken at different depths [96, 174]. On the other hand, although not comparable with the darkfield TEM that is able to resolve small dislocation width, ECCI is none-destructive and thus is suitable for continuous deformation study of bulk material [140, 141]. As an SEM-based technique, a broader field of view of ECCI offers the deformation information from the macroscopic level to the dislocation level. This technique links the macroscopic and the microscopic world, which is good for both detailed mechanism study and statistical analysis.

1.3 The objective of this research and design plan

This Ph.D. thesis aims to solve several open questions about how plastic strain is accommodated within grains and across grain boundaries during the plastic deformation. The answers to these questions will provide better guidance for the establishment of a reliable plastic model in the future.

ECCI will be used to study the dislocation slip evolution during heterogeneous plastic deformation, with a particular focus on slip band/grain boundary interactions. This objective will be carried out in a number of steps: First, a robust comparison of a number of approaches for characterizing heterogeneous deformation will be carried out. This will include how these various techniques give consistent and/or complementary information. Second, how grain boundary strain accommodation is achieved between the interacting slip systems in order to maintain grain boundary integrity. These studies will examine this behavior across 3-D volumes by carrying out ECCI studies at different depth from the surface. It will be shown that this approach allows a more robust assessment of the parameters that affect the accommodation behavior than is facilitated by surface studies alone. Finally, it will be shown that ECCI facilitates the assessment of the sequence of slip activity across patches of multiple grains, facilitating a better understanding of the development of heterogeneous deformation.

In order to address the first objective, a surface analytical experiment was performed on a Ti-7-Al tensile sample to facilitate the comparison of ECCI with AFM, HR-EBSD, and DIC. The highlight is to emphasize the convenience of using ECCI in the identification of slip systems. An additional consequence of this study is to introduce a method of removing DIC patterning without damaging the surface, facilitating further EBSD and ECCI analysis. To fulfill the second and third goals, two commercially pure α titanium samples were deformed to 1-1.5% plastic strain by four-point-bending. With controlled electropolishing techniques, comparison of images of slip bands at and below surface reveal how the free surface is biases the slip interactions at grain boundaries. Additionally, with the subsequent “3-D” assessment of the slip planes and grain boundary planes available from the images at and below the surface, several slip transfer parameters have been used to evaluate slip transmission at the grain boundary. After the identification of the propagation direction of dislocation following slip bands within series of neighboring grains, it is possible to estimate the direction of deformation flow traveling within the grain patches, facilitating the determination of deformation sequences, and locate the grain boundary where the plastic strain was not sufficiently resolved.

2. Experimental Procedures

2.1 Samples preparation

Sample 1 was a Ti-7Al α-titanium sample provided by Professor Samantha Daly's group , which had already been cut by electron discharge machining (EDM) into a 42 x 8.2 x 2.2 mm tensile bar with a 10 mm gauge length. The dimensions of sample 1 are shown in **Figure 14a**. Samples 2 and 3 were EDM sectioned into two 25 x 3 x 2.5 mm bars, as shown in **Figure 14b**, from the α-titanium provided by Dr. Christopher Cowen (formerly at National Energy Technology Laboratory). The sectioned samples experienced several grinding steps using silicon carbide (SiC) grinding paper from 400, 600, 1200, down to 4000 grit using a polishing wheel at a speed of 200rpm. Final polishing of the samples was accomplished on a Struers MD-Chem polishing cloth at 300rpm with the mixture of 5:1 volumetric ratio of 0.05 μm colloidal silica suspension (Struers OP-S) and 30% hydrogen peroxide solution for 30 minutes. All three samples were electropolished with a polishing cell, as sketched by **Figure 15**, using different electrolytes and different parameters [175-179]. Samples 1 and 2 were electropolished in a

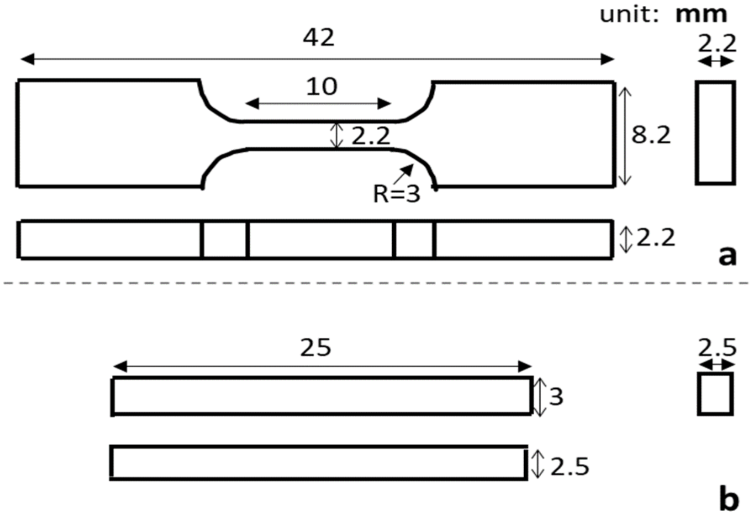

Figure 14a) The dimension of the Ti-7Al dog-bone tensile sample 1. b) The dimension of the CP Ti bending sample 2 & 3.

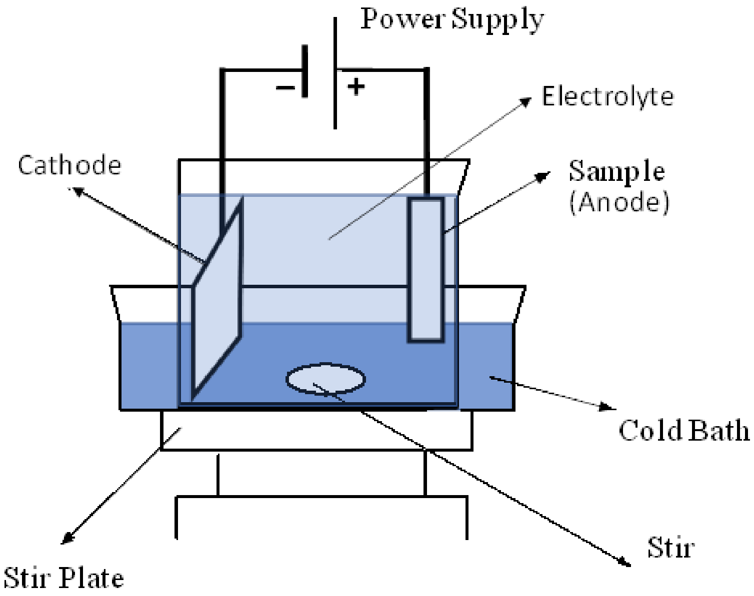

Figure 15 Sketch of the electropolishing stage. Based on what type of electrolyte is used, the voltage, temperature while electropolishing, the distance between cathode (stainless steel) and sample (anode), and the agitating speed of the stir bar will be different and recorded in **Appendix A**.

solution that contained 30 ml perchloric acid, 200 ml butanol, and 300ml methanol, using an applied voltage of 38 V at -35 ^{o}C. Sample 3 was electropolished using 24 V at -30 ^{o}C using a solution containing 10 wt% magnesium perchlorate and 90 wt% methanol. Detail of the electropolishing mechanisms, parameters, and a comparison between the two methods are recorded in **Appendix A**.

Before deformation, grain orientations of the samples were characterized using EBSD, with grain boundary and surface conditions (after electropolishing) checked by general secondary electron (SE) and backscattered electron (BSE) imaging mode using a Tescan Mira III FEG-SEM equipped with an EDAX-TSL orientation imaging system. EBSD was performed using a 30 kV accelerating voltage with a 148 μA probe emission current, a 20.0 nm spot size, and an 18 mm working distance with the samples tilted to 70^{o}. The instrument parameters for SE/BSE (and later ECCI) observations were the same as used for EBSD, but the working distance was around 8-10 mm (with a maximum stage tilt of 20^o for ECCI analysis). If not specifically mentioned, all images and analysis (including AFM) during each experimental stage were taken at consistent conditions, with the sample placed in the same orientation on stage.

2.2 Samples deformation

2.2.1 Deformation of Ti-7Al sample and uncoating

After mapping the crystal orientation distribution of sample 1 using EBSD, it was sent back to Professor Daly's group, where it was patterned using a polymer film with densely deposited gold nanoparticles (AuNP) through surface condensation reactions [162, 163]. It was then plasticly deformed to ~3% tensile strain (the coordinate system for deformation, observation, and analysis remained consistent and is sketched in **Figure 16a1**), with a full-field displacement of particles and strain development monitored through DIC at different strain levels.

After receiving the sample back from the Daly group, the sample 1 was soaked for a total of 4 hours at 30 ^oC in a solution of tetra-n-butylammonium fluoride (TBAF) [180-184], chloroform, and ethylene glycol with a weight ratio of 10: 1: 1 respectively. During this uncoating process, sample 1 was taken out every 1 hour and cleaned with soap water using sonication for 5-10 minutes. Final cleaning was accomplished by dipping the sample into dishwashing soap, wiping off the soap with cotton, flashing with ethanol-water-ethanol, and air drying. The overall uncoating approach was successful, with no AuNPs left on the surface, resulting in a smooth surface and sharp SACPs. The detailed coating removal procedure is recorded in **Appendix B**.

2.2.2 Deformation of samples 2 and 3

Samples 2 and 3 were plasticly deformed in a four-point-bending stage to around 1.5% and 1% surface tensile strain, respectively, with tensile strain measured as outlined in **Appendix C** (the coordinate systems for samples 2 and 3 are shown in **Figures 16b1&c1**).

2.3 Samples analysis

All deformed samples (1-3) were placed on the SEM stage for the observation of slip traces developed during the deformation, with post-deformation EBSD data collected to update the crystal orientations from deformation. Combined with the information from the slip traces and the corresponding EBSD orientation profiles, surficial slip trace analysis was performed using an in-house developed MATLAB code [24], where the crystal orientation, the slip plane that may leave the slip trace on the surface, and the potential Burgers vector were input, with the global Schmid factor M calculated based on the Euler angle of the crystal and the geometry of potential slip systems relative to the surface tensile direction. Based on the geometry of slip planes and the crystal orientation of a grain and its neighboring grains, the alignment of slip systems across their grain boundaries was assessed using the geometric compatibility factor m' [95].

2.3.1 ECCI analysis on sample 1 and electropolished samples 2&3

ECCI analysis was carried out directly on the plasticly deformed Ti-7Al sample 1, both within grains and near grain boundaries, facilitating the identification of dislocations (the alignment of SEM for ECCI is in **Appendix D**). The Burgers vectors were identified through ECCI $\mathbf{g} \cdot \mathbf{b} = 0$ and $\mathbf{g} \cdot \mathbf{b} \times \mathbf{u} = 0$ contrast analysis [140, 150, 154], and the slip planes and line directions were roughly estimated by tilting along one of the Kikuchi bands, with detailed procedure presented in **Appendix E**. Subsequent to this characterization, samples 2 and 3 were further electropolished using the same electropolishing conditions outlined in **Appendix A**, which eliminated all surface topography. The depth of material removed was determined by applied current and electropolishing time and was directly measured by the Vickers indent. The resulting materials removal was approximately 5 µm from sample 2 and approximately 20 µm being from sample 3.

EBSD was again carried out on these samples following this surface removal. ECCI was then performed on samples 2 and 3 in order to identify dislocations, dislocation propagation investigation behavior, and dislocation interactions at grain boundaries.

2.3.2 AFM analysis on sample 1

The topography developed due to slip band development during the deformation was measured using a VEECO Dimension 3100 AFM operating in tapping mode at a speed of 10 µm/min for every 40 x 40 µm^2 area. The data from AFM was processed using the Gwyddion software package[8], with the background surface normalized (polynomial 3) and the regions having the lowest height were automatically assigned as zero during the analysis.

2.3.3 HR-EBSD analysis on sample 1

HR-EBSD was performed on the areas where ECCI was performed on sample 1, using a sample tilt of 70^o, a working distance of 20 mm, and a 20.0 nm spot size. Each high-resolution pattern for the cross-correlation was taken at an exposure time of 0.1 s with a 480 x 480-pixel resolution and the EBSD patterns were saved. As indicated by Dunlap et al. [137] and Ruggles et al. [138], the step size will affect the GND density distribution determinations; the GND

---

[8] Available free at http://gwyddion.net/

analysis in this research was based on 200 nm effective step size, a parameter that can resolve dislocations as best as possible [136, 137]. This facilitated a semi-quantitative comparison between the GND measurements and the ECCI and AFM data.

3. Results and Discussions

The results presented here are primarily in the form of a large number of ECC images that allow the determination of crystallographic details, primarily Burgers vectors, dislocation line directions, and slip band morphologies. These are related to underlying crystallographically dependent parameters based on EBSD analysis, including global Schmid factors, the angle between slip plane intersections in grain boundaries, ϴ, and the resulting compatibility factors m’ and LRB. These interdependent factors vary from case to case. Thus, rather than presenting the results of various experiments in isolation, the author believes the best way to descriptively convey the research is to combine the results and discussion, presenting combined results for various cases in order to tell complete stories without leaving unanswered questions, rather than laying out results fragmentally. Nevertheless, **sections 3.1&3.2** will outline the generalized approaches and observations used for carrying out the specific studies. **Sections 3.3-3.5** will outline the advantages of ECCI technique over other technique in the heterogeneous plastic deformation study, especially in terms of slip accommodation activities within grain interior and at grain boundary area.

3.1 The overall status of as deformed samples 1-3

The deformation of samples 1-3 at their respective strain levels (sample 1 at 3%, sample 2 at 1.5%, and sample 3 at 1%) was dominated by heterogeneous slip systems. No deformation twins were observed within the targeted areas, which was confirmed by the SE images and EBSD orientation map of these areas, as shown in **Figure 16**. Although comparisons before and after deformation are not shown, the crystal orientations were not distinguishably changed with deformation. As shown in **Figure 16a1**, the collections of lines lying at the surface of

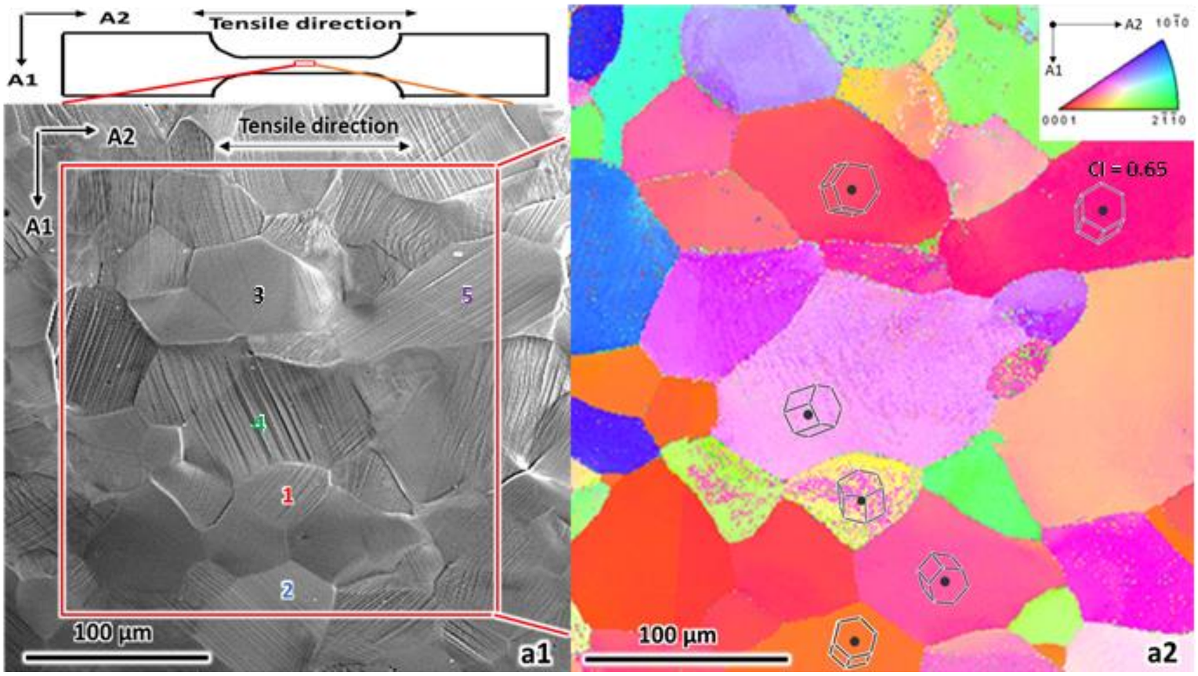

Figure 16a1) The SE image from the center of the 3% tensile strained Ti-7Al sample 1, with the tensile direction along A2 axis. Almost all grains were deformed, with some grains having more than one type of slip traces. Surface and grain boundary elevation could be indicated by the brighter contrast against the dark grains. a2) The corresponding EBSD data in the red region of a1, which was collected under the same coordinate system as a1. Despite the noises due to higher deformation strain that disrupts the diffraction (with confident index only 0.65), color gradient within grains can be clearly seen, especially where slip bands were densely packed. Slip traces appear mostly straight, while some curved traces were found near grain boundaries or in the grains which were heavily deformed. b1) An example of one of the grain boundaries between two neighboring grains in the center area of sample 2 after 1.5% deformation on four-point-bending stage. Again, most slip traces appear straight, while the bright and dark contrast on the slip traces may indicate they may not share the same Burgers vector. Despite some primary slip traces that were fully propagated across the grains, some of the slip traces disappear as they propagated out of the grain boundary. b2) The corresponding EBSD map of the red area of b1, indicating the formation of slip bands was not significant enough to affect the quality of the EBSD, with a high confident index of 0.81, and the topography developed during deformation was not big enough to be shown in the EBSD compared to a2.

Figure 16 (cont'd) c1) SE image of a patch of 4 consecutive grains in the center of sample 3, which was deformed in the same manner with sample 2 to 1% plastic strain. Slip traces in grains 2-4 appear straight while traces in grain 1 are wavy. Some traces disappear near the grain boundary in grain 2, which is indicated by the white arrow. Traces in grains 1 and 2 meet at the same point on the grain boundary, so are the traces in grains 3 and 4, while traces in grains 2 and 3 do not meet at the same point on the grain boundary. c2) EBSD map of the grain patch in c1. The deformation is not large enough for EBSD to recognize the formation of slip bands at 1% strain level. No crystal rotation is detected. It should be noted that all the prism cells in a2, b2, and c2 indicate the crystal orientations of the grains they were located, with the black dots indicating the optical axis.

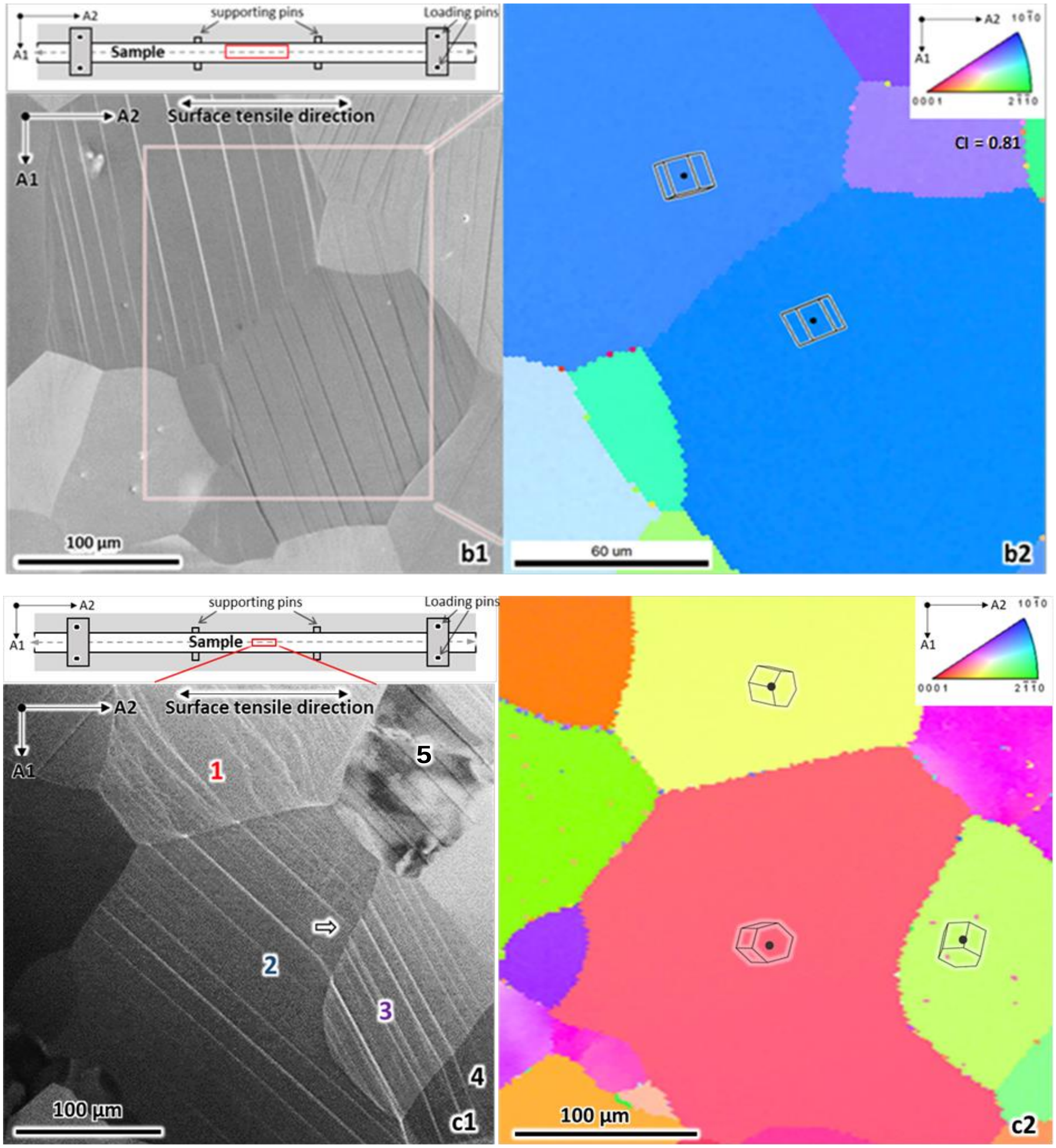

sample 1 indicate the traces of the slip systems [185]. It can be seen that the slip traces have varying directions, suggesting the grains were deformed in different directions due to shear in different directions. With the exception of a few grains, almost all grains in the red region show apparent slip traces, with half of the grains showing more than one type of slip traces. The overall grain size in sample 1 was somewhat smaller than that in samples 2&3, and it appears that the distance between slip traces in sample 1 were smaller. It is also noticeable that some grains and grain boundaries show a significant contrast difference than their surrounding environment as a result of local lattice rotation due to deformation leading to different electron channeling contrast. For example, the upper grain boundary and the right region of grain 3 show a much brighter contrast than the rest area in this grain, which indicates there is a large variation of lattice orientation in that area due to the deformation. The orientation change due to plastic deformation was also captured by the EBSD orientation map (**Figure 16a2)**. For example, the densely packed slip traces are seen as fine purple lines in contrast to the overall pink background in grain 4, suggesting a large local orientation change in those areas. In contrast, the orientation variations of samples 2&3 appeared much straightforward since they experienced a much lower plastic strain. At 1~1.5% plastic strain, only ~30% of grains in the observed areas show clear slip traces on the surface. In addition, at this low plastic strain, all of the traces within a deformed grain (**Figure 16b1&c1**) had the same orientation, suggesting that no other slip systems were activated. It is noticeable that some grains are not fully recrystallized and have shown interesting diffraction features (grain 5 in **Figure 16c1**), such grains are rarely observed and not the focus of this research.

3.2 Slip system identifications

3.2.1 EBSD based slip trace analysis

In order to understand the heterogeneous deformation of a polycrystal, it is critical to correctly identify the slip systems that are active during the plastic deformation. Based on the slip traces developed during the plastic deformation and crystal orientation information from the EBSD, the active slip systems can be readily identified with the EBSD based slip trace analysis [24]. An example of slip trace analysis is shown in **Figure 17**. **Figure 17a** shows grain 2 in sample 1 after 3% plastic deformation [185]. Two types of straight slip traces are observed in grain 2, with one lying from the upper left to the bottom right (#1) and the other from the upper right to the bottom left (#2). The hexagonal cells on the right represent the lattice

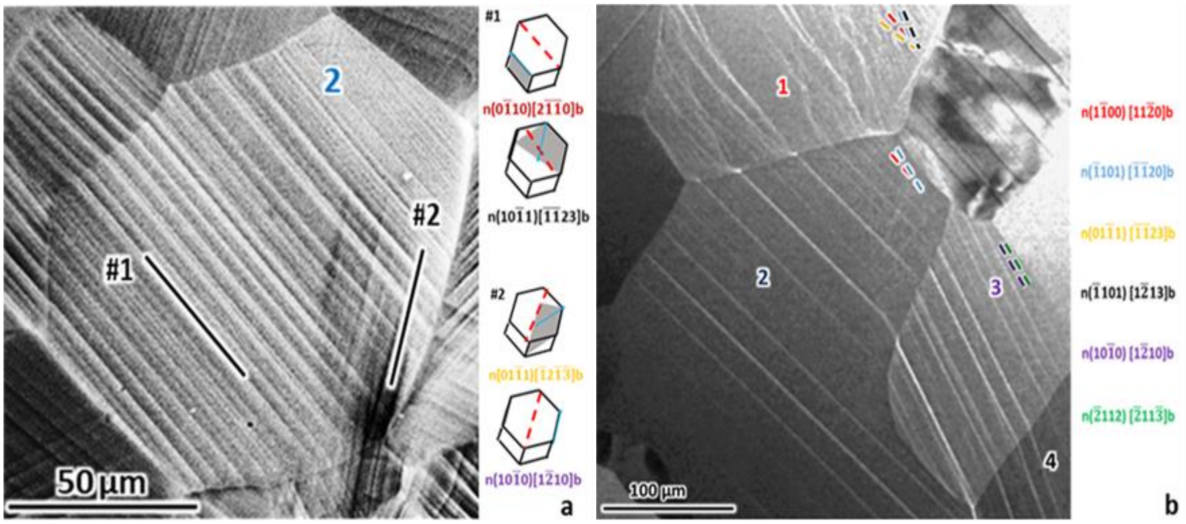

Figure 17a) BSE image of grain 2 in sample 1. Two straight and planar slip traces can be clearly observed, with their trace outlined as black lines. The hexagonal cells on the right indicate the orientation of this grain. The shaded plane in each cell indicates the slip plane, the blue line indicates the slip direction, and the red dashed line is the plane trace on the sample surface. For a potential slip system active during deformation, the red dashed line should match the trace on the surface. b) BSE image of a patch of grains 1~3. Some slip systems with different Burgers vectors or slip planes may exhibit similar slip traces at the surface, resulting in uncertainties. The colored dashed lines in each grain represent the possible slip systems that leave similar slip traces. The Burgers vectors and slip planes of all possible slip systems are listed on the right. The color of the slip system is using the same color with the dashed line.

orientation of grain 2. The grey shaded planes in the cell represent the slip plane, and the blue lines are the slip directions. The red dashed lines in the cells, referred as the slip (plane) traces, show the intersection line of the slip plane with the sample surface. If the red dash line is parallel to the observed traces on the sample, then the slip plane that leaves this slip trace on the surface is identified as the deformation plane (similarly, the colored dashed lines are the slip traces from the corresponding slip systems in **Figure 17b**). Because there is generally only one Burgers vector on each specific plane due to lower symmetry of α-titanium (with the exception of the (0001) basal plane, which can have three Burgers vector $[11\bar{2}0]$, $[1\bar{2}10]$, and $[\bar{2}110]$), the slip system can thus be identified.

In some cases, slip systems with different Burgers vectors or slip planes may show similar slip traces, adding some uncertainty in the slip system identifications. In **Figure 17a**, particularly, $(0\bar{1}10)$ $[2\bar{1}\bar{1}0]$ prism <a> slip system and $(10\bar{1}1)$ $[\bar{1}\bar{1}23]$ pyramidal <c + a> slip system both show similar traces with the observed trace #1. Similarly, $(01\bar{1}1)$ $[\bar{1}2\bar{1}3]$ pyramidal <c + a> slip system and $(10\bar{1}0)$ $[1\bar{2}10]$ prism <a> slip system show similar traces that match the observed trace #2. Slip trace analysis is also not capable if identifying a specific plane for wavy traces, since it is difficult to match curvy surface traces with the calculated ones. An example of this can be found in grain 1 of sample 3 (**Figure 17b** [96]), due to the curved traces, four possible slip systems may be active according to the EBSD-based slip trace analysis. Additionally, grain 2 and grain 3 may deform differently and might have different slip interactions based on how the slip systems are identified. In general, previous studies [43, 74,75, 97, 98] using this EBSD-based slip trace analysis have overcome this difficulty by selecting the slip system with the highest global Schmid factor (in this study this was calculated using an in-house MATLAB code), by choosing the slip system with the lower CRSS value[9], or a combination of these approaches. The latter approach is statistically reasonable because such slip systems are more likely to be active. However, this statistical hypothesis is not safe to use in the study of slip interactions at grain boundaries, and it is not viable in extreme conditions (i. e. slip systems having similar Schmid factor/CRSS ratio). In **Figure 17b**, there are a total of 6 possible slip systems within grains 1-3 (uncertainties cannot be eliminated), resulting in a more complicated situation in the evaluation of slip transfer events. Thus, a more reliable method is needed to facilitate the identification of slip systems. In this thesis, the difficulty is overcome by identifying the Burgers vector using ECCI.

3.2.2 Identification of slip systems using ECCI

To eliminate the uncertainties from surface trace analysis, ECCI was either directly carried out on the as-deformed sample surfaces or after electropolishing to remove some of the near-surface material. The Burgers vectors of the slip systems can be identified by ECCI based $\mathbf{g} \cdot \mathbf{b} = 0$ and $\mathbf{g} \cdot \mathbf{b} \times \mathbf{u} = 0$ invisibility criteria [140, 150, 154], where **g** is the channeling vector, **b** is the Burgers vector, and **u** is the dislocation line direction. Once the Burgers vector **b** is identified, the slip system that forms a certain slip trace can be identified[10] based on the combined knowledge of the Burgers vector and the subset of possible slip planes from the slip trace analysis.

One example of the ECCI identification of dislocation Burgers vectors is given for grain 1

---

[9] In α-titanium, prism <a> slip system is more likely to be activated than the pyramidal <c + a> due to a lower CRSS value. Thus, it is more likely to consider prism <a> slip system is the active one than other candidates, unless the Schmid factor of prism <a> slip is extremely low and is not possible to be activated.

[10] Dislocation line direction **u** can be used to reveal the inclination of the slip plane, and thus eliminate the situation when a pyramidal <a> and a prism <a> slip system shows a similar trace with the same Burgers vector.

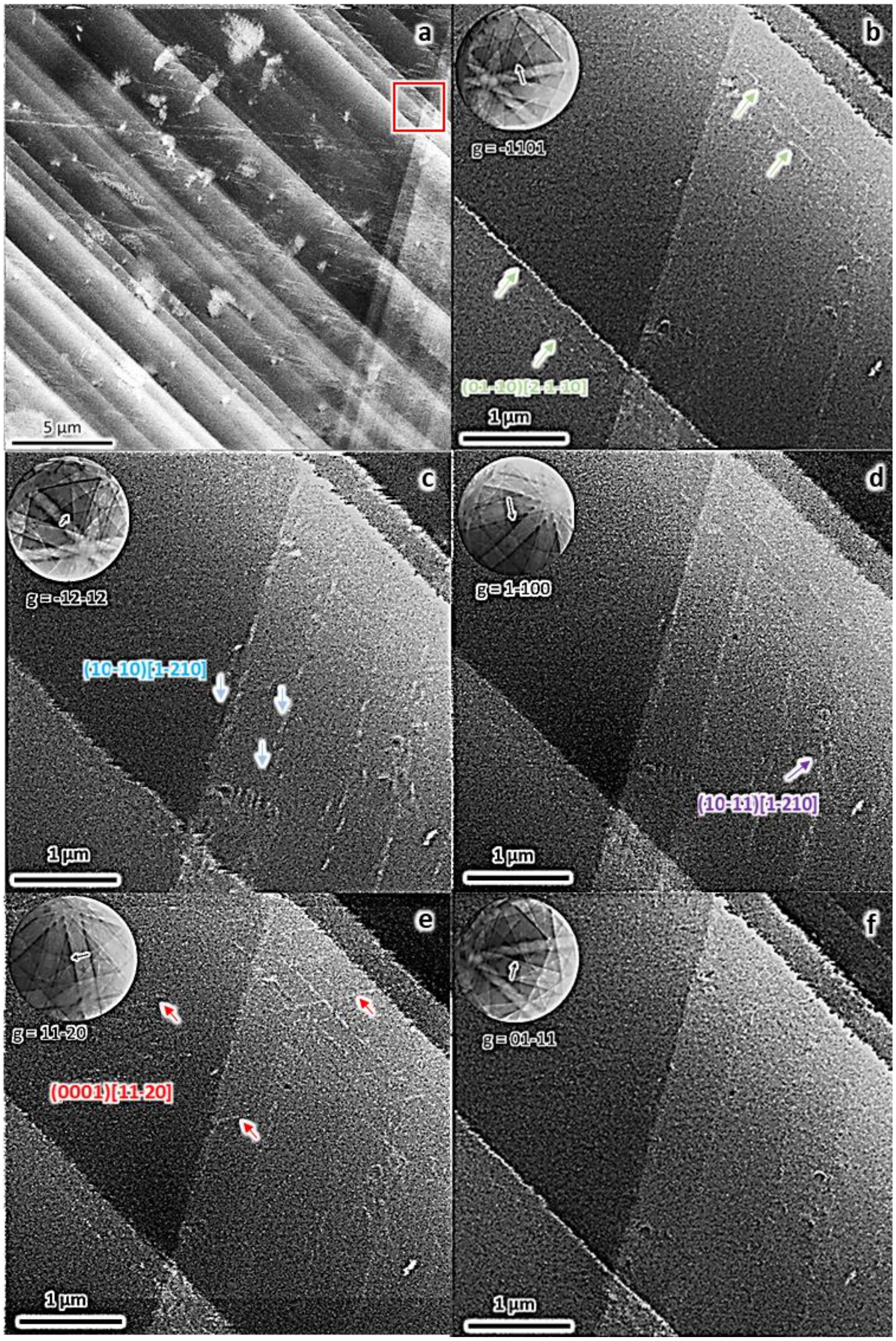

Figure 18a) BSE image of one of the areas of interest after deformation of sample 1. b-f) ECC images taken at different channeling conditions from the red boxed area. The upper left circles are the Kikuchi patterns. Each black arrow across a Kikuchi band indicates the specific channeling band, and the arrowhead is where the optic axis is focused. Each channeling condition is identified from the T. O. C. A software. The Burgers vectors of dislocations are identified by $\mathbf{g} \cdot \mathbf{b} = 0$ and $\mathbf{g} \cdot \mathbf{b} \times \mathbf{u} = 0$ contrast analysis, and the slip plane can be revealed through different tilting and rotating along a certain channeling band (**Appendix E**). A total of four different slip systems are identified and labeled by colored arrows, namely: $(01\bar{1}0)[2\bar{1}\bar{1}0]$ prism <a> slip system (green), $(10\bar{1}0)[1\bar{2}10]$ prism <a> slip system (blue), $(10\bar{1}1)[1\bar{2}10]$ pyramidal <a> slip system (purple), and $(0001)[11\bar{2}0]$ basal <a> slip system (red). Amended from [185]

of sample 1 in **Figure 18** [185]. A series of ECC images of the same area have been taken at different channeling conditions (at different **g**). If the dislocation shows little or no contrast at a certain **g**, then the Burgers vector can be identified through the ECCI $\mathbf{g} \cdot \mathbf{b} = 0$ and $\mathbf{g} \cdot \mathbf{b} \times \mathbf{u} = 0$ contrast analysis. For example, dislocations with the Burgers vector of $[2\bar{1}\bar{1}0]$ should show good contrast at **g** = $[\bar{1}101]$, $[\bar{1}2\bar{1}2]$, $[1\bar{1}00]$, $[11\bar{2}0]$ (**Figure 18b-e**), and show weak contrast at **g** = $[01\bar{1}1]$ (**Figure 18f**). In this particular example, a total of three different Burgers vector were identified. After combining the Burgers vector and the slip plane traces, four different slip systems were finally identified, namely: the $(01\bar{1}0)[2\bar{1}\bar{1}0]$ prism <a> slip system (green), the $(10\bar{1}0)[1\bar{2}10]$ prism <a> slip system (blue), the $(0001)[11\bar{2}0]$ basal <a> slip system (red), and a small number of $(10\bar{1}1)[1\bar{2}10]$ pyramidal <a> slip system (purple). The majority of dislocations that contributed to the formation of slip bands in grain 1 were the $(01\bar{1}0)[2\bar{1}\bar{1}0]$ prism <a> slip system (green) and the $(10\bar{1}0)[1\bar{2}10]$ prism <a> slip system (blue). Additionally, with the Euler angle acquired from the EBSD software, the global Schmid factor can be calculated based on the global stress state. Based on the experimental observation, it is clear that the $(01\bar{1}0)[2\bar{1}\bar{1}0]$ prism <a> slip system (#1 slip system in **Figure 17a**, green in **Figure 18**) is more active since the global Schmid factor (M) is 0.49, while the other prism <a> slip system, $(10\bar{1}0)[1\bar{2}10]$ (#2 slip system in **Figure 17a**, blue in **Figure 18**) is less active because it has a much smaller M, 0.23. The <a> type dislocations on pyramidal and basal planes do not contribute to the deformation due to the low Schmid factor (0.19 and 0.09 respectively) and higher CRSS value.

Similar approaches were also applied on the electropolished samples 2 & 3 (**Appendix F**), and perfectly confirmed the slip systems active during the plastic deformation. For example, in sample 3 (**Figure 17b**), the active slip system in grain 1 was dominated by the $(1\bar{1}00)[11\bar{2}0]$

prism <a> slip system (M= 0.15), with dislocation cross-slip on $(1\bar{1}01)$ pyramidal plane (M=0.23). The active slip system in grain 2 was also identified to be $(1\bar{1}00)[11\bar{2}0]$ prism <a> slip system (M=0.41), and the slip system in grain 3 was the $(10\bar{1}0)[1\bar{2}10]$ prism <a> slip system (M=0.48). With precise identification of slip systems, the study of shear associated with each slip band during heterogeneous deformation and the investigation of slip/grain boundary activities is thus reliable.

3.3 The comparisons of surface-based techniques

The main purpose for analysis of the deformation of sample 1 was to compare different surface-based technologies in the evaluation of plastic deformation. Relative techniques involved in this study were ECCI, atomic force microscopy (AFM), and EBSD cross-correlation. Meanwhile, digital image correlation (DIC) data was provided by Dr. Zhe Chen in Professor Samantha Daly's group and was used for a comparison of local shear distribution with the AFM data [185, 186].

3.3.1 Local shear distribution across the surface

AFM was used to monitor the topography change due to deformation slip activation during the plastic deformation of sample 1. Each AFM grid covered a maximum area of 40 x 40 µm^2 to maintain considerable accuracy (large area scan will sacrifice accuracy)[11]. An example of AFM topography map is shown in **Figure 19**. **Figure 19b** is a color-scale topography map from the black boxed area in grain 2 (SE image) as shown in **Figure 19a.** The topography change due to two different slip systems can be detected from the AFM (no research has used AFM to

---

[11] Higher scanning speed will sacrifice the preciseness, so the tiny surface change will not be recorded by the system.

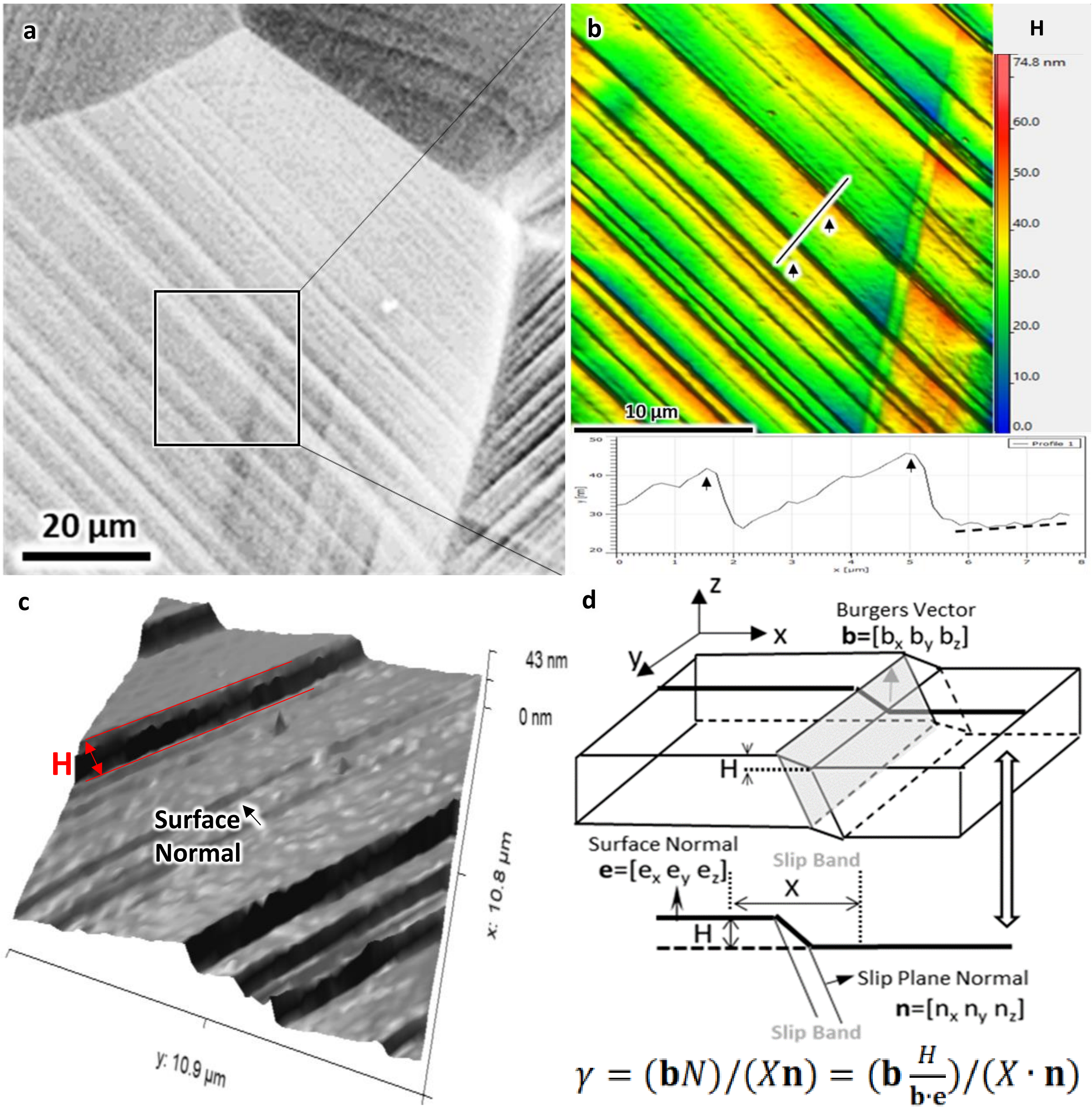

Figure 19a) SE image of the upper right corner of grain 2 in Ti-7Al sample 1. b) AFM color-scale map from the black boxed area in figure a). The black line is the AFM line profile showing the topography change across the line. The black arrows indicate the edges of slip bands, and the dashed line indicates the undistorted surface plane and is the basis of the height measurement. c) 3-D Greyscale topography map around the line sectioned area, the surface normal is calculated based on undistorted surface, H is the step of the slip band. d) A sketch of the mechanism to calculate the local shear distribution across the slip bands. The Burgers vector **b** and slip plane normal **n** can be directly achieved from the EBSD data once the slip system is confirmed by ECCI contrast analysis. Height difference across a slip band H can be directly measured from the AFM line profile. The distance across a slip band X is 0.3 µm in this study. (Amended from [185])

identify slip systems), which is consistent with the SEM observation (**Figure 18a**). In the AFM data analysis, the background is subtracted and the lowest point in the map is set to zero height, so it is easier to find the undistorted surface plane that has not experienced deformation (surface plane normal **e**). Based on the line section profile across the area (**Figure 19b&c**), the height change H (nm) across a certain distance (X µm) due to the activation of each slip system can be acquired. With the crystal orientation achieved from the EBSD, the Burgers vector **b** and slip plane normal **n** of each identified slip system (by ECCI) can also be calculated from the in-house MATLAB code [24], as outlined earlier. The method for local shear distribution was established by Yang et al. [44], with the mechanism shown in **Figure 19d** [185]. For a certain slip system that contributes to the formation of a slip band, the number of relative slip planes N can be calculated from the height change across the slip band H and the projection of the Burgers vector **b** $[b_x\ b_y\ b_z]$ onto the surface plane normal **e** $[e_x\ e_y\ e_z]$:

$$\mathrm{N} = \frac{H}{\boldsymbol{b}\cdot\boldsymbol{e}} \tag{6}$$

The calculation of shear is tile based. With equation (6), the averaged shear contributed by each slip band Υ along a certain distance X in each tile can be estimated as:

$$\Upsilon = (\boldsymbol{b}\ \mathrm{N})/(X\cdot\boldsymbol{n}) = \left(\boldsymbol{b}\ \frac{H}{\boldsymbol{b}\cdot\boldsymbol{e}}\right)/(X\cdot\boldsymbol{n}) \tag{7}$$

Where **n** $[n_x\ n_y\ n_z]$ is the slip plane normal of the certain slip system. The map of relative local shear distribution across one area in grain 2 is shown in **Figure 20b**, which reveals the topography change of this area according to the AFM map (**Figure 20a**). The deformation shear contributed by the $(01\bar{1}0)[2\bar{1}\bar{1}0]$ prism <a> slip system is from 0.3 to 0.7, and the shear from the $(10\bar{1}0)[1\bar{2}10]$ prism <a> slip system ranges from 0.08 to 0.15. This is also consistent with the argument that $(01\bar{1}0)[2\bar{1}\bar{1}0]$ prism <a> slip system (M = 0.49) is more active than the $(10\bar{1}0)[1\bar{2}10]$ prism <a> slip system (M = 0.23) in slip trace analysis and the SEM observation.

Based on a similar mechanism shown in **Figure 19d**, the local shear distribution of slip systems can also be calculated by measuring the difference of in-plane displacement [185, 186]:

$$\Upsilon = S/(X \cdot \boldsymbol{n}) \tag{8}$$

Where S [Δx Δy Δz] is the relative displacement that can be calculated from the Burgers vector and in-plane displacement across a slip band:

$$S = b\,\Delta x/b_x \tag{9a}$$

or

$$S = b\,\Delta y/b_y \tag{9b}$$

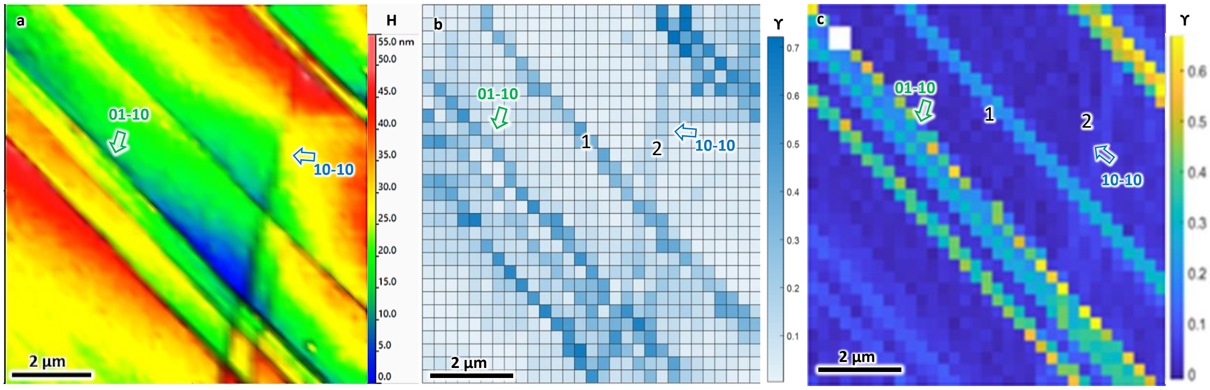

Figure 20a) color-scale AFM map from an area in grain 2. b) The heat map of local shear distribution across individual slip bands. The local shear contributed by the $(01\bar{1}0)[2\bar{1}\bar{1}0]$ prism <a> slip system ranges from 0.3 to 0.7, and the shear caused by the $(10\bar{1}0)[1\bar{2}10]$ prism <a> slip system ranges from 0.08 to 0.15. c) The relative shear distribution map of the same area calculated by the DIC method [185].

The resulting shear distribution map calculated by the DIC is shown in **Figure 20c** [185]. The deformation shear across each slip band calculated by the DIC method is similar with the AFM result. For example, the shear contributed by slip band #1 is ranging from 0.26 to 0.48 and the shear caused by slip band #2 is ~0.16 calculated by the AFM method. Similarly, the DIC method shows a similar shear amount from slip band #1 (0.25~0.45) and #2 (~0.14). The difference might come from differences in the accuracy of AFM and DIC data collection (DIC is more sensitive to in-plane displacement, while AFM is more focused on out-of-plane measurements) or the position variance used in the calculation (the two points at a distance of X µm across the slip band are different in AFM and DIC calculation), etc. Nevertheless, the overall results from the two methods are consistent with each other. Besides this typical example, comparisons between both methods have been made across several other slip bands, all giving reasonable results. This suggests the two methods are reliable and consistent in revealing the local shear distribution in the plastic deformation.

3.3.2 Dislocation based characterizations of plastic deformation

Different from the AFM and DIC approaches that directly reveal the shear that cause deformation, the EBSD cross-correlation method is able to estimate the residual elastic shear after slip band formations by investigating the distribution of geometrically necessary dislocations (GNDs). Since the methodology study of parameter selection of GNDs is not the focus of this study and has been well illustrated by Fullwood et al.[117, 136-138], the specific parameter selection for this approach will not be discussed. In this study a 990 nm step size was used for the cross-correlation calculation in the open source OPEN-XY software[12] [187], which gives a relatively stable GNDs density (990 nm is where GND does not significantly change with step size) and eliminates potential noises from data collection. Since the dislocations are visible by ECCI, it is possible to compare the reliability of the GNDs to ECCI [137, 138]. The resulting comparison of total GND map (i.e. all dislocation types; split GNDs for α titanium is currently unavailable) and ECCI is shown in **Figure 21**. **Figure 21a** shows ECCI

---

[12] The latest OPEN-XY has added the GNDs calculation of α titanium, however, the split GNDs for α titanium is currently unavailable. This is the reason for showing only total GNDs, rather than GNDs for each types of dislocations in this study.

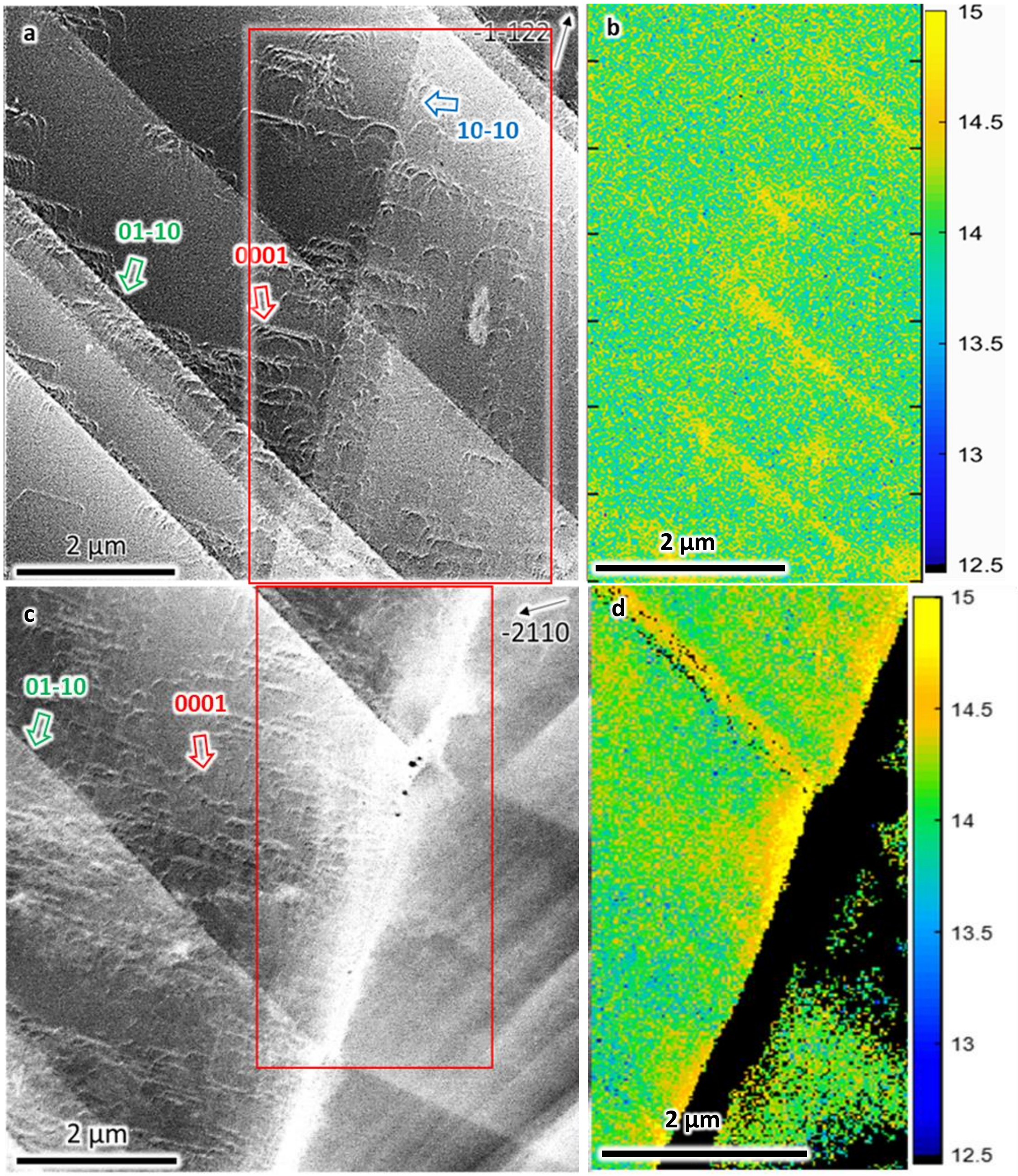

Figure 21a) ECC image of the same area with Figure 20. Besides the $(01\bar{1}0)[2\bar{1}\bar{1}0]$ (green) and $(10\bar{1}0)[1\bar{2}10]$ (blue) two prism <a> slip systems identified in the slip trace analysis, (0001) $[11\bar{2}0]$ (red) basal <a> dislocations are revealed by the contrast analysis. The prism <a> type dislocations appear to align perfectly along the slip bands, while the basal <a> dislocations are less uniformly distributed across the observed area. b) The GND logarithm map of the red boxed area of a). The GND map is consistent with ECCI observation, although individual dislocations cannot be resolved as good as the ECCI observation. c) The ECC image at the grain boundary of grain 2, with $(01\bar{1}0)[2\bar{1}\bar{1}0]$ (green) and (0001) $[11\bar{2}0]$ (red) dislocations. Prism <a> dislocations align close to the slip bands and basal <a> dislocations are more randomly distributed across the surface. d) The GND map from the red box area of c). The GND on the other side of the grain boundary is not available due to misorientation angle exceeding the threshold from the reference point in grain 2. The GND map is consistent with ECCI observation.

observation of the same area with **Figure 20**, where the shear is calculated by the AFM and DIC. ECCI correctly reveals the two prism <a> slip systems, $(01\bar{1}0)[2\bar{1}\bar{1}0]$ (green) and $(10\bar{1}0)[1\bar{2}10]$ (blue), that have been identified in the slip trace analysis. The dislocations of the two types are uniformly aligned on the slip bands. More importantly, ECCI contrast analysis also reveals a number of (0001) $[11\bar{2}0]$ basal <a> dislocations (red) that are less uniformly distributed within the vicinity of the slip bands. **Figure 21b** shows the logarithm map of total GNDs from the red boxed area in **Figure 21a**. It appears the dislocation density along the slip band ($10^{14.5\sim15}$) is more than one magnitude larger than the overall background ($10^{13\sim13.5}$), with some dislocations ($10^{14\sim14.5}$) distributed randomly near between slip bands. The total GND density is consistent with the ECCI observation (10^{14} corresponds to 50 nm between dislocations) that dislocations are more localized around the slip bands. Similarly, ECCI and GND map at one of the grain boundary in grain 2 also consistent dislocation distributions on the left side of the grain boundary (**Figure 21c&d**), although only $(01\bar{1}0)[2\bar{1}\bar{1}0]$ (green) prism <a> dislocations and (0001) $[11\bar{2}0]$ basal <a> dislocations (red) are detected. Again, the prism <a> dislocations are found confined in the slip bands, whereas the basal <a> dislocations are less uniformly distributed between slip bands.

3.3.3 Comparison between the classic EBSD based slip trace analysis and ECCI

It may be noticeable in the discussion of **Figure 21** that EBSD based slip trace analysis is not able to identify all the slip systems developed during the plastic deformation. Some slip systems may not develop well defined slip bands for a number of reasons: if cross slip is easy, dislocations may not form well defined slip traces or if the slip plane is aligned close to parallel to the observed surface. Additionally, if an experimentally observed slip trace does not match

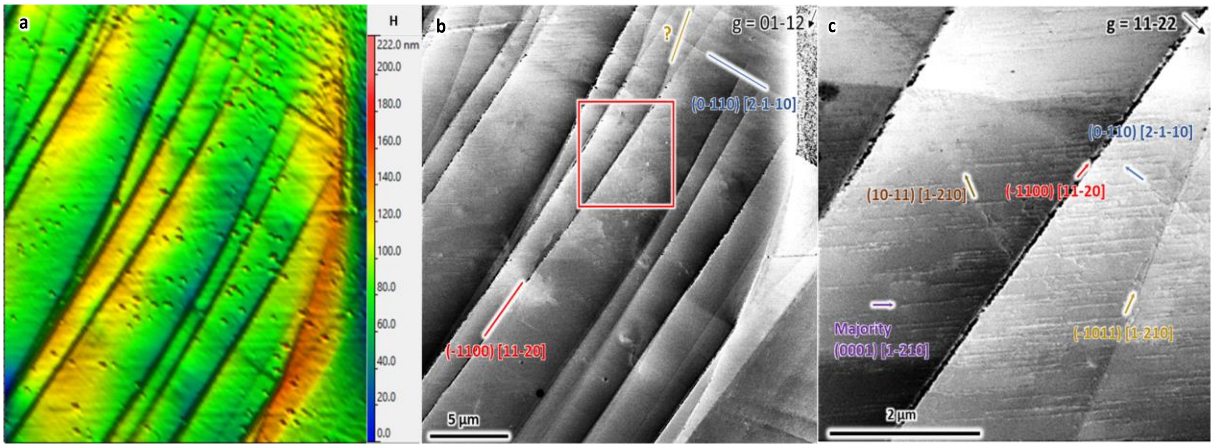

Figure 22a) AFM color-scale topography map at the upper right corner of the grain 1 in sample 1. Two different deformation shear system can be observed by the AFM. b) ECC image of the same area, two slip systems were identified through the EBSD-based slip trace analysis, which are the $(0\bar{1}10)[2\bar{1}\bar{1}0]$ prism <a> slip system (blue) and the $(\bar{1}100)[11\bar{2}0]$ prism <a> slip system (red). The slip trace marked in light brown cannot be identified by the slip trace analysis. c) High magnification ECC image of the red box area in b). Contrast analysis shows several additional dislocations, including $(10\bar{1}1)[1\bar{2}10]$ and $(\bar{1}011)[1\bar{2}10]$ two pyramidal <a> slip systems and a mixture of basal <a> dislocations with majority belong to $(0001)[1\bar{2}10]$ slip system. The unknown branched slip trace is caused by the $(\bar{1}011)[1\bar{2}10]$ pyramidal <a> slip system.

the theoretical trace, the slip system for that trace cannot be identified. Slip system identification in grain 1 of sample 1 is an example showing these limitations of current slip trace analysis (**Figure 22**). Both AFM topography map and the SEM image show two different slip traces. EBSD-based slip trace analysis indicates the slip traces are caused by $(\bar{1}100)[11\bar{2}0]$ (red) and $(0\bar{1}10)[2\bar{1}\bar{1}0]$ (blue) prism <a> slip systems (**Figure 22a&b**). But there is another type of slip trace observed close to the upper grain boundary of grain 1 (brown), which cannot be identified, since the slip trace does not match any of the theoretical traces. ECCI contrast analysis reveals this unidentified slip system to be $(\bar{1}011)[1\bar{2}10]$ pyramidal <a> slip system (light brown in **Figure 22c**). The slip trace might be distorted by local lattice rotation or the topography development during the plastic deformation, and thus deviate from the theoretical traces. Additionally, a large number of basal <a> dislocations are detected by ECCI, with the majority belonging to $(0001)[1\bar{2}10]$ slip system. Based on the MATLAB code calculation, at this crystal orientation, the basal plane is close to parallel to the sample surface, thus no slip band can be easily developed that can be identified in the slip trace analysis. Furthermore, the basal <a> and $(10\bar{1}1)[1\bar{2}10]$ pyramidal <a> dislocations are also observed (brown), but the density is small compared to other dislocation types. Thus, these dislocations have not developed slip bands on the surface. Similar situations where more dislocation types can be identified by ECCI than the slip trace analysis were also observed in other grains of sample 1 (**Appendix G**).

3.3.4 Advantages and disadvantages of EBSD, DIC/AFM, and ECCI

A summary of slip system identification using EBSD based slip trace analysis, ECCI, and AFM/DIC [185] is shown in Table 1. Classic EBSD-based slip trace analysis is not good at differentiating slip systems that have similar slip traces[13]. With the help of the Schmid factor/CRSS ratio, some pyramidal <c + a> slip systems can be eliminated (i.e. $(2\bar{1}\bar{1}2)[\bar{2}113]$ in

Table 1. Slip systems identified by EBSD slip trace analysis, ECCI, and AFM/DIC

	Grain 1	Grain 2	Grain 3	Grain 5
EBSD-slip trace analysis	$(0\bar{1}10)[2\bar{1}\bar{1}0]$ $(0\bar{1}11)[\bar{1}2\bar{1}3]$ $(\bar{1}100)[11\bar{2}0]$ $(2\bar{1}\bar{1}2)[\bar{2}113]$	$(0\bar{1}10)[2\bar{1}\bar{1}0]$ $(10\bar{1}1)[\bar{1}\bar{1}23]$ $(01\bar{1}1)[\bar{1}2\bar{1}3]$ $(10\bar{1}0)[1\bar{2}10]$	$(0\bar{1}10)[2\bar{1}\bar{1}0]$ $(01\bar{1}1)[\bar{1}\bar{1}23]$ $(10\bar{1}0)[\bar{1}2\bar{1}0]$ $(10\bar{1}1)[\bar{1}\bar{1}23]$	$(1\bar{1}00)[11\bar{2}0]$ $(2\bar{1}\bar{1}2)[\bar{2}113]$
ECCI	$(0\bar{1}10)[2\bar{1}\bar{1}0]$ $(\bar{1}100)[11\bar{2}0]$ $(\bar{1}011)[1\bar{2}10]$ $(0001)[1\bar{2}10]$ $(10\bar{1}1)[1\bar{2}10]$	$(01\bar{1}0)[2\bar{1}\bar{1}0]$ $(10\bar{1}0)[1\bar{2}10]$ $(10\bar{1}1)[1\bar{2}10]$ $(0001)[11\bar{2}0]$	$(0\bar{1}10)[2\bar{1}\bar{1}0]$ $(10\bar{1}0)[\bar{1}2\bar{1}0]$ $(0\bar{1}11)[2\bar{1}\bar{1}0]$ $(\bar{1}100)[11\bar{2}0]$	$(1\bar{1}00)[11\bar{2}0]$ $(01\bar{1}0)[2\bar{1}\bar{1}0]$
AFM and DIC [185]	$(0\bar{1}10)[2\bar{1}\bar{1}0]$ $(\bar{1}100)[11\bar{2}0]$	$(01\bar{1}0)[2\bar{1}\bar{1}0]$ $(10\bar{1}0)[1\bar{2}10]$	N. A.	N. A.

Note: Colored fonts indicate different slip traces, black fonts are dislocations that are only observed in ECCI. Shadowed slip systems are not likely to be activated because of the lower Schmid factor/CRSS ratio.

---

[13] This is partially resolved by the EBSD cross-correlation that use lattice rotation across a slip band to determine the possible slip system [189]. This method is not the classic slip trace analysis.

grain 1&5), however, this estimation is not always safe (such as grain 2&3). On the other hand, AFM and DIC [185, 186] are more precise in the slip system identification, since the physical displacement[14] across a slip band indicates shear direction (i.e. Burgers vector), which supplements the trace analysis. Unfortunately, these methods are not good for traces that do not match the theoretical generated traces (grain 1 in **Figure 22**) or the slip systems that do not show apparent slip traces (i.e. (0001) dislocations in grain 1&2). On the contrary, ECCI is especially good for the identification for slip systems since this identification is based on dislocation contrast rather than topography/displacement change. Compared to the classic slip trace analysis [24, 185, 186] that need to “guess” the slip system by calculating the deviation factor (a factor defines the deviation of an observed trace from a theorical one. Zero deviation means a perfect match), of an observed trace to the theoretical one dislocation contrast approach is more likely a “yes or no” determinant analysis. Once enough ECC images at different channeling conditions **g** are taken, there is almost no uncertainty in the identification of dislocations regardless of the morphology of the slip traces. Thus, ECCI is able to identify every dislocation slip activation during the deformation that is ignored by the classic slip trace analysis (ECCI row in **Table 1**). This is particularly important when studying the strain accommodation and slip transfer since some “hidden” dislocations may also play significant roles in these events.

Slip system identification techniques, no matter ECCI or DIC/AFM, need the crystal orientation information achieved from the EBSD. Although not shown in this study, most

---

[14] Currently, this method is only available on DIC, however, since the mechanism are similar, it is possible to develop a program for AFM.

recent EBSD cross-correlation is able to more precisely identify slip systems by relating the GND-induced rotation gradient across the slip bands to the slip system identifications [185, 188]. Yet EBSD cross-correlation is time consuming and needs extremely large data volume (30 Gb for an area shown in **Figure 21** at a step size of 200 nm, 5 hours per scan).

DIC and AFM are generally useful tools for studying plasticity. DIC is more accurate in monitoring the in-plane displacement, while AFM is good for determining out-of-plane topography change. With the crystal orientation information, both methods give reliable information of the local shear distribution across slip bands. Particularly, by correlating the relative displacement across a slip band to a theoretical slip system, DIC is more precise in the identification of the slip plane, thus improve the reliability of the slip trace analysis. However, this improved slip trace analysis is still blind to the curvy traces that will develop from cross-slip, traces that deviate from theoretical traces, and slip systems that do not form a slip trace. This is a chronic issue that all the slip trace analysis techniques suffer from. Although this issue may not be significant in the study of overall plasticity development in the bulk sample, this issue may lead to severe problems in slip transfer studies, since such irregular or hidden slip traces usually exist near the grain boundary. Incorrect identification of these slip systems may bias the understanding of slip interactions at the grain boundary.

Compared to the techniques discussed above, ECCI is extremely strong in the slip system identification since it is able to identify the Burgers vector of a slip system by contrast analysis. This means ECCI is not affected by the morphologies of slip traces at the free surface. By revealing all types of dislocations, it is possible to investigate the accommodating events at the grain boundaries at dislocation level, which is generally ignored in the studies that heavily rely on the slip trace analysis. Thus, ECCI is a perfect solution to the establishment of a precise slip trace analysis. The only drawback for ECCI is the time-consuming issue, since it generally need at least 6 different **g** vectors (must include at least one $\mathbf{g} \cdot \mathbf{b} \times \mathbf{u} = 0$ or $\mathbf{g} \cdot \mathbf{b} = 0$) to identify Burgers vector and several more tilt & rotate operation to reveal slip planes. Additionally, too much topography change after the high strain deformation will add difficulty for the establishment of channeling condition and resolving individual dislocations.

3.4 The reveal of the geometry of slip systems at grain boundaries

As discussed in the previous section, one of the benefits of using ECCI in the study of slip accommodation is the capability to precisely identify all active slip systems at grain boundaries. This is particularly important in the understanding of slip transfer events between grains in hcp titanium. The stress state at the grain boundary may not be the same as it is within the grain, thus slip activation may be completely different at the grain boundary. Such local activation of unexpected slip systems may not be correctly revealed by the slip trace analysis due to lack of slip traces[15]. This leads to a bias in the evaluation of slip transfer events during heterogeneous deformation due to the ignorance of local slip accommodation mechanisms at the grain boundary.

3.4.1 Categories of slip system interaction at surface

Different slip transfer mechanism may be revealed by varied interactions between an “incoming” dislocation and an “outgoing” dislocation. The interactions of dislocation slip at the grain boundary were generally categorized into three types in early studies of slip transfer events based on the TEM observations [25, 77- 87]. These classifications are still widely used in

---

[15] If the slip plane of a slip system is close to parallel to the surface, slip band is hard to be revealed at the surface.

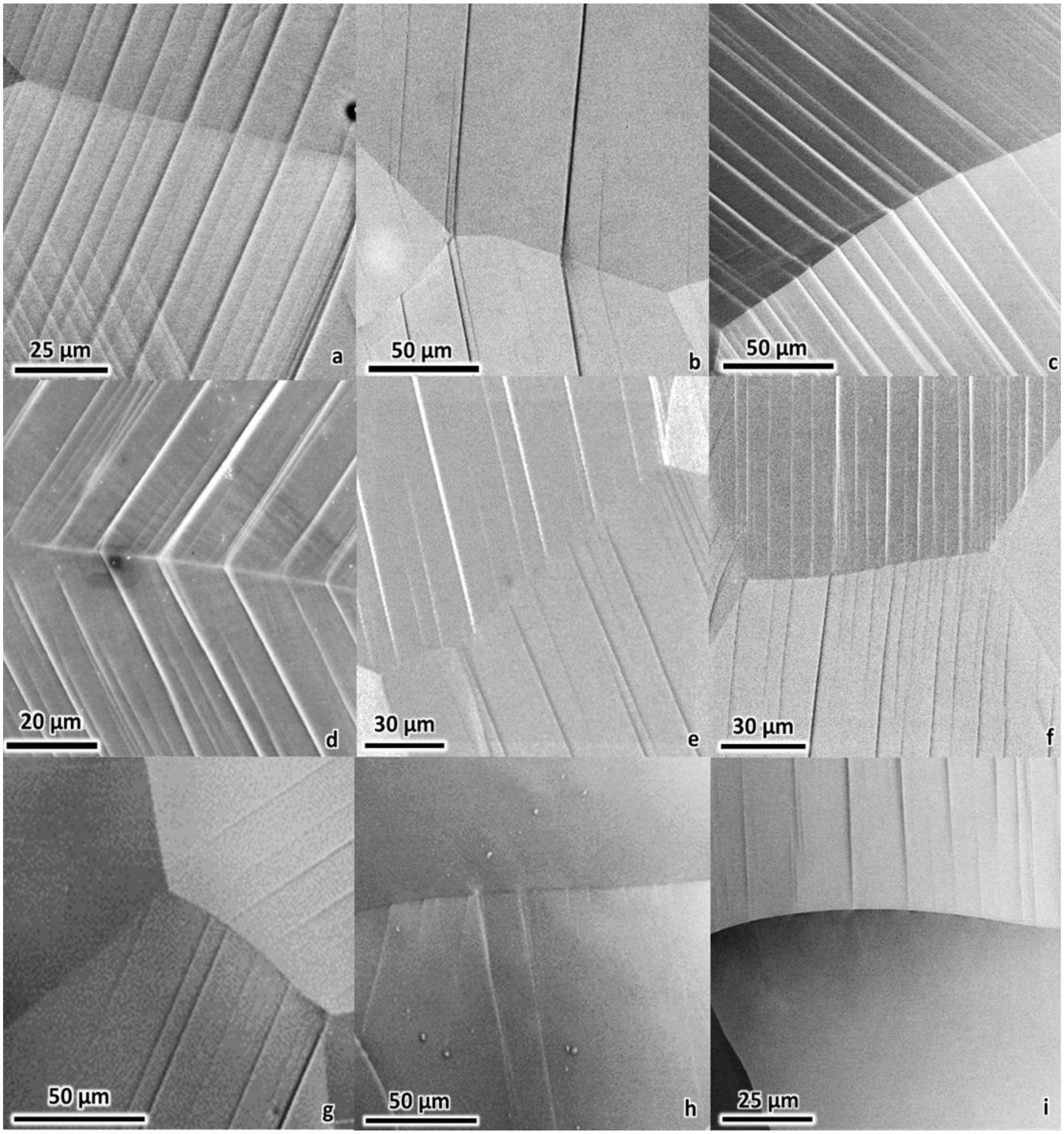

Figure 23a-d) SE images of "well-correlated" slip systems with the slip traces meeting at the same points on the grain boundary at surface in sample 2. It appears that slip traces that area far from parallel can also be "well-correlated". e-g) SE images of "non-correlated" slip systems in sample 2. The slip traces do not intersect at the same point on the grain boundary at surface, despite the slip system is highly activated. h-i) SE images of "blocked" slip systems in sample 2. The strong activation of slip systems that propagate up to the grain boundary only occurs in one of the grains, with the other grain undeformed. At certain circumstances, the unresolved shear from the "blocked" slip system may activate new slip systems that are travelling back into the originated grain.

the studies of heterogeneous deformation to describe how slip systems interact at the free surface. The first type describes the situation that two slip systems in their respective grains meet at the same point at the grain boundary. It appears the dislocation slip coming from a “parent” grain easily activates new dislocation slip in the “receiving” grain right at the intersection point with the grain boundary. The interaction between the two slip systems is referred as “well-correlated”. As shown in **Figure 23a-d**, such well-correlated slip interaction can happen not only between slip traces that are close to parallel to each other (Figure 23a-c), but also between those that are far from parallel (Figure 23d). The second type of slip interaction is shown in Figure 23e-g. Despite the strongly activation of slip bands in both grains, the slip bands do not meet at the same point at the grain boundary, regardless of whether or not their slip traces appear to be parallel aligned. This type of interaction is defined as “non-correlated”. It may suggest the slip activation within each of the neighboring grain is independent, or alternatively the deformation shear from the “parent” grain is not able to be directly transferred into the adjacent “receiving” grain. The last type of interaction is shown **Figure 23h&i**. The slip system is highly activated only in one of the grains. It appears the slip band activity in the more deformed grain is efficiently “blocked” by the grain boundary in between, and no shear is transferred across the grain boundary. This slip interaction is then called “blocked”.

3.4.2 Limitations of the current category system and free surface biasing effects

It seems convenient to directly apply the concepts that were used in TEM thin film studies (in-situ slip transfer studies) of slip transfer in polycrystal heterogeneous deformation. However, it has been long ignored that neither the “2-D” SEM images of the slip trace

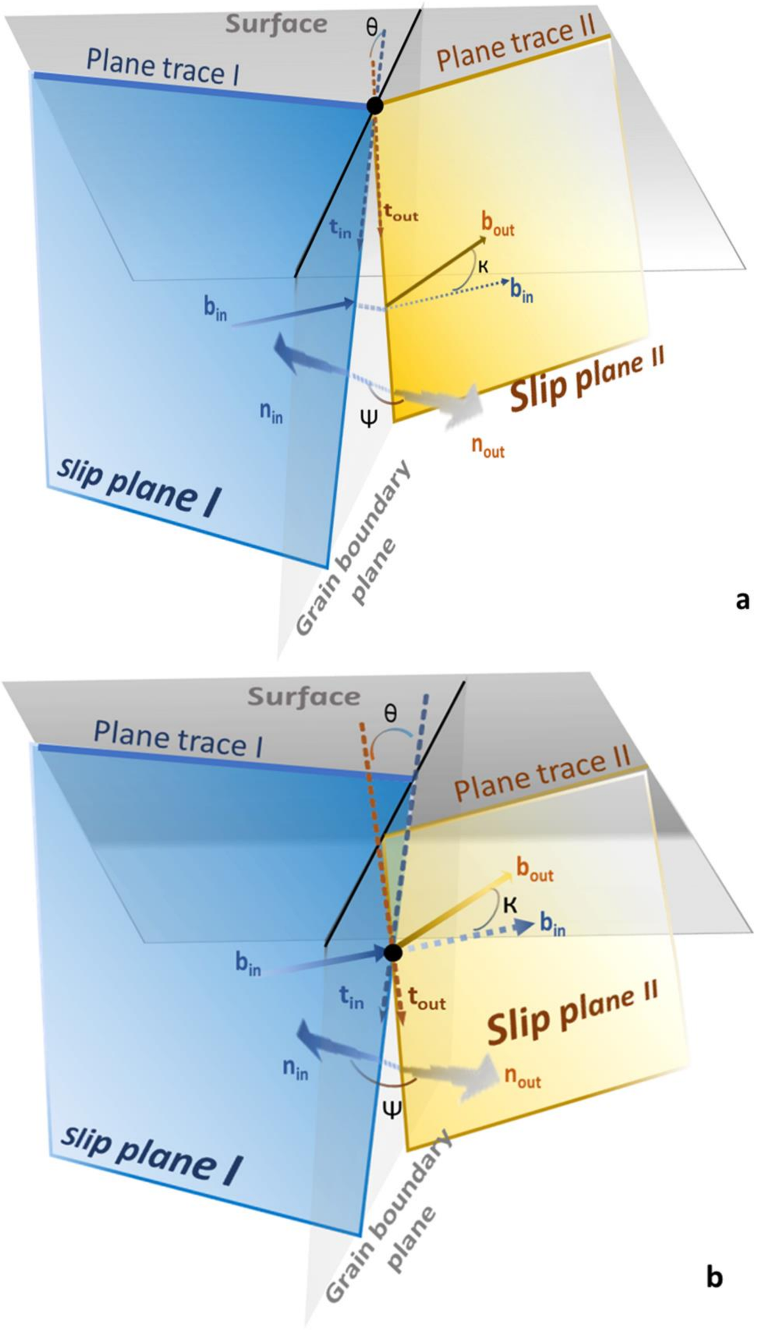

Figure 24a) 3-D geometry of slip system interactions at a grain boundary. The two slip systems are considered as well-correlated slip systems since they intersect at the same point at the grain boundary on the free surface. Although slip systems intersect at the same black point at the surface, it can be clearly seen that they do not meet below the surface since the geometric orientations of the two slip systems are different, with $\Theta \neq 0^{o}$. b) Another 3-D geometry of slip bands interactions in the vicinity of a grain boundary. The two slip systems are defined as non-correlated since they do not meet at the surface. However, they may meet at the grain boundary plane somewhere below the surface. Although the slip transfer mechanism may be different between a) and b), current studies of slip transfer ignore this potential difference and directly use the slip transfer criteria to evaluate the strain accommodating events at the grain boundary.

interactions at the surface, nor TEM thin-film [79-86] observations are able to fully represent the full “3-D” geometry of the slip systems and the grain boundaries. **Figure 24a&b** show the ideal 3-D geometry of both “well-correlated” and “non-correlated” slip systems on opposite sides of a grain boundary plane. The two slip bands from the two neighboring grains will only meet at one point at the grain boundary plane, since generally $\Theta \neq 0^o$, except in very limited cases. If this is true, then it is hard to rationalize that slip transfer only occurs at the common points. Thus, the deformation shear transfer in the regions away from the common point is currently unclear. In addition to this, not only in this study, but also others [45, 74, 75], have found that there are more observations of “well-correlated” slip systems than “non-correlated” slip systems. This may suggest the free surface is biasing the observations by creating more “well-correlation” slip systems at the surface through unknown mechanism. Nonetheless, the alignment of slip bands and the slip transfer among slip systems ($\Theta \neq 0^o$) below the surface will be revealed by ECCI after removing approximately five microns of material through electropolishing [171, 175].

3.4.3 Comparison of slip system alignment at and below surface

One example of “well-correlated” slip systems at the surface is shown in **Figure 25a**. Despite the large angle between the slip traces, slip traces from the two slip systems consistently meet at the same points on the grain boundary. ECCI facilitated slip trace analysis reveals the slip system in the upper grain is the $(0\bar{1}10)[\bar{2}110]$ prism <a> slip system with a higher Schmid factor of 0.48, and its well-correlated counterpart in the lower grain is the $(10\bar{1}0)[\bar{1}2\bar{1}0]$ prism <a> slip system (lower M=0.36). It seems dislocation slip is more easily activated in the upper grain than in the lower grain due to a higher Schmid factor M with the

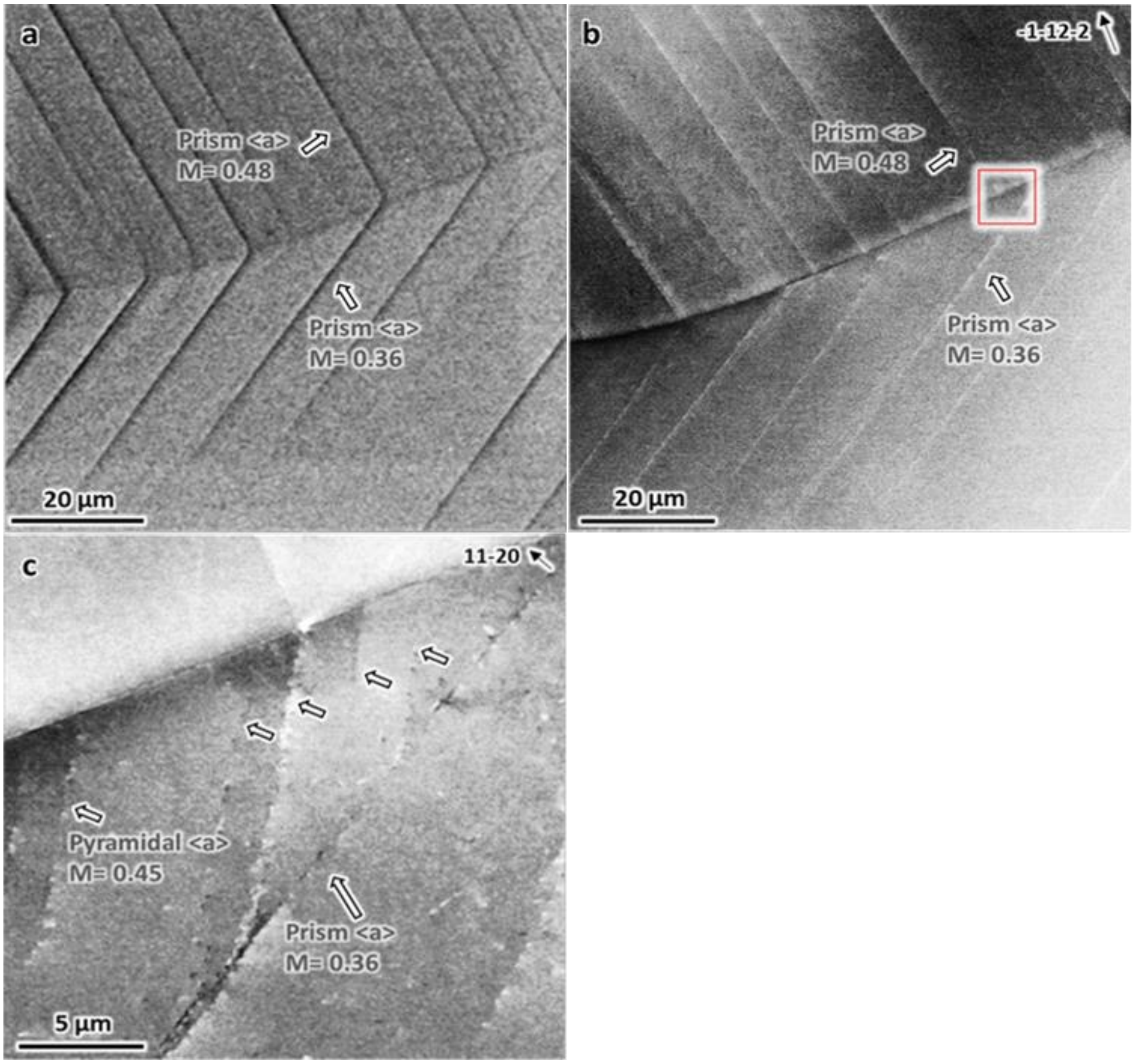

Figure 25a) SE image showing two slip traces that are well-correlated at the surface. The despite a large angle between the slip traces, they intersect at the same points on a grain boundary. ECCI facilitated slip trace analysis indicates the slip system in the upper grain is the $(0\bar{1}10)[\bar{2}110]$ prismatic <a> slip system with the Schmid factor 0.48. The slip system in the lower grain is $(10\bar{1}0)[\bar{1}2\bar{1}0]$ prismatic <a> slip system, with a lower Schmid factor of 0.36. The white arrows mark one of the well-correlated slip traces for comparison. b) ECC image of the same region, but 5 µm below the surface. The observed slip bands are now due to dislocation contrast, rather than topography. It can be clearly seen that the slip bands are misaligned in the electropolished area, which is indicated by the relative position change of the white arrows. Nevertheless, the relative spacing and distributions of the slip bands remains unchanged. c) high magnification ECC image of the area in the red boxed area in figure (b). It shows the activation of $(\bar{1}011)[\bar{1}2\bar{1}0]$ pyramidal <a> secondary slip systems (M =0.45) in the lower grain from an intersection point of the slip system form the upper grain at the grain boundary. The secondary slip system propagates a short distance and appears to merge into the primary slip system in the lower grain. There might be multiple activation of such secondary slip system, possibly from different sources at different depth in the grain boundary plane, which is indicated by the small arrows.

same CRSS value, which is also consistent with the observation that deformation slip only propagates a short distance in the lower grain. It also appears the slip system in the lower grain is nucleated from the intersection points between the slip system in the upper grain at the grain boundary to accommodate the induced deformation shear, although it is not clear where the slip system in the upper grain is originated. Despite the correlation of these slip bands (i.e. two big arrows), the two slip systems do not align perfectly as they might appear to. The geometric compatibility factor between the two slip systems is m' = 0.61 (the angle between the Burgers vectors is 15.4°), suggesting the two slip systems are still misaligned. Since the slip plane normals of the two slip systems are far from parallel (the angle Ψ between the slip plane normal is 50.4°), as shown in **Figure 24a**, it can be imagined that unless Θ = 0, there will be significant misalignment of the slip planes below the surface.

Figure 25b is an ECC image of the same area after electropolishing. Different from **Figure 25a,** where the slip bands are observed due to topographical contrast, the observation of the slip bands come from the contrast of dislocations at certain channeling condition (in this case **g** = $[\bar{1}\bar{1}2\bar{2}]$). By comparing **Figure 25a&b**, it appears that the spatial distribution of the slip bands remains the same (i.e. the spacings and distributions of the slip bands on either side of the boundary are the same at and below the surface). It also appears that the propagation of all slip bands in each grain are consistent in the two images (slip bands move to the right in the upper grain, while the slip bands move to the left in the lower grain). But critically, despite the spatial distribution of the slip bands remaining the same between surface and subsurface observation, the intersection points of the slip bands at the grain boundary are now offset by approximately 7 μm (indicated by big arrows). This is consistent with the expectation that the slip systems will no longer be well-correlated below surface. Detailed ECCI analysis of the red boxed area is shown in **Figure 25c**. A number of secondary slip systems in the lower grain are found to be well-correlated with the primary slip system in the upper grain (indicated by small arrows). These secondary slip systems appear to nucleate from where the slip system in the upper grain intersects the grain boundary. The secondary slip systems then propagate a short distance and merge into the primary slip system in the lower grain. ECCI contrast analysis reveals the Burgers vectors of the dislocations associated with the secondary slip system are the same as those in the primary slip system, $[\bar{1}2\bar{1}0]$. However, these secondary slip bands are on the $(\bar{1}011)$ pyramidal plane, different from the $(10\bar{1}0)$ plane of the primary slip system. Nevertheless, the shear accommodation at grain boundary appears to be facilitated by the activation of the secondary slip system ($m' = 0.86$). Strong correlation with the "incoming" primary slip system in the upper grain is still achieved by the secondary slip system in the lower grain. By correlating the surface and subsurface images, the approximate 3-D geometry of the slip systems and the grain boundary can be reconstructed (**Appendix H**), and the angle Θ between the intersection lines of slip systems at the grain boundary (and the grain boundary inclination angle ε) can be calculated. This allows the interactions between slip systems at grain boundaries to be assessed in a more comprehensive way. In this particular case (**Figure 25**), based on the seven microns offset between the intersections points of the slip systems at the grain boundary at five microns below the surface, the grain boundary plane inclination angle ε is around 20°. The angle $\Theta_{p\text{-}p}$ between the "incoming" primary slip system in the upper grain and the "outgoing" primary slip system in the lower grain is approximately 36°, while the $\Theta_{p\text{-}s}$ between the "incoming" primary slip system and the "outgoing" secondary slip system is around 17°. It can be also determined that the m' between the "outgoing" secondary slip system and the "incoming" primary slip system is 0.88, higher than that between the two primary slip systems, m' = 0.61. Nevertheless, despite the "outgoing" secondary slip system has a higher Schmid factor (M = 0.45) than the "outgoing" primary slip system (M = 0.36), slip activity of this secondary pyramidal <a> slip system is suppressed due to a much larger CRSS value to the prism <a> slip system (1.3~8:1 [25-28,24-37]). It is reasonable to conclude that the local activation of secondary slip system facilities strain accommodation at the grain boundary. The much stronger alignment of the secondary slip system with the "incoming" primary slip system helps to compensate the incompatibility between the primary slip systems within the grain boundary below the surface. Since dislocation propagation on the pyramidal plane is not favorable, these dislocations begin to cross-slip and glide onto the prism plane at a short distance away from the boundary, where the propagation is much easier under global stress state. In conclusion, different from the overall deformation of grain interior, which is strongly controlled by the primary slip systems with high Schmid factor/CRSS, local accommodation at the grain boundary generally requires the activation of secondary slip systems that are better aligned with the "incoming" slip system.

The local accommodation at the grain boundary below surface can also be found between "well-correlated" slip systems with a small angle between their slip traces in the boundary. One example is shown in **Figure 26**. The prism <a> slip system (M = 0.49) in the upper grain appears to be well-correlated with the basal <a> slip system (M = 0.40) at the grain boundary in the as-deformed sample. Comparison of **Figures 26a&b** reveals that the relative spacing and distribution of the slip lines remain the same before and after electropolishing,

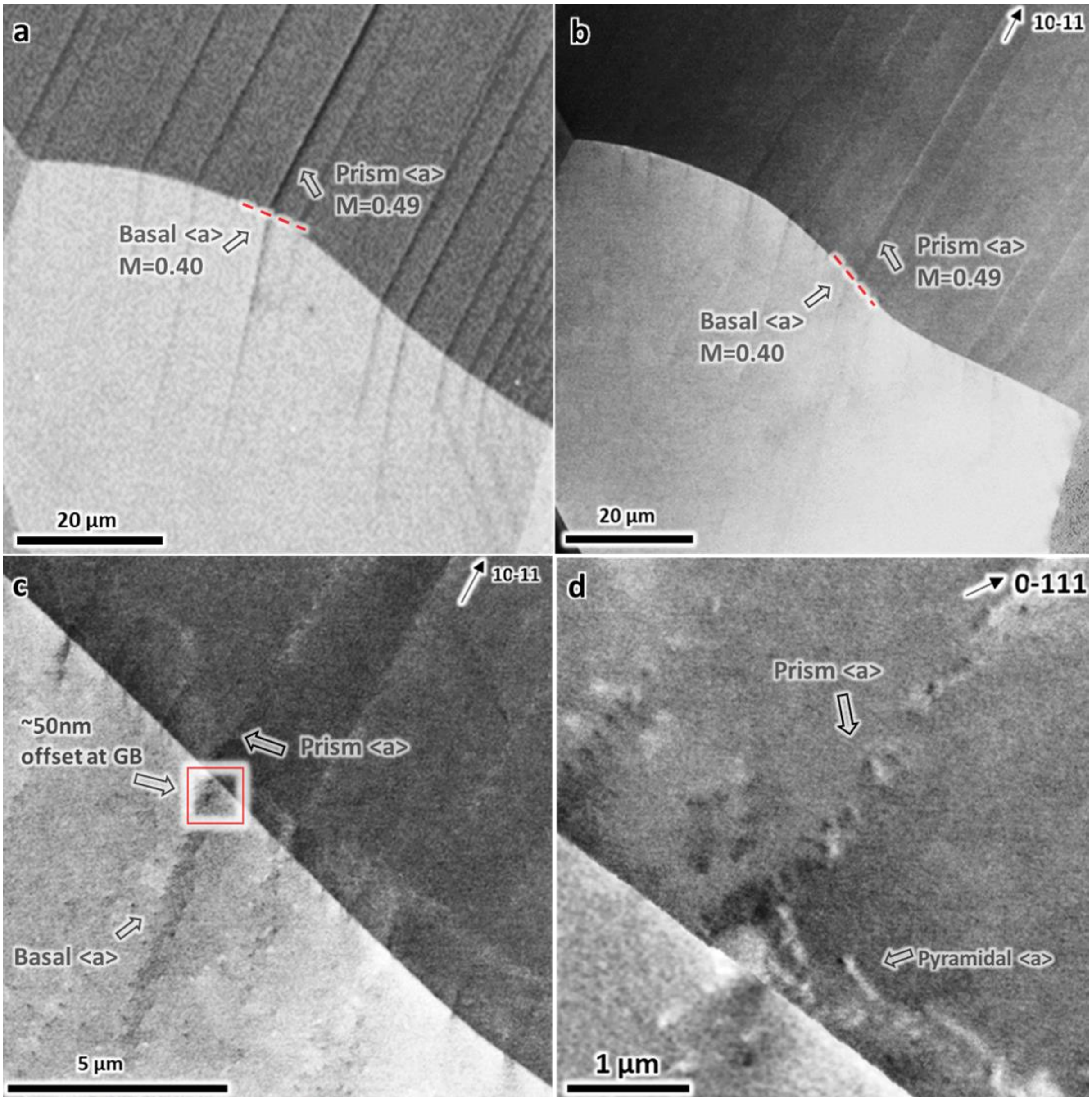

Figure 26a) The SE image shows the "incoming" prism <a> slip system in the upper grain is well correlated with the "outgoing" basal <a> slip bands in the lower grain at the grain boundary. The red dashed tangent line represents the trace of the grain boundary at the intersection point with the strongest band in the upper grain. b) ECC image of the same area after removing 5 µm through electropolishing. The grain boundary orientation is significantly changed, which is indicated by the change of the red dashed tangent line around the same strongest activated slip band. The slip band spacings and relative distributions remain the same before and after surface removal. c) Higher magnification ECC image of red tangent line area. A ~50 nm misalignment between the two slip systems below the surface has been observed. d) ECC image of the red boxed area in figure (c). A small number of secondary slip system is observed in the upper grain in this case.

although the grain boundary orientation has changed significantly, as is reflected by the change of the red dashed line. Closer examination on the previously “well-correlated” slip lines at the grain boundary reveals an approximately 50 nm offset between the intersection points at the grain boundary after electropolishing (**Figure 26c**). This very small deviation between the primary slip systems across the grain boundary is consistent with the relative high geometric compatibility (m’ = 0.84), suggesting shear accommodation at this grain boundary is not so difficult as the previous case (m’= 0.61). ECCI analysis around the intersection points shows a limited number of pyramidal <a> dislocations in the lower grain, as well as one pyramidal <a> secondary slip system in the upper grain. Particularly, as shown in **Figure 26d**, despite the Burgers vector of the secondary slip system being the same with the primary slip system in the upper grain, ECCI contrast analysis shows the dislocations are in different contrast. This indicates the dislocations have different line directions and different edge and screw components. Although not shown specifically, the dislocations associated with the secondary slip system also have the same Burgers vector with the primary slip system in the lower grain. The angle $\Theta_{p\text{-}p}$ between the two primary slip system is relatively small, ~15°, which is consistent with the larger m’ between these systems. In this special case, since secondary slip systems exist in both grains, it is necessary to calculate the $\Theta_{p\text{-}s}$ separately[16]. The $\Theta_{p\text{-}s}$ between “incoming” primary basal <a> slip system in the lower grain and the “outgoing” secondary pyramidal <a> slip system in the upper grain is ~ 37°, while the $\Theta_{p\text{-}s}$ between “incoming” primary prism <a> slip system in the upper grain and the “outgoing” secondary pyramidal <a>

---

[16] It needs to define a primary slip system in one grain as the “incoming” system to evaluate the interactions with all other “outgoing” ones. Same approach is then applied on the other primary slip system across the boundary to complete the other half of the analysis.

slip in the lower grain is ~22^o. Other secondary slip systems combinations have also been studied, including $\Theta_{p\text{-}s}$ between primary and secondary slip systems in the upper grain (~ 25^o), $\Theta_{p\text{-}s}$ limited to the lower grain (~36^o), and $\Theta_{s\text{-}s}$ (~60^o). These suggest the secondary slip system is primarily accommodating the shear from the primary slip system across the boundary, rather than the shear within the own grain. Additionally, it might not be necessary for the secondary slip systems to be well-correlated with each other. Although the detailed mechanism of this accommodation event may be more complicated than it appears, it doesn't change the fact that local accommodation can still occur by the activation of secondary slip systems despite the two primary slip systems being well-aligned. Atomic studies of such slip well correlated surface slip transfer with varying Θ would be insightful for understanding the details of the dislocation mechanisms at these boundaries, but are beyond the scope of the present study.

One detailed analysis for "non-correlated" slip systems is shown in **Figure 27**. At the surface, the $(0\bar{1}10)[\bar{2}110]$ prism <a> slip bands (M= 0.30) in the upper grain and the $(10\bar{1}0)[\bar{1}2\bar{1}0]$ prism <a> slip bands (M= 0.28) in the lower grain do not meet at the same points on the grain boundary (**Figure 27a**). The lack of correlation between the two primary slip system is also consistent with the low m'=0.49 ($\Theta_{p\text{-}p}$ =58^o), despite the slip systems being readily active within their respective grains. Following electropolishing, it can be clearly seen that the relative spacing and distribution of the slip bands remain the same in each grain below the surface, suggesting the slip bands are confined in their own slip planes (**Figure 27b**). However, as indicated by the small white arrows, the relative positions of the intersection points at the grain boundary are significant deviated, by ~20 µm. This suggests the observed slip traces across the grain are not associated with each other and the slip transfer between them is

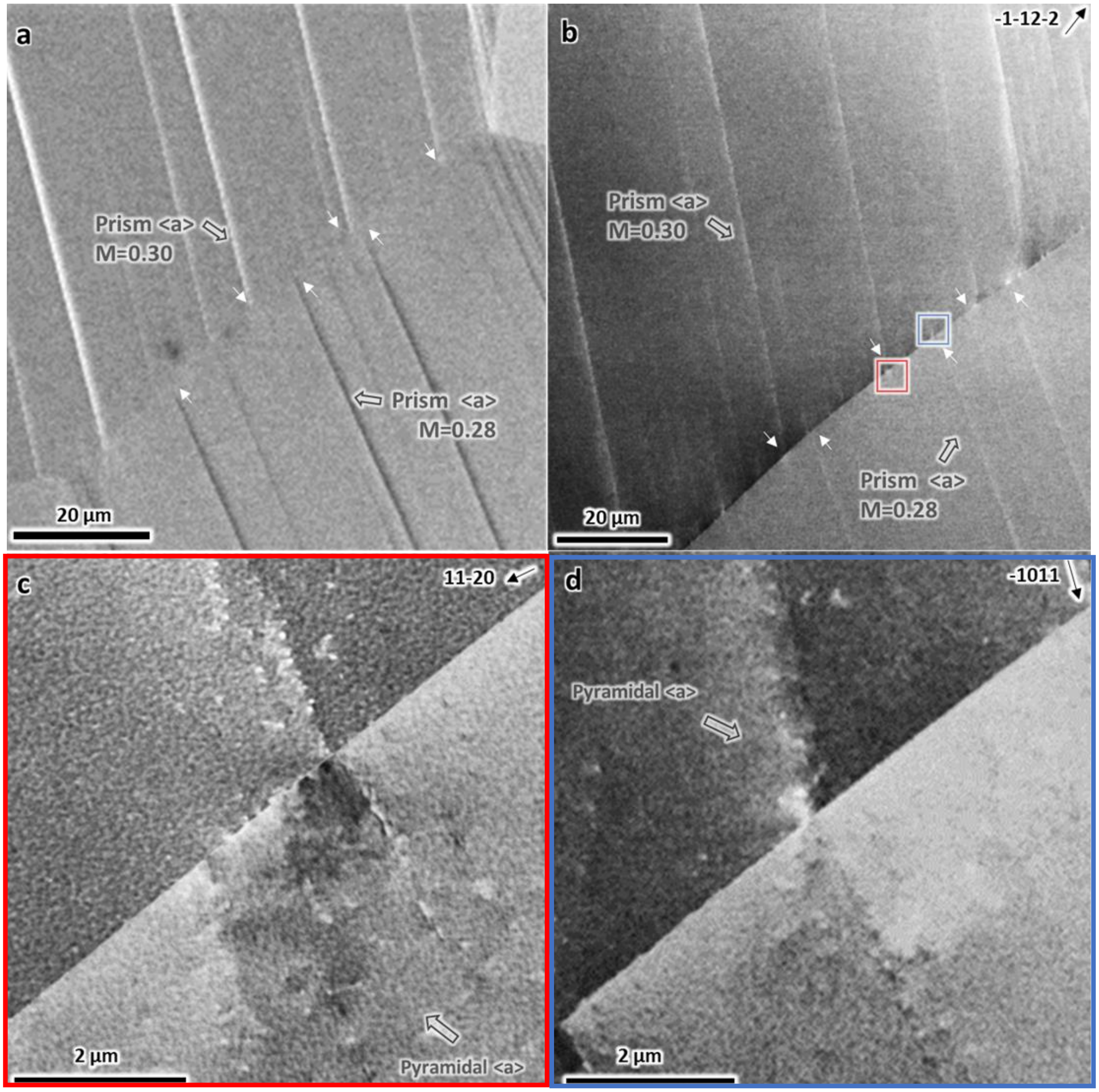

Figure 27a) SE image of non-correlated slip systems on the surface. The small white arrows indicate the relative positions of the selected slip bands on the surface. It can be clearly seen that these slip bands do not intersect at the same point on the grain boundary. b) ECC image of the same region below the surface. The relative spacing and distributions of the slip lines remain unchanged within either grain, but the relative intersection points on the grain boundary changes, as indicated by the small white arrows. c) ECC image of the grain boundary area in the red box. Pyramidal <a> secondary slip system is activated from the intersection points of the incoming prism <a> slip system in the upper grain at the grain boundary. d) ECC image of the grain boundary area in the blue box. Secondary pyramidal <a> slip system is activated to accommodate the strain induced by the prism <a> slip system in the lower grain.

limited. The closer examination at the grain boundary area within the lower grain (red) and the upper grain (blue) is shown in **Figures 27c&d**, in order to further investigate the local accommodation activities. It appears the "incoming" $(0\bar{1}10)[\bar{2}110]$ prism <a> slip system in the upper grain is accommodated by the "outgoing" $(\bar{1}011)[1\bar{2}10]$ secondary slip system (M = 0.32) that only propagate a short distance from the grain boundary (m' = 0.52, $\Theta_{p\text{-}s}$= 46°). Similarly, the "incoming" $(10\bar{1}0)[\bar{1}2\bar{1}0]$ prism <a> slip system is also accommodated by a limited number of dislocations associated with the "outgoing" $(0\bar{1}11)$ $[\bar{2}110]$ secondary slip system (M= 0.31) in the upper grain (m' = 0.50, $\Theta_{p\text{-}s}$ = 38°). Compared to the poor compatibility between the two primary slip systems in the adjoining grains (m'=0.49, $\Theta_{p\text{-}p}$ = 58°), the induced shear from each primary slip system is resolved by the activation of better aligned secondary slip systems. These secondary slip systems also have the same Burgers vector as the primary slip systems within the respective grains, but on different slip planes. But due to a larger CRSS value of the secondary slip systems, the activity of the dislocation slip is found localized around the grain boundary. It is speculated that if the sample were to be strained further, these regions might be sources for easier primary slip system activation, due to dislocation cross-slip.

The accommodation behavior at an "impenetrable" grain boundary is shown in **Figure 28**. In this case, the "incoming" $(10\bar{1}0)[\bar{1}2\bar{1}0]$ prism <a> slip system (M=0.45) in the upper grain is efficiently "blocked" by the grain boundary since no active slip system is observed on the other side of the grain boundary (**Figure 28a**). However, close examination on the other side of the grain boundary has found the local activation of multiple dislocation slip systems in the lower grain (limited to a small zone), with the majority of the dislocations being associated with the $(0001)[1\bar{2}10]$ basal <a> slip system (M = 0.28, m' = 0.78, $\Theta_{p\text{-}s}$ = 38°). A number of dislocations on the pyramidal slip system is also found, but with even smaller M = 0.23 and m' =0.67. These dislocations appear to be activated to accommodate the strain at the grain boundary through a better alignment with the impinged "incoming" slip system. But they are not able to propagate out of the grain boundary area due to a low Schmid factor. This observation is consistent with a latest work by Gioacchino et al. [189] that strain can be partially transferred out in a more compatible way through the localized crystal lattice rotation.

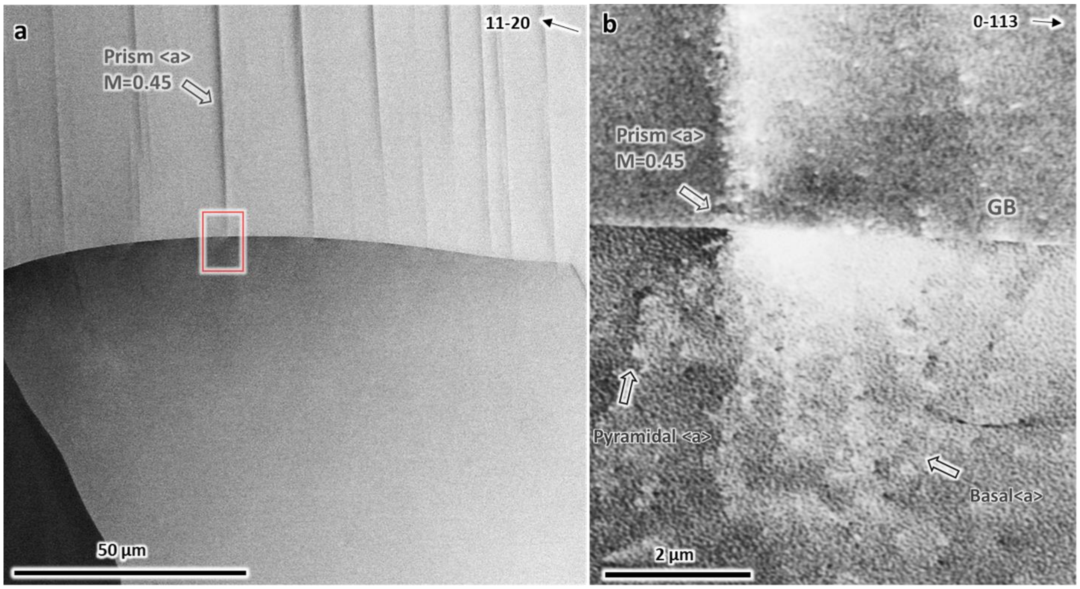

Figure 28a) SE image of the third interaction type. The slip system appears to be blocked by the grain boundary and no active slip system is observed in the lower grain. b) ECC image in the red boxed area. A number of dislocations within a limited zone is observed, with majority belong to the basal plane, and some on the pyramidal plane.

Nevertheless, this analysis shows there is no such thing as an "impenetrable" grain boundary, and there will always be some strain relaxation at the grain boundary area through dislocation activations, or alternatively fracture at the grain boundary.

3.4.4 Comparison of slip transfer parameters among slip system interaction types

With all the crystal orientation information from EBSD and the geometry of slip systems at grain boundaries, it is able to assess the slip accommodation events at the grain boundary, as outlined **Section 3.4.3**. This geometric analysis is shown in **Figures 29a&b**, which involves numeric factors, namely: the angle Θ between intersection lines of different slip planes on a grain boundary plane (a key factor in the LRB criteria [83-86]), the geometric compatibility

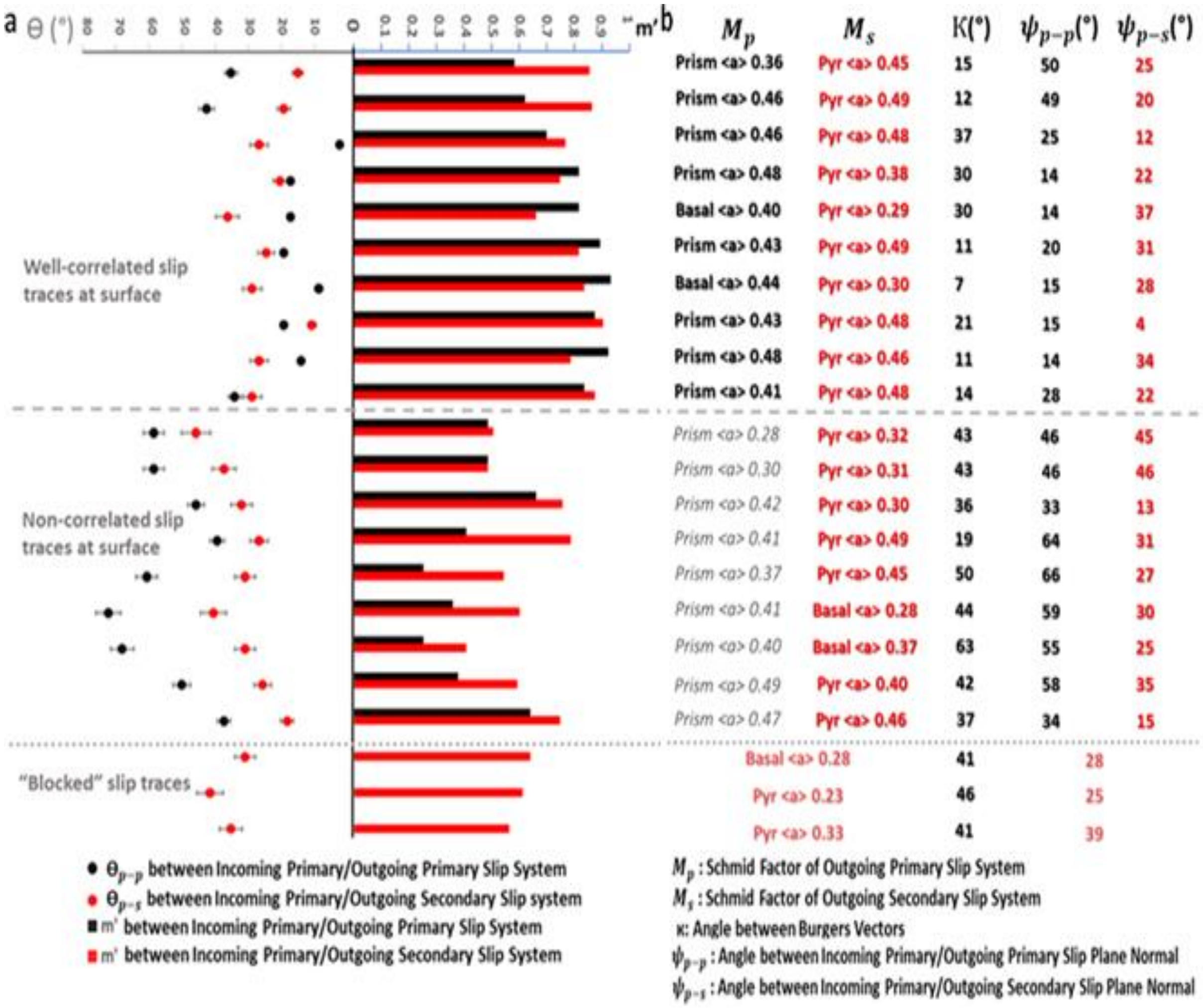

M_p	M_s	K(°)	ψ_{p-p}(°)	ψ_{p-s}(°)
Prism <a> 0.36	Pyr <a> 0.45	15	50	25
Prism <a> 0.46	Pyr <a> 0.49	12	49	20
Prism <a> 0.46	Pyr <a> 0.48	37	25	12
Prism <a> 0.48	Pyr <a> 0.38	30	14	22
Basal <a> 0.40	Pyr <a> 0.29	30	14	37
Prism <a> 0.43	Pyr <a> 0.49	11	20	31
Basal <a> 0.44	Pyr <a> 0.30	7	15	28
Prism <a> 0.43	Pyr <a> 0.48	21	15	4
Prism <a> 0.48	Pyr <a> 0.46	11	14	34
Prism <a> 0.41	Pyr <a> 0.48	14	28	22
Prism <a> 0.28	Pyr <a> 0.32	43	46	45
Prism <a> 0.30	Pyr <a> 0.31	43	46	46
Prism <a> 0.42	Pyr <a> 0.30	36	33	13
Prism <a> 0.41	Pyr <a> 0.49	19	64	31
Prism <a> 0.37	Pyr <a> 0.45	50	66	27
Prism <a> 0.41	Basal <a> 0.28	44	59	30
Prism <a> 0.40	Basal <a> 0.37	63	55	25
Prism <a> 0.49	Pyr <a> 0.40	42	58	35
Prism <a> 0.47	Pyr <a> 0.46	37	34	15
	Basal <a> 0.28	41		28
	Pyr <a> 0.23	46		25
	Pyr <a> 0.33	41		39

M_p : Schmid Factor of Outgoing Primary Slip System
M_s : Schmid Factor of Outgoing Secondary Slip System
κ: Angle between Burgers Vectors
ψ_{p-p} : Angle between Incoming Primary/Outgoing Primary Slip Plane Normal
ψ_{p-s} : Angle between Incoming Primary/Outgoing Secondary Slip Plane Normal

Figure 29 Comprehensive analysis of slip transfer parameters between well-correlated slip (top 10 lines), non-correlated slip (middle 9 lines), and "blocked" slip (bottom 3 lines). a) comparison of the angles Θ between incoming primary and outgoing primary (black)/ secondary (red) slip system intersection lines at the grain boundary plane, and the geometric compatibility factor m' between the incoming primary and outgoing primary (black)/ secondary (red) slip systems. b) Comparison of the global Schmid factors M of the outgoing primary (black)/ secondary (red) slip systems, angle κ between the Burgers vectors of incoming and outgoing slip systems, and angle Ψ between the incoming primary and outgoing primary (black)/ secondary (red) slip plane normal. Only one value of κ is given because the outgoing primary and secondary slip systems have the same Burgers vectors. Schmid factors for the outgoing primary slip systems are shown in italics in the cases where there is no correlated slip observed between the incoming primary and outgoing slip systems. Only one Schmid factor is given for the "blocked" cases because only limited slip was observed in the outgoing grains in the vicinity of the primary incoming slip systems. The fine dotted line between the non-correlated and 'blocked' slip band interactions indicates the similarity in the accommodating behavior.

factor m' by Luster and Morris [95] which involves the angle κ between the Burgers vectors and the angle ψ between slip plane normals, and the global Schmid factors M [45, 46, 74]. Overall, despite the interactions between the slip systems, the "incoming" and "outgoing" primary slip systems in all cases are mostly prism <a> slip systems, with some basal <a> slip systems. Likewise, the majority of the "outgoing" secondary slip systems are associated with the pyramidal <a> slip systems, with a limited number of basal <a> slip systems. It should be noted that there are indeed other types of dislocations observed during the ECCI analysis, however, this number is small and don't affect the overall results.

Cumulative distribution plots of m', Ɵ, and M are provided in **Figure 30** in order to discover the influences of these parameters on the accommodation behavior. The cumulative distribution plots of m' (**Figure 30a**) shows the importance of alignment of slip systems in the slip transfer. There is reasonable alignment between the "incoming" and the "outgoing" primary slip system when they are well-correlated. On the contrary, the m' are much lower when the slip systems are not correlated. Similarly, it also appears to have a good correlation between high values of m' and the secondary accommodating slip systems. In addition, there does not seem to be a significant difference in the distribution of m' between the primary-to-primary and primary-to-secondary slip systems. In general, it is expected that significant slip transfer will occur between well-correlated slip bands, with relatively good alignment between slip systems. As the primary slip systems become more poorly aligned, it is possible that secondary slip systems will be more active to compensate the lack of slip from the primary systems.

For "non-correlated" slip systems, the m' between primary slip systems are usually low,

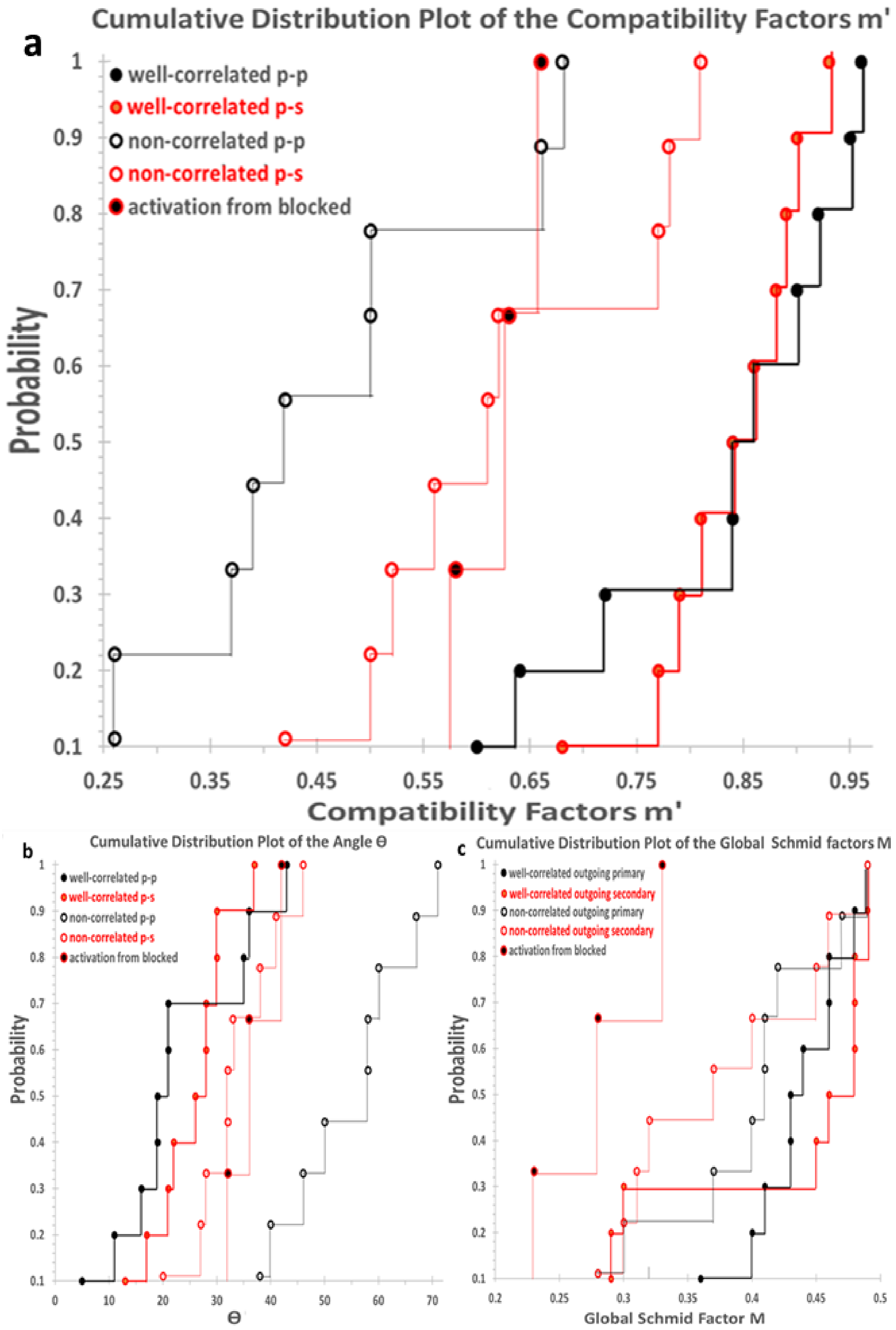

Figure 30 Cumulative distribution plots of the a) the compatibility factors m' between the various slip systems, b) the angles ϴ between the various outgoing slip systems and the incoming primary slip system, and c) global Schmid factors M of the outgoing slip systems.

which is consistent with the lack of interactions between the primary slip systems. Meanwhile, the secondary slip systems are activated with a significant higher m' than the "non-correlated" primary slip system to accommodate the accumulated strain at grain boundaries. This trend is clearly shown in **Figure 29a** ("non-correlated" section) that all the m' values between the "outgoing" secondary slip systems and the "incoming" primary slip systems are no smaller than those between the "non-correlated" primary slip systems.

For the "blocked" cases, the average m' values between the "incoming" slip systems and the limited accommodating dislocations are similar to those between the "incoming" primary slip systems and the "outgoing" secondary slip systems in the "non-correlated" cases. Meanwhile, the distributions of m' values are also similar as those in the local accommodating events (compare the middle two red plots). This suggests the "non-correlated" slip interactions can also be interpreted as two "blocked" slip interacting at a same grain boundary, with each primary slip system across the grain boundary being accommodated by the limited activation of secondary slip systems in the opposite grain.

The analysis of Θ in **Figure 30b** shows a similar correlation as that shown for m'. Slip systems that are in "well-correlation" generally have a smaller $\Theta_{p\text{-}p}$ (and $\Theta_{p\text{-}s}$) than those that are "non-correlated". The value of $\Theta_{p\text{-}s}$ is generally smaller than $\Theta_{p\text{-}p}$, but in some cases larger. It appears the strong correlation is related to the strong alignment of the slip plane intersections at the grain boundary and may directly affect the ease of slip transfer. In one case (the third row in **Figure 29a**), the $\Theta_{p\text{-}p}$ is much smaller than $\Theta_{p\text{-}s}$, while the m' between primary slip systems is lower. In this case (not shown specifically due to low image quality, **Figure A25** in **Appendix F**), the activity of secondary slip system is rarely observed. One hypothesis is the angle Θ might have a more direct influence in the slip transfer mechanism than the m', thus the local activation of secondary accommodating slip system is not necessary since the deformation shear is easily carried away by the "outgoing" primary slip system. For "non-correlation" and "blocked" cases, the accommodating slip systems also have smaller angles Θ with the "incoming" primary slip systems than the "blocked" systems. Without the extensive slip transfer in these cases, local strain can still be partially resolved by the local activation of slip systems with relatively low Θ.

Figure 30c is the cumulative distribution plot of the global Schmid factor M. The global Schmid factors M for "outgoing" secondary slip systems in "well-correlated" cases are generally higher than those in "non-correlated", and even much higher than in "blocked" cases. This indicates the "outgoing" secondary slip systems are easier to be activated by the "well-correlated incoming" primary slip systems. Although the distribution of M of "outgoing" primary (majority prism <a>) and secondary (majority pyramidal <a>) slip systems are not so significant, it is generally believed these secondary slip systems are more difficult to be activated due to much higher CRSS values [25-28,24-37]. This indicates the global Schmid factor is not an important element in the local activation of secondary slip systems, although it controls the activation and propagation of the primary slip systems.

3.4.5 Conclusions on grain boundary local accommodation activities

The correlation of (ECCI) images on and below the surface reveals the 3-D geometry of the slip systems at the grain boundaries, allowing the comprehensive assessment of slip accommodation behavior between slip systems at the grain boundaries. In general, the slip bands are confined within their respective slip planes on and below surface, with the relative spacing and distributions remaining the same. Despite the detailed mechanism unknown, the free surface is indeed biasing the behavior of slip systems at the grain boundary region. The "well-correlated" slip systems observed at the surface lose the well-correlation, and the resulting offsets between slip systems locally activate the secondary slip system to accommodate the divergency, trying to restore the integrity between the slip systems. The Burgers vectors of these secondary slip systems are generally the same as the primary slip systems in the same grain, however, are associated with different slip planes. Due to higher CRSS values, the secondary slip systems are not readily activated, and cross-slipping into the primary slip systems at a short distance from the grain boundaries. Nevertheless, the apparent "well-correlated" interactions happen between slip systems that have high Schmid factors, are well geometrically aligned (large m'), and have small misalignment between slip plane/grain boundary intersection lines (small ϴ). Consequently, as the slip systems become less and less correlated, local activation of these secondary slip systems become more prominent. Overall, the local shear accommodation at the grain boundary in the heterogeneous deformation are more complicated than it appears. Thus extra care should be taken in the study of slip transfer due to free surface biasing effect.

3.4.6 Short discussion on the tangential continuity theory

The frequent observations of the local activation of secondary slip systems at grain boundary regions brought back the concept of the "tangential continuity" developed by Livingston and Chalmers [71, 80]. The observation in this study agree with the tangential continuity that the accumulated strain at the grain boundary cannot be fully accommodated between two (primary) slip systems. Although ECCI analyses in this study have found some other types of dislocations that are not associated with the primary or secondary slip systems around the grain boundary, it is not known if they have contributed to the strain accommodation activities and their densities are usually very low. Nevertheless, the constraint (**Section 1.1.4**) cannot be fully fulfilled since it requires four slip systems to fully accommodate the strain at the grain boundary. These observations reveal the fact that current understanding of the grain boundary accommodation activities in polycrystal deformation is still incomplete[17] [104]. The slip transfer studies that only involve the interactions between two primary slip systems are far from realistic to fully represent the plasticity behavior at the grain boundaries.

3.5 The direction of slip propagation within polycrystals

The direction of slip transferring within a grain and across a grain boundary is always ignored by plastic models and majority slip transfer studies. Most studies are insensitive to the direction of slip transfer, and assume the shear is always following one direction [75-77, 87-89]. This may be reasonable in ideal experiments such as bicrystals since slip transfer parameters such as m', ϴ do not have a direction vector [83-86, 95]. However, deformation is not always in one direction in real-life deformation of polycrystals. There might be multiple nucleation sources, either within a grain, or at a grain boundary [190]. For example, one may expect two primary slip systems nucleated from a left grain boundary and a right boundary will propagate in a different direction. Yet no research has been done on the propagation direction of a dislocation slip. This long-ignored element help capture the overall flow of deformation shear

---

[17] The author carried out analysis based on tangential continuity model, trying to find the number of active slip systems to minimize the residual strain on the grain boundary from a known "incoming" slip system in the "parent" grain. However, most of the accommodating systems were typically predicted to be in the "parent" grain. Furthermore, the primary observed accommodating systems were typically not consistent with these predictions. It seems the model prefers self-accommodation if no external shear is applied as a driving force.

travelling within polycrystals, and may further improve the plasticity model in the deformation prediction. Luckily, during the throughout ECCI analysis across several neighboring grain patches in sample 3 after the electropolishing, it is found that ECCI is able to reveal the potential travelling direction of individual slip system.

After the EBSD-based slip trace analysis on the as-deformed sample (**Figure 17b**), ECCI was applied on the electropolished sample for the identification of Burgers vectors (**Figure 31**). Despite the change in the overall grain shape during the electropolishing (**Figure 31b**), crystal orientation before and after electropolishing is not changed [96]. Dislocations on the slip bands[18] can be identified through the contrast analysis as outlined in **section 3.2.2** (shown in **Figure 31d-i**). With the information from the slip trace analysis, the primary slip system in grain 1 is identified to be $(1\bar{1}00)[11\bar{2}0]$ prism <a> slip system (M= 0.15), with additional cross-slip dislocations on $(1\bar{1}01)$ pyramidal plane (M=0.23). Likewise, the primary slip system in grain 2 and 3 is $(1\bar{1}00)[11\bar{2}0]$ prism <a> slip system (M=0.41) and $(10\bar{1}0)[1\bar{2}10]$ prism <a> slip system (M=0.48), respectively. Based on the observation on the as-deformed sample (**Figure 31a**), the deformation slip propagation within these grains is linked by the slip bands that propagate through three grains. Some of the slip bands are quite distinct in grain interior (grain 2&3), while some slip bands in grain 2 become less distinct as they approach the grain boundary with grain 3. Additionally, despite the distinct slip bands in grains 2&3, they do not appear to meet at the same points on the grain boundary in between. Meanwhile, it appears the slip bands in grains 1 and 2 meet at the grain boundary, however, the slip propagation in grain 1 is not easy,

---

[18] The correlation of the slip bands at and below surface is possible since the relative spacing and distributions of the slip bands remain the same, as outlined in **Section 3.4.3**. Thus it is able to find the specific slip system after electropolishing.

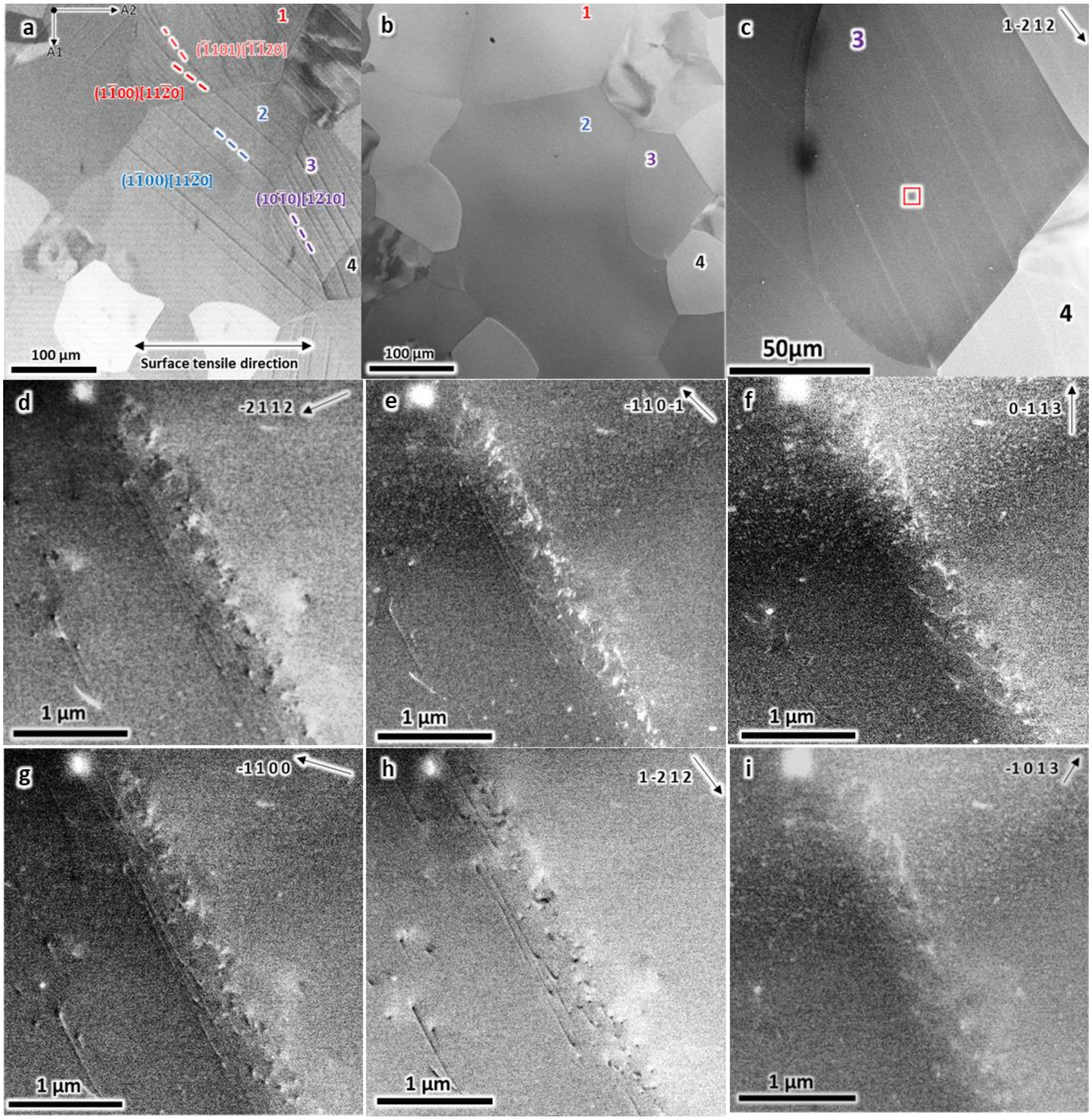

Figure 31a) SE image of grains 1-3 in the as-deformed sample 3. The slip systems are identified by the ECCI facilitated slip trace analysis, which are marked by dash lines in different colors and labelled in different colored fonts. It appears the slip lines in grain 2 and 3 are not well-correlated. The slip systems in grain 1 appear to meet the slip systems in grain 2 at the boundary, while the slip propagation in grain 1 is difficult. b) General BSE image of the same grains 1-3 in the electropolished sample 3. All the slip traces are removed by the electropolishing and no clear contrast is seen because the sample is not under a channeling condition. c) One example of ECCI analysis on the electropolished surface. At g = $[1\bar{2}12]$, the slip line contrasts are distinct. These contrasts come from dislocation contrasts rather than topography. d-i) High Mag ECC images taken from the red boxed area in grain 3 for the Burgers vector identification. The Burgers vector is $[1\bar{2}10]$. With the information from the slip trace analysis, the slip system that is active in grain 3 is $(10\bar{1}0)[1\bar{2}10]$ prism <a> slip system. ECCI identification of slip system in grain 1 and 2 can be found in the **Appendix F**, following the same approach.

as reflected by the wavy slip bands. Overall, the deformation evolution within the grain patch is quite complicated. As a “united” patch, the shear in one grain is expected to be accommodated by the neighboring grain to maintain the overall integrity. It will be easy to study the accommodation behavior if the direction of deformation flow within the patch is known.

3.5.1 Slip transfer direction identified by ECCI contrast analysis

The ECCI analysis reveals that dislocation morphologies appear differently when following a certain direction. One example can be found in **Figure 32**. After electropolishing, at a certain channeling condition, the contrast of slip bands is a direct consequence of the channeling contrast of the individual dislocation in the slip band. Slip bands that show strong contrast reflect a large number of dislocations in the slip band, suggesting this slip band is carrying a large shear (**Figure 32a**). It appears that dislocations are nucleated from the grain boundary between grain 2 and grain 3, based on the following argument. The slip band width is very small near the grain boundary (~0.02 μm in **Figure 32b**), but the slip line broadens towards the center of the grain to around 0.5 μm at positions c and d, and become even broader approaching the other side of the grain boundary at position e (1 μm) by dislocation cross-slip, although the mechanism is not clear. Once the dislocation slip band reaches the grain boundary with grain 4, dislocations become widely distributed along the grain boundary region ~2.6 μm at position f.

Despite the change in slip band width, it is interesting to note that the contrast of dislocations appears different at different positions along the slip line. When the dislocations are nucleated from the grain boundary with grain 2 (**Figure 32a**), they appear as dots, suggesting the dislocations are close to perpendicular to the surface at this channeling

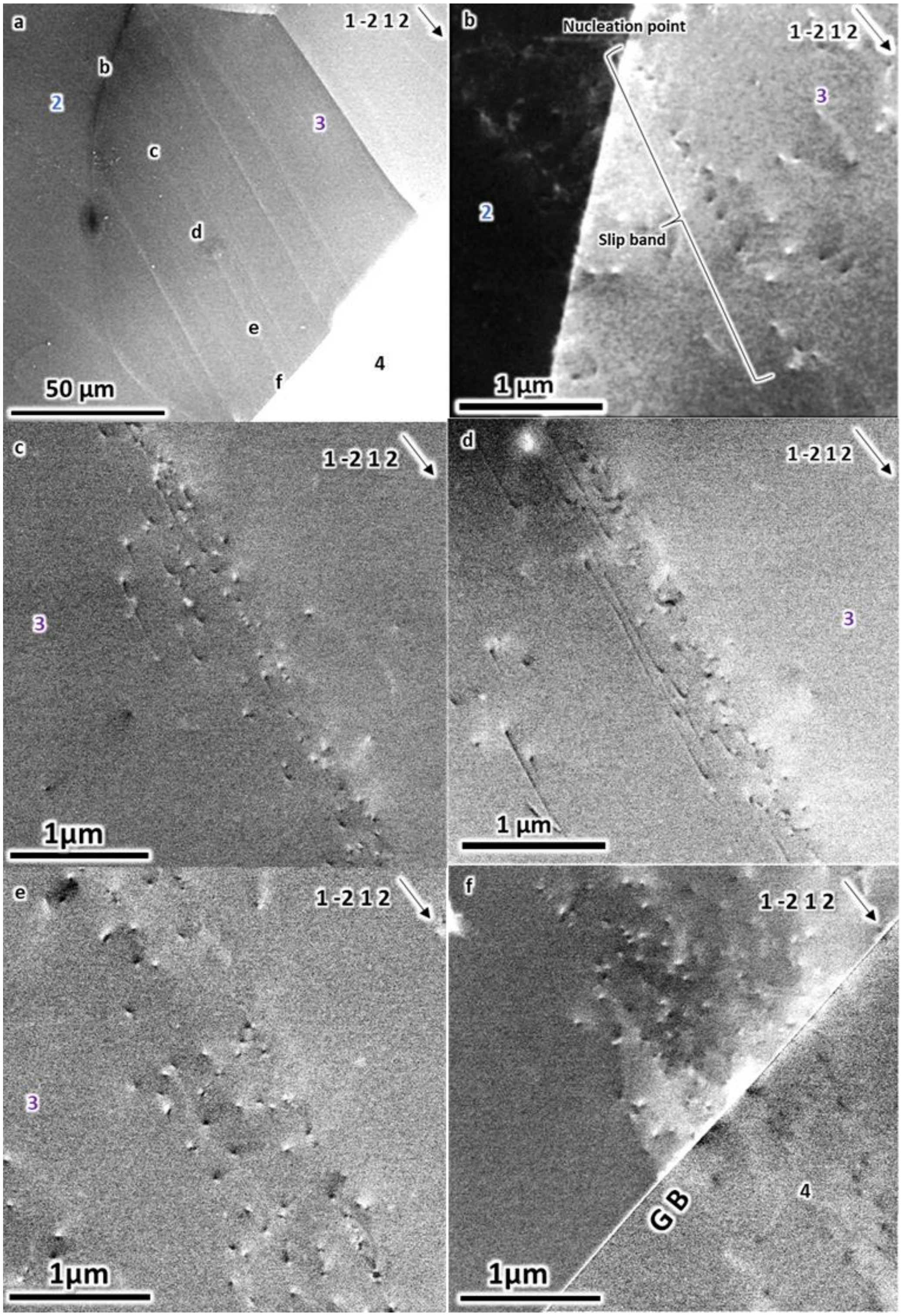

Figure 32a) electropolished surface of grain 3. b-f) ECC images taken at the same channeling condition at different positions along a slip line. Dislocations are limited in a sharp and narrow line from the nucleation point at the grain boundary with grain 2, and spreading out as going deeper into the grain and will finally distributed around the grain boundary with grain 4.

condition. Based on the sense of black/white contrast of the dislocations, almost all of the dislocations along the slip band at the grain boundary area have the same Burgers vector sign. As the dislocations propagate into the grain interior, more dislocations show opposite contrast, suggesting they have the opposite sign of Burgers vectors (10% at position c, ~30% at position d, ~ 50% at position e, and ~65% at position f at the grain boundary with grain 4). Additionally, in the center of grain 3 at positions c and d, ECCI also reveals more dislocations appear as lines, with a round “head” and a “tail”. This indicates the dislocations are aligned more parallel (or less inclined) with the sample surface, with the round “head” formed at the surface due to local elastic relaxation [140-144]. The observation of more dislocations with opposite sign Burgers vectors and the “line-type” dislocations may be a result of more dislocation loop formation as dislocations cross-slip become more prevalent.

Based on the change of slip band width, and the observations of more cross-slip activity, it is reasonable to believe that once a slip system is nucleated from a source, the slip band is sharp and all the dislocations are limited strictly in one plane. As the dislocation slip propagates forward into the grain interior, the slip band becomes broader due to dislocation cross-slip. Once the slip system reaches the grain boundary with grain 4, more cross-slip event is expected to happen as the dislocations pile up at the boundary, resulting in a wider spread of dislocations in the grain boundary region. This indicates the overall slip transfer direction within grain 3 is from the upper left boundary with grain 2 to the bottom right boundary with grain 4. Similar analysis has been done on other primary slip bands showing strong contrast (**Appendix I**), all the slip transfer direction in grain 3 is from the upper left to the bottom right.

However, there are indeed some slip bands with weak contrast propagating in the

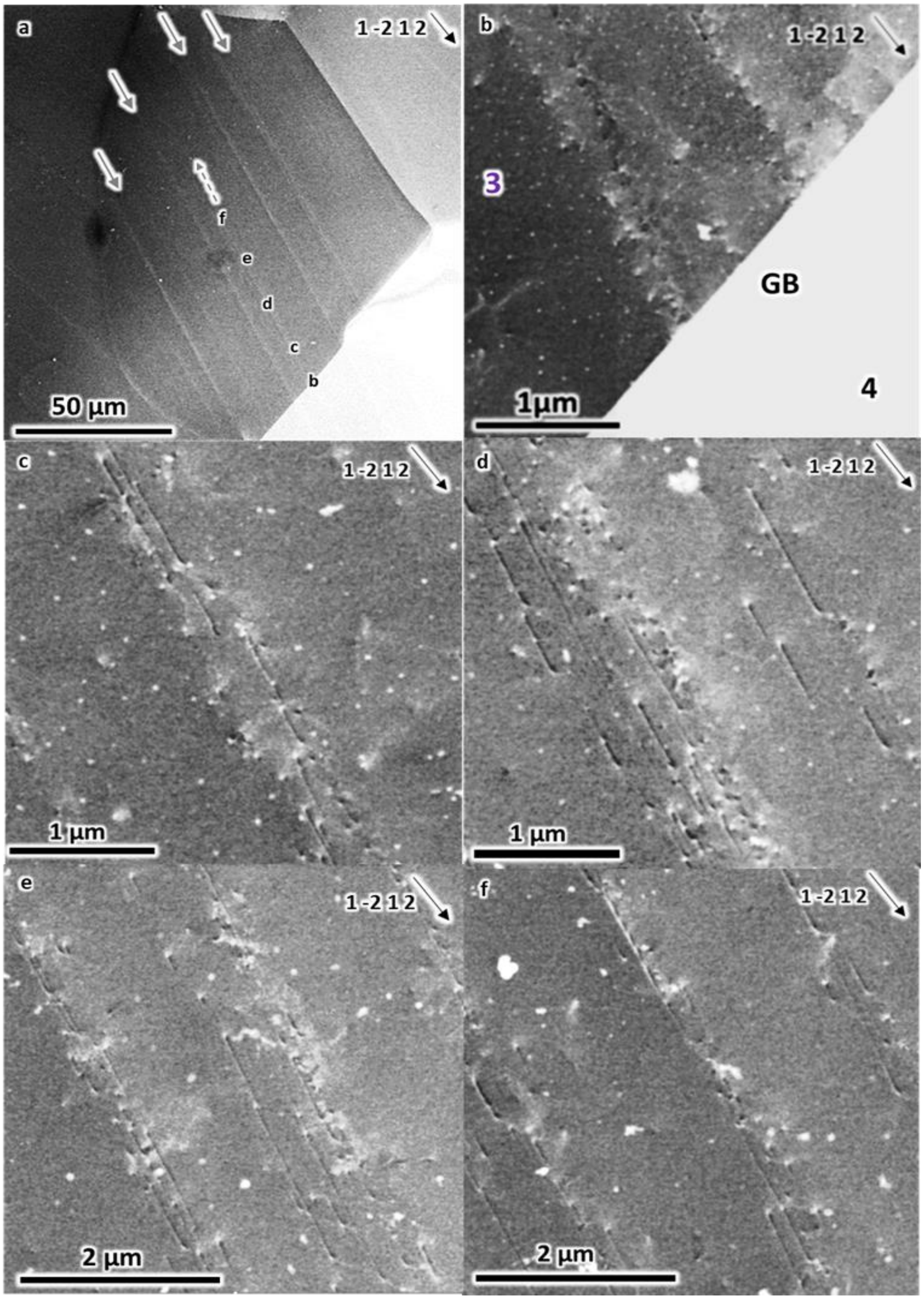

Figure 33a) Low mag ECC image of grain 3, the four arrows indicate the slip transfer directions of slip bands with strong ECC contrast. The dashed arrow indicates the opposite transfer direction of a slip band with weak contrast, and “disappeared” around position f. a-f) ECC images following the slip band from the boundary with grain 4 into grain interior. Overall dislocation density is low compared with the case in Figure 31. As the slip band broadening effect further dilutes the dislocation concentration, the dislocation contrast of the slip band is hardly detectable.

opposite direction. One typical example is shown in **Figure 33**. A low mag ECC image (**Figure 33a**) reveals this apparent weak slip band nucleate from the boundary with grain 4 and propagate towards the upper left. The contrast of the slip band becomes even weaker during its propagation, and finally fades around position f, becoming “invisible”. A higher magnification ECC image at the grain boundary confirms the observation that dislocation nucleated from the grain boundary as a narrow band (**Figure 33b**). Additionally, the contrast analysis also reveals these dislocations are dot-like, with the majority showing opposite contrast with those in **Figure 32b**. This indicates these dislocations have Burgers vectors of opposite sign (and opposite propagating direction) than those in the primary, high contrast slip bands. Consequentially, dislocation cross-slip occurs during the propagation towards the upper left of the grain. As the dislocation have not propagated as far, the slip band finally become “invisible”. This observation may be an inciteful reminder that a slip band that shows weak SEM topography contrast does not always mean the slip band is less activated. The apparent “disappearance” of a slip band around a grain boundary doesn’t mean the slip band is not reaching the grain boundary, it might be a result of broadening effects that dissipates the dislocations in a wider region along the grain boundary.

3.5.2 Comprehensive analysis of deformation within grain 1-3 patch

By and large, the complete ECCI analysis provides an understanding of the deformation evolution of the grain patch. The analysis suggests the majority deformation shear is carried away from the upper left boundary with grain 2 to the lower right boundary with grain 4 through dislocation slip. However, deformation also occurs from the lower right boundary and moves in an opposite direction, although the shear is not significant. This might be a result of accommodation to the shear from the grain 4. By the application of similar analyses along most of the slip bands in grains 1&2, it is possible to outline the potential deformation evolution history within the grains of the polycrystal patch.

As indicated by the wavy slip band at the surface (**Figure 17b&31a**), the deformation shear in grain 1 appears difficult, as indicated by the low Schmid factor (M=0.15). This is consistent with the observation of wide spread of dislocations along the slip band after electropolishing (**Figure 34a**), as the slip band propagates to the upper left into the grain interior. However, due to the highly active slip system in grain 2 (M=0.41) nucleated from the grain boundary, grain 1 needs to accommodate the shear by the activation of dislocation slip that is better aligned[19] with the slip system in grain 2 (m' = 0.83, ϴ = 32°)(**Figure 34b**), although the further propagation of the accommodated slip system is difficult in grain 1. It is worthy to point out that none of the high Schmid factor deformation systems (<c + a> slip systems and twinning) are observed. This suggests grain 1 is passively activated in the heterogeneous deformation.

On the other hand, despite the activation of some "free" dislocations due to strain accumulation at the grain boundary, shear can be carried away through dislocations to the lower right into grain 2 by the easy activated slip system (M =0.41). Again, the initial slip band in grain 2 nucleated from the boundary with grain 1 is sharp and has a small band width (**Figure 34c**). Due to slip band broadening effect, the slip band width is increasing as it is propagating inside grain 2 (**Figure 34d**). Once the slip band in grain 2 reaches the lower right grain boundary

---

[19] The slip transfer parameters can also be calculated in the situation that a grain boundary kicks out two "outgoing" slip systems into the opposite grains at the same time since the calculation is insensitive to the direction of slip transfer.

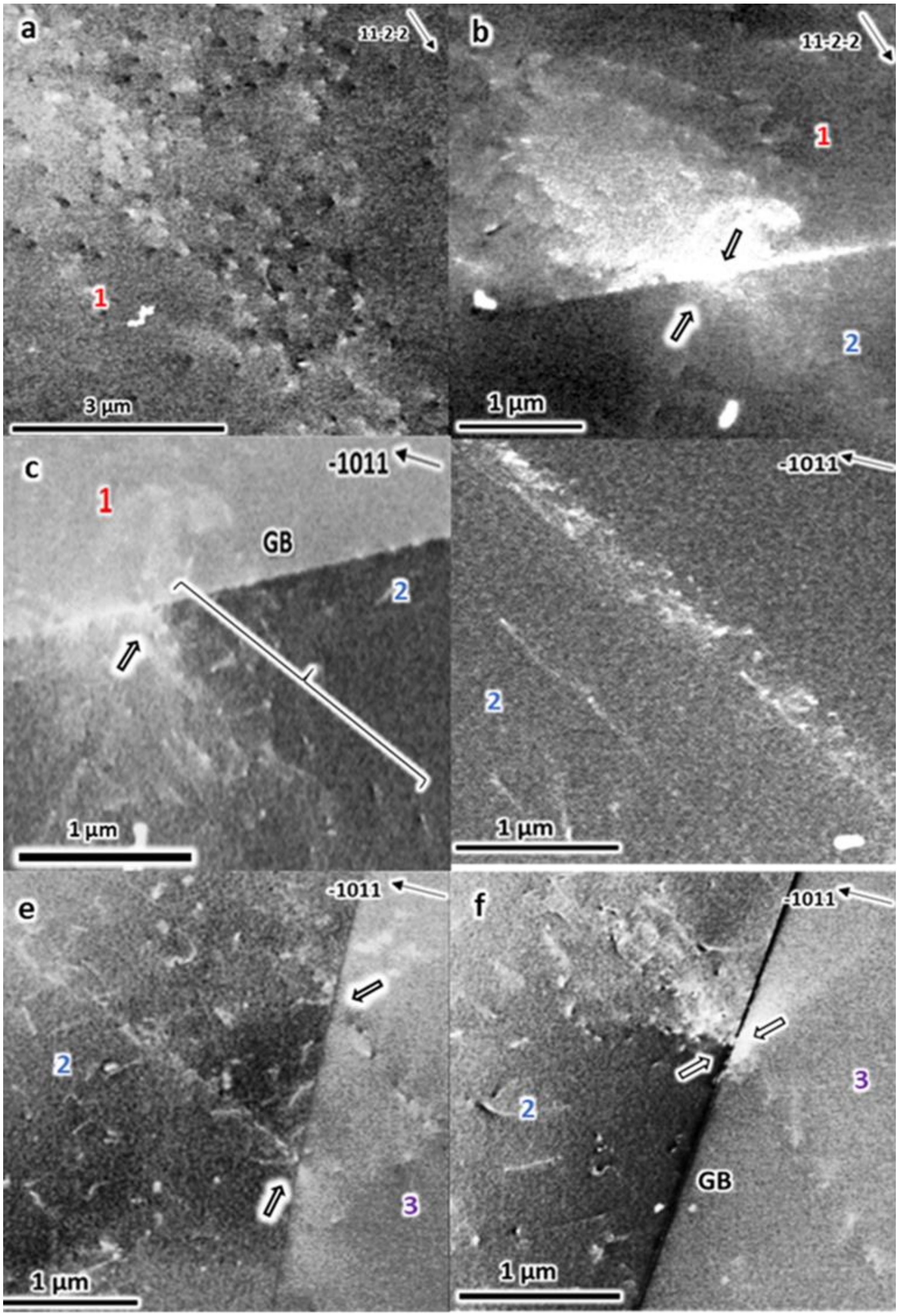

Figure 34a) A wide spread of dislocations in grain 1 from where a dislocation slip in grain 2 is nucleated at the grain boundary. b) Wide spread of dislocations in grain 1 interior. c) a sharp slip band is nucleated from the boundary in grain 2. d) The slip band is wider in grain interior than it is at the grain boundary. e) Intersection of dislocation slip at the grain boundary with grain 3, slip systems in grain 2 and 3 are not correlated. Dislocation density is high in grain 2. F) Accommodating dislocations nucleate from the intersection point of a slip system in grain 3, and propagate only a short distance with significant broadening effect.

with grain 3, dislocations are diffused along the grain boundary area in grain 2 (left side of the boundary in **Figure 34e**) to partially relief strain accumulation [75].

Despite the strong activity of the slip system in grain 3 (M =0.48), the two primary slip systems in grain 2&3 do not correlate well (m' =0.42, ϴ = 40^o), as reflected by the offset between intersection points of the two slip bands at the grain boundary (**Figure 34e**). This suggests the shear from grain 2 is not efficiently transferred to grain 3, thus the grain boundary needs extra efforts to accommodate the accumulated shear to maintain its integrity. Meanwhile, accommodating secondary slip system in grain 2 is found nucleated in "well-correlation" (m' =0.81, ϴ =28^o) with the highly active slip system in grain 3 (**Figure 34f**). This observation indicates that slip systems can be nucleated from the same point at the grain boundary and propagated in an opposite direction into their respective grains. This can be interpreted as slip systems in both grains are activated to accommodate the shear at the grain boundary.

3.5.3 Conclusions of polycrystal deformation identification

As would be expected, the detailed deformation evolution of polycrystal patch is complicated. Nonetheless, slip bands are found to spread out during their propagation, which gives a key to understanding the deformation evolution. With additional information of the change of dislocation contrasts and morphologies at different positions following the slip band, it is possible to identify the slip transfer direction within a certain grain. Based on the observations of the nucleation of different slip systems, it is very interesting to point out that in this very study, it appears most dislocation slip systems are nucleated from the grain boundary, rather than somewhere within grain interiors. This agrees well with arguments that grain boundary can be dislocation sinks and sources [52-55, 190]. As there might be more defects on the grain boundary plane due to irregular atomic arrangement in that region, the grain boundary is expected to be more “fragile” than grain interior in the heterogeneous deformation. This might be insightful to the plasticity modeling that both grain boundary and grain interior can be sources for slip activations. It is also interesting to find out that the slip systems of the same type within one grain may not propagating towards the same direction, this depends on where the dislocation is nucleated (i.e. slip systems nucleated from the left grain boundary will propagate in a opposite direction with those nucleated from the right boundary within the same grain). Additionally, grain boundary accommodation can happen between an “incoming” slip system with an “outgoing” slip system, it can also happen between two “outgoing” slip systems from the same boundary and propagate into their respective grains. Although the slip transfer parameter is not affected by the direction to slip transfer, understanding the transfer direction and the deformation sequences within polycrystal is critical for the comprehensive understanding of polycrystal engineering material (i.e. local work hardening, crack nucleation, etc.).

4. Summary

In order to correctly understand the heterogeneous deformation of hcp titanium, post-deformation analysis need to be precise and comprehensive. The preciseness refers to the correct identification of slip systems activated during the deformation, and the collectiveness requires the analytical method to identify all the slip systems activated in the accommodation. This comprehensive analysis cannot be simply achieved through one approach and needs assistance from other analytical techniques. Slip system identification is mostly based on the crystal orientation data from EBSD and the SEM observation of traces at the surface. With the improvement of EBSD and cross-correlation techniques that detect local lattice rotations [185, 188], and the AFM and DIC [162-165] that measure the displacements resulting from dislocation slip, slip system identification and quantification is becoming more precise. Nevertheless, the current analyses are not able to identify the slip systems that do not contribute to the slip traces. On the other hand, ECCI can precisely identify the Burgers vector of the slip systems based on dislocation contrast analysis [144-151]. This is a “yes or no” determinant analysis and avoids the calculation of potential deviation factor in DIC and cc-EBSD [185, 186, 188]. Implementation of the ECCI technique in concert with the current approaches moves the characterization of local slip behavior in heterogeneous deformation substantially forward.

Slip accommodation at grain boundary regions in polycrystal deformation is quite complicated. By correlating SEM images at the surface with subsurface ECCI images, the 3-D geometry of the slip systems at the grain boundary area is revealed, allowing the assessments of the local accommodation behavior using m’ and, particularly, ϴ. Additionally, subsurface

ECCI analysis reveals the biasing effect of "well-correlation" on the free surface, and reveals the locally activation of secondary slip systems that help compensate the incompatibility between the primary slip systems at the grain boundary area in the subsurface. This observation agrees well with the long-forgotten tangential continuity theory [71, 80], that indicates that the interactions between two primary slip systems are not enough to accommodate the strain at the grain boundary. Although this study only finds the local activation of secondary slip systems, this does not mean there cannot be more dislocations involved in the accommodation, especially at higher strain levels. Nevertheless, the current research extends the understanding of the complete nature of the accommodating mechanisms at the grain boundary, and again, suggests the slip transfer mechanisms developed based on the slip trace analysis may be limited.

In addition, the slip band broadening effect is clearly revealed through ECCI analysis in electropolished hcp titanium samples. The comparison of dislocation morphologies, dislocation contrast, and dislocation density at different positions in slip bands suggests that the vast majority of dislocations are nucleated from the grain boundary, rather than sources within the grains, at least in the early stages of deformation. However, this does not suggest dislocation sources cannot be found in grain interiors, as evidence shows that as the slip bands propagates, more dislocations with opposite sign are observed in the slip bands. It should be noted, however, it is not known if this broadening effect is unique to hcp metals due to the lower crystal symmetry, or is a universal phenomenon in all metals. Regardless, this discovery does help to establish an understanding of the deformation evolution in polycrystals.

5. Outlook and Future Direction of ECCI

In the latest future, one of the easiest things that can be achieved is whether slip band broadening effect is present in cubic materials or other hcp metals. This effect will be valuable if it can be widely applied on different materials.

It will also be interesting to investigate the slip/twin interactions by ECCI in hcp titanium since deformation twin are also common in the plastic deformation in some other titanium materials. One example is shown in **Figure 35**. In this figure, deformation twin is observed in the upper grain, whereas two types of dislocation slip systems are observed in the lower grain. It is interesting to investigate how the slip/twin interactions are at the grain boundary. Additionally, it is interesting to find <c+ a> dislocations kicking out of the tip of the deformation twin and propagate into grain interior. It is also interesting to investigate the relationship between dislocation slip and the twin, and how dislocations become a part of twinning during the deformation (in-situ if necessary). Sequential electropolishing of the sample may also

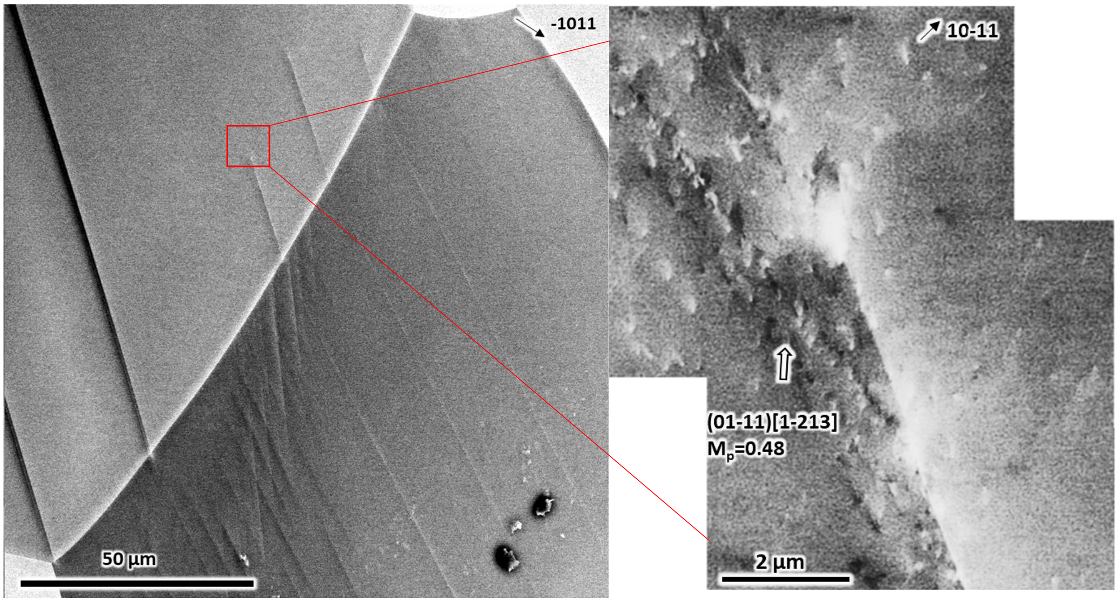

Figure 35 Deformation slip in the lower grain interacting with the deformation twin in the upper grain. ECCI analysis in the red boxed area shows the dislocation propagating out of the tip of the deformation twin.

reveal the geometry of the twin in the subsurface, which may also bring more insights in the twin evolution.

Since 3-D printing of titanium gears or other consumables are becoming more and more important in the aerospace industries, it will be an interesting and short project to correlate the mechanical behaviors of 3-D printed titanium samples (using different methods, such as powders or wires) during different stages of processing with the dislocation densities, phase changes, etc. This may help guide the industry to improve the overall quality of 3-D printed titanium materials.

By and large, ECCI is a strong SEM near-surface-based analysis technique that is complementary to many other techniques. This non-destructive technique is especially useful for the in-situ study of continuous polycrystal deformation without destructively damaging the sample. Thus far, this study only reveals that post-deformation analysis is able to provide some clues to deformation history. With careful design in future, one may be able to observe the deformation evolution from the initiation to the final structure of a slip band. This may be useful for understanding how the dislocation density, morphology, and contrast changes with increasing strain, and thus provide the opportunity to link the macroscopic deformation with the dislocation-scale activities simultaneously on the same target area. This approach is very advantageous over the other destructive studies, such as FIB-lift-out TEM, since it is extremely hard to find two same grains with even similar grain and boundary orientation characteristics in assessable polycrystalline groups.

Unfortunately, the electropolishing in this study is hard to control precisely. Removing the surface topography typically requires about 2 μm removal, and establishing precise uniform removal rates can be difficult. As a result, the surface removal in this study are typically around 5 μm or more. It is anticipated that it will not be possible to remove material with enough precision to track individual dislocations with electropolishing. An alternative approach may be the Xe^+ plasma FIB technique [191, 192], which is able to precisely control the surface removal. This approach has the potential to allow high resolution real 3-D reconstruction of a full dislocation structures below the surface (One should note the potential artifact induction and titanium hydride precipitation during plasma FIB). With proper coding facilitation, in future ECCI may be extended to automated identification of Burgers vectors, slip line directions, slip planes and the edge/screw component of a dislocation. Currently, as ECCI is effectively a manual technique, the identification of all of these parameters is done tediously by collecting five or more ECC images at different channeling conditions and long scan times (10 minutes per scan).

APPENDICES

APPENDIX A

Electropolishing mechanisms and parameters used in this study

The sample was electropolished in a proper setup, consisting a power supply (can switch between 0 ~ 120 V and 0 ~ 30V), a cathode (6 x 6 x 2 mm stainless steel plate) and anode (sample with the polished area facing the plate), a magnetic stir (50 mm in length) with a magnetic stir plate, electrolyte (in a 1000 ml baker) and cold bath (200 ~ 300 ml methanol cooled by liquid nitrogen/dry ice or a more stable control of temperature during electropolishing). Two different electrolyte compositions were used in the study with correlated electropolishing parameters, as listed in **Table A1**. It is worthwhile to mention that the experimental parameters and composition of electrolytes may be different if the minor element components of titanium are different. Nevertheless, the parameters in the table are based on freshly made electrolyte, which can be safely used for cumulative 10 ~ 20 times without changing the electropolishing result.

Table A1. Electropolishing parameters

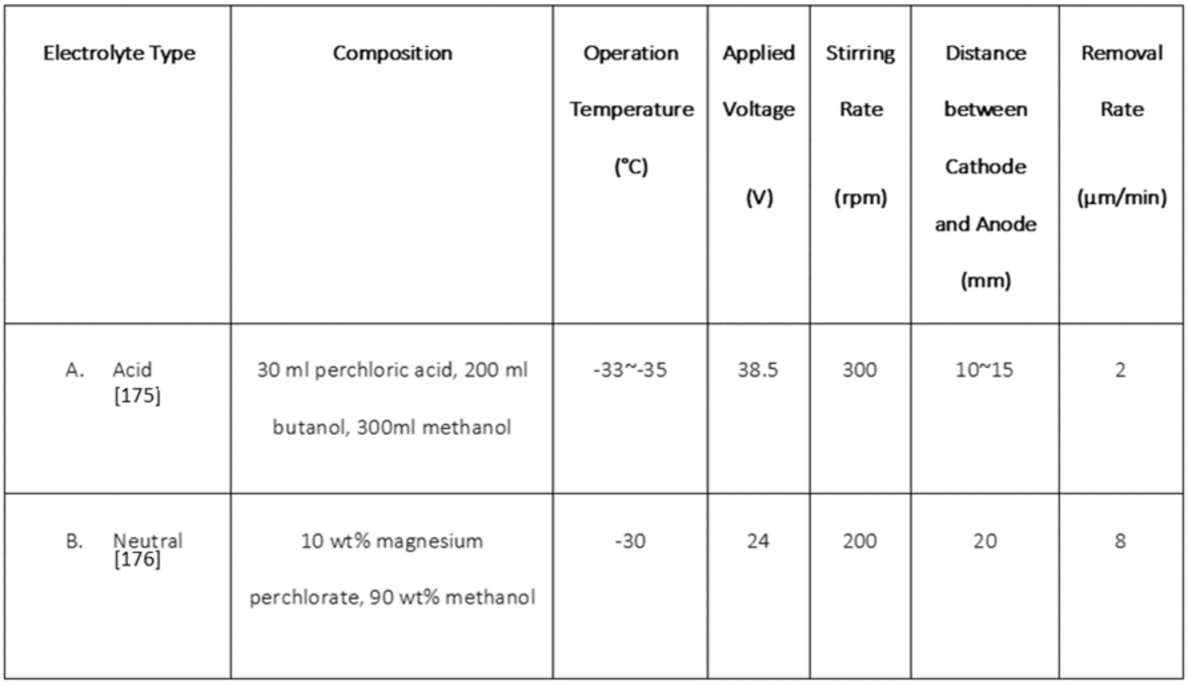

Electrolyte Type	Composition	Operation Temperature (°C)	Applied Voltage (V)	Stirring Rate (rpm)	Distance between Cathode and Anode (mm)	Removal Rate (µm/min)
A. Acid [175]	30 ml perchloric acid, 200 ml butanol, 300ml methanol	-33~-35	38.5	300	10~15	2
B. Neutral [176]	10 wt% magnesium perchlorate, 90 wt% methanol	-30	24	200	20	8

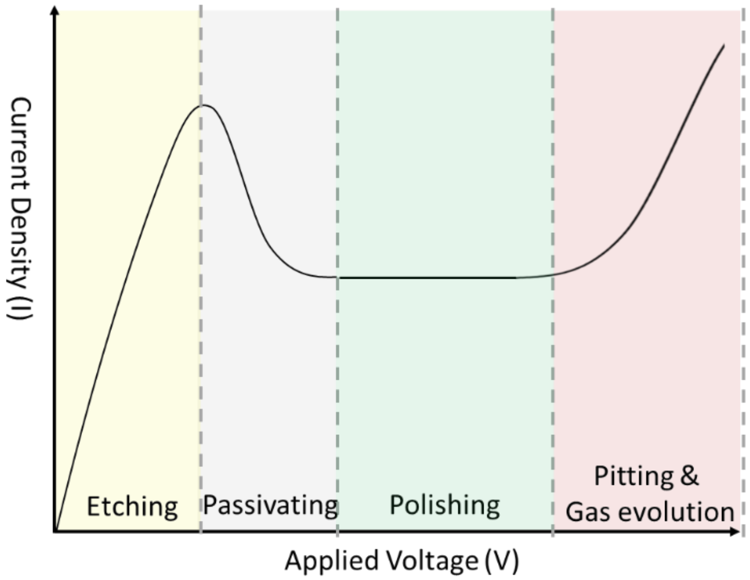

Figure A1 A scheme shows the general four stages of electropolishing with respect to different voltage and current density ratio.

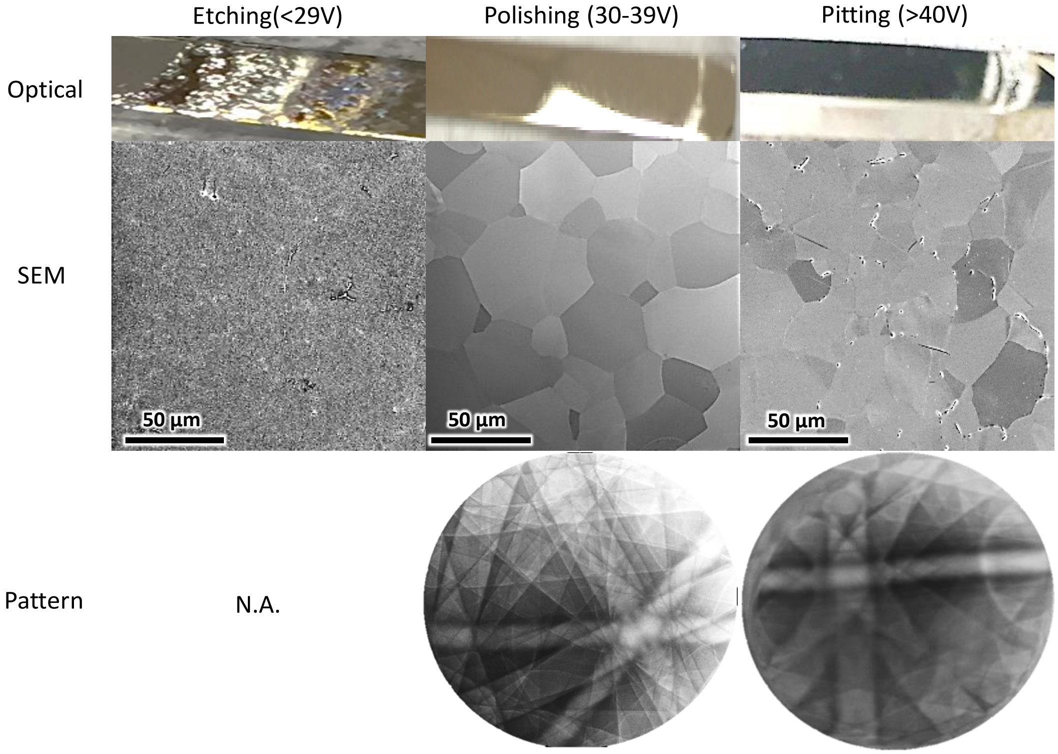

Figure A2 Left) Below 29 V results in etching of metal with rough surface under optical & electron microscope. Middle) A good polishing zone results in shinning & smooth surface with good contrast under electron microscope. Right) Above 40 V results in a dimmer surface in optical microscope. Under electron microscope, pitting occurs, especially at grain boundaries, with slightly worse SACPs.

The electropolishing outcome is quite complicated based on the applied voltage and current (**Figure A1**). The general process usually falls into several stages [175, 176, 177], which include: I. The etching of metal through a direct dissolution at low voltage; II. The passivation of the metal surface by creating an oxidized layer at slightly elevated voltage; III. The polishing of the metal by the consistent dissolution & diffusion of anions through the stabilized passivated layer; IV. Pitting and gas evolution that induces imperfections on the surface beyond the polishing voltage. The comparisons of optical, microstructures under scanning electron microscopy, and electron channeling patterns are shown in **Figure A2**, indicating the perfect surface finish after optimization of electropolishing parameters. As it is shown in the **Table A1**, electrolyte A is specially used for the controlled removal of surface material during electropolishing with 2 μm/min (the surface removal is calculated in **Figure A3**) and the electropolishing can be finished within 2 minutes (it needs 10 ~ 20 s to reach a steady-state that the polish process is homogeneous throughout the sample), however, some grains are suffered with hydride precipitation (around 1 out of 100 grains). On the contrary, electrolyte B is free from hydride formation [174], but it is almost impossible to control the electropolishing rate (~ 8 μm/min).

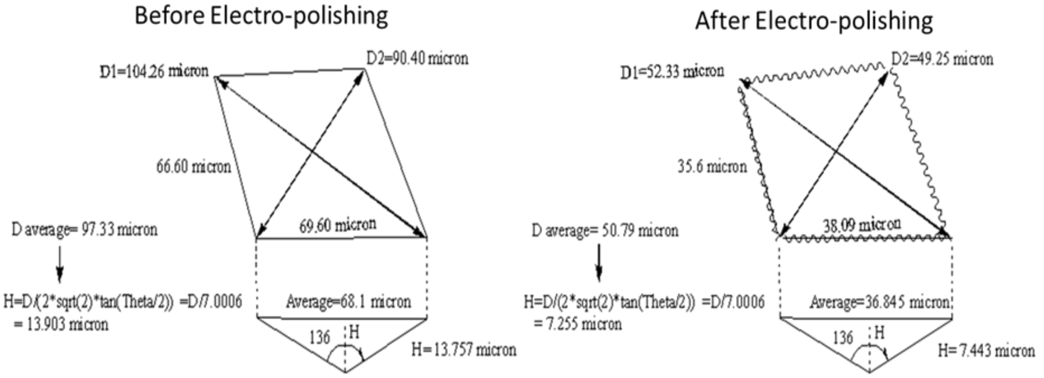

Figure A3 Calculation of the surface removal by the Vickers indent. Several Vickers indents are placed at the surface before electropolishing and final result is the average of each calculated one.

APPENDIX B

Removal of polymer film and gold nanoparticles (AuNPs) for DIC patterning

Introduction:

As indicated from recent papers [161, 162], with the addition of gold (III) chloride trihydrate (HAuCl4•3H_2O) and trisodium citrate dihydrate ($C_6H_5Na_3O_7$•2H_2O) to produce AuNPs as the patterning material, organosilanes such as (3-aminopropyl) trimethoxysilane (APTMS) or (3-mercaptopropyl)methyl) dimethoxysilane (MPMDMS) was added as to covalently bonding to the dangling hydroxyl group on the metal surface to form a monolayer that was able to immobilize AuNPs through coupling reactions. Although the patterned DIC technique offers precise strain measurement during deformation without relying on complicated and much expensive experimental set-ups, the only limitation of this technique is the coating itself. Due to overshadowing of the organic coating and nanoparticle which disturb electron interactions with the sample, and because of artifacts created on the sample surface, no other studies have been accomplished after DIC patterning, such as CC-EBSD and AFM that are also capable of monitoring strain development, or perform surficial analysis such as ECCI. The general approach is to mechanically polish off the surface polymer within a short time, however in reality, this approach is nearly impossible to peel off the layers without damaging the surface of the sample. As a result, using a chemical reaction which is selectively targeting only the nanoparticles and polymer without touching the metal is the ultimate way to perfectly address this issue. This short paragraph is provided, describing how the patterning layer is removed through chemical reactions.

Based on many synthetic papers [178-182], the best way of removing AuNP as well as cleaving off the polymeric silyl ether layer was to use strong halogen reagents, such as F^-. A general concern is to use hydrofluoric acid (HF), however upon consideration, the reagent has to be able to penetrate the polymer layer and react with the AuNPs but blind to the titanium, which is also vulnerable in the acid, a mild organic fluorine source should be selected. In this research, tetra-n-butylammonium fluoride (TBAF $\cdot 3H_2O$ and 1mol/L TBAF in THF) is used (from Sigma-Aldrich) since this is also considered as a phase transfer catalyst which can bring water and immiscible organic solvents together. Although TBAF is not the only reagent or the best among all alternatives (fluorotrimethylsilane, referred as the TMS-F, may also work but much expensive), picking the best reagent is not the main purpose of this paper.

Experimental procedures:

The as-deformed Ti-7Al (**Figure 13 a**) dog-bone tensile sample was provided by Professor Samantha Daly's group, with DIC patterns coated on surface and strain map collected. The final ingredients used in this experiment were 10: 1: 1 weight ratio of TBAF, chloroform, and ethylene glycol. The detailed procedure of uncoating is as follows:

1. Merge the sample completely in the solution at around 30 ~ 35^{o}C for 1 hour.
2. Take the sample out, clean by 5 - 10 mins sonication (20 - 40 kHz) in a baker of soap water (pH ~ 8), flash with ethanol- DI water- ethanol, air dry and track the progress.
3. Repeat 1 and 2 until the surface is cleaned enough.
4. Place hand soap on the surface, which is then swept off by cotton stick, go through final ethanol-DI water- ethanol washing and air dry.

Results and discussion:

After an accumulates four hours' reaction, the sample surface was particle-free, with little residual AuNP remained. Nonetheless, the detailed uncoating progress with time was

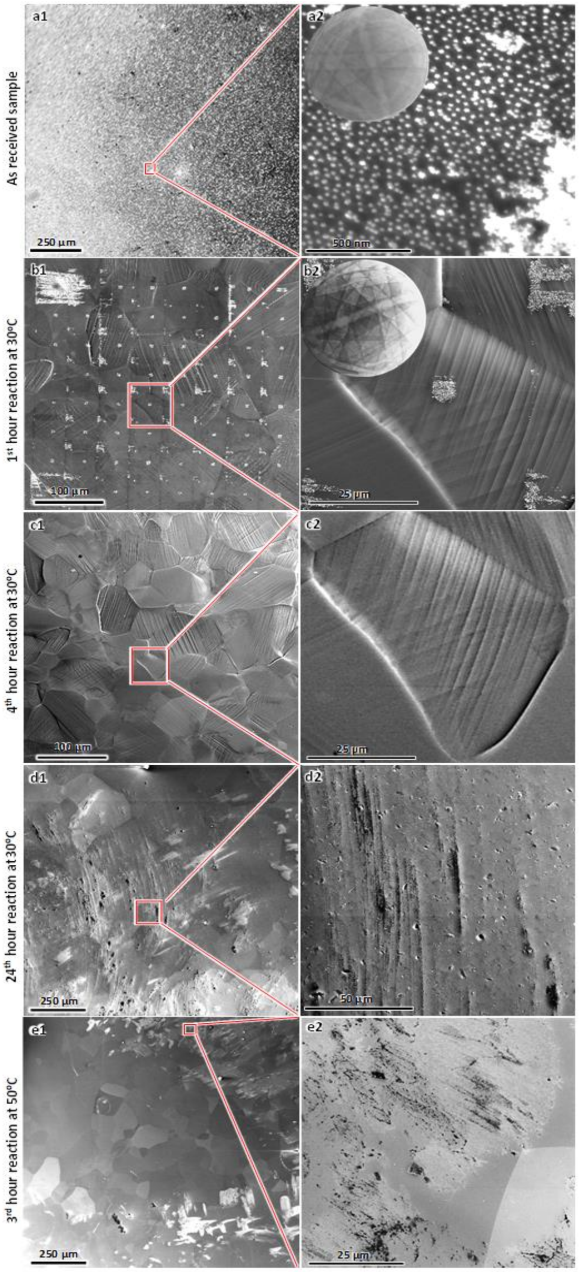

Figure A4a1) Surface condition of as received sample. a2) SE image of AuNPs taken at high magnification from the red box, with weak SACPs due to interference. b1) Surface condition after 1 hour at 30 ^{o}C, showing removal of majority patterning material. b2) SE image showing one of the unremoved clusters of AuNPs, with sharp SACPs. Particles in these areas are the focused point during DIC data acquisition. Long time exposure of beam may condense the NPs into the material or strengthen the bonding interaction, with detailed mechanism unknown. The patterns c1) At 4th hour, all nanoparticles are consumed, including the clusters. c2) SE image of the same area with b2, showing clean sample, with sharp slip traces and grain boundaries. d1) 24-hour reaction time of an undeformed control sample 1, showing the slightly etching of material. d2) SE image of the etched area in the red box, showing line type etched marks and small etched cavities. e1) Surface condition of an undeformed control sample 2 after the 3rd hour in solution at 50 ^{o}C, also showing large areas being etched. e2) SE image of the red box area, showing surface material has been etched away.

shown in **Figure A4**, with extra uncoating information (i. e. uncoating at elevated temperature, longer reaction time, etc.) acquired from control samples. In **Figure A4 b1&2**, after one hour, it can be seen that major particles have been washed away, with clusters of AuNPs (and some fiducial marks, although not shown in the image) left on the surface. Those were possibly segregated due to long exposure to the high energy electron beam during DIC data acquisition. The reagents are hard to get access to the clusters as the surface to ratio was diminished after segregation. Meanwhile, dramatic improvement of SACPs before and after uncoating (**Figure A4 a2**&**b2**) suggests the removal of particles as well as the polymer layer. With longer reaction time up to the 4th hour, all particles have disappeared, even the robust clusters, suggesting the completion of the uncoating process, which is shown in **Figure A4 c1&2**. It should be noted that although F^- anions are mostly locked in the organic environment so that they are only targeting the polymer and the nanoparticles with higher "reactivity", F^- are still considered to be aggressive to Ti metal. This has been proved that longer reaction time (i. e. 24 hours as shown in **Figure A4 d1&2**) and higher temperature (i. e. 50 ^{o}C as shown in **Figure A4 e1&2**). Although not shown specifically in this manuscript, similar progress can be achieved by simply

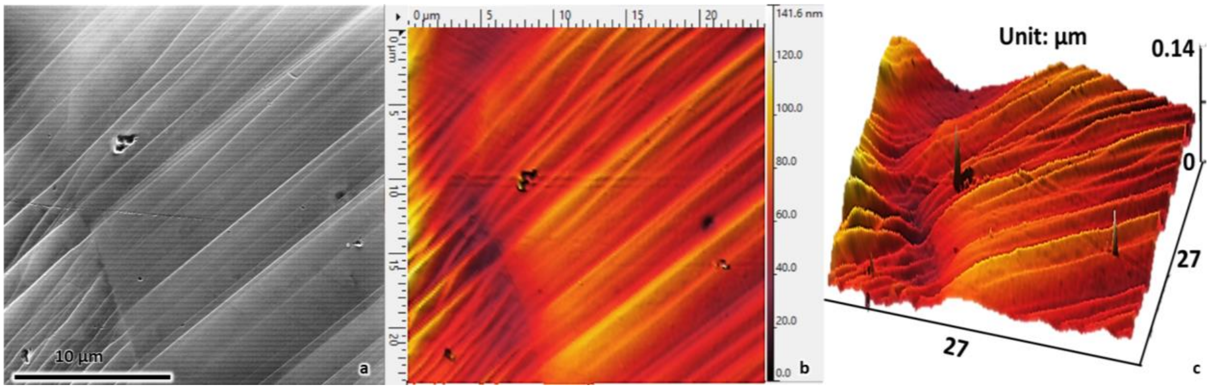

Figure A5a) SE image of a random area, showing clear slip traces on surface after the uncoating. b) 2-D AFM map showing topographic information of the same area. c) 3-D AFM map showing clear steps from the slip band and the grain boundary (concaved).

using 1 mol/L TBAF in Tetrahydrofuran (THF), with little residual AuNPs clusters left on the surface (7 hours), thus this can serve as alternative reagent if not asking for complete extinction of AuNPs. Neither approach harms the surface within the reaction time and the surface is able to perform ECCI and AFM analysis on the sample with little interference, as shown in **Figure A5**.

Conclusion:

A weight ratio of TBAF: $CHCl_3$: $(CH_2OH)_2$ = 10: 1: 1 (or 1mol/L TBAF in THF) has been proved to be efficient in removing the pattern after DIC with almost no harm to the surface if using properly.

APPENDIX C

Strain measurement after four-point bending

As the sample surface between supporting pins is experiencing uniaxial tensile stress, at low strain level that the sample does not have too much bend curvature, the tensile strain is approximately measured from the distance change between triple points of different grains along/close to the tensile direction before and after deformation using Image J^{TM} or other image processing software, as shown in **Figure A6**.

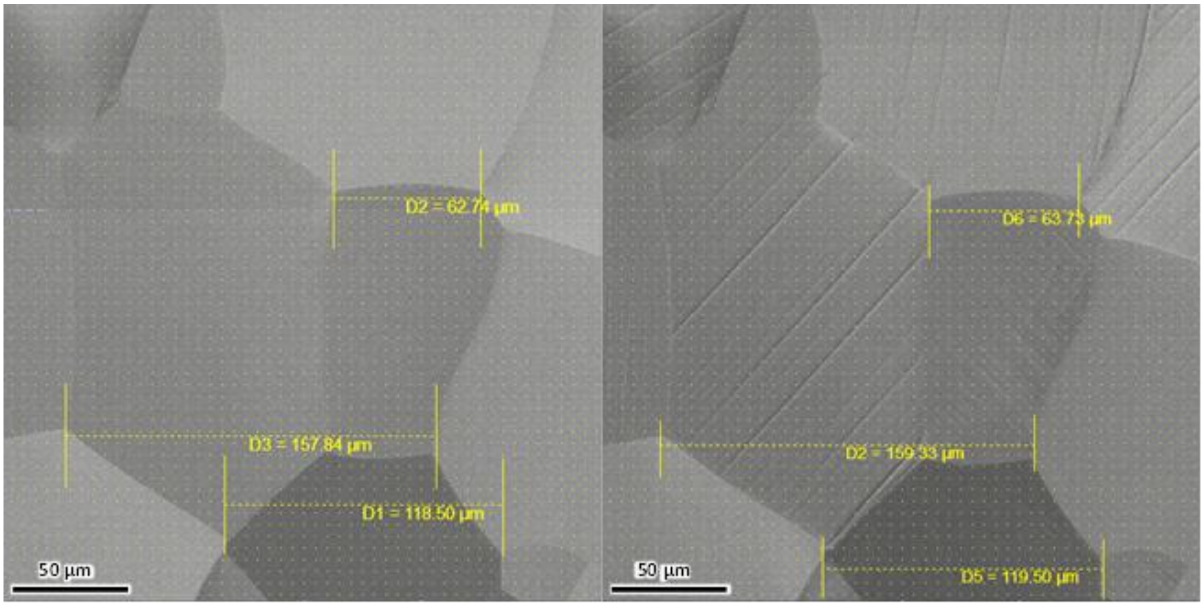

Figure A6 Left) The distance between triple points before deformation. Right) The distance between same triple points after deformation.

APPENDIX D

The calibration of MIAR III FEG-SEM with SACPs module for ECCI and CC-EBSD analysis

As it is of critical importance to ensure the calibrated status of the SEM for the accuracy of ECCI and CC-EBSD analysis, this section provides a detailed procedure on the calibration of MIRA III FEG-SEM. Before proceeding, it is highly recommended to read the manual from MIRA III and understand the terms that are frequently used in electron microscopes: focus, magnification, stigmation, wobble, etc.

Proper alignment of column and gun:

There are several modes provided in MIRA III FEG-SEM in the CMSC center of MSU, namely: resolution mode, depth mode, field mode, wide filed mode, and channeling mode. ECCI images are taken in the resolution mode, while the SACPs are collected in field mode with beam rocking and shown in the channeling mode for the establishment of a diffraction vector **g**. Thus, it is critical to ensure the beam alignment in each mode. The general alignment usually starts with "auto gun centering" and "auto column centering" which bring the parameters close to the conditions for ECCI analysis. First, in resolution mode, repeat focusing and increasing image magnification until an out-of-focus target (**Figure A7a**) is in focus (**Figure A7b**) at the field of view 2 ~ 3 µm. Astigmatism at high magnification is corrected during focusing using the

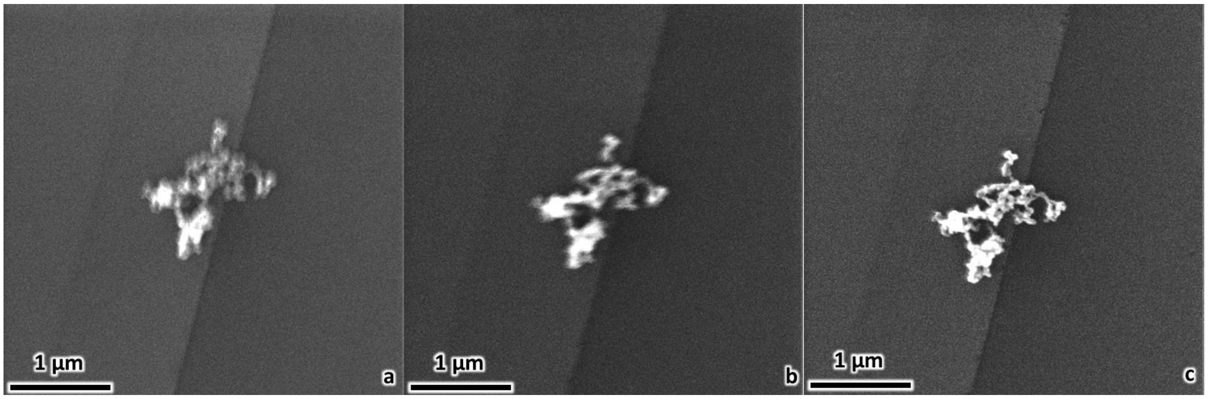

Figure A7 Secondary electron (SE) images taken at the field of view of 3.86 µm that shows: a) The particle is out of focus. b) The dirt is in focus, but astigmatic. c) The dirt is stigmatic and in perfect focus.

“stigmator” operation until the target is crispy sharp (**Figure A7c**). During this adjustment, the aperture should also be well centered in the “wobble” operation, that the image is not swinging when the electron beam is moving back and forth across the focus.

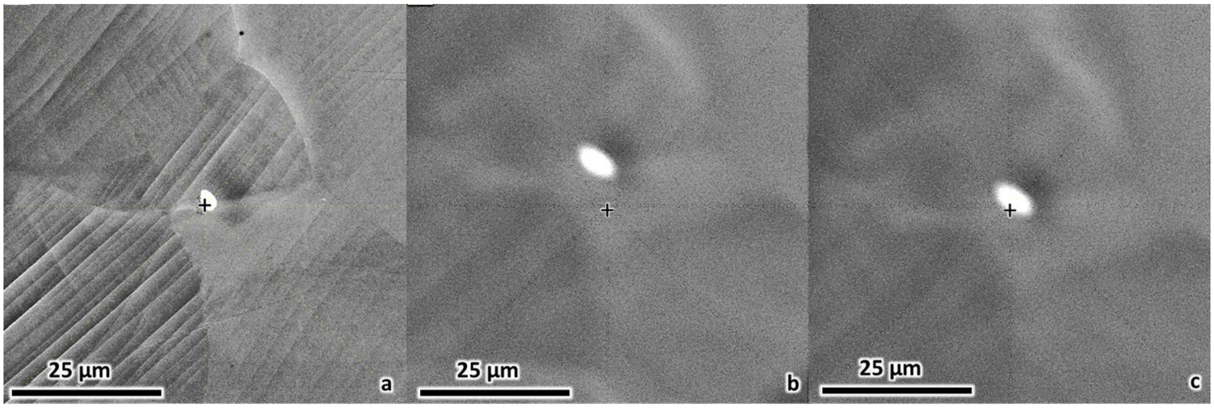

Figure A8a) SE image in resolution mode (field of view 3.86 µm) that shows the optic axis (black cross) is on a particle. b) SE image in field mode (field of view 65.3 µm) that shows the deviation of optical axis from the resolution mode. Although it appears blurry, this particle is already in focus in field mode since the resolution between modes is different. c) SE image in field mode that shows the optical axis is moved back to the same position after aperture alignment after “wobble” operation.

After the beam alignment in the resolution mode is finished, the second alignment is done in the field mode. Additional focusing operation in this mode is not necessary since this operation is already done in the resolution mode, but the aperture should be well aligned using the same “wobble” operation. More importantly, one must ensure that the optical axis is

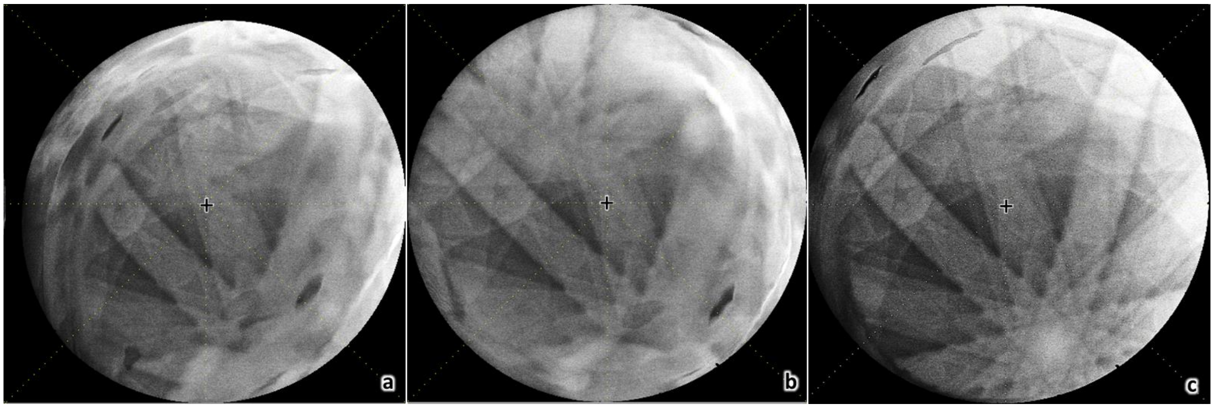

Figure A9a) An asymmetric SACP aperture with overlapping of patterns from surrounding grains. b) A symmetric, perfect round aperture with interference signals from surrounding grains. c) A perfect circular aperture within pattern only from the target grain.

targeting the same position both in the resolution mode and field mode, so that the pattern is collected from the target area (**Figure A8c**). This step is critical when the ECCI analysis is performed near grain boundaries, at high tilt conditions (> 10^o), or in small grains (grain size larger than 20 µm for a perfect SACP in this MIRA SEM) for the diffraction condition set-up. The final SACP aperture alignment is achieved in the channeling mode through "wobble" operation. After the aperture alignment, the aperture should appear to be a perfect circle, with an un-overlapped pattern (**Figure A9c**). Crisp ECC images with precise pattern information can be achieved after all these alignments were done properly.

APPENDIX E

Procedures of ECC image acquisition and data analysis

This section provides detailed information on the establishment of channeling condition, obtain dislocation contrast by following a Kikuchi band, and the identification of channeling bands using T. O. C. A. software.

Establishing a channeling condition:

The fundamental mechanism for setting-up of an ECCI channeling condition is analogous to the establishing of two-beam diffraction condition to transmission electron microscopy (TEM), by moving the optic axis/un-tilted electron beam (indicated by the black cross in **Figure A10**) approaching the edge of the channeling band through proper tilt and rotation [141, 147]. It is noticeable that the deviation from the Bragg condition **s** = 0 is the imaging condition to get maximum contrast in ECCI analysis [140] (as illustrate in **Figure A10b**). It is more challenging to correctly set up **s** = 0 channeling condition if the target area is highly textured or having an orientation gradient due to higher strain level deformation, one have to manually adjust the relevant position of the optic axis and the band edge for a best ECC image, which may need several attempts. It should be mentioned that the orientation deviation after plastic deformation can be solved by using a higher resolution SACP module that can collect the

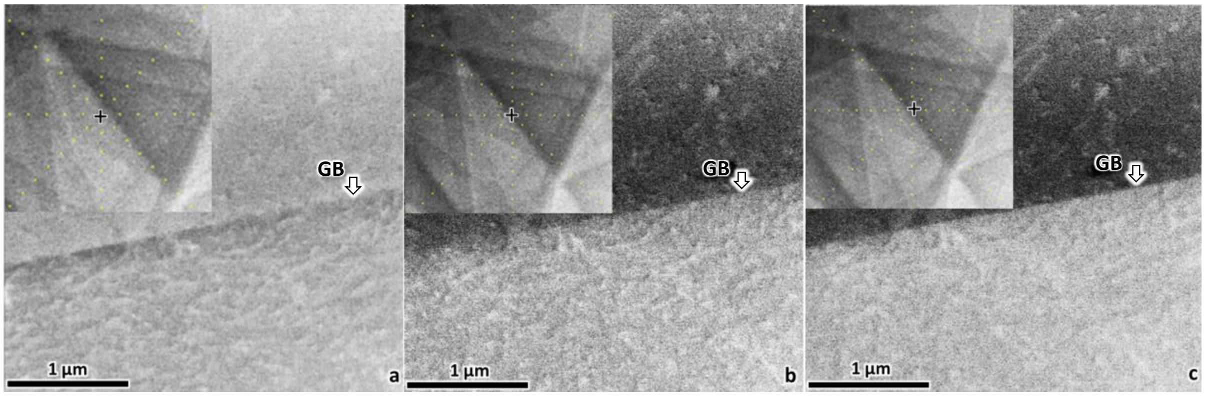

Figure A10a) ECC image taken at s <0, the contrast of dislocations in the lower grain is not perfect. b) ECC image taken at s = 0, a crisp image of sharp dislocations in perfect contrast. c) ECC image taken at s > 0, the dislocations in the same area are badly resolved with poor contrast.

accurate from smaller areas (currently SACP module in MIRA III requires at least a 10 µm diameter area in order to set up a channeling condition, and ~ 20 µm to get a perfect, un-overlapped pattern).

To get a crisp ECC image on a proper channeling condition, it is necessary to take multiple ECC images as the optic axis is traveling following the same channeling band as shown in **Figure A11**. Some dislocations appear as dots with strong black contrast on one side and white contrast on the other side, suggesting the dislocations are more inclined near the surface, while some dislocations appear as lines, indicating these dislocations are more parallel close to the surface. It can be easily recognized that the dislocations labeled by small white arrows have opposite black & white contrast with those marked by small black arrows, a reflection of the opposite Burgers vectors. By comparing the same dislocations taken near different zone axis, it

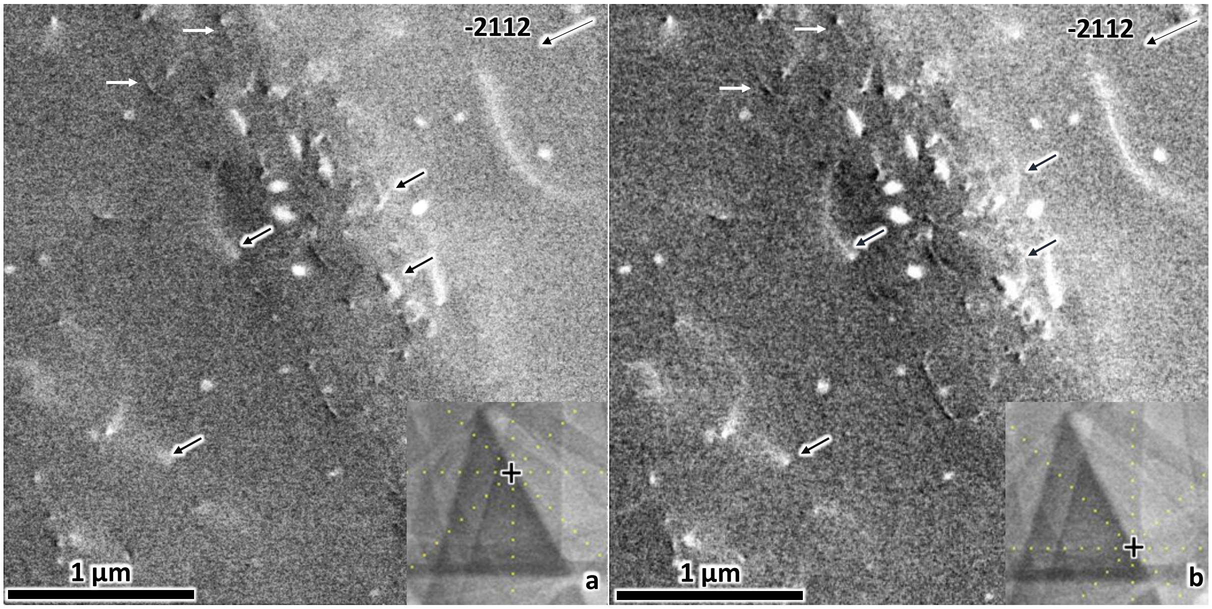

Figure A11a) The dislocation tails are in weak contrast, as indicated by the small black arrows while some other dislocation tails are in strong contrast, as indicated by the small white arrows when ECCI is taken close to the upper zone axis. b) The dislocations indicated by the small black arrow are in strong contrast, on the contrary, the tails marker by the small white arrows are in weak contrast when the optic axis moves closer to the lower zone axis.

is easy to find that dislocations labeled by the small black arrows have shorter tails with weaker contrast in **Figure A11 a)** than in **b)**, while the ones with opposite black & white contrast, indicated by the white arrows, show slightly longer tails and better contrast in **a)**. This suggests the dislocations with opposite Burgers vector also have opposite line directions or, dislocation inclinations, near the free surface. Nevertheless, the difference in length of the dislocation tails with respect to the position on the channeling band also provides a clue to identify the near-surface dislocation line directions of these dislocations.

Identification of the channeling band:

The identification of the channeling band was accomplished using “Tools for Orientation Determination and Crystallographic Analysis in SEM and TEM” (T. O. C. A.) software [142, 149], version No. 2.2, developed by Dr. Stefan Zaefferer in the year 2010. T. O. C. A. is specifically used for the identification of channeling bands in both TEM with the interface shown in **Figure A12**. The channeling band identification is done in the SEM mode, although the difference between simulated patterns in TEM and SEM mode is minimal. The procedure for getting the simulated pattern of a target crystal after loading the α-Ti crystal dataset is as followed:

I. Input the Euler angle, which is acquired from the EBSD-OIM software, in the “Ti-alpha” module.

II. Manually rotate the crystal 90^{o} along the Z-axis in the “Goniometer” module.

III. Input the accelerating voltage for ECCI analysis (30 kV in this study) in the “High Tension” in the “Microscope” module.

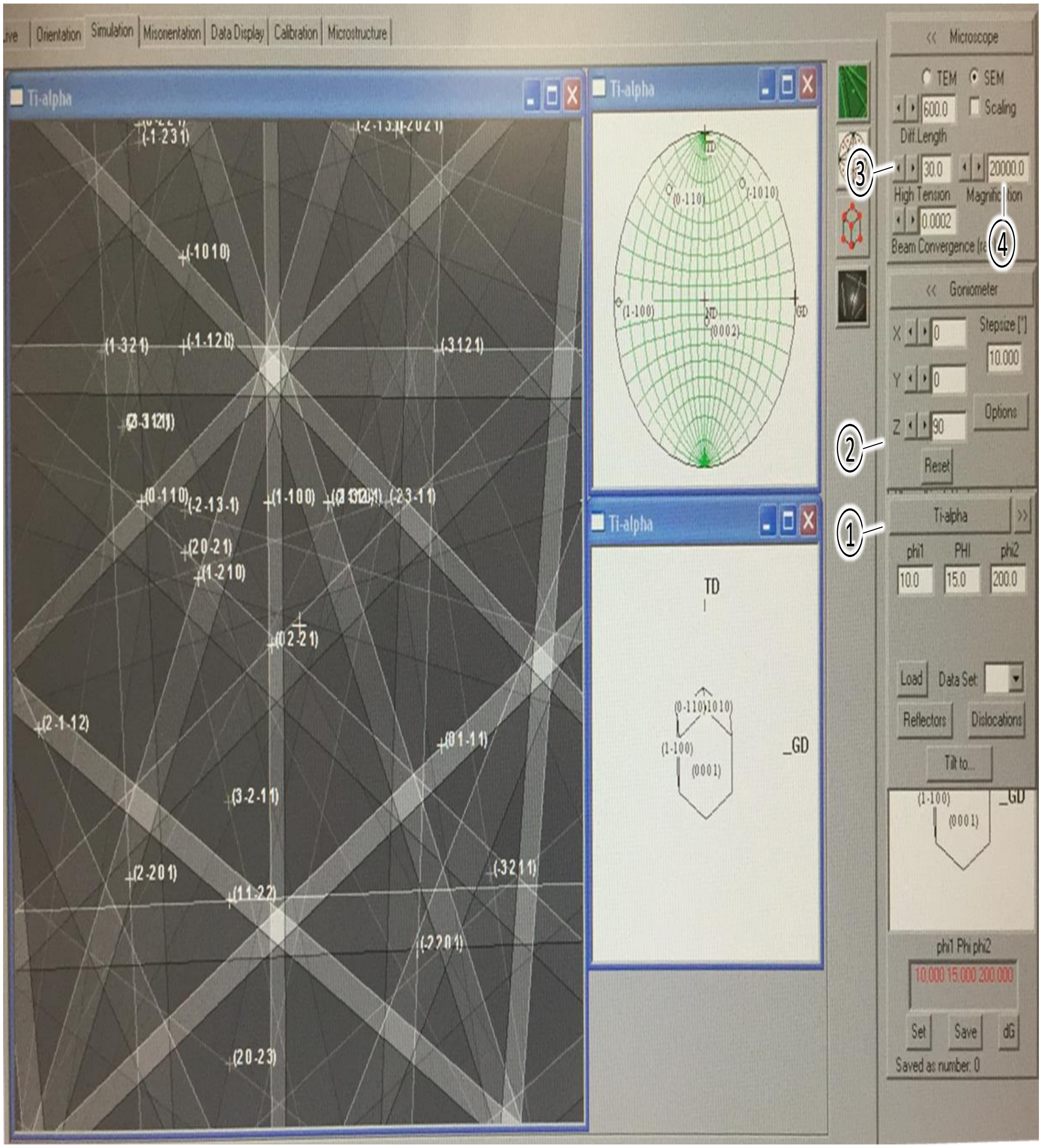

○ TEM ● SEM

600.0 ☐ Scaling

Diff.Length

High Tension 30.0

Magnification 20000.0

Beam Convergence 0.0002

X 0

Y 0

Z 90

Stepsize [°] 10.000

phi1 10.0 PHI 15.0 phi2 200.0

Data Set:

phi1 Phi phi2

10.000 15.000 200.000

Saved as number: 0

Figure A12 The interface of T. O. C. A. software shows 3 components in the simulation display, including the simulated patterns shown on the left pop-up window, the corresponding pole figure shown on the upper-right window, and the crystal orientation shown on the bottom-right window. The most useful parameters input in the control panel are listed as: 1. The Euler angle; 2. The 90° rotation; 3. The acceleration voltage at which ECCI is taken; 4. The magnification at which ECCI is taken.

IV. Input the magnification value at which ECCI is taken in the “Microscope” module.

V. (Optional) Adjust the width of the channeling band by changing the number in the “Diff Length” in the “Microscope” module.

The simulated pattern should look similar to the real patterns collected from the channeling mode in MIRA III SEM, which is shown in **Figure A13**. The dislocation Burgers vector **b** can be determined through $\mathbf{g} \cdot \mathbf{b} = 0$ invisibility analyses as **g** is correctly labeled by T. O. C. A.

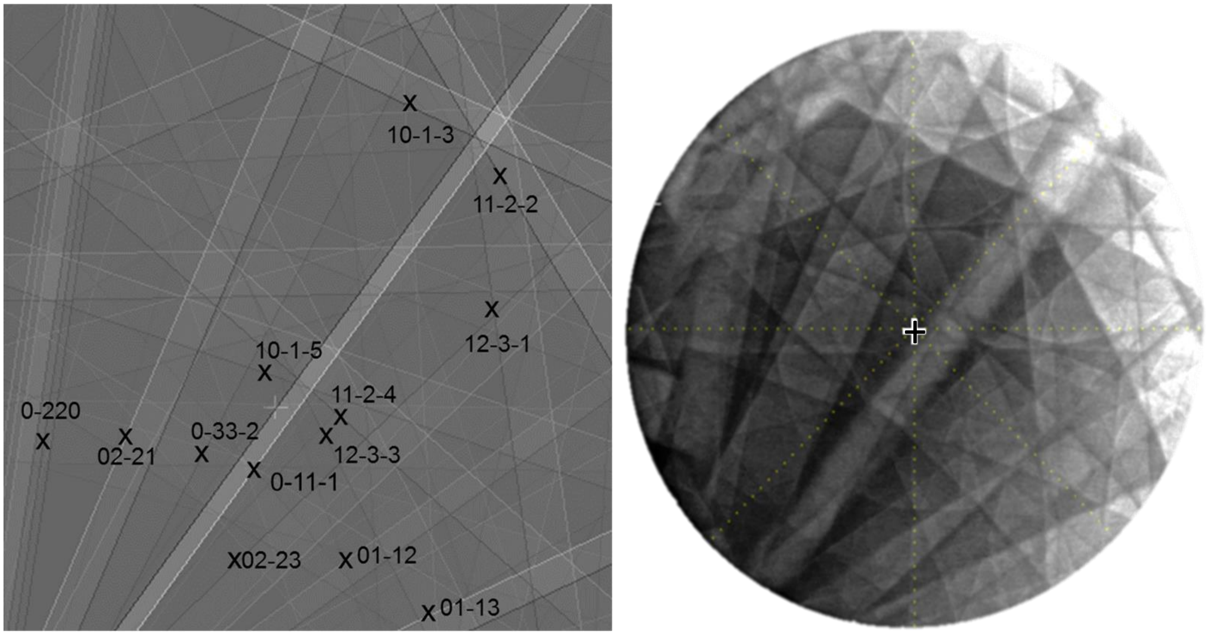

Figure A13 Left) Simulated channeling patterns with these bands labeled. Right) The real patterns collected from channeling mode in MIRA III SEM, with the optic axis labeled as black cross.

APPENDIX F

Dislocation identifications

This section only includes high quality ECC images that were not shown in the manuscript, some rough (poor quality) ECC images that were used to quickly identify dislocations' Burgers vectors were not attached in this section.

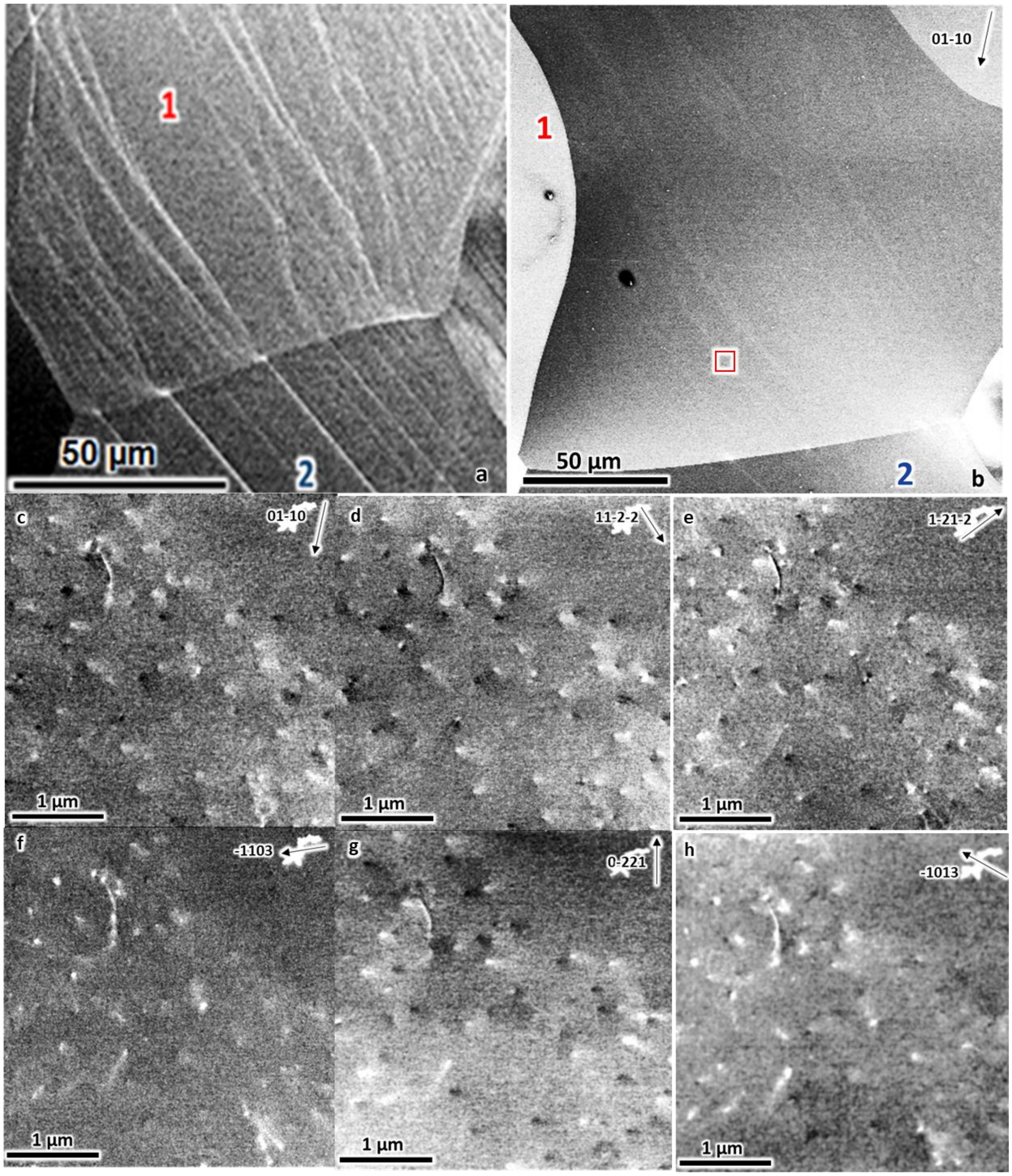

Figure A14a) Grain 1 as deformed. b) grain 1 after electropolishing. c-h) ECC images from the red box area taken at different **g** vectors, dislocations are $(1\bar{1}00)[11\bar{2}0]$ and $(1\bar{1}01)[11\bar{2}0]$.

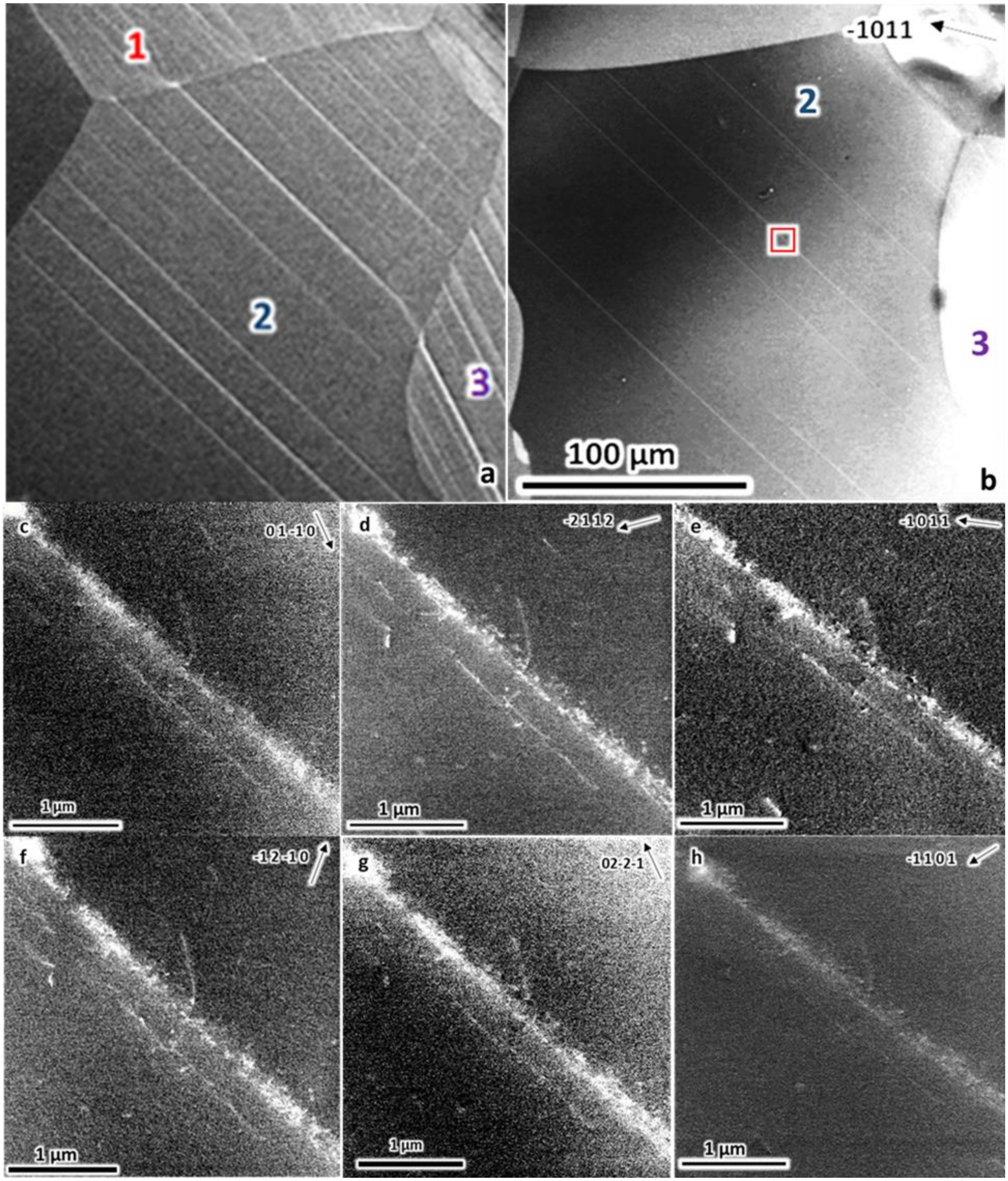

Figure A15a) Grain 2 as deformed. b) Grain 2 after electropolishing. c-h) ECC images from the red box area taken at different **g** vectors. Dislocations are $(1\bar{1}00)[11\bar{2}0]$.

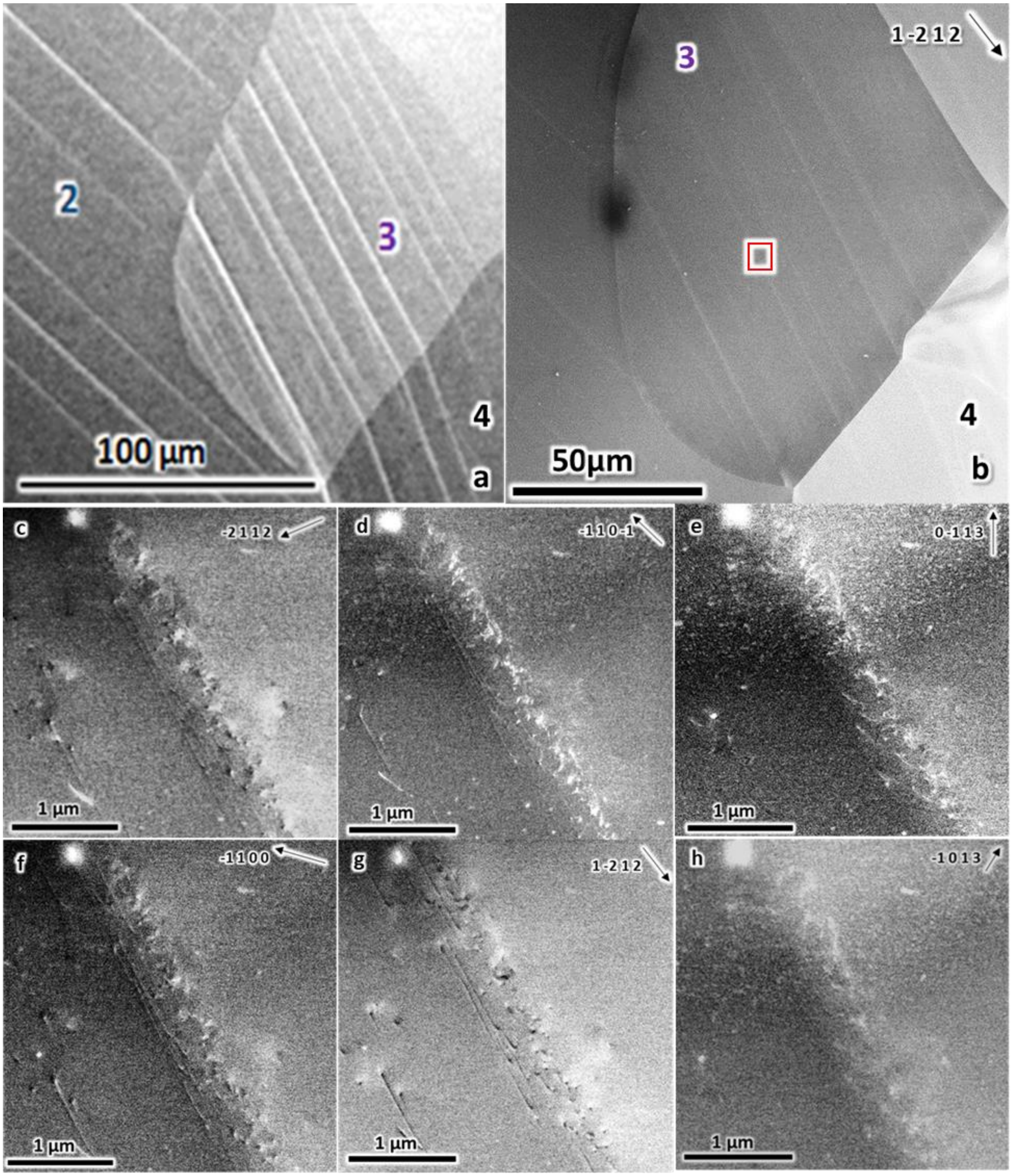

Figure A16a) Grain 3 as deformed. b) Grain 3 after electropolishing. c-h) ECC images from the rex boxed area at different channeling conditions. Dislocations are $(10\bar{1}0)[1\bar{2}10]$.

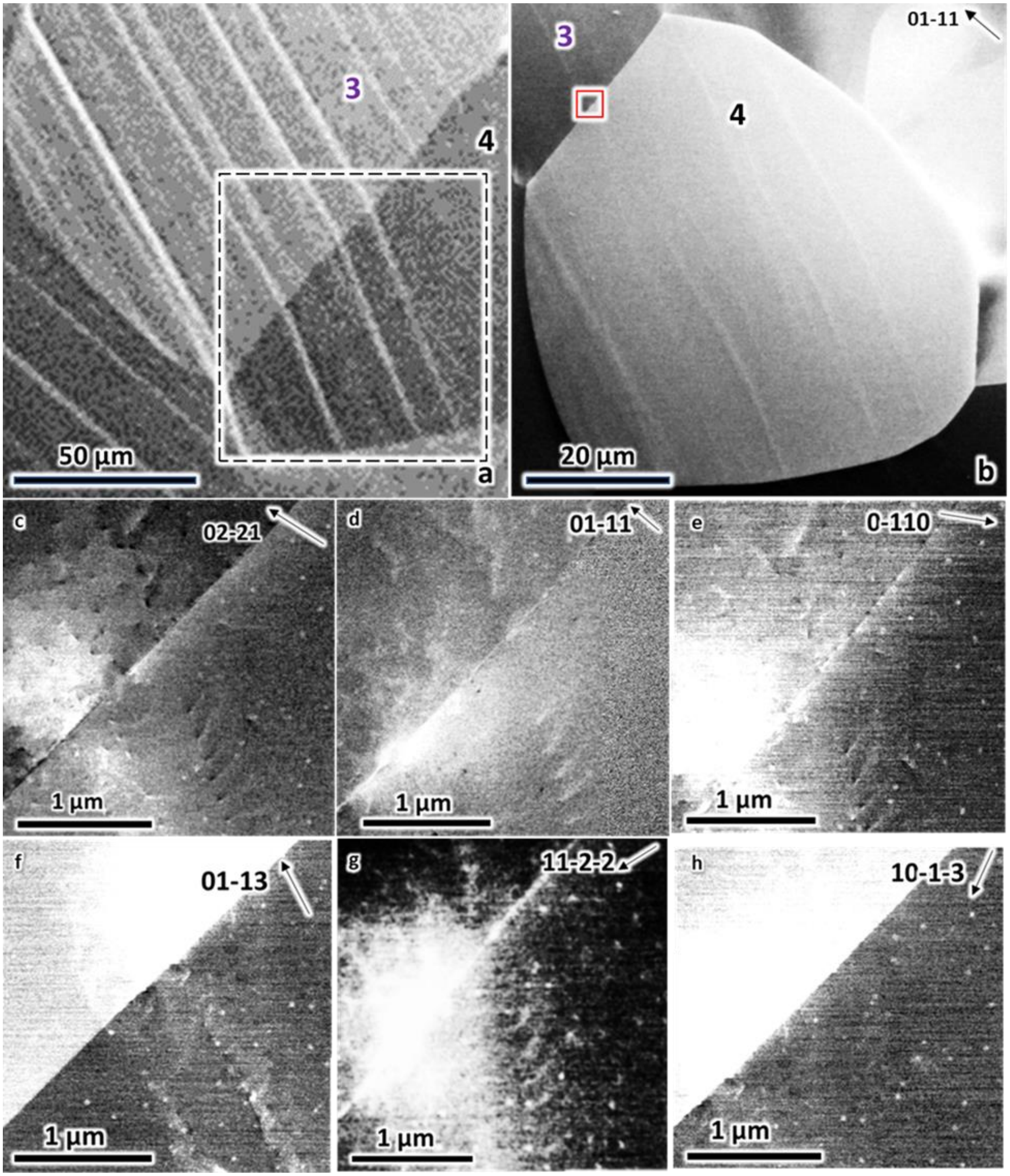

Figure A17a) Grain 4 as deformed. b) Grain 4 after electropolishing. c-h) Dislocations at the boxed area (grain boundary between grains 3 and 4) taken at different channeling conditions. Dislocations are majority $(10\bar{1}0)[\bar{1}2\bar{1}0]$.

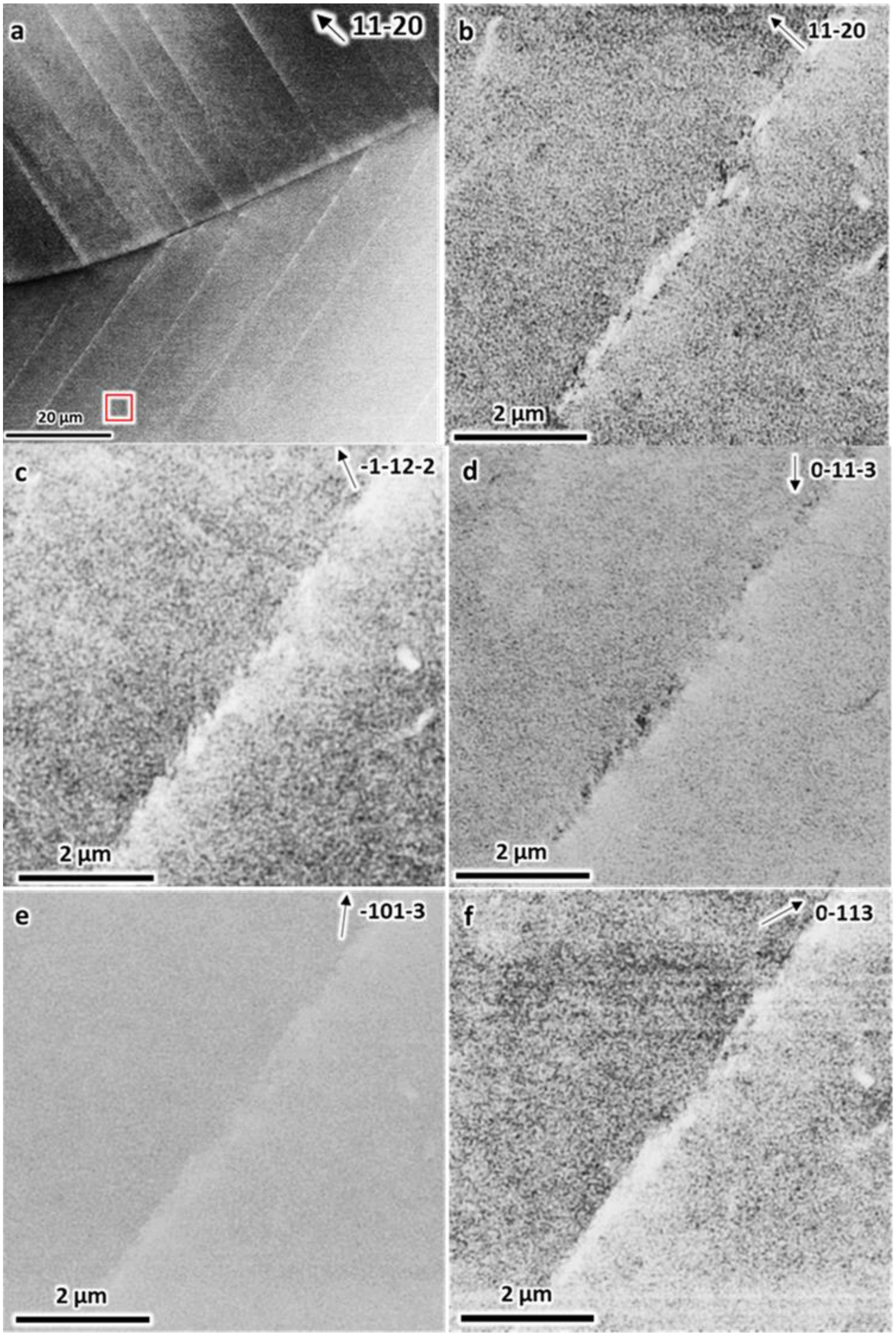

Figure A18 One example of dislocations identification in sample 2 after electropolishing. a) ECC image of slip traces after electropolishing. The contrast is not due to topography but from the contrast of dislocations. b-f) Dislocations taken at different **g** vector. Dislocations are $(10\bar{1}0)$ $[\bar{1}2\bar{1}0]$.

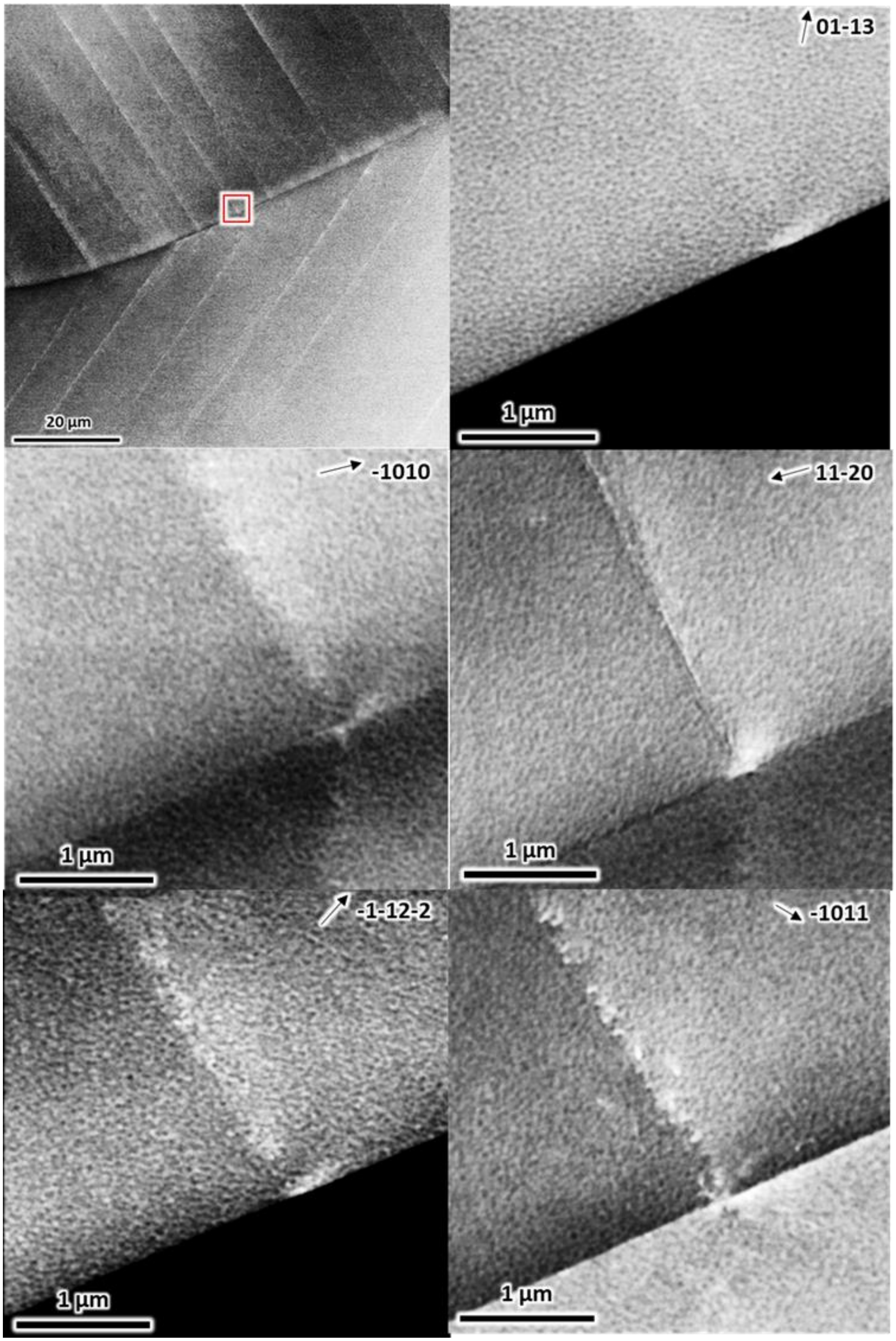

Figure A19 One example of dislocations identification in sample 2 after electropolishing on the other side of the grain. Dislocations are (01$\bar{1}$0) [$\bar{2}$110].

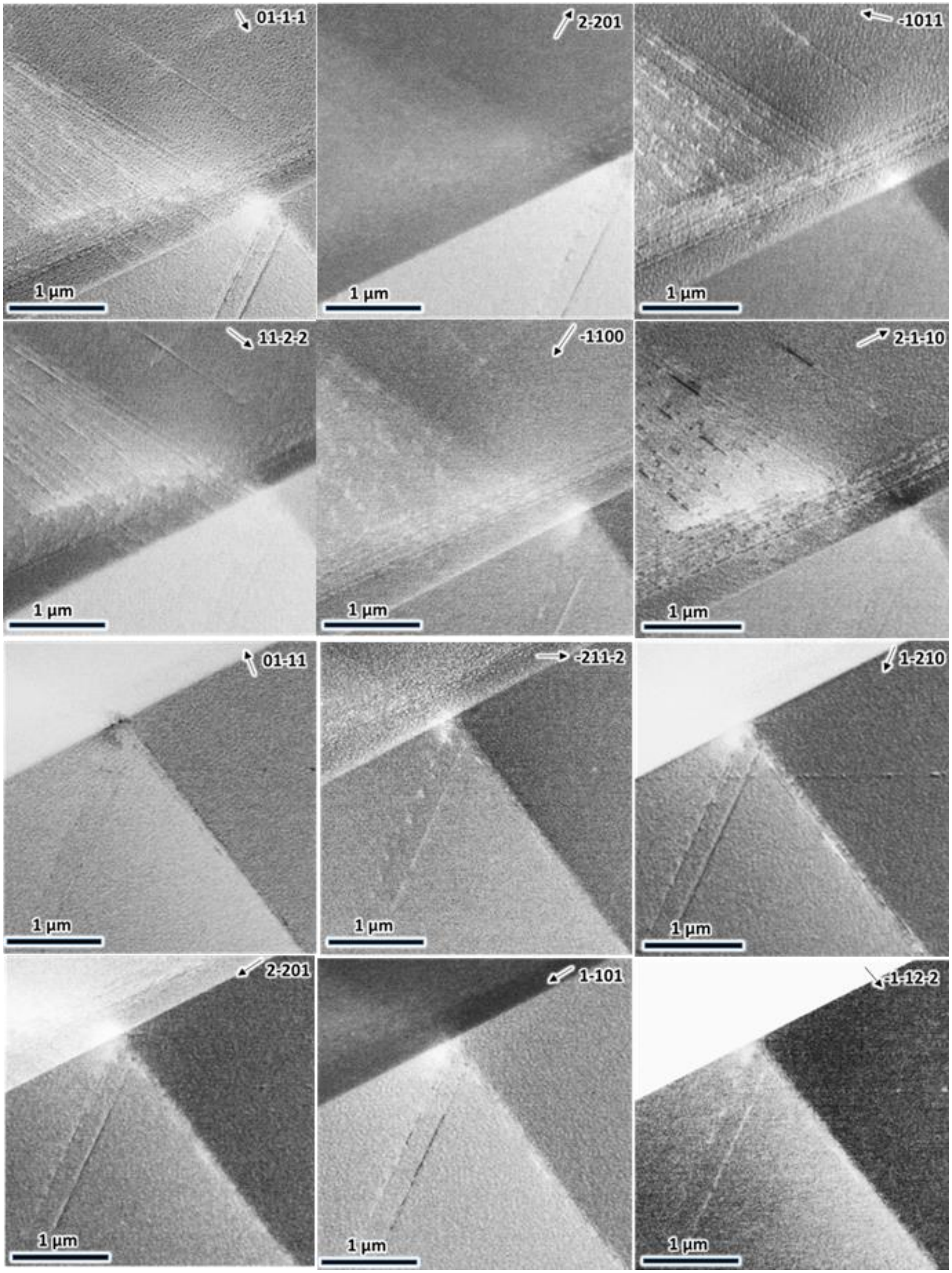

Figure A20 Neighboring grains in Sample 2. First six ECC images) Identified dislocations are $(1\bar{1}00)[11\bar{2}0]$. Second six ECC images) Identified dislocations are $(1\bar{1}00)[11\bar{2}0]$ and $(1\bar{1}01)[11\bar{2}0]$.

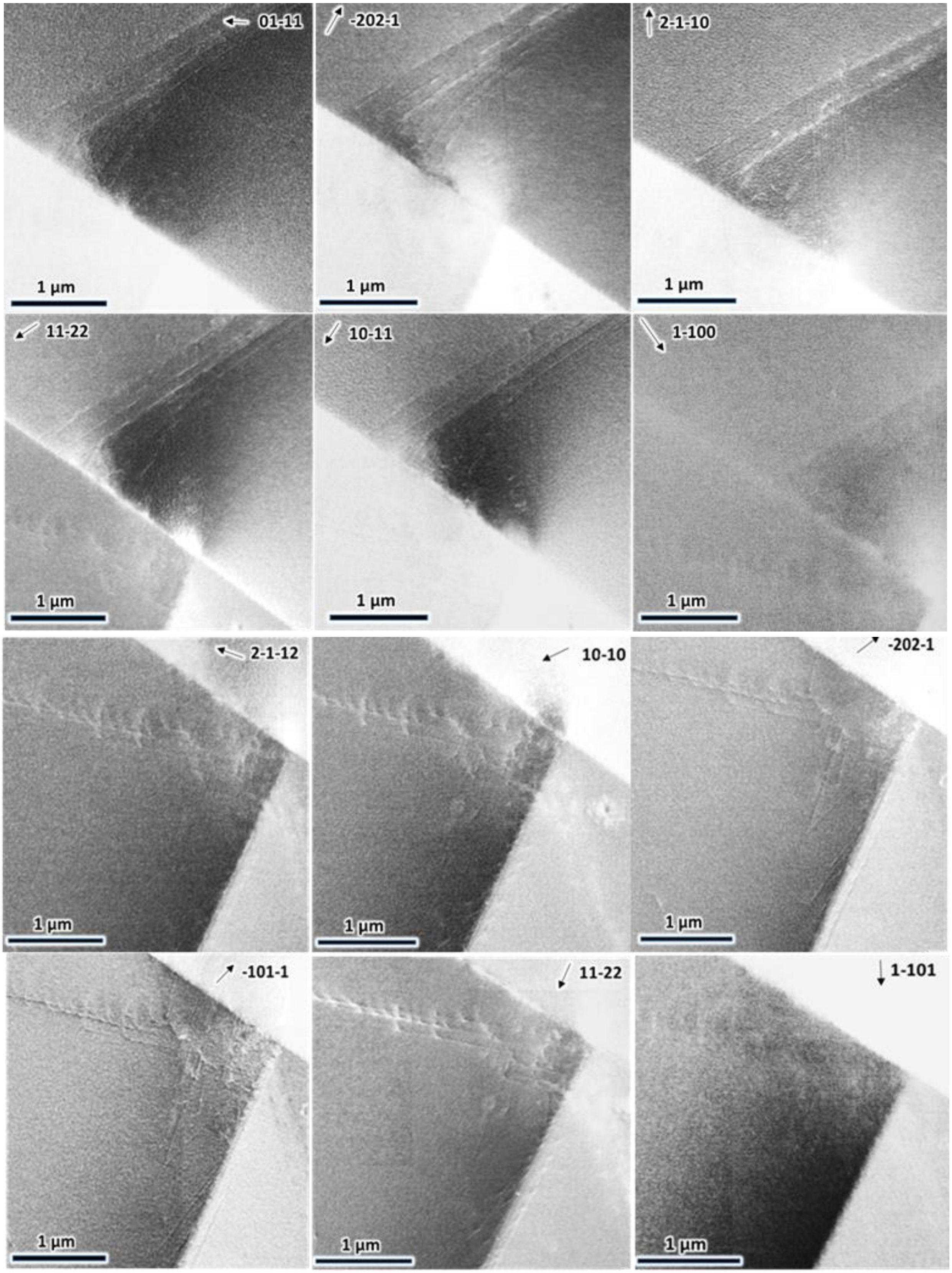

Figure A21 Neighboring grains in Sample 2. First six) Identified dislocations are $(1\bar{1}00)[\bar{1}\bar{1}20]$ and $(\bar{1}101)[11\bar{2}0]$. Second six) Identified dislocations are $(1\bar{1}00)[\bar{1}\bar{1}20]$ and $(1\bar{1}01)[11\bar{2}0]$.

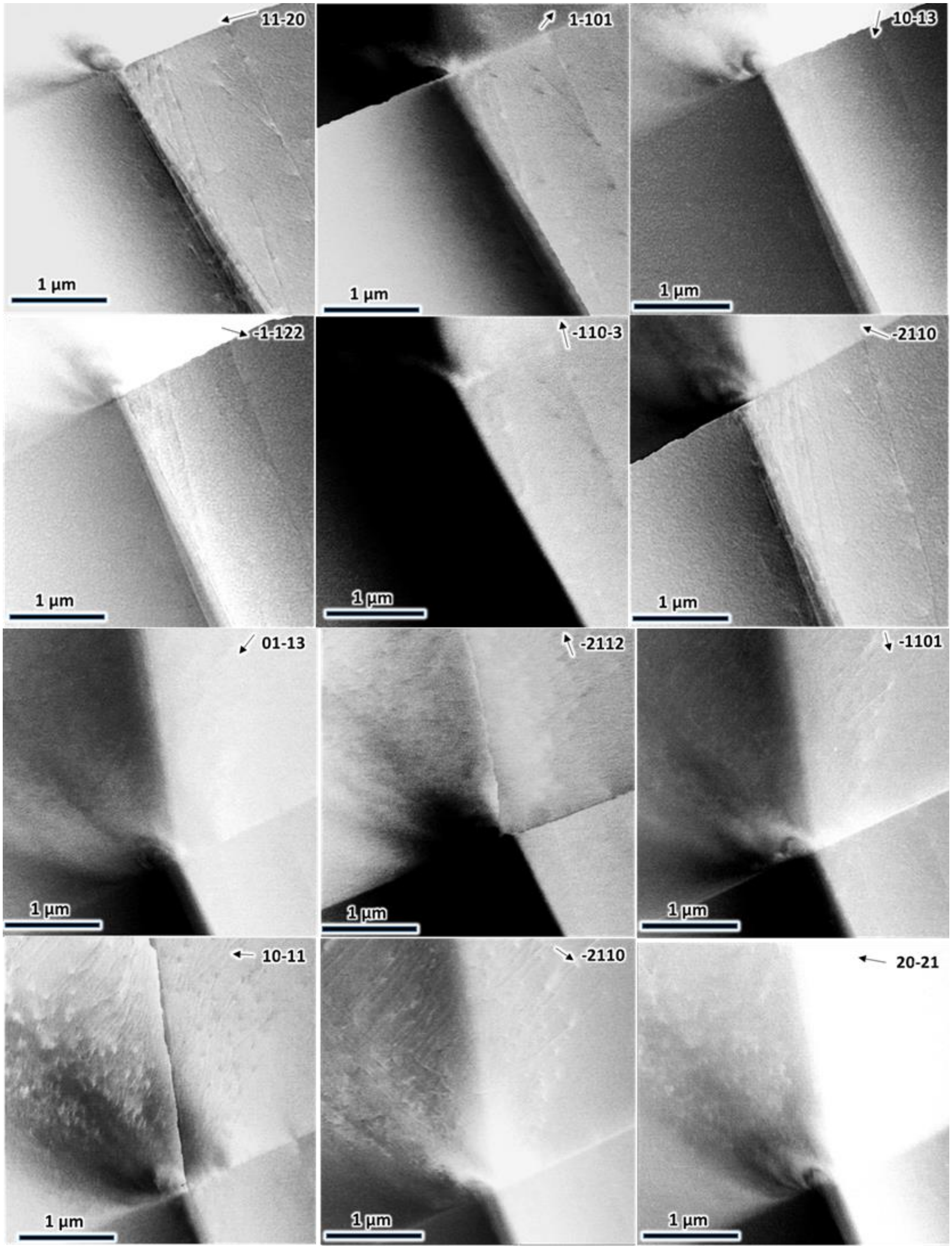

Figure A22 Neighboring grains in Sample 2. First six) Identified dislocations are $(10\bar{1}0)[\bar{1}2\bar{1}0]$ and $(\bar{1}011)[1\bar{2}10]$. Second six) Identified dislocations are $(0\bar{1}10)[2\bar{1}\bar{1}0]$ and $(01\bar{1}1)[\bar{2}110]$.

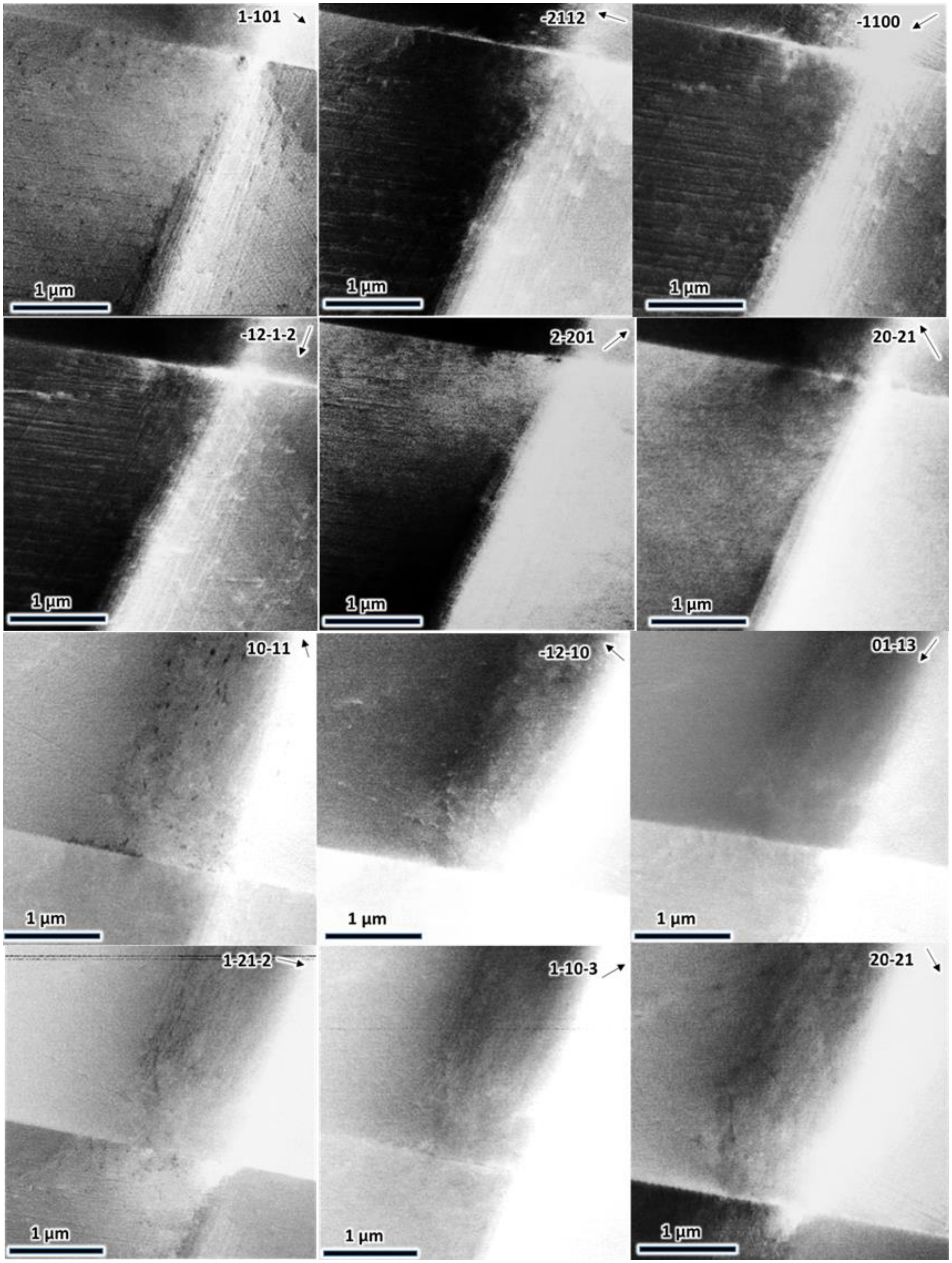

Figure A23 Neighboring grains in Sample 2. First six) Identified dislocations are $(10\bar{1}0)[\bar{1}2\bar{1}0]$ and $(\bar{1}011)[1\bar{2}10]$. Second six) Identified dislocations are $(0\bar{1}10)[2\bar{1}\bar{1}0]$.

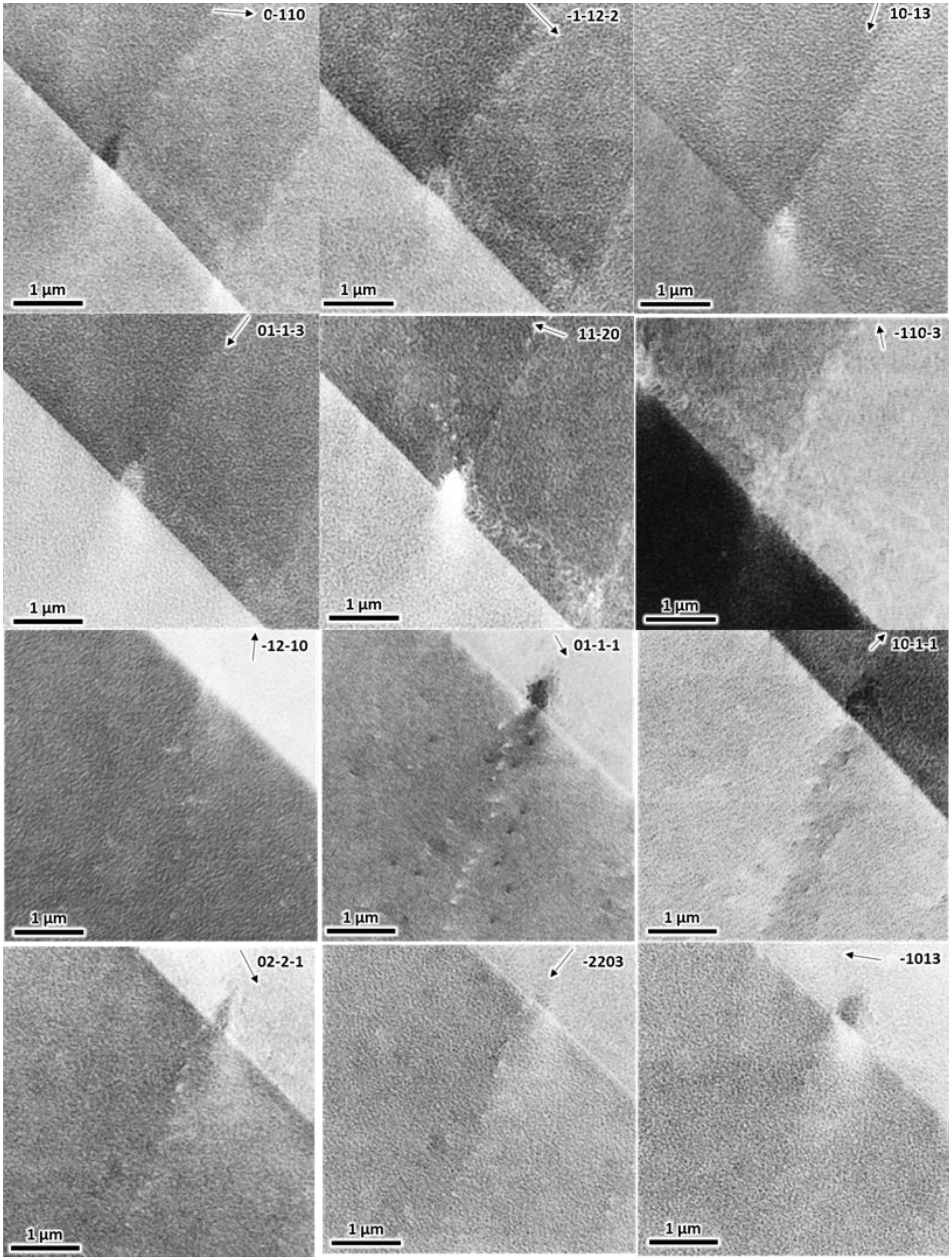

Figure A24 Neighboring grains in Sample 2. First six) Identified dislocations are $(10\bar{1}0)[\bar{1}2\bar{1}0]$ and $(\bar{1}011)[1\bar{2}10]$. Second six) Identified dislocations are $(0001)[\bar{1}\bar{1}20]$.

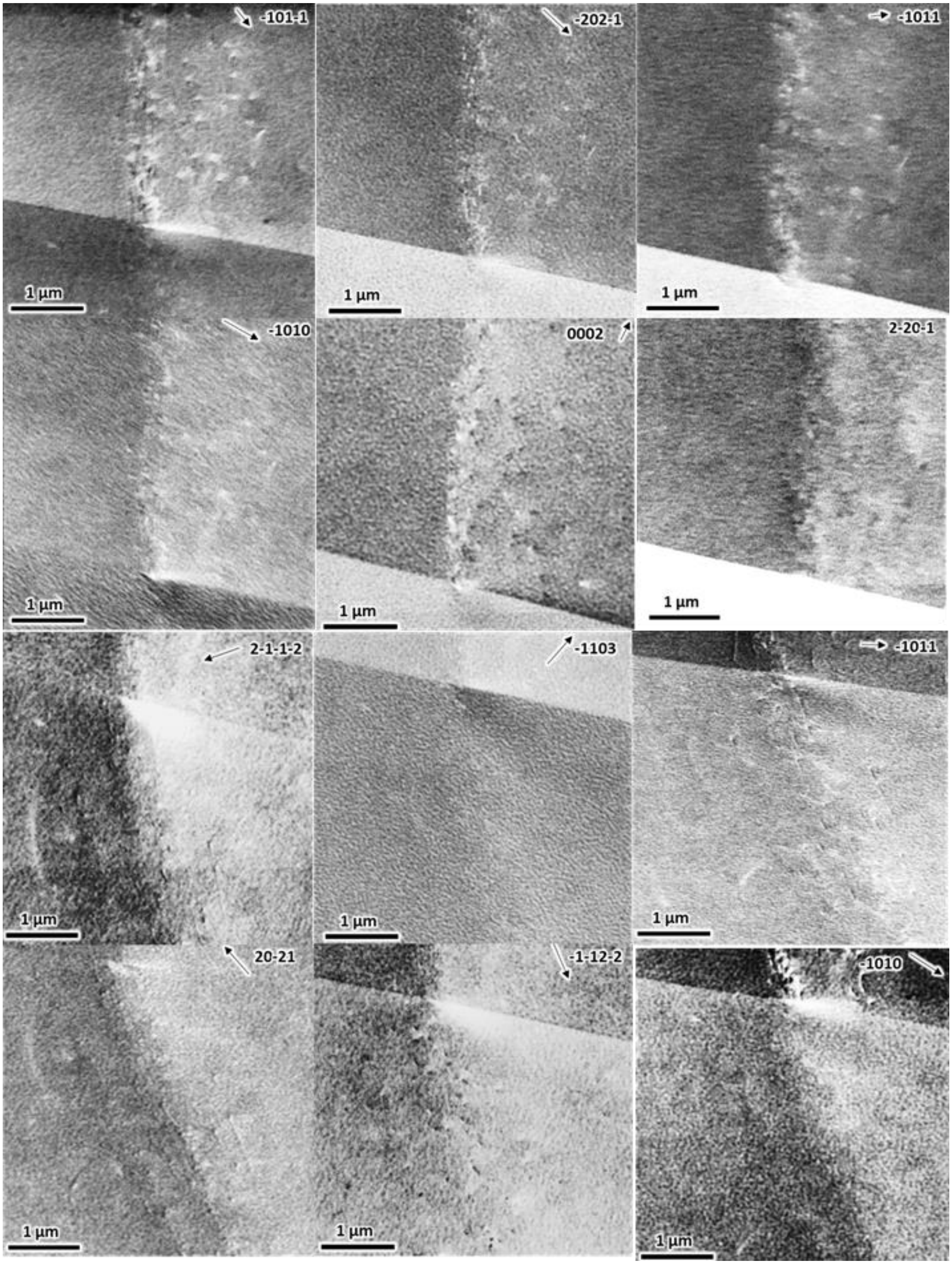

Figure A25 Neighboring grains in Sample 2. First six) Identified dislocations are $(1\bar{1}00)[\bar{1}\bar{1}20]$ and $(1\bar{1}01)[11\bar{2}0]$. Second six) Identified dislocations are $(1\bar{1}00)[\bar{1}\bar{1}20]$.

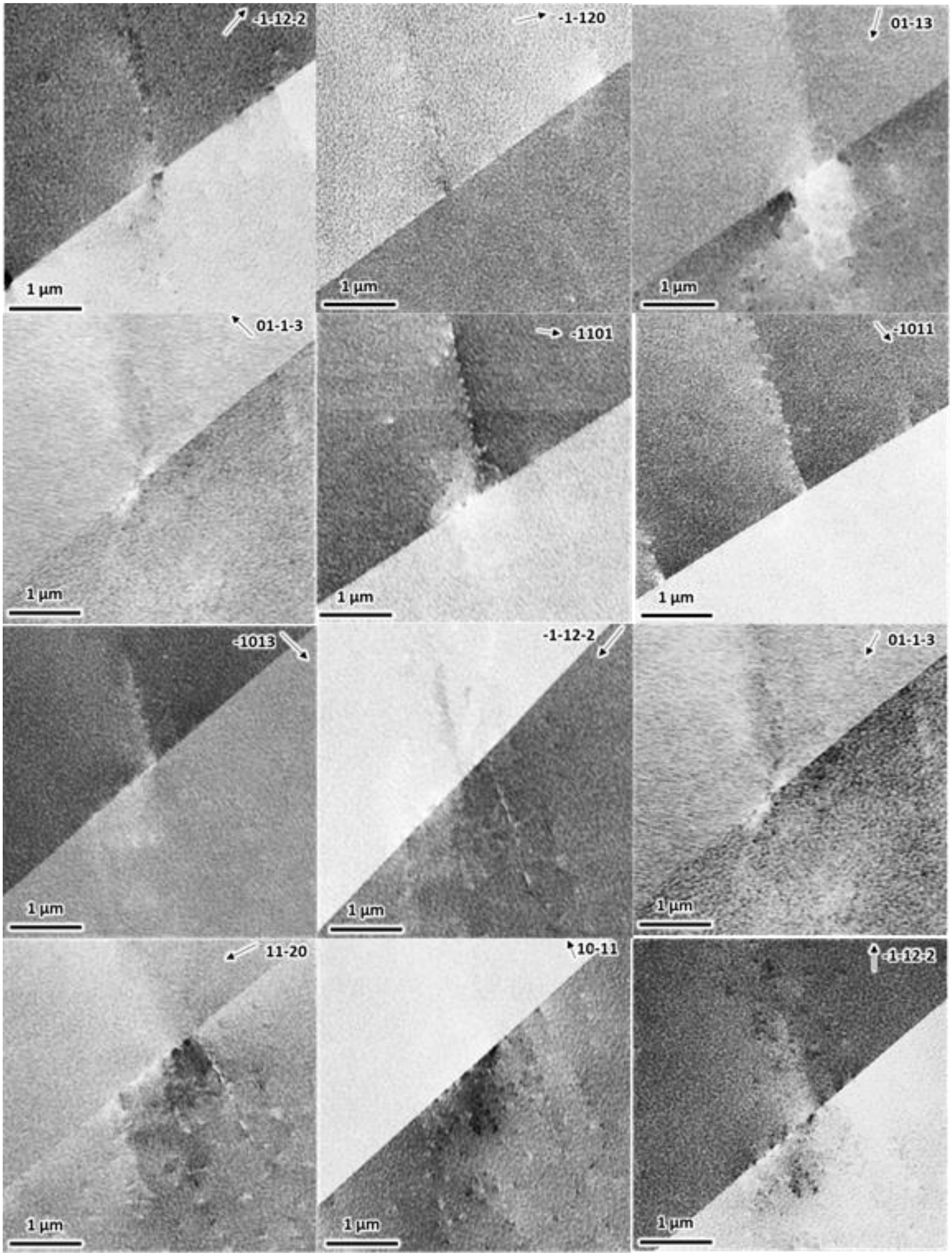

Figure A26 Neighboring grains in Sample 2. First six) Identified dislocations are $(0\bar{1}10)[\bar{2}110]$. Second six) Identified dislocations are $(10\bar{1}0)[\bar{1}2\bar{1}0]$.

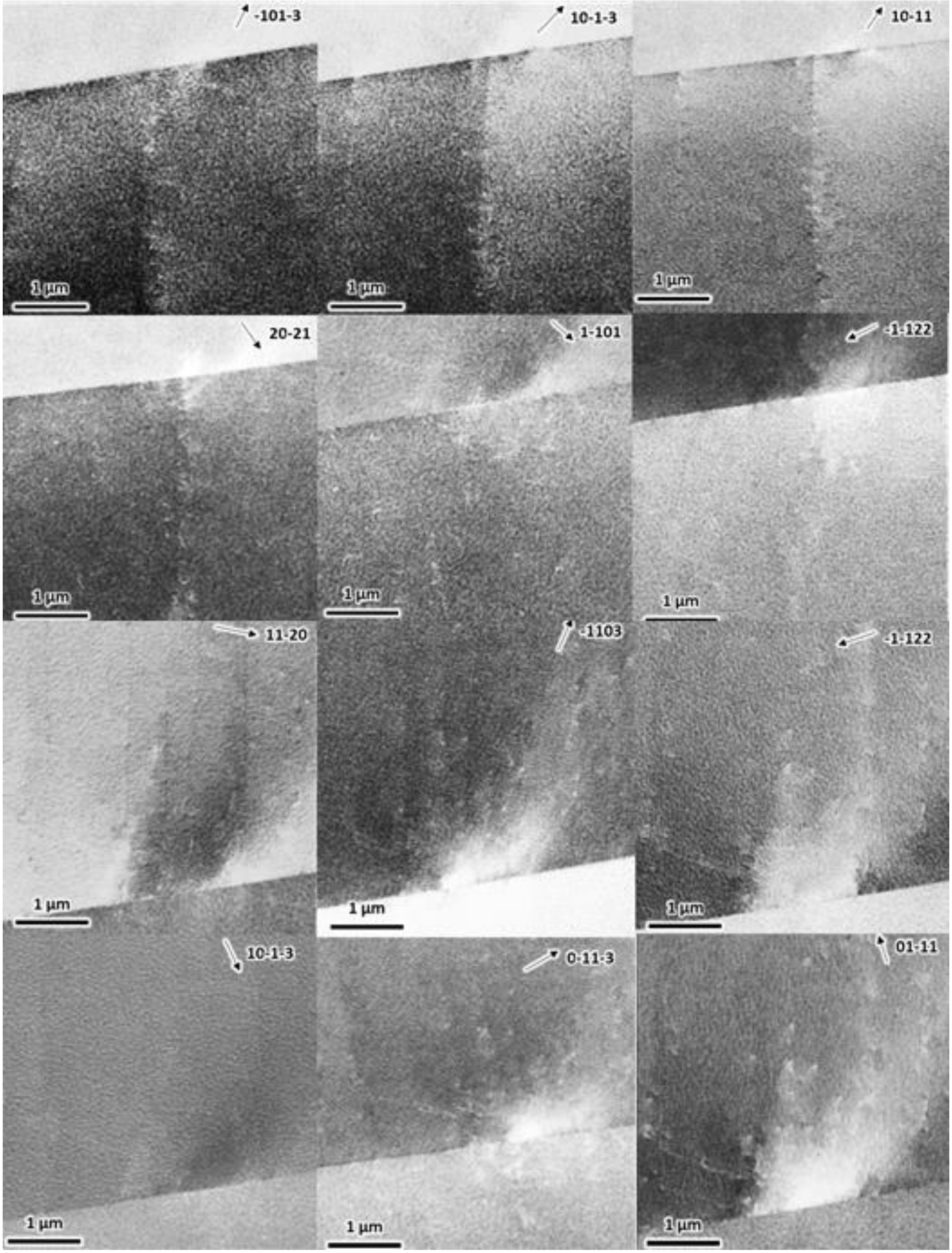

Figure A27 Neighboring grains in Sample 2. First six) Identified dislocations are $(1\bar{1}00)[11\bar{2}0]$. Second six) Identified dislocations are $(10\bar{1}0)[\bar{1}2\bar{1}0]$.

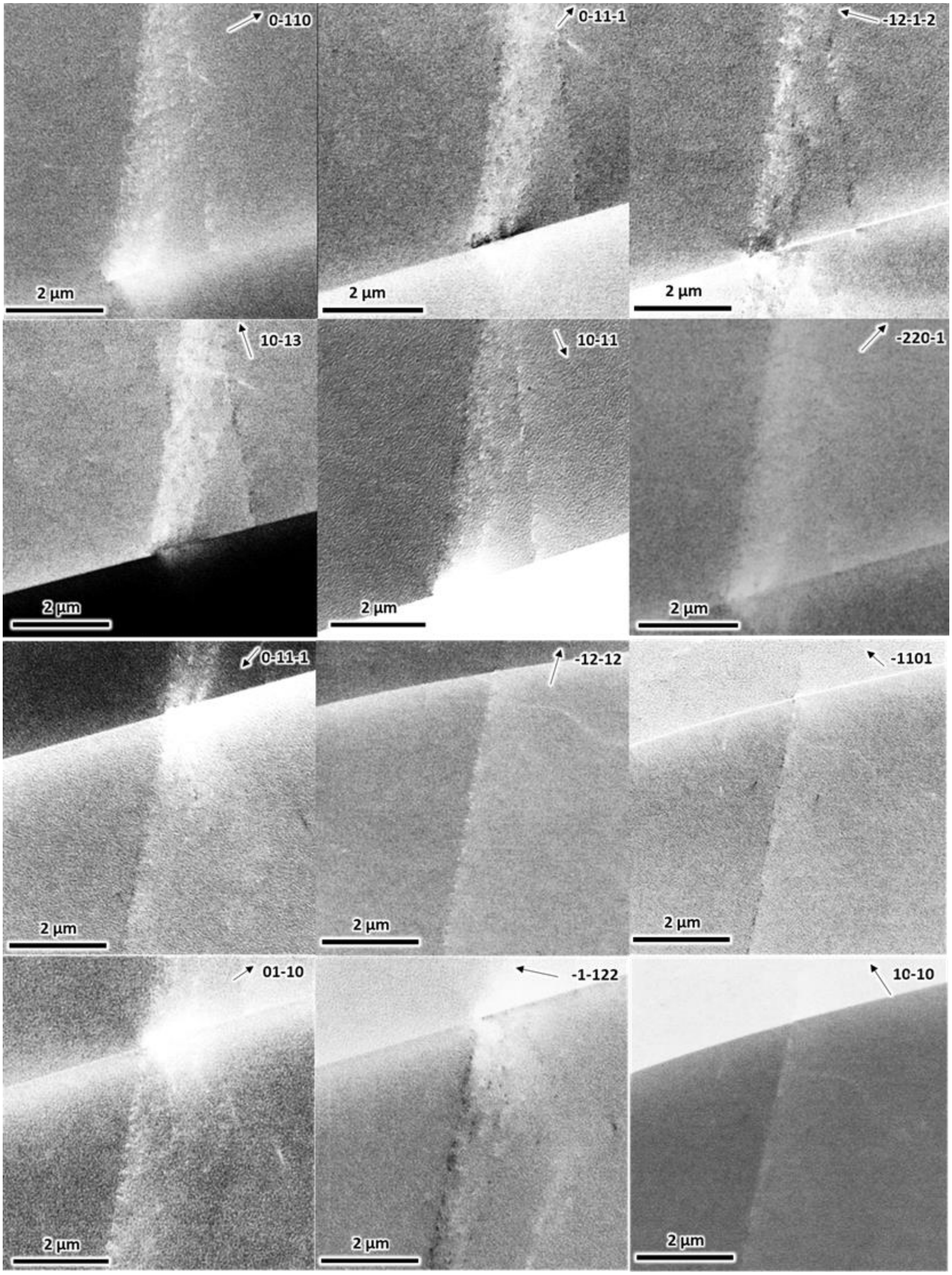

Figure A28 Neighboring grains in Sample 2. First six) Identified dislocations are (1$\bar{1}$00)[11$\bar{2}$0] and(1$\bar{1}$01)[11$\bar{2}$0]. Second six) Identified dislocations are (10$\bar{1}$0)[$\bar{1}$2$\bar{1}$0].

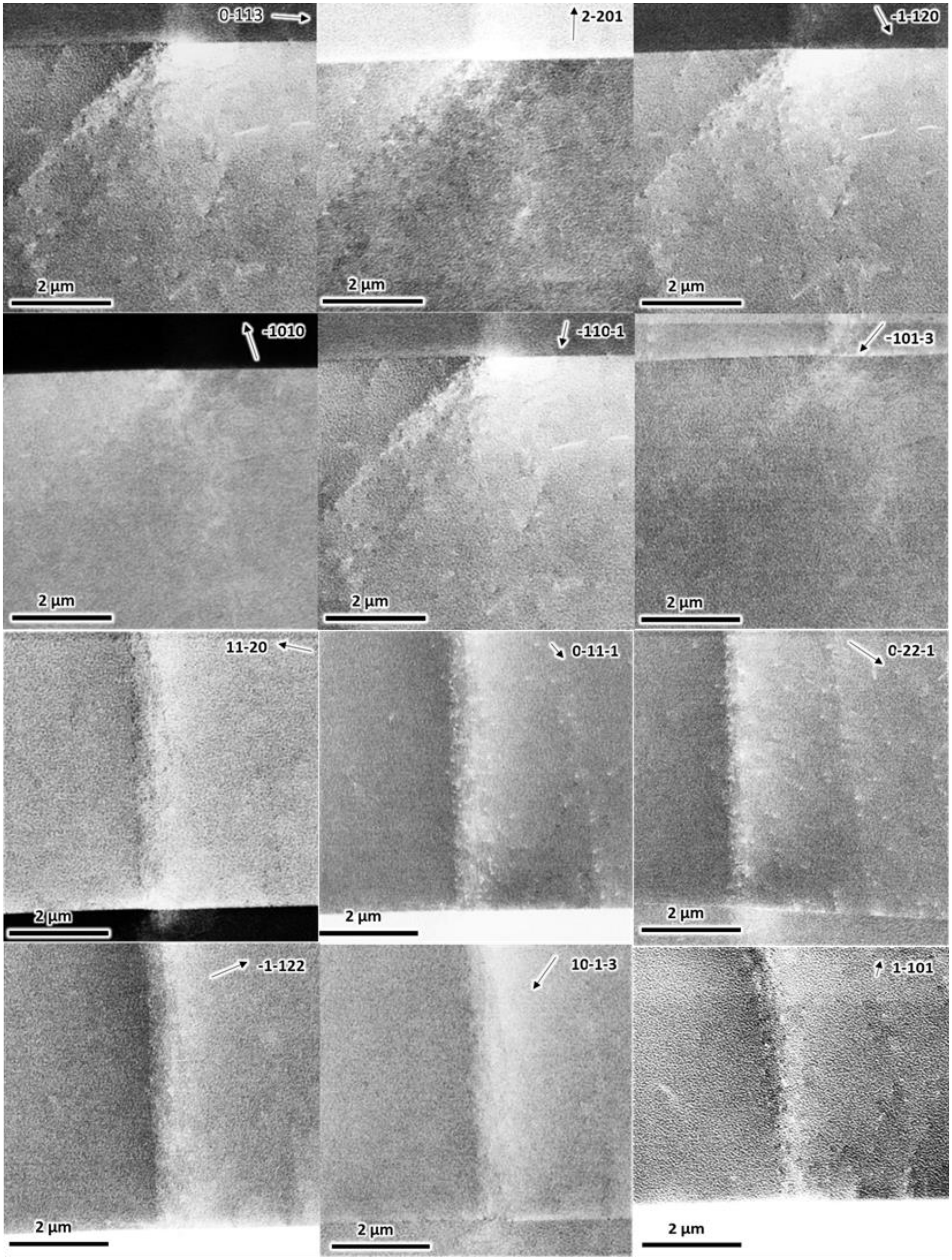

Figure A29 Neighboring grains in Sample 2. First six) Identified dislocations are $(0001)[1\bar{2}10]$ and $(\bar{1}011)[1\bar{2}10]$. Second six) Identified dislocations are $(10\bar{1}0)[\bar{1}2\bar{1}0]$.

APPENDIX G

AFM, slip trace analysis and ECCI of grains 3&5 in sample 1

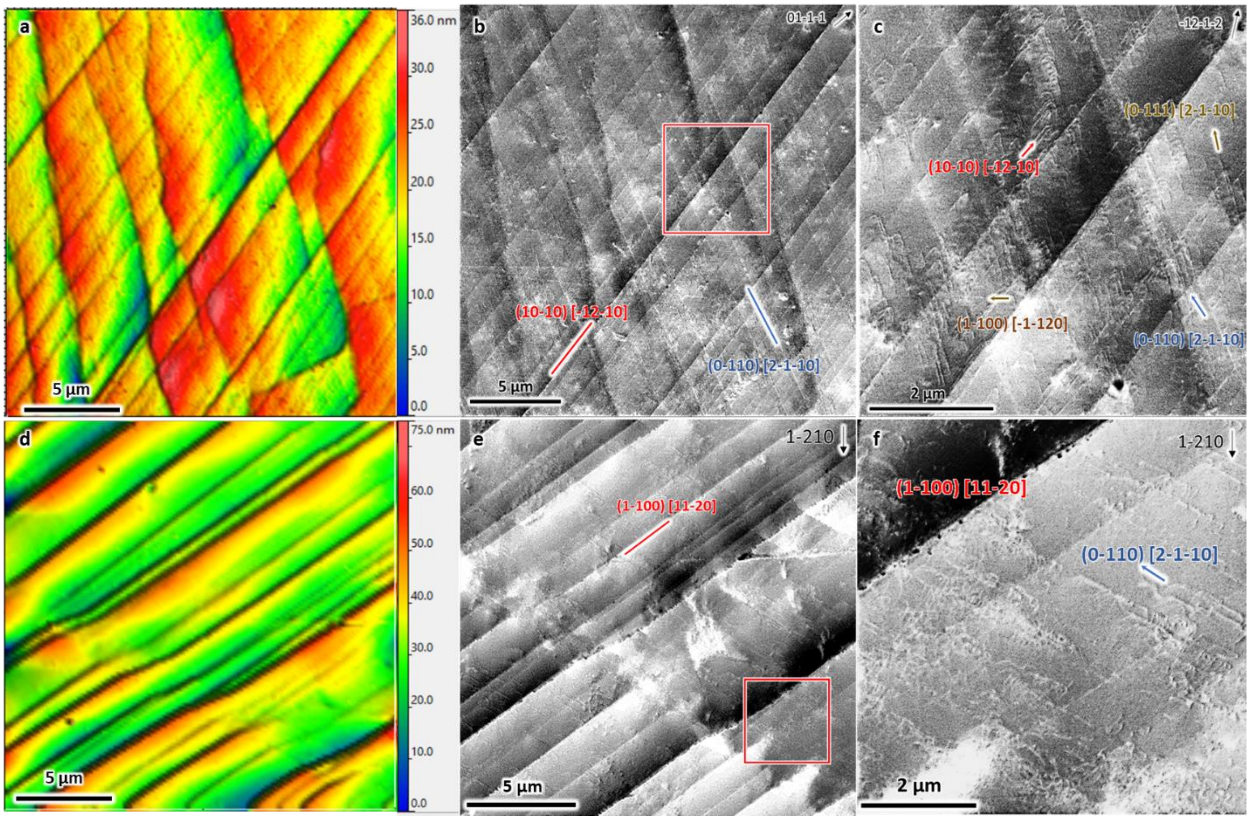

Figure A30a) AFM color-scale topography map of grain 3 in sample 1. b) Slip systems identified by the trace analysis are the $(10\bar{1}0)[\bar{1}2\bar{1}0]$ and $(0\bar{1}10)[2\bar{1}\bar{1}0]$ prism <a> slip systems. c) ECC image of the red box area in b). Contrast analysis also reveals two additional slip systems, which are $(1\bar{1}00)[\bar{1}\bar{1}20]$ prism <a> slip system and the $(0\bar{1}11)[2\bar{1}\bar{1}0]$ pyramidal <a> slip system. The pyramidal <a> dislocations are responsible for the curvy slip traces. d) AFM color-scale topography map of grain 5 in sample 1. e) $(1\bar{1}00)[11\bar{2}0]$ prism <a> slip system is identified by the slip trace analysis. f) ECC images of the red box area in e). Contrast analysis also reveals a significant number of $(0\bar{1}10)[2\bar{1}\bar{1}0]$ prism <a> dislocations within the observed area.

APPENDIX H

Calculation of the geometry of slip systems at a grain boundary

The correlation of **Figures 25 a and b** is used in this section as a particular example to show how 3-D geometry of the slip systems at the grain boundary is revealed. With the 3-D geometry, it is able to characterize the angle ϴ between the intersection lines of slip planes on both sides of the grain boundary with the grain boundary plane. **Figure A31** (left) is a sketch of the geometry of the grain boundary plane and slip planes of the two interacting primary slip systems. The upper right figure is the surface image which is associated with the upper plane in the left sketch, and the lower right figure is corresponding to the subsurface image, which is sketched as the bottom plane to the left figure. In order to correctly correlate the two images, an arbitrary coordinate system is established, with the z direction perpendicular to the surface, x direction pointing down, and y direction pointing right on the surface. The origin O (0, 0, 0) is set to the intersection between the two slip bands at the grain boundary, as shown in the upper right figure. The depth of material removal, d, is the vertical distance between the surface and subsurface. It can be calculated from the electropolishing current and time, and this value can be verified using microindentation removal measurements [96]. The overall electropolished surface is flat and smooth, with d varied between 4.8 and 5.2 µm across the examined area. Thus, values of 4.8, 5.0, and 5.2 µm were used in the calculations to determine the variability of the results.

On the subsurface, the grain boundary trace may not pass through the origin O’ (0, 0, -d). Instead, it will intersect with the X’ and Y’ axes at points A’ and B’. Similarly, the slip traces of the two slip systems also move away from the O’, and intersect with the grain boundary trace at points C’ and D’. It is not necessary to know the exact position of slip traces and grain boundary traces in the subsurface since all the parameters can be calculated during the

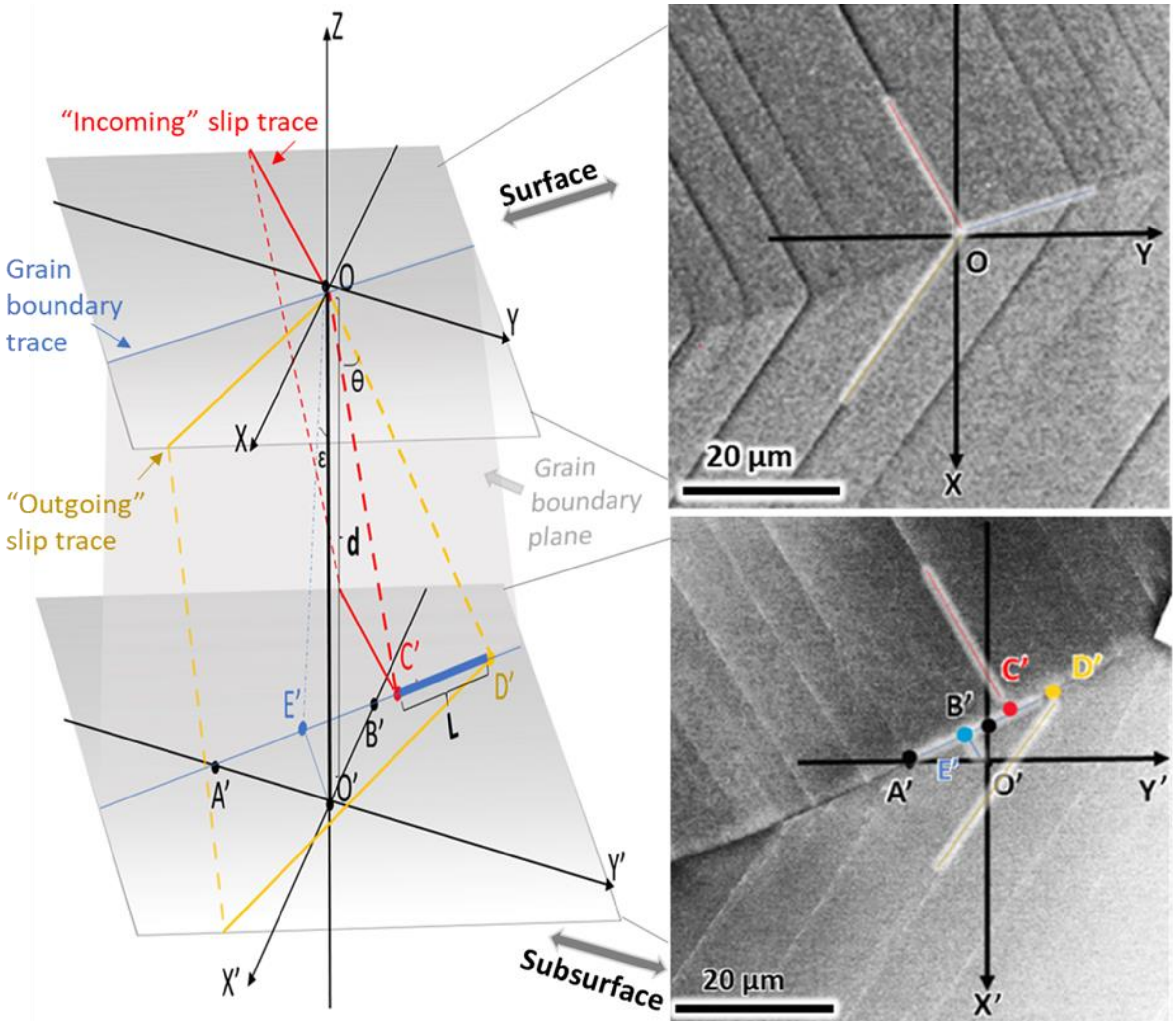

Figure A31 3-D geometry of the well-correlated slip systems at the grain boundary by the correlation of surface and subsurface images. (Amended from [171])

construction of 3-D geometry. However, in this calculation, it is assumed that the each of the slip band is confined within its own slip plane, and there is no height variation on the subsurface at a given d. The calculation of the inclination of the grain boundary plane ε and more importantly, Θ, is carried out as follows:

The grain boundary trace on the electropolished surface can be expressed as a straight line:

$$y = k*x - b \qquad \ldots\ldots 1$$

where k is the slope of the grain boundary trace (assume the trace is close to a straight line). In some cases, the grain boundary line orientation may vary between the as-deformed surface and the electropolished surface. Thus, k is the averaged value between the $k_{surface}$ and $k_{sub\text{-}surface}$ that are measured on each image.

Points A' (0, -b, -d) and B' ($\frac{b}{k}$, 0, -d), are the intersection points of the grain boundary trace with the Y' and X' axes in the subsurface. Points C' (x_1, $k*x_1 - b$, -d) and D' (x_2, $k*x_2 - b$, -d) are the intersections of the slip traces with the grain boundary trace. The L (7 µm) is the offset between C' and D' along the grain boundary trace, and can be calculated by:

$$L = |\overrightarrow{\boldsymbol{C'D'}}| = \sqrt{(x_2 - x_1)^2(1 + k^2)} \quad \text{.........} \quad 2$$

The directions of $\overrightarrow{\boldsymbol{OC'}}$ and $\overrightarrow{\boldsymbol{OD'}}$ are the respective intersections of the incoming (red) and outgoing (yellow) slip planes with the grain boundary plane (**Figure A31** left). These will be perpendicular to the respective slip plane normal, $\mathbf{N_1}$ and $\mathbf{N_2}$, which are readily available from the MATLAB codes based on the crystal orientation information from the EBSD software:

$$\mathbf{N_1} \cdot \overrightarrow{\boldsymbol{OC'}} = 0 \quad \text{.........} \quad 3$$

$$\mathbf{N_2} \cdot \overrightarrow{\boldsymbol{OD'}} = 0 \quad \text{.........} \quad 4$$

Simultaneous solution of equations 1-4 allows determination of $\overrightarrow{\boldsymbol{OC'}}$ and $\overrightarrow{\boldsymbol{OD'}}$. The angle Ɵ between slip plane intersections on the grain boundary plane is then simply expressed as:

$$\Theta = \cos^{-1} (\overrightarrow{\boldsymbol{OC'}} \cdot \overrightarrow{\boldsymbol{OD'}}) \quad \text{.........} \quad 5$$

Once the positions A', B', and O' are established, position E' is defined by the projection O' on to the $\overrightarrow{\boldsymbol{A'B'}}$, and the corresponding grain boundary inclination angle, ε, is given by:

$$\varepsilon = \tan^{-1}\left(\frac{|\overrightarrow{\boldsymbol{O'E'}}|}{d}\right) \quad \text{……} \quad 6$$

The value of Θ reported in this study is Θ_{avg}, which is calculated on the basis of d = 5 µm and $k_{average}$. The true value of Θ has a variation range of ~3° to ~5° since different values of d = 4.8, 5.2 µm and k = $k_{surface}$, $k_{subsurface}$ have been used. The uncertainty can be calculated by:

$$\Theta_{uncertain} = \Theta_{max} - \Theta_{min} \quad \text{……} \quad 7$$

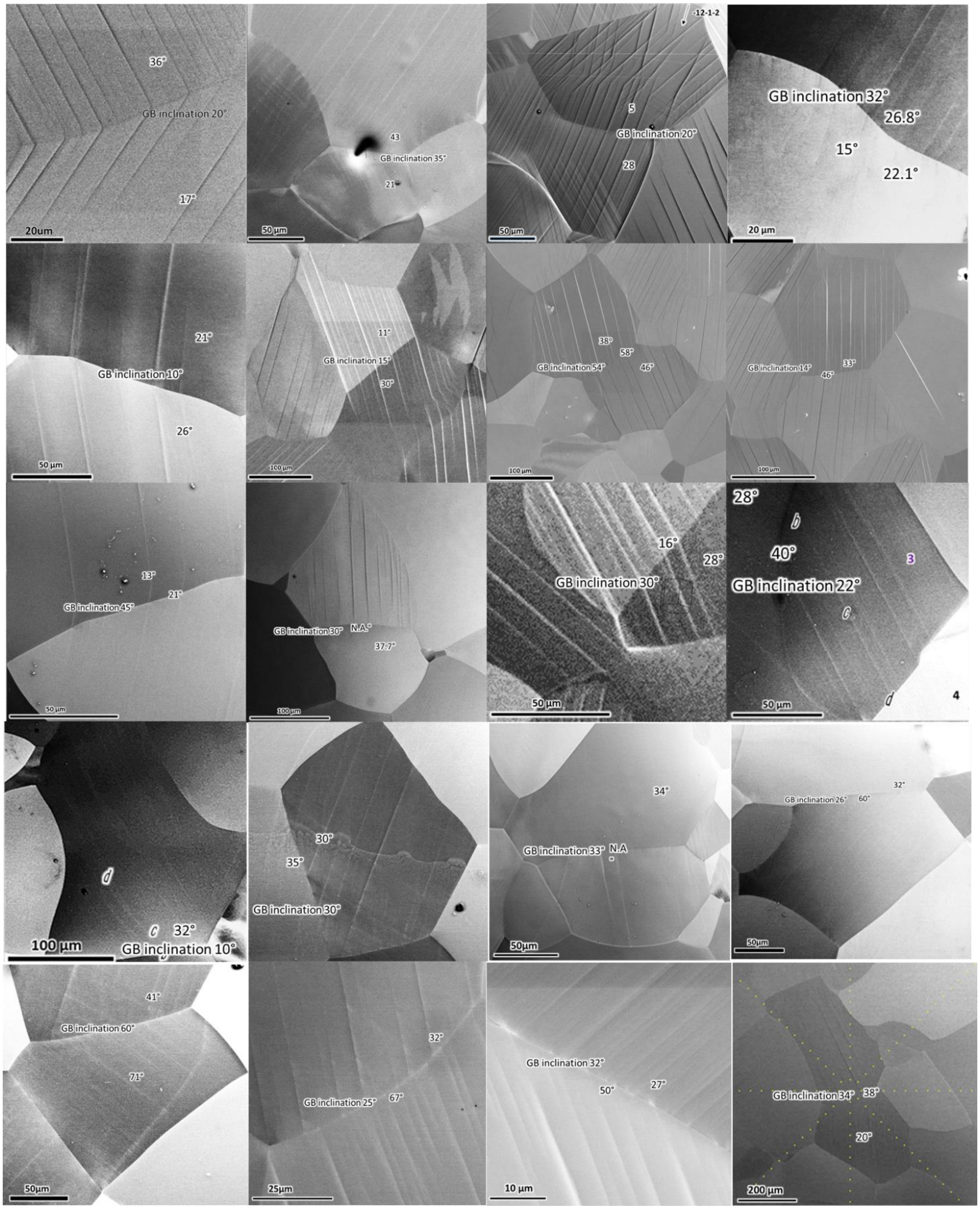

Figure A32 All cases slip interactions at grain boundaries with calculated results.

APPENDIX I

Slip band broadening in grain 3 of sample 3

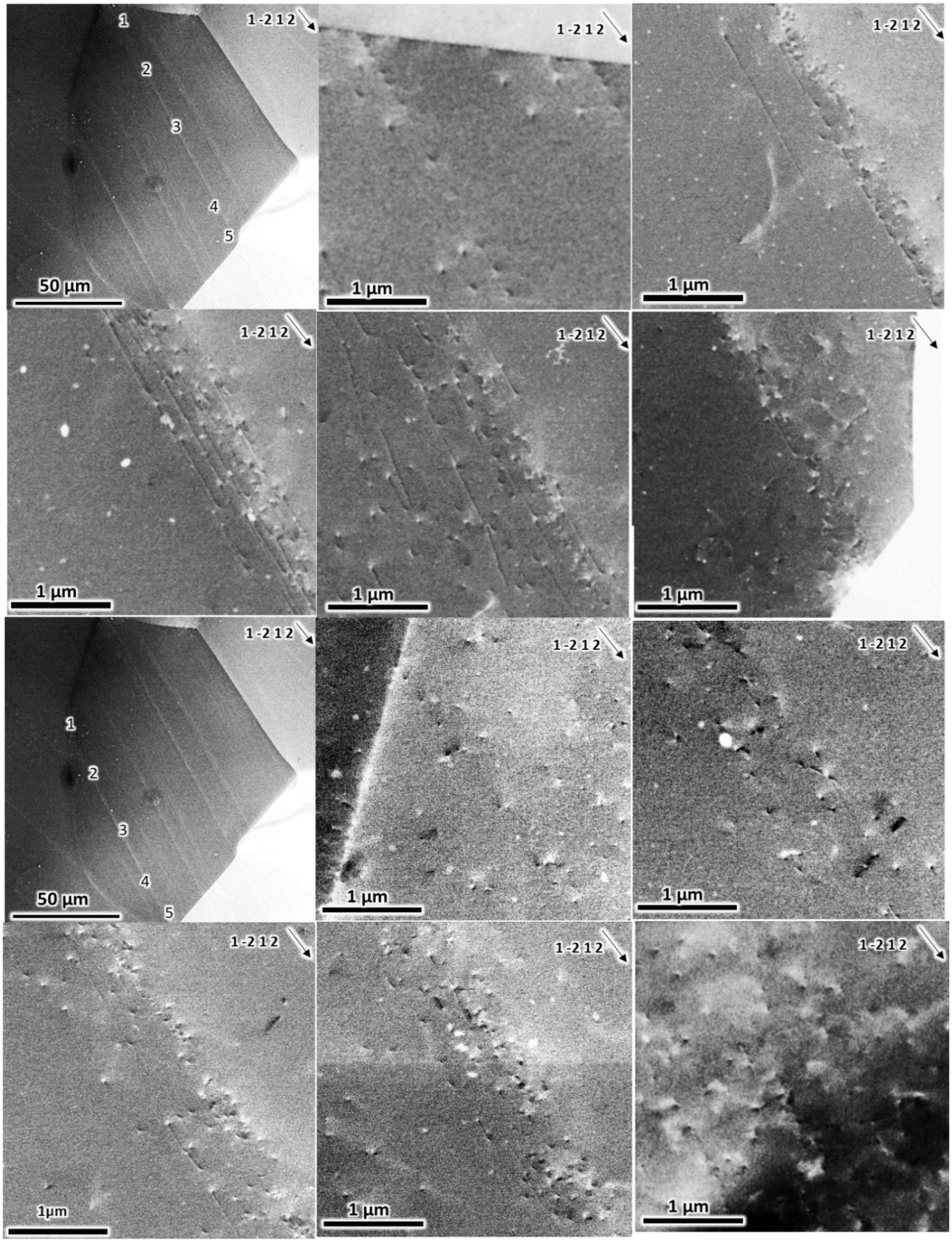

Figure A33 Slip band broadening effect observed along two different slip bands.

BIBLIOGRAPHY

BIBILOGRAPHY

[1] K. Wang, The use of titanium for medical applications in the USA, Material Science and Engineering: A, 213 (1-2), 1996, 134-137, https://doi.org/10.1016/0921-5093(96)10243-4.

[2] C. Leyens, M. Peters, Titanium and titanium alloys: Fundamentals and Applications, Weinheim: Wiley-VCH, 2003, https://doi.org/10.1002/3527602119.

[3] M. Geetha, A. K. Singh, R. Asokamani, A. K. Gogia, Ti based biomaterials, the ultimate choice for orthopaedic implants – A review, Progress in Material Science, 54 (3), 2009, 397-425, https://doi.org/10.1016/j.pmatsci.2008.06.004.

[4] D. Banerjee, J. C. Williams, Perspectives on Titanium Science and Technology, Acta Materialia, 61, 2013, 844-879, https://doi.org/10.1016/j.actamat.2012.10.043.

[5] M. R. Bache, W. J. Evans, Dwell Sensitive Fatigue Response of Titanium Alloys for Power Plant Applications, Journal of Engineering for Gas Turbines and Power, 125 (1), 2003, 241-245, https://doi.org/10.1115/1.1494094.

[6] J. Hirsch, K. Lücke, Overview no. 76: Mechanism of deformation and development of rolling textures in polycrystalline f.c.c. metals—I. Description of rolling texture development in homogeneous CuZn alloys, Acta Metallurgica, 36 (11), 1988, 2863-2882, https://doi.org/10.1016/0001-6160(88)90172-1.

[7] Y. Zhou, J. J. Jonas, J. Savoie, A. Makinde, S. R. MacEwen, Effect of texture on earing in FCC metals: Finite element simulations, International Journal of Plasticity, 14 (1–3), 1998, 117-138, https://doi.org/10.1016/S0749-6419(97)00044-2.

[8] I. Samajdar, P. Ratchev, B. Verlinden, E. Aernoudt, Hot working of AA1050—relating the microstructural and textural developments, Acta Materialia, 49 (10), 2001, 1759-1767, https://doi.org/10.1016/S1359-6454(01)00083-0.

[9] S. Suwas, R. K. Ray, A. K. Singh, S. Bhargava, Evolution of hot rolling textures in a two-phase (α_2+β) Ti_3Al base alloy, Acat Materialia, 47 (18), 1999, 4585-4598, https://doi.org/10.1016/S1359-6454(99)00327-4.

[10] J. D. Picksley, F. R. Hall, I. Pillinger, Metal forming of titanium: Experimentation, microstructure and computer simulation, Journal of Materials Processing Technology, 45 (1-4), 1994, 491-496, https://doi.org/10.1016/0924-0136(94)90387-5.

[11] Y. N. Wang, J. C. Huang, Texture analysis in hexagonal materials, Materials Chemistry and Physics, 81 (1), 2003, 11-26, https://doi.org/10.1016/S0254-0584(03)00168-8.

[12] A. K. Singh, R. A. Schwarzer, Texture and Anisotropy of Mechanical Properties in Titanium and Its Alloys, Zeitschrift für Metallkunde/Materials Research and Advanced Techniques, 91(9), 2000, 702-716.

[13] H. Conrad, Effect of interstitial solutes on the strength and ductility of titanium, Progress in Material Science, 26 (2-4), 1981, 123-403, https://doi.org/10.1016/0079-6425(81)90001-3.

[14] M. Ghazisaeidi, D. R. Trinkle, Interaction of oxygen interstitials with lattice faults in Ti, Acta Materialia, 76 (1), 2014, 82-86, https://doi.org/10.1016/j.actamat.2014.05.025.

[15] G. I. Taylor, Plastic strain in metals, Journal of the Institute of Metals, 62, 1938, 307–324, http://pajarito.materials.cmu.edu/rollett/27750/Taylor_1938.pdf.

[16] P. V. Houtte, On the equivalence of the relaxed Taylor theory and the Bishop-Hill theory for partially constrained plastic deformation of crystals, Materials Science and Engineering, 55 (1), 1982, 69-77, https://doi.org/10.1016/0025-5416(82)90085-4.

[17] Lei Bao, Contribution to the study of deformation twinning in titanium, Other, Université Paul Verlaine - Metz, 2011, English, NNT: 2011METZ014Sff. fftel-01749050ff

[18] C. Zambaldi, Y. Yang, T. R. Bieler, Orientation informed nanoindentation of a-titanium: Indentation pileup in hexagonal metals deforming by prismatic slip, Journal of Materials Research, 27 (1), 2011, 356-367, https://doi.org/10.1557/jmr.2011.334.

[19] P. G. Partridge, The crystallography and deformation modes of hexagonal close-packed metals, Metallurgical Reviews, 12 (1), 1967, 169-194, https://doi.org/10.1179/mtlr.1967.12.1.169.

[20] H. Numakura, M. Koiwa, Dislocations in metals and alloys with the hexagonal close-packed structure, Metallurgical Science and Technology, 16 (1), 1998.

[21] M. P. Biget, G. Saada, Low-temperature plasticity of high-purity α-titanium single crystals, Philosophical Magazine A, 59 (4), 1989, 747-757, https://doi.org/10.1080/01418618908209818.

[22] S. Naka, A. Lasalmonie, P. Costa, P. Kubin, L. P. Kubin, The low-temperature plastic deformation of α-titanium and the core structure of a-type screw dislocations, Philosophical Magazine A, 57 (5), 1988, 717-740, https://doi.org/10.1080/01418618808209916.

[23] S. Naka, L. P. Kubin, C. Perrier, The plasticity of titanium at low and medium temperatures, Philosophical Magazine A, 63 (5), 1991, 1035-1043, https://doi.org/10.1080/01418619108213935.

[24] F. Bridier, P. Villechaise, J. Mendez, Analysis of the different slip systems activated by tension in a α/β titanium alloy in relation with local crystallographic orientation, Acta Materialia, 53 (3), 2005, 555-567, https://doi.org/10.1016/j.actamat.2004.09.040.

[25] J. C. Williams, R. G. Baggerly, N. E. Paton, Deformation behavior of HCP Ti-Al alloy single crystals, Metallurgical and Materials Transactions A, 33, 2002, 837-850, https://doi.org/10.1007/s11661-002-0153-y.

[26] W. Hutchinson, M. Barnett, Effective values of critical resolved shear stress for slip in polycrystalline magnesium and other hcp metals, Scripta Materialia, 63 (7), 2010, 737-740, https://doi.org/10.1016/j.scriptamat.2010.05.047.

[27] B. Barkia, V. Doquet, J. Couzinié, I. Guillot, E. Héripré, In situ monitoring of the deformation mechanisms in titanium with different oxygen contents, Materials Science and Engineering: A, 636 (11), 2015, 91–102, https://doi.org/10.1016/j.msea.2015.03.044.

[28] H. Li, D. E. Mason, T. R. Bieler, C. J. Boehlert, M. A. Crimp, Methodology for estimating the critical resolved shear stress ratios of α-phase Ti using EBSD-based trace analysis, Acta Materialia, 61 (20), 2013, 7555–7567, https://doi.org/10.1016/j.actamat.2013.08.042.

[29] J. Gong, A. J. Wilkinson, Micro-cantilever testing of <a> prismatic slip in commercially pure Ti, Philosophical Magazine, 91 (7–9), 2011, 1137–1149, https://doi.org/10.1080/14786435.2010.495359.

[30] S. Zaefferer, A study of active deformation systems in titanium alloys: dependence on alloy composition and correlation with deformation texture, Materials Science and Engineering: A, 344 (1-2), 2003, 20-30, https://doi.org/10.1016/S0921-5093(02)00421-5.

[31] A. Poty, J. M. Raulot, H. Xu, J. Bai, C. Schuman, J.-S. Lecomte, M.-J. Philippe, C. Esling, Classification of the critical resolved shear stress in the hexagonalclose-packed materials by atomic simulation: application to α-zirconium and α-titanium, Journal of Applied Physics, 110 (1), 2011, 014905, https://doi.org/10.1063/1.3599870.

[32] J. Gong, A. J. Wilkinson, A microcantilever investigation of size effect, solid solution strengthening and second-phase strengthening for <a> prism slip in α-Ti, Acta Materialia, 59, 2011, 5970–5981, https://doi.org/10.1016/j.actamat.2011.06.005.

[33] K. E. K. Amouzou, T. Richeton, A. Roth, M. A. Lebyodkin, T. A. Lebedkina, Micromechanical modeling of hardening mechanisms in commercially pure α-titanium in tensile condition, International Journal of Plasticity, 80, 2016, 222-240, https://doi.org/10.1016/j.ijplas.2015.09.008.

[34] N. Benmhenni, S. Bouvier, R. Brenner, T. Chauveau, B. Bacroix, "Micromechanical modelling of monotonic loading of CP a-Ti: Correlation between macroscopic and microscopic behavior", Materials Science and Engineering: A -Struct, 573, 2013, 222–233, https://doi.org/10.1016/j.msea.2013.02.022.

[35] J. Kacher, I. M. Robertson, In situ and tomographic analysis of dislocation/grain boundary interactions in α-titanium, Philosophical Magazine. 94, 2014, 814-829, https://doi.org/10.1080/14786435.2013.868942.

[36] J. L. W. Warwick, N. G. Jones, K. M. Rahman, D. Dye, Lattice strain evolution during tensile and compressive loading of CP Ti, Acta Materialia, 60 (19), 2012, 6720-6731, https://doi.org/10.1016/j.actamat.2012.08.042.

[37] D. Gloaguen, G. Oum, V. Legrand, J. Fajoui, S. Branchu, Experimental and theoretical studies of intergranular strain in an alpha titanium alloy during plastic deformation, Acta Materialia, 61 (15), 2013, 5779-5790, https://doi.org/10.1016/j.actamat.2013.06.022.

[38] A. Chakraborty, C. Zhang, S. Balachandran, T. R. Bieler, P. Eisenlohr, Assessment of surface and bulk-dominated methodologies to measure critical resolved shear stresses in hexagonal materials, Acta Materialia, 184 (1), 2020, 241-253, https://doi.org/10.1016/j.actamat.2019.11.023.

[39] R. V. Mises, Mechanik der festen Körper im plastisch deformablen Zustand, Göttin. Nachvodeg Mathematics, 1913, 582-592, http://www.digizeitschriften.de/dms/resolveppn/?PID=GDZPPN002503697.

[40] R. A. Lebensohn, C. N. Tomé, A self-consistent anisotropic approach for the simulation of plastic deformation and texture development of polycrystals: Application to zirconium alloys, Acta Metallurgica, 41 (9), 1993, 2611-2624, https://doi.org/10.1016/0956-7151(93)90130-K.

[41] I. Karaman, H. Sehitoglu, A. J. Beaudoin, Y. I. Chumlyakov, H. J. Maier, C. N. Tomé, Modeling the deformation behavior of Hadfield steel single and polycrystals due to twinning and slip, Acta Materialia, 48 (9), 2000, 2031-2047, https://doi.org/10.1016/S1359-6454(00)00051-3.

[42] M. J. Philippe, M. Serghat, P. V. Houtte, C. Esling, Modelling of texture evolution for materials of hexagonal symmetry—II. application to zirconium and titanium α or near α alloys, Acta Metallurgica, 43 (4), 1995, 1619-1630, https://doi.org/10.1016/0956-7151(94)00329-G.

[43] Y. Yang, L. Wang, C. Zambaldi, P. Eisenlohr, R. Barabash, W. Liu, M. R. Stoudt, M. A. Crimp, T. R. Bieler, Characterization and modeling of heterogeneous deformation in commercial purity titanium, The Journal of The Minerals, Metals & Materials Society (TMS), 63 (9), 2011, 66-73, https://doi.org/10.1007/s11837-011-0161-8.

[44] Y. Yang, L. Wang, T. R. Bieler, P. Eisenlohr, M. A. Crimp, Quantitative atomic force microscopy characterization and crystal plasticity finite element modeling of heterogeneous deformation in commercial purity titanium, Metallurgical and Materials Transactions A, 42, 2011, 636-644, https://doi.org/10.1007/s11661-010-0475-0.

[45] T. R. Bieler, M. A. Crimp, L. Yang, L. Wang, P. Eisenlohr, D. E. Mason, W. Liu, G. E. Ice, Strain heterogeneity and damage nucleation at grain boundaries during monotonic deformation in commercial purity titanium, Journal of The Minerals, Metals & Materials Society (TMS), 61 (12), 2011, 45-52, https://doi.org/10.1007/s11837-009-0180-x.

[46] T. R. Bieler, P. Eisenlohr, F. Roters, D. Kumar, D. E. Mason, M. A. Crimp, D. a, The role of heterogeneous deformation on damage nucleation at grain boundaries in single phase metals, International Journal of Plasticity, 25 (9), 2009, 1655-1683, https://doi.org/10.1016/j.ijplas.2008.09.002.

[47] F. C. Frank, The Frank- Read source, Proceedings of the Royal Society A, 371 (1744), 1980, 136-138, https://doi.org/10.1098/rspa.1980.0069.

[48] F. C. Frank, W. T. Read Jr., Multiplication Processes for Slow Moving Dislocations, Physical Review, 79 (4), 1950, 722-723, https://doi.org/10.1103/PhysRev.79.722.

[49] (a) E. O. Hall, The deformation and ageing of mild steel: III discussion of results, Proceedings of the Physical Society. Section B, 64 (9), 1951, 747-753, https://doi.org/10.1088/0370-1301/64/9/303. (b) N. J. Petch, The cleavage strength of polycrystals, The Journal of the Iron and Steel Institute, 173 (5), 1953, 25–28.

[50] V. Doquet, B. Barkia, Combined AFM, SEM and crystal plasticity analysis of grain boundary sliding in titanium at room temperature, Mechanics of Materials, 103, 2016, 18-27, https://doi.org/10.1016/j.mechmat.2016.09.001.

[51] T. Matsunaga, T. Kameyama, S. Ueda, E. Sato, Grain boundary sliding during ambient-temperature creep in hexagonal close-packed metals, Philosophical Magazine, 90 (30), 2010, 4041-4054, https://doi.org/10.1080/14786435.2010.502883.

[52] M. W. Grabski, R. Korski, Grain boundaries as sinks for dislocations, The Philosophical Magazine: A Journal of Theoretical Experimental and Applied Physics, 22 (178), 1970, 707-715, https://doi.org/10.1080/14786437008220941.

[53] H. Gleiter, Grain boundaries as point defect sources or sinks—Diffusional creep, Acta Metallurgica, 27 (2), 1979, 187-192, https://doi.org/10.1016/0001-6160(79)90095-6.

[54] A. Sarce, E. J. Savino, Grain Boundary Sink Strength in Anisotropic Materials, Physica Status Solidi b, 159 (2), 1990, 557- 570, https://doi.org/10.1002/pssb.2221590205.

[55] B. P. Uberuaga, L. J. Vernon, E. Martinez, A. F. Voter, The relationship between grain boundary structure, defect mobility and grain boundary sink efficiency, Scientific Reports, 5, 2015, 9095, https://doi.org/10.1038/srep09095.

[56] C. Goux, Structure des joints de grains: considérations cristallographiques et méthodes de calcul des structures, The Canadian Journal of Metallurgy and Materials Science, 13 (1), 1974, 9-31, https://doi.org/10.1179/cmq.1974.13.1.9.

[57] M. A. Fortes, Tilt and Twist Boundaries, Acta Crystallographica A, 29, 1973, 68-70, https://doi.org/10.1107/S0567739473000148.

[58] M. A. Tschopp, S. P. Coleman, D. L. McDowell, Symmetric and asymmetric tilt grain boundary structure and energy in Cu and Al (and transferability to other fcc metals), Integrating Materials and Manufacturing Innovation, 4, 2015, 176-189, https://doi.org/10.1186/s40192-015-0040-1.

[59] R. C. Pond, D. A. Smith,V. Vitek, A model for grain boundary structure based on random close packing, Scripta Metallurgica, 12 (8), 1978, 699-702, https://doi.org/10.1016/0036-9748(78)90311-3.

[60] D. Smith, V. Vitek, R. Pond, Computer simulation of symmetrical high angle boundaries in aluminium, Acta Metallurgica, 25 (5), 1977, 475-483, https://doi.org/10.1016/0001-6160(77)90187-0.

[61] K. L. Merkle, D. Wolf, Low-energy configurations of symmetric and asymmetric tilt grain boundaries, Philosophical Magazine A, 65 (2), 1992, 513-530, https://doi.org/10.1080/01418619208201536.

[62] M. D. Sangid, T. Ezaz, H. Sehitoglu, I. M. Robertson, Energy of slip transmission and nucleation at grain boundaries, Acta Materialia, 59 (1), 2011, 283-296, https://doi.org/10.1016/j.actamat.2010.09.032

[63] R. J. Kurtz, R. G. Hoagland, J. P. Hirth, Computer simulation of extrinsic grain-boundary defects in the $\sum 11$, 〈101〉 {131} symmetric tilt boundary, Philosophical Magazine A, 79 (3), 1999, 683-703, https://doi.org/10.1080/01418619908210325.

[64] A. P. Sutton, V. Vitek, On the structure of tilt grain boundaries in cubic metals I. Symmetrical tilt boundaries, Philosophical Transactions of the Royal Society of London, Series A: Mathematical, Physical and Engineering Sciences, 309 (1506), 1983, 1-68, https://doi.org/10.1098/rsta.1983.0020.

[65] H. Grimmer, W. Bollmann, D. H. Warrington, Coincidence-site lattices and complete pattern-shift in cubic crystals, Acta Crystallographica Section A, 30 (2), 1974, 197-207, https://doi.org/10.1107/S056773947400043X.

[66] V. Thaveepringsriporn, G. S. Was, The role of CSL boundaries in creep of Ni-16Cr-9Fe at 360°C, Metallurgical and Materials Transactions A, 28, 1997, 2101-2112, https://doi.org/10.1007/s11661-997-0167-6.

[67] V. Y. Gertsman, S. M. Bruemmer, Study of grain boundary character along intergranular stress corrosion crack paths in austenitic alloys, Acta Materialia, 49 (9), 2001, 1589-1598, https://doi.org/10.1016/S1359-6454(01)00064-7.

[68] K. Glowinski, A. Morawiec, Twist, tilt, and symmetric grain boundaries in hexagonal materials, journal of Materials Science, 49, 2014, 3936- 3942, https://doi.org/10.1007/s10853-013-7958-5.

[69] P. Delavignette, T. Karakostas, G. Nouet, F. W. Schapink, Grain Boundary Orientation Determination in Transmission Electron Microscopy, physica status solidi A, 107 (2), 1988, 551-558, https://doi.org/10.1002/pssa.2211070209.

[70] M. A. Tschopp, D. L. McDowell, Dislocation nucleation in Σ3 asymmetric tilt grain boundaries, International Journal of Plasticity, 24 (2), 2008, 191-217, https://doi.org/10.1016/j.ijplas.2007.02.010.

[71] E. Bayerschen, A. T. McBride, B. D. Reddy, T. Boehlke, Review on slip transmission criteria in experiments and crystal plasticity models, Journal of Materials Science, 51, 2016, 2243-2258, https://doi.org/10.1007/s10853-015-9553-4.

[72] L. Priester, Grain Boundaries: From theory to engineering, Springer Series in Materials Science, 2013, ISBN 978-94-007-4969-6

[73] S. Zaefferer, J. -C. Kuo, Z. Zhao, M. Winning, D. Raabe, On the influence of the grain boundary misorientation on the plastic deformation of aluminum bicrystals, Acta Materialia, 51 (16), 2003, 4719-4735, https://doi.org/10.1016/S1359-6454(03)00259-3.

[74] T. R. Bieler, P. Eisenlohr, C. Zhang, H. J. Phukan, M. A. Crimp, Grain boundaries and interfaces in slip transfer, Current Opinion in Solid State and Materials Science, 18 (4), 2014, 212-226, https://doi.org/10.1016/j.cossms.2014.05.003.

[75] Y. Guo, T. B. Britton, A. J. Wilkinson, Slip band–grain boundary interactions in commercial-purity titanium, Acta Materialia, 76 (1), 2014, 1-12, https://doi.org/10.1016/j.actamat.2014.05.015.

[76] Z. Li, C. Hou, M. Huang, C. Ouyang, Strengthening mechanism in micro-polycrystals with penetrable grain boundaries by discrete dislocation dynamics simulation and Hall–Petch effect, Computational Materials Science, 46 (4), 2009, 1124-1134, https://doi.org/10.1016/j.commatsci.2009.05.021.

[77] Z. Shen, R. H. Wagoner, W. A. T. Clark, Dislocation and grain boundary interactions in metals, Acta Metallurgica, 36, 1988, 3231-3242, https://doi.org/10.1016/0001-6160(88)90058-2.

[78] S. Kondo, T. Mitsuma, N. Shibata, Y. Ikuhara, Direct observation of individual dislocation interaction processes with grain boundaries, Science Advances, 2, 2016, e1501926, https://doi.org/10.1126/sciadv.1501926.

[79] D. E. Spearot, M. D. Sangid, Insights on slip transmission at grain boundaries from atomistic simulations, Current Opinion in Solid State and Materials Science, 18 (4), 2014, 188-195, https://doi.org/10.1016/j.cossms.2014.04.001.

[80] J. D. Livingston, B. Chalmers, Multiple slip in bicrystal deformation, Acta Metallurgica. 5, 1957, 322– 327, http://dx.doi.org/10.1016/0001-6160(57)90044-5.

[81] Z. Shen, R. H. Wagoner, W. A. T. Clark, Dislocation pile-up at grain boundary interactions in 304 stainless steel, Scripta Materialia. 20, 1986, 921–926, https://doi.org/10.1016/0036-9748(86)90467-9.

[82] Z. Shen, R. H. Wagoner, W. A. T. Clark, Dislocation and grain boundary interactions in metals, Acta Metallurgica, 36, 1988, 3231-3242, https://doi.org/10.1016/0001-6160(88)90058-2.

[83] T. C. Lee, I. M. Robertson, H. K. Birnbaum, Prediction of slip transfer mechanisms across grain boundaries, Scripta Materialia. 23, 1989, 799–80, https://doi.org/10.1016/0036-9748(89)90534-6.

[84] T. C. Lee, I. M. Robertson, H. K. Birnbaum, TEM in situ deformation study of the interaction of lattice dislocations with grain boundaries in metals, Philosophical Magazine A. 62, 1990, 131–153, http://dx.doi.org/10.1080/01418619008244340.

[85] T. C. Lee, I. M. Robertson, H. K. Birnbaum, An in situ transmission electron microscope deformation study of the slip transfer mechanisms in metals, Metallurgical Transactions A, 21, 1990, 2437-2447, https://doi.org/10.1007/BF02646988.

[86] T. C. Lee, I. M. Robertson, H. K. Birnbaum, Anomalous slip in an FCC system, Ultramicroscopy, 29 (1-4), 1989, 212-216, https://doi.org/10.1016/0304-3991(89)90248-9.

[87] W. A. T. Clark, R. H. Wagoner, Z. Y. Shen, T. C. Lee, I. M. Robertson, H. K. Birnbaum, On the criteria for slip transmission across interfaces in polycrystals, Scripta Metallurgica, 26, 1992, 203-206, https://doi.org/10.1016/0956-716X(92)90173-C.

[88] R. S. Davis, R. L. Fleischer, J. D. Livingston, B. Chalmers, Effect of orientation on the plastic deformation of aluminum single crystals and bicrystals, The Journal of The Minerals, Metals & Materials Society, 9, 1957, 136-140, https://doi.org/10.1007/BF03398471.

[89] R. C. Pond, W. A. T. Clark, R. H. Wagoner, On the crystallography of slip transmission in hexagonal metals, Scripta Metallurgica, 20 (9), 1986, 1291-1295, https://doi.org/10.1016/0036-9748(86)90051-7.

[90] Th. Kehagias, Ph. Komninou, R. Grigoriadis, G. Dimitrakopulos, J. G. Antonopoulos, Th. Karakostas, Pyramidal slip in electron beam heated deformed titanium, Interface Science, 3 (3),1996, 195-201, https://doi.org/10.1007/BF00191046.

[91] Th. Kehagias, Ph. Komninou, G. P. Dimitrakopulos, J. G. Antonopoulos, Th. Karakostas, Slip transfer across low-angle grain boundaries of deformed Titanium, Scripta Metallurgica, 33 (12), 1995, 1883-1888, https://doi.org/10.1016/0956-716X(95)00351-U.

[92] J. Shirokoff, I. M. Robertson, H. K. Birnbaum, The Slip Transfer Process Through Grain Boundaries in HCP Ti, Symposia CB – Defect-Interface Interactions, 319, 1993, 263, https://doi.org/10.1557/PROC-319-263.

[93] T. B. Britton, F. P. E. Dunne, A. J. Wilkinson, On the mechanistic basis of deformation at the microscale in hexagonal close-packed metals, Proceedings of The Royal Society A Mathematical Physical and Engineering Sciences, 471 (2178), 2015, https://doi.org/10.1098/rspa.2014.0881.

[94] T. B. Britton, A. J. Wilkinson, Stress fields and geometrically necessary dislocation density distributions near the head of a blocked slip band, Acta Materialia, 60 (16), 2012, 5773-5782, https://doi.org/10.1016/j.actamat.2012.07.004.

[95] J. Luster, M. A. Morris, Compatibility of deformation in two-phase Ti-Al alloys: Dependence on microstructure and orientation relationships, Metallurgical and Materials Transactions A. 26, 1995, 17451756, https://doi.org/10.1007/BF02670762.

[96] S. Han, P. Eisenlohr, M. A. Crimp, ECCI based characterization of dislocation shear in polycrystalline arrays during heterogeneous deformation of commercially pure titanium, Materials Characterization. 142, 2018, 504-514, https://doi.org/10.1016/j.matchar.2018.06.003.

[97] R. Alizadeh, M. Peña-Ortega, T. R. Bieler, J. LLorca, A criterion for slip transfer at grain boundaries in Al, Scripta Materialia, 178, 2020, 408-412, https://doi.org/10.1016/j.scriptamat.2019.12.010.

[98] T. R. Bieler, R. Alizadeh, M. Peña-Ortega, and J. LLorca, An analysis of (the lack of) slip transfer between near-cube oriented grains in pure Al, International Journal of Plasticity, 118, 2019, 269-290, https://doi.org/10.1016/j.ijplas.2019.02.014.

[99] L. Nervo, A. King, A. Fitzner, W. Ludwig, M. Preuss, A study of deformation twinning in a titanium alloy by X-ray diffraction contrast tomography, Acta Materialia, 105, 417-428, https://doi.org/10.1016/j.actamat.2015.12.032.

[100] M. G. Wang, A. H.W. Ngan, Indentation strain burst phenomenon induced by grain boundaries in niobium, Journal of Materials Research, 19 (8), 2004, 2478-2486, https://doi.org/10.1557/JMR.2004.0316.

[101] E. Werner, W. Prantl, Slip transfer across grain and phase boundaries, Acta Metallurgica, 38 (3), 1990, 533-537, https://doi.org/10.1016/0956-7151(90)90159-E.

[102] H. Wang, C. J. Boehlert, Q. D. Wang, D. D. Yin, W. J. Ding, In-situ analysis of the slip activity during tensile deformation of cast and extruded Mg-10Gd-3Y-0.5Zr (wt.%) at 250 °C, Materials Characterization, 116, 2016, 8-17, https://doi.org/10.1016/j.matchar.2016.04.001.

[103] T. Tsuru, Y. Shibutani, and T. Hirouchi, A predictive model for transferability of plastic deformation through grain boundaries, American Institute of Physics (AIP) Advances, 6 (1), 2016, 015004, https://doi.org/10.1063/1.4939819.

[104] Y. Su, S. Han, P. Eisonholr, M. A. Crimp, Slip trace accommodation at grain boundaries in alpha titanium, In preparation.

[105] R. Ding, J. Gong, A. J. Wilkinson, I. P. Jones, A study of dislocation transmission through a grain boundary in hcp Ti-6Al using micro-cantilevers, Acta Materialia, 103, 2016, 416-423, https://doi.org/10.1016/j.actamat.2015.10.023.

[106] J. A. Venables, C. J. Harland, Electron back-scattering patterns—A new technique for obtaining crystallographic information in the scanning electron microscope, The Philosophical Magazine: A Journal of Theoretical Experimental and Applied Physics 8, 27 (5), 1973, https://doi.org/10.1080/14786437308225827.

[107] A. J. Schwartz, M. Kumar, B. L. Adams, Electron backscatter diffraction in materials science, Springer- Verlag US, Boston, MA, 2000, https://doi.org/10.1007/978-1-4757-3205-4.

[108] M. N. Alam, M. Blackman, D. W. Pashley, High-angle Kikuchi patterns, Proceedings of the Royal Society A Mathematical, Physical and Engineering Sciences, 221 (1145), 1954, 224-242, https://doi.org/10.1098/rspa.1954.0017.

[109] F. J. Humphreys, Grain and subgrain characterisation by electron backscatter diffraction, Journal of Material Science, 36, 2001, 3833-3854, https://doi.org/10.1023/A:1017973432592.

[110] D. Dingley, Progressive steps in the development of electron backscatter diffraction and orientation imaging microscopy, Journal of Microscopy, 213 (3), 2004, 214-224, https://doi.org/10.1111/j.0022-2720.2004.01321.x.

[111] S. Zaefferer, On the formation mechanisms, spatial resolution and intensity of backscatter Kikuchi patterns, Ultramicroscopy, 107 (2-3), 2007, 254-266, https://doi.org/10.1016/j.ultramic.2006.08.007.

[112] S. Wright, M. Nowell, J. Basinger, Precision of EBSD based Orientation Measurements, Microscopy and Microanalysis, 17 ,2011, 406–407, https://doi.org/10.1017/S143192761100290X.

[113] K. Kunze, S. I. Wright, B. L. Adams, D. J. Dingley, Advances in automatic EBSP single orientation measurements, Proceedings of the Symposium Microscale Textures of Material, 20, 1993, 41-54, https://doi.org/10.1155/TSM.20.41.

[114] N. C. K. Lassen, Source point calibration from an arbitrary electron backscattering pattern, Journal of Microscopy, 195 (3), 1999, 204-211, https://doi.org/10.1046/j.1365-2818.1999.00581.x.

[115] J. Kacher, C. Landon, B. L. Adams, D. Fullwood, Bragg's Law diffraction simulations for electron backscatter diffraction analysis, Ultramicroscopy, 109 (9), 2009, 1148-1156, https://doi.org/10.1016/j.ultramic.2009.04.007.

[116] J. Basinger, D. Fullwood, J. Kacher, B. Adams, Pattern center determination in electron backscatter diffraction microscopy, Microscopy and Microanalysis, 17 (3), 2011, 330-340, https://doi.org/10.1017/S1431927611000389.

[117] D. Fullwood, T. Ruggles, B. Adams, Mesoscopic Characterization of Heterogeneous Plastic Deformation, Reference Module in Materials Science and Materials Engineering, 2016, https://doi.org/10.1016/B978-0-12-803581-8.02884-8.

[118] K. Z. Troost, P. V. D. Sluis, D. J. Gravesteijn, Microscale elastic‐strain determination by backscatter Kikuchi diffraction in the scanning electron microscope, Applied Physics Letters, 62 (10), 1993, 1110-1112, https://doi.org/10.1063/1.108758.

[119] A. J. Wilkinson, G. Meaden, D. J. Dingley, High-resolution elastic strain measurement from electron backscatter diffraction patterns: New levels of sensitivity, Ultramicroscopy, 106 (4-5), 2006, 307–313, https://doi.org/10.1016/j.ultramic.2005.10.001.

[120] A. J. Wilkinson, A new method for determining small misorientations from electron back scatter diffraction patterns, Scripta Materialia, 44 (10), 2001, 2379-2385, https://doi.org/10.1016/S1359-6462(01)00943-5.

[121] D. Fullwood, M. Vaudin, C. Daniels, T. Ruggles, S. I. Wright, Validation of kinematically simulated pattern HR-EBSD for measuring absolute strains and lattice tetragonality, Materials Characterization, 107, 2015, 270-277, https://doi.org/10.1016/j.matchar.2015.07.017.

[122] A. J. Wilkinson, T. B. Britton, J. Jiang, P. S. Karamched, A review of advances and challenges in EBSD strain mapping, IOP Conf. Series: Materials Science and Engineering, 55, 2014, 012020, http://dx.doi.org/10.1088/1757-899X/55/1/012020.

[123] A. Winkelmann, Principles of depth‐resolved Kikuchi pattern simulation for electron backscatter diffraction, Journal of Microscopy, 239 (1), 2010, 32-45, https://doi.org/10.1111/j.1365-2818.2009.03353.x.

[124] P. B. Hirsch, M. J. Whelan, A kinematical theory of diffraction contrast of electron transmission microscope images of dislocations and other defects, Philosophical Transactions of the Royal Society of London. Series A, Mathematical and Physical Sciences, 252 (1070), 1960, 499–529, https://doi.org/10.1098/rsta.1960.0013.

[125] A. Howie, M. J. Whelan, Diffraction contrast of electron microscope images of crystal lattice defects. III. Results and experimental confirmation of the dynamical theory of dislocation image contrast, Philosophical Transactions of the Royal Society of London. Series A, Mathematical and Physical Sciences, 267 (1329), 1962, 206-230, https://doi.org/10.1098/rspa.1962.0093.

[126] P. B. Hirsch, R. W. Horne, M. J. Whelan, LXVIII. Direct observations of the arrangement and motion of dislocations in aluminum, Philosophical Magazine, 1 (7), 1956, 677-684, https://doi.org/10.1080/14786435608244003.

[127] M. Knoll, J. Kügler, Subjective light pattern spectroscopy in the encephalographic frequency range, Nature (London), 184, 1959, 1823–1824, https://doi.org/10.1038/1841823a0.

[128] R. Erni, M. D. Rossell, C. Kisielowski, U. Dahmen, Atomic-resolution imaging with a sub-50-pm electron probe, Physical Review Letters, 102 (9), 2009, https://doi.org/10.1103/PhysRevLett.102.096101.

[129] C. Kisielowski, B. Freitag, M. Bischoff, H. van Lin, S. Lazar, G. Knippels, P. Tiemeijer, M. van der Stam, S. von Harrach, M. Stekelenburg, M. Haider, S. Uhlemann, H. Müller, P. Hartel, B. Kabius, D. Miller, I. Petrov, E. A. Olson, T. Donchev, E. A. Kenik, A. R. Lupini, J. Bentley, S. J. Pennycook, I. M. Anderson, A. M. Minor, A. K. Schmid, T. Duden, V. Radmilovic, Q. M. Ramasse, M. Watanabe, R. Erni, E. A. Stach, P. Denes, U. Dahmen, Detection of single atoms and buried defects in three dimensions by aberration-corrected electron microscope with 0.5-Å information limit, Microscopy and Microanalysis, 14 (5), 2008, 469-477, https://doi.org/10.1017/S1431927608080902.

[130] M. H. F. Overwijk, F. C. van den Heuvel, C. W. T. Bulle‐Lieuwma, Novel scheme for the preparation of transmission electron microscopy specimens with a focused ion beam, Journal of Vacuum Science & Technology B: Microelectronics and Nanometer Structures Processing, Measurement, and Phenomena, 11 (6), 1993, 2021-2024, https://doi.org/10.1116/1.586537.

[131] F. A. Stevie, T. C. Shane, P. M. Kahora, R. Hull, D. Bahnck, V. C. Kannan, E. David, Applications of focused ion beams in microelectronics production, design and development, Surface and Interface Analysis, 23 (2), 1995, 61-68, https://doi.org/10.1002/sia.740230204.

[132] L. A. Giannuzzi, F. A. Stevie, A review of focused ion beam milling techniques for TEM specimen preparation, Micron, 30 (3), 1999, 197-204, https://doi.org/10.1016/S0968-4328(99)00005-0.

[133] A. J. Leslie, K. L. Pey, K. S. Sim, M. T. F. Beh, G. P. Goh, TEM sample preparation using FIB: Practical problems and artifacts, 21st International Symposium for Testing and Failure Analysis, ASM International, 1995, 53, https://www.osti.gov/servlets/purl/1426988.

[134] M. Andrzejczuk, T. Płociński, W. Zieliński, K. J. Kurzydłowski, TEM characterization of the artefacts induced by FIB in austenitic stainless steel, Journal of Microscopy, 237 (3), 2010, 439-442, https://doi.org/10.1111/j.1365-2818.2009.03288.x.

[135] F. Lagattu, F. Bridier, P. Villechaise, J. Brillaud, In-plane strain measurements on a microscopic scale by coupling digital image correlation and an in situ SEM technique, Materials Characterization, 56 (1), 2006, 10-18, https://doi.org/10.1016/j.matchar.2005.08.004.

[136] T. J. Ruggles, D. T. Fullwood, Estimations of bulk geometrically necessary dislocation density using high resolution EBSD, Ultramicroscopy, 133, 2013, 8-15, https://doi.org/10.1016/j.ultramic.2013.04.011.

[137] B. E. Dunlap, T. J. Ruggles, D. T. Fullwood, B. Jackson, M. A. Crimp, Comparison of dislocation characterization by electron channeling contrast imaging and cross-correlation electron backscattered diffraction, Ultramicroscopy, 184, 2018, 125-133, https://doi.org/10.1016/j.ultramic.2017.08.017.

[138] T. J. Ruggles, Y. S. J. Yoo, B. E. Dunlap, M. A. Crimp, J. Kacher, Correlating results from high resolution EBSD with TEM- and ECCI-based dislocation microscopy: Approaching single dislocation sensitivity via noise reduction, Ultramicroscopy, 210, 2020, 112927, https://doi.org/10.1016/j.ultramic.2019.112927.

[139] P. Morin, M. Pitaval, D. Besnard, G. Fontaine, Electron-channelling imaging in scanning electronmicroscopy, Philosophical Magazine A, 40(4), 1979, 511-524, https://doi.org/10.1080/01418617908234856.

[140] B. A. Simkin, M. A. Crimp, An experimentally convenient configuration for electron channeling contrast imaging, Ultramicroscopy, 77 (1-2), 1999, 65-75, http://dx.doi.org/10.1016/S03043991(99)00009-1.

[141] M. A. Crimp, Scanning electron microscopy imaging of dislocations in bulk materials, using electron channeling contrast, Microscopy Research and Technique, 69 (5), 2006, 374-381, https://doi.org/10.1002/jemt.20293.

[142] S. Zaefferer, N.-N. Elhami, Theory and application of electron channeling contrast imaging under controlled diffraction conditions, Acta Materialia, 75, 2014, 20-50, http://dx.doi.org/10.1016/j.actamat.2014.04.018.

[143] H. Mansour, J. Guyon, M. A. Crimp, N. Gey, B. Beausir, N. Maloufi, Accurate electron channeling contrast analysis of dislocations in fine grained bulk materials, Scripta Materialia, 84-85, 2014, 11-14, http://dx.doi.org/10.1016/j.scriptamat.2014.03.001.

[144] M. A. Crimp, B. Simkin, B. Ng, Demonstration of the $g \cdot b \times u = 0$ edge dislocation invisibility criterion for electron channeling contrast imaging, Philosophical Magazine Letters, 81 (12), 2001, 833-837, https://doi.org/10.1080/09500830110088755.

[145] Y. N. Picard, M. E. Twigg, J. D. Caldwell, C. R. Eddy Jr., M. A. Mastro, R. T. Holm, Resolving the Burgers vector for individual GaN dislocations by electron channeling contrast imaging, Scripta Materialia, 61 (8), 2009, 773-776, https://doi.org/10.1016/j.scriptamat.2009.06.021.

[146] D. C. Joy, D. E. Newbury, D. L. Davidson, Electron channeling patterns in the scanning electron microscope, Journal of Applied Physics, 53 (8), 1982, 81-122, https://doi.org/10.1063/1.331668.

[147] J. Guyon, H. Mansour, N. Gey, M. A. Crimp, S. Chalal, N. Maloufi, Sub-micron resolution

selected area electron channeling patterns, Ultramicroscopy. 149 (2015) 34–44. https://doi.org/10.1016/j.ultramic.2014.11.004.

[148] R. D. Kerns, S. Balachandran, A. H. Hunter, M. A. Crimp, Ultra-high spatial resolution selected area electron channeling patterns, Ultramicroscopy, 210, 2020, 112915, https://doi.org/10.1016/j.ultramic.2019.112915.

[149] I. G. Urrutia, S. Zaefferer, D. Raabe, Electron channeling contrast imaging of twins and dislocations in twinning-induced plasticity steels under controlled diffraction conditions in a scanning electron microscope, Scripta Materialia, 61 (7), 2009, 737-740, https://doi.org/10.1016/j.scriptamat.2009.06.018.

[150] J. T. Czernuszka, N. J. Long, E. D. Boyes, P. B. Hirsch, Imaging of dislocations using backscattered electrons in a scanning electron microscope, 62 (4), 1990, 227-232, https://doi.org/10.1080/09500839008215127.

[151] A. J. Wilkinson, G. R. Anstis, J. T. Czernuszka, N. J. Long, P. B. Hirsch, Electron channeling contrast imaging of interfacial defects in strained silicon-germanium layers on silicon, Philosophical Magazine A, 68 (1), 1993, 59-80, https://doi.org/10.1080/01418619308219357.

[152] L. Han, B. Gamm, Optimizing electron channeling contrast imaging condition in scanning electron microscope, European Microscopy Congress 2016: Proceedings, https://doi.org/10.1002/9783527808465.EMC2016.6188.

[153] H. Kriaa, A. Guitton, N. Maloufi, Fundamental and experimental aspects of diffraction for characterizing dislocations by electron channeling contrast imaging in scanning electron microscope, Scientific Report, 7, 2017, 9742, https://doi.org/10.1038/s41598-017-09756-3.

[154] P. Morin, M. Pitaval, D. Besnard, G. Fontaine, Electron-channeling imaging in scanning electron microscopy, Philosophical Magazine A, 40 (4), 1979, 511-524, https://doi.org/10.1080/01418617908234856.

[155] M. A. Sutton, W. J. Wolters, W. H. Peters, W. F. Ranson, S. R. McNeill, Determination of displacements using an improved digital correlation method, Image and Vision Computing, 1 (3), 1983, 133-139, https://doi.org/10.1016/0262-8856(83)90064-1.

[156] H. A. Bruck, S. R. McNeill, M. A. Sutton, W. H. Peters III, Digital image correlation using Newton-Raphson method of partial differential correction, Experimental Mechanics, 29, 1989, 261-267, https://doi.org/10.1007/BF02321405.

[157] Y. L. Loo, R. L. Willett, K. W. Baldwin, J. A. Rogers, Additive, nanoscale patterning of metal films with a stamp and a surface chemistry mediated transfer process: Applications in plastic electronics, Applied Physics Letters, 81 (3), 2002, 562, https://doi.org/10.1063/1.1493226.

[158] M. A. Sutton, N. Li, D. C. Joy, A. P. Reynolds, X. Li, Scanning electron microscopy for quantitative small and large deformation measurements part i: sem imaging at magnifications from 200 to 10,000, Experimental Mechanics, 47, 2007, 775-787, https://doi.org/10.1007/s11340-007-9042-z.

[159] W. A. Scrivens, Y. Luo, M. A. Sutton, S. A. Collette, M. L. Myrick, P. Miney, P. E. Colavita, A. P. Reynolds, X. Li, Development of patterns for digital image correlation measurements at reduced length scales, Experimental Mechanics, 47, 2007, 63-77, https://doi.org/10.1007/s11340-006-5869-y.

[160] M. Fan, A. G. Brolo, Silver nanoparticles self-assembly as SERS substrates with near single molecule detection limit, Physical Chemistry Chemical Physics, 11 (34), 2009, 7381-7389, https://doi.org/10.1039/B904744A.

[161] I. Liascukiene, N. Aissaoui, S. J. Asadauskas, J. Landoulsi, J. -F. Lambert, Ordered nanostructures on a hydroxylated aluminum surface through the self-assembly of fatty acids, Langmuir, 28 (11), 2012, 5116-5124, https://doi.org/10.1021/la2051542.

[162] A. D. Kammers, S. Daly, Self-assembled nanoparticle surface patterning for improved digital image correlation in a scanning electron microscope, Experimental Mechanics, 53, 2013, 1333-1341, https://doi.org/10.1007/s11340-013-9734-5.

[163] Z. Chen, W. Lenthe, J. C. Stinville, M. Echlin, T. M. Pollock, S. Daly, High-resolution deformation mapping across large fields of view using scanning electron microscopy and digital image correlation, Experimental Mechanics, 58, 2018, 1407-1421, https://doi.org/10.1007/s11340-018-0419-y.

[164] F. Ohnesorge, G. Binnig, True atomic resolution by atomic force microscopy through repulsive and attractive forces, Science, 260 (5113), 1993, 1451-1456, https://doi.org/10.1126/science.260.5113.1451.

[165] F. J. Giessibl, Atomic resolution of the silicon (111)-(7x7) surface by atomic force microscopy, Science, 267 (5194), 1995, 68-71, https://doi.org/10.1126/science.267.5194.68.

[166] F. Gołek, P. Mazur, Z. Ryszka, S. Zuber, AFM image artifacts, Applied Surface Science, 304, 2014, 11-19, https://doi.org/10.1016/j.apsusc.2014.01.149.

[167] B. Voigtländer, Artifacts in AFM. In: Atomic Force Microscopy, NanoScience and Technology, Springer, Cham, 2019, https://doi.org/10.1007/978-3-030-13654-3_8.

[168] T. Strahlendorff, G. Dai, D. Bergmann, R. Tutscha, Tip wear and tip breakage in high-speed atomic force microscopes, Ultramicroscopy, 201, 2019, 28-37, https://doi.org/10.1016/j.ultramic.2019.03.013.

[169] C. Blochwitz, J. Brechbühl, W. Tirschler, Analysis of activated slip systems in fatigue nickel polycrystals using the EBSD-technique in the scanning electron microscope, Materials Science and Engineering: A, 210 (1-2), 1996, 42-47, https://doi.org/10.1016/0921-5093(95)10076-8.

[170] J. Veselý, M. Cieslar, C. Coupeau, J. Bonneville, Quantitative numerical method for analysing slip traces observed by AFM, Surface Topography: Metrology and Properties, 1, 2013, 015002, http://iopscience.iop.org/2051-672X/1/1/015002.

[171] S. Han, M. A. Crimp, ECCI analysis of shear accommodations at grain boundaries in commercially pure alpha titanium, International Journal of Plasticity, in press, 2020, https://doi.org/10.1016/j.ijplas.2020.102731.

[172] Y. Su, C. Zambaldi, D. Mercier, P. Eisenlohr, T. R. Bieler, M. A. Crimp, Quantifying deformation processes near grain boundaries in a titanium using nanoindentation and crystal plasticity modeling, International Journal of Plasticity, 86, 2016, 170-186, https://doi.org/10.1016/j.ijplas.2016.08.007.

[173] D. E. J Armstrong, A. J. Wilkinson, S. G. Roberts, Measuring local mechanical properties using FIB machined microcantilevers, Symposium II – Probing Mechanics at Nanoscale Dimensions, 1185, 2009, 1185-I102-08, https://doi.org/10.1557/PROC-1185-II02-08.

[174] D. E. J Armstrong, A. J. Wilkinson, S. G. Roberts, Micro-mechanical measurements of fracture toughness of bismuth embrittled copper grain boundaries, Philosophical Magazine, 92, 2012, 394-400, https://doi.org/10.1080/09500839.2011.573813.

[175] G. Thomas, M. J. Goringe, Transmission Electron Microscopy of Materials, John Wiley & Sons, New York, 1979.

[176] I. Epelboin, Amincissement électrolytique très poussé et ses applications, Rev. Met. Paris, 49 12 (1952) 863-875, https://doi.org/10.1051/metal/195249120863.

[177] P. A. Jacquet, On the anodic behavior of copper in aqueous solutions of orthophosphoric acid, Trans. Electrochem. Soc., 1936, 69, 629– 655. https://doi.org/10.1149/1.3498234.

[178] G. Yang, B. Wang, K. Tawfiq, H. Wei, S. Zhou, G. Chen, Electropolishing of surfaces: theory and applications, Surface Engineering, 2017, 33:2, 149-166, https://doi.org/10.1080/02670844.2016.1198452.

[179] A. Chandra, On the Mechanism of Niobium Electropolishing, Thesis, 2012, Ohio State University

[180] H. Oguri, S. Hishiyama, T. Oishi, M. Hirama, Enantio-controlled synthesis of the ab ring moiety of ciguatoxin, Synlett, 12, 1995, 1252-1254, https://doi.org/10.1055/s-1995-5259.

[181] E. J. Corey, A. Venkateswarlu, Protection of hydroxyl groups as tert-butyldimethylsilyl derivatives, Journal of the American Society, 94 (17), 1972, 6190-6191, https://doi.org/10.1021/ja00772a043.

[182] S. Higashibayashi, K. Shinko, T. Ishizu, K. Hashimoto, H. Shirahama, Selective deprotection of t-butyldiphenylsilyl ethers in the presence of t-butyldimethylsilyl ethers by tetrabutylammonium fluoride, acetic acid, and water, Synlett, 9, 2000, 1306-1308, https://doi.org/10.1055/s-2000-7158.

[183] B. F. Bonini, M. C. Franchini, M. Fochi, G. Mazzanti, A. Ricci, Desilylation of (Z)-á-dimethylphenylsilyl vinyl sulfides with fluorideion: revised mechanism for phenyl group migration in substrates containing an electron-withdrawing group β to the sulfur, Journal of Chemical Society, Perkin Transactions 1, 21, 1997, 3211-3217, https://doi.org/10.1039/A703662K.

[184] T. W. Greene, P. G. M. Wuts, Protective groups in organic synthesis, 3rd ed.; John Wiley & Sons: New York, 1999, https://doi.org/10.1002/0471220574.

[185] R. Sperry, S. Han, Z. Chen, S. H. Daly, M. A. Crimp, D. Fullwood, Comprehensive study and comparison of various deformation measurement methods in Ti7Al alloy, in preparation.

[186] Z. Chen, S. H. Daly, Active Slip System Identification in Polycrystalline Metals by Digital Image Correlation (DIC), Experimental Mechanics 57 (1), 2017, 115-27. https://doi.org/10.1007/s11340-016-0217-3.

[187] GitHub - BYU-MicrostructureOfMaterials/OpenXY, https://github.com/BYUMicrostructureOfMaterials/OpenXY.

[188] R. Sperry, A. Harte, J. Q. da Fonseca, E. R. Homer, R. H. Wagoner, D. T. Fullwood, Slip band characteristics in the presence of grain boundaries in nickel-based superalloy, Acta Materialia, 193, 2020, 229-238, https://doi.org/10.1016/j.actamat.2020.04.037.

[189] F. D. Gioacchino, T. E. J. Edwards, G. N. Wells, W. J. Clegg, A new mechanism of strain transfer in polycrystals, Scientific Reports, 10, 2020, 10082, https://doi.org/10.1038/s41598-020-66569-7.

[190] L. E. Murr, Dislocation ledge sources: dispelling the myth of Frank–Read source importance, Metallurgical and Materials Transactions A, 47, 2016, 5811–5826, https://doi.org/10.1007/s11661-015-3286-5.

[191] T. L. Burnett, R. Kelley, B. Winiarski, L. Contreras, M. Daly, A. Gholinia, M. G. Burke, P. J. Withers, Large volume serial section tomography by Xe Plasma FIB dual beam microscopy, Ultramicroscopy, 161, 2016, 119-129, https://doi.org/10.1016/j.ultramic.2015.11.001.

[192] L. F. Allard, D. N. Leonard, J. D. Poplawsky, M. F. Chisholm, B. D. Eckhart, A. Shyam, F. S. Walden, B. B. Larson, R. Kelly, A. Stokes, W. C. Bigelow, The Utility of Xe-Plasma FIB for Preparing Aluminum Alloy Specimens for MEMS-based In Situ Double-Tilt Heating Experiments, Microscopy and Microanalysis, 25, 2019, 1442-1443, https://doi.org/10.1017/S1431927619007943.